SYNTHESIS OF TETRA-AZAPORPHYRINS, PHTHALOCYANINES AND LANTHANIDE DOUBLE-DECKER SANDWICH COMPLEXES

Nelson Giménez Agulló

UNIVERSITAT ROVIRA I VIRGILI
SYNTHESIS OF TETRA-AZAPORPHYRINS, PHTHALOCYANINES AND LANTHANIDE DOUBLE-DECKER SANDWICH COMPLEXES
Nelson Giménez Agulló

UNIVERSITAT ROVIRA I VIRGILI
SYNTHESIS OF TETRA-AZAPORPHYRINS, PHTHALOCYANINES AND LANTHANIDE DOUBLE-DECKER SANDWICH COMPLEXES
Nelson Giménez Agulló

PhD Thesis

SYNTHESIS OF TETRA-AZAPORPHYRINS, PHTHALOCYANINES AND LANTHANIDE DOUBLE-DECKER SANDWICH COMPLEXES

Nelson Giménez Agulló

Supervised by

Prof. Dr. Pablo Ballester and

Prof. Dr. José Ramón Galán Mascarós

Tarragona, July 2016

UNIVERSITAT
ROVIRA i VIRGILI

UNIVERSITAT ROVIRA I VIRGILI
SYNTHESIS OF TETRA-AZAPORPHYRINS, PHTHALOCYANINES AND LANTHANIDE DOUBLE-DECKER SANDWICH COMPLEXES
Nelson Giménez Agulló

Av. Països Catalans, 16
43007 Tarragona
Tel +34 977 920 200
Fax +34 977 920 224

Prof. Dr. Pablo Ballester, Group Leader of the Institute of Chemical Research of Catalonia (ICIQ) and Research Professor of the Catalan Institution for Research and Advanced Studies (ICREA), and Prof. Dr. José Ramón Galán Mascarós, Group Leader of the Institute of Chemical Research of Catalonia (ICIQ) and Research Professor of the Catalan Institution for Research and Advanced Studies (ICREA),

CERTIFIES that the present research work entitled "**Synthesis of Tetra-azaporphyrins, Phthalocyanines and Lanthanide Double-Decker Sandwich Complexes**" that Nelson Giménez Agulló presents to obtain the PhD degree in Chemistry, has been carried out under our supervision in the ICIQ and fulfils all the requirements to be awarded with the Doctor Mention.

Tarragona, July 2016

PhD Thesis supervisors

Prof. Dr. Pablo Ballester

Prof. Dr. José Ramón Galán Mascarós

UNIVERSITAT ROVIRA I VIRGILI
SYNTHESIS OF TETRA-AZAPORPHYRINS, PHTHALOCYANINES AND LANTHANIDE DOUBLE-DECKER SANDWICH COMPLEXES
Nelson Giménez Agulló

"Perquè hi haurà un dia que no podrem més i llavors ho podrem tot"

Vicent Andrés Estellés

UNIVERSITAT ROVIRA I VIRGILI
SYNTHESIS OF TETRA-AZAPORPHYRINS, PHTHALOCYANINES AND LANTHANIDE DOUBLE-DECKER SANDWICH COMPLEXES
Nelson Giménez Agulló

Acknowledgements

Primerament voldria agrair als meus supervisors, Pau Ballester i José Ramón Galán, per l'oportunitat que m'han donat de formar part d'aquest projecte i poder desenvolupar la tesi als seus grups de recerca. Moltes gràcies a tots dos per tot el que m'heu ensenyat i per tot el vostre suport durant aquests quatre anys.

I also want to thank the current and former members from both research groups. I will never forget all the moments we have shared together. Thanks to : Louis Adriaenssens, Moira Ciardi, Virginia Valderrey, Mónica Espelt, Saša Korom, Albano Galán, Gemma Aragay, Daniel Hernández, Ramón Romero, Frank Arroyave, Alejandro Díaz, Luís Escobar, Rajesh Pudi, Giulia Moncelsi, Jordi Aguilera and Guillem Peñuelas from Ballester's lab. Special thanks to Gemma Aragay for her dedication in the lab, amiability and all the papers and thesis' corrections. I would also like to thank to: Sara Goberna, Sara Pintado, Veronica Gómez, YS, Joaquin Soriano, Vanesa Lillo, Cristina Sáenz, Neus Corella, Pilar Maldonado, Bárbara Rodríguez, Marta Blasco, Franziska Hegner, Lijuan Han, Mabel Torréns, Felipe Garcés and Jesus González from JR's lab. It was a pleasure to work with you guys, I wish you all the best. Thanks to Beatriz Martín and Paula Segovia for your help and support during these years.

Thanks to Prof. Willi Auwärter for giving me the opportunity to carry out part of my research in his laboratories during my short stay at the Munich University. I also want to thanks Tobias Kaposi and Felix Bischoff for their kind attention and for teaching me how to perform STM measurements. I would like to thank to Prof. David Ecija and his PhD researcher Borja Cirera for their hospitality and support during my stay in his laboratory at IMDEA (Madrid). Part of this thesis would not be possible without your collaboration.

Acknowledgements

Gràcies al club de la nicotina format per Ximo i Jordi Ampurdanés, sempre vos estaré agraït per oferir-me la vostra amistat i per tots els moments que hem viscut junts al llarg d'aquests quatre anys.

Als meus pares que tant han lluitat per a que tant la meua estimada germana Jéssica com jo seguirem estudiant. Perquè mai heu dubtat de que aconseguirem tot el que ens proposem i sempre heu estat al nostre costat en els bons moments i en els no tant bons. Perquè gràcies a vosaltres sóc la persona qui sóc hui en dia, sempre vos estaré agraït. A la meua germana Jéssica, tu que des que vas néixer et vas convertir en el tresor més volgut que una persona pot tenir. Als meus avis paterns, Teresa i Pepe "el ferrer", sempre guardaré un bon record de vosaltres, allà on estigau va per vosaltres. Uelo, encara recorde com si fos ahir quan tornava de València i em deies: "els experiments s'han de fer a casa i amb gaseosa". I a tu uela, com un record d'infantesa sempre et recordaré a tu, Teresa… Als meus avis materns, Gregoria i Pepe "el socarrat", gràcies per haver format part de la meua educació com a persona i per tots els vermudets dels dissabtes que hem fet i ens queden per fer. Vos he trobat molt a faltar durant aquests quatre anys…

A Sanela, la millor companya de vida que hagués pogut trobar en aquest immens món. Per fer-me sempre sentir especial al teu costat i per no deixar mai de creure en mi, inclús en els moments més difícils. Volim te.

We thank MINECO for support through Severo Ochoa Excellence Accreditation 2014-2018 (SEV-2013-0319)

Als meus pares,

UNIVERSITAT ROVIRA I VIRGILI
SYNTHESIS OF TETRA-AZAPORPHYRINS, PHTHALOCYANINES AND LANTHANIDE DOUBLE-DECKER SANDWICH COMPLEXES
Nelson Giménez Agulló

Table of Contents

Table of contents

UNIVERSITAT ROVIRA I VIRGILI
SYNTHESIS OF TETRA-AZAPORPHYRINS, PHTHALOCYANINES AND LANTHANIDE DOUBLE-DECKER SANDWICH COMPLEXES
Nelson Giménez Agulló

Chapter 1

General Introduction

UNIVERSITAT ROVIRA I VIRGILI
SYNTHESIS OF TETRA-AZAPORPHYRINS, PHTHALOCYANINES AND LANTHANIDE DOUBLE-DECKER SANDWICH COMPLEXES
Nelson Giménez Agulló

1.1 Tetrapyrrolic macrocycles

The fascinating structures of naturally occurring porphyrins and their metal complexes have been engineered by nature to give functional pigments. Tetrapyrrolic macrocycles are hetero-macrocycles that play essential roles in vital biological processes, including photosynthesis and oxygen transport in blood. Hence, they are named "the colors of life". They occur widely in nature with many important biological representatives, and these include heme, chlorophylls and vitamin B_{12} for porphyrins amongst several others (Figure 1.1).[1] Heme is responsible for the transport of oxygen while chlorophyll is useful for the transformation of light into chemical energy in plants during the photosynthesis. In the blood, most of the tetrapyrrolic macrocycles are in the red cells in very small quantities as protoporphyrin and coproporphyrin.

Porphyrins are intensely colored compounds containing a macrocyclic core of twenty carbon atoms and four nitrogen atoms. The word "porphyrin" derives from "porphura" meaning "purple" in Greek. The aromatic macrocycle is constructed from four bridged pyrrole rings held together by carbon atoms. The structure of porphyrins was first proposed by W. Kuster in 1912 and was received with skepticism at that time, because the macrocycle seemed to be intrinsically unstable. The scientific community has shown a great interest in the development of tetrapyrrole macrocyclic compounds, especially after the structure elucidation of protoporphyrin IX by Fisher in 1929 and the synthesis of chlorophyll *a* by Woodward in 1960.[2]

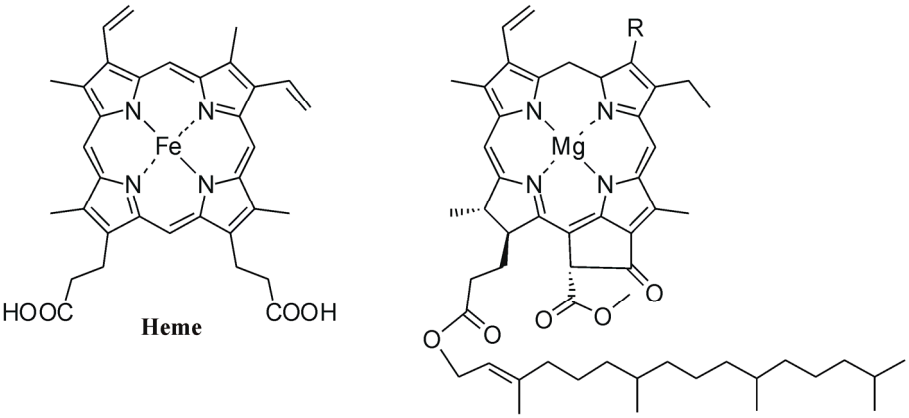

Heme

Chlorophyll a (R = CH_3)
Chlorophyll b (R = CHO)

Figure 1.1 Line-drawing chemical structures of naturally occuring tetrapyrrole macrocycles

Porphyrins and their best known synthetic analogs, phthalocyanines represent one of the most widely studied macrocyclic ring like systems. Besides the central role of porphyrin derivatives in photosynthesis, respiration and other vital functions, they have a promising future in several fields such as catalysis, medicine and preparation of electronic materials.

Among the huge variety of porphyrinoids known, phthalocyanines are of special interest due to their interesting electronic and physicochemical properties. Phthalocyanines (Pcs) are synthetic planar macrocycles constituted by four isoindole units linked via sp^2 hybridized nitrogen atoms. They present a 18 π-electrons aromatic system delocalized over an arrangement of alternated carbon and nitrogen atoms. Pcs are closely related to the naturally occurring porphyrin ring system being their major distinction the presence of the four *meso* nitrogen atoms in their aromatic core (Figure 1.2).

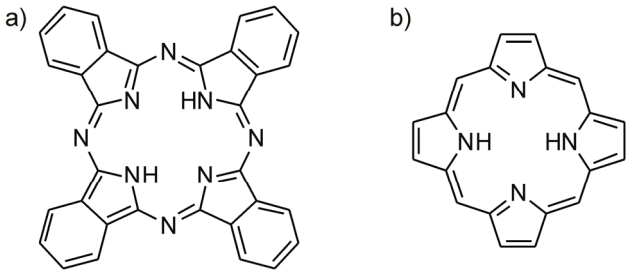

Figure 1.2 a) Line-drawing chemical structure of a phthalocyanine and b) chemical structure of a porphyrin

The name phthalocyanine was given by Reginald P. Linstead and is a combination of the prefix *phthal*, originally from the Greek *naptha* (rock oil), to emphasise the association with its various phthalic acid-derived precursors, and the Greek *cyanine* (blue). He was the first academic to investigate the structure of Pcs after their accidental discovery. Braun and Tcherniac recognized phthalocyanine for the first time in 1907 as a bluish insoluble by-product during the preparation of *o*-cyanobenzamide from phthalimide and acetic anhydride at the South Metropolitan Gas Company in London.[3] However, this discovery was of no special interest at that time. The industrial discovery of the Pcs was made at the Grangemouth plant of Scottish Dyes Ltd., in 1928. During the industrial preparation of phthalimide form phthalic anhydride and ammonia, a greenish blue impurity constantly appeared. This blue substance was iron phthalocyanine formed by the reaction of phthalimide in the iron wall of the reaction vessel. After a series of investigations, Linstead and coworkers at the University of London proposed the molecular structure of Pc and developed improved synthetic methods for several metallophthalocyanines (MPcs) from 1929 to 1939.[4] However, it was not until 1936 that the structure of the iron phthalocyanine was determined by Robertson using X-ray diffraction showing their characteristic ring structure.[5]

Almost all early reported phthalocyanine complexes possessed low solubility in most known organic solvents due to they were unsubstituted on the periphery of the ring. A great variety of functional groups has been used to decorate the Pc scaffold, and increase its solubility. There are different ways of modifying the phthalocyanine structure such as the change of the central atom and/or its axial coordination, change of the meso-atoms and its

peripheral substitution. The introduction of the substituent groups can be performed directly on an already synthesized Pc scaffold or they can be incorporated on the phthalonitrile precursors prior their condensation to afford the Pc ring. The functional groups are usually introduced as substituents in the six-membered ring of the isoindole units. The substituents located at position 1, 4, 8, 11, 15, 18, 22 and 25 of the phthalocyanine ring are called α-substituents, while those located at position 2, 3, 9, 10, 16, 17, 23 and 24 are named as β-substituents (Figure 1.3). The introduction of peripheral substituents on the phthalocyanine ring can increase their solubility in common organic solvents or in water. For example, alkyl chains,[6] ethers[7], amines[8] and thiols[9] have been introduced as solubilizing groups of Pc in organic solvents. On the other hand, sulphonic acids are the preferred substituents to promote solubility of the Pc in aqueous media.[10]

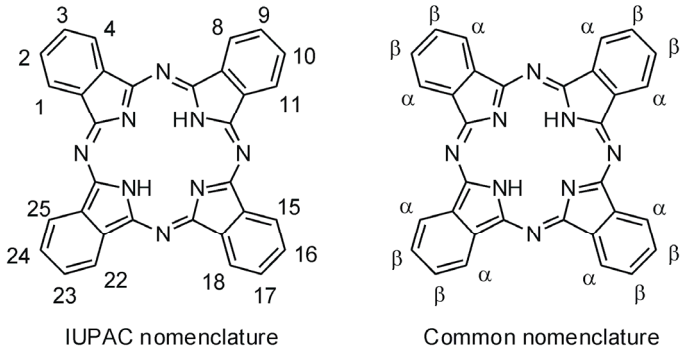

Figure 1.3 Nomenclature scheme of the potential sites for the phthalocyanine substitution.

Phthalocyanines are able to coordinate metals through their isoindole nitrogen atoms producing MPcs. The hydrogen atoms of the central cavity can be replaced by more than 70 different elements, generating the MPcs (Figure 1.4). As the coordination number of the macrocycle is four, according to the size and oxidation state of the metal, the metal atom is located in the central cavity of the Pc ring. With the metals that prefer higher coordination number, one or two axial ligands coordinate the central metal atom giving rise to structures with pyramidal, tetrahedral or octahedral geometries. However, when metals having large van der Waals radii are used (i.e. lanthanides or actinides) in the metallation process, 1:2 or

2:3 metal:Pc complexes are obtained instead of the simple 1:1 metal-Pc complex. The 1:2 complexes, usually referred as double-decker sandwich complexes, consist in a trivalent lanthanide ion located in the central position created by two parallel but staggered phthalocyanine ligands. The two phthalocyanine rings can be identical or they can differ by their substituents. The former compounds are named homoleptic whereas the latter are called heteroleptic complexes. This last designation also applies for the species in which one ring is not a phthalocyanine, but rather is another tetrapyrrolic ligand. Sandwich-type metal complexes of tetrapyrrolic macrocycles have been known since 1936, with the first synthesis of tin(IV) bis(phthalocyanine) by Linstead and co-workers.[11] The complex displayed a sandwich-type double-decker structure formed by the tetra positively charged central metal ion that coordinates to two negatively doubly charged phthalocyanine anions in a distorted square-antiprism geometry. 2:3 complexes are formed by two metal cations sandwiched between three phthalocyanine rings and are often called triple-decker complexes. The term homonuclear is used when the 2:3 complex is built with the same two cations whereas structures with different metal cations are named heteronuclear triple-deckers.

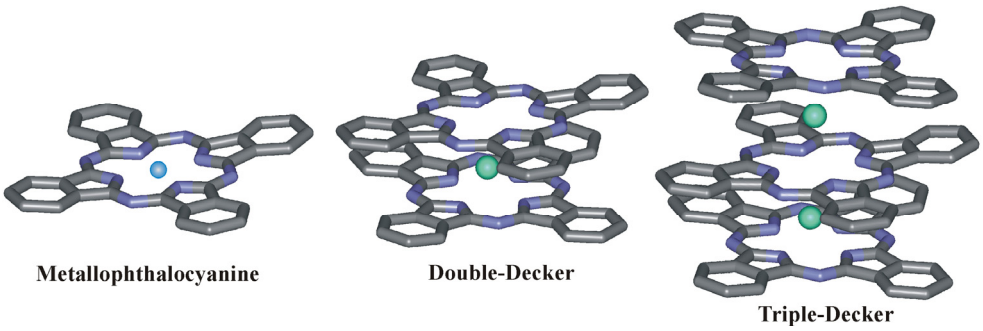

Figure 1.4 Model structures representing a metallophthalocyanine, 1:2 metal:Pc double-decker complex and 2:3 metal:Pc triple-decker complex.

1.2 Synthesis of Phthalocyanines

Several strategies can be applied to synthesize phthalocyanines according to the literature (Figure 1.5). Linstead's initial series of papers contained the experimental details for the preparation of Pcs from phthalodinitrile (*ortho*-dicyanobenzene), which is considered the best precursor for Pc synthesis on a laboratory scale. Pcs are generally formed upon heating substituted derivatives of *ortho*-phthalic acid (i.e. imides, amides, anhydrides and nitriles) that contain nitrogen functional groups via reductive cyclotetramerization reaction. Although the classical precursors for the Pc formation are phthalonitriles and diiminoisoindolines, phthalic acid, phthalic anhydride, phthalimide, *o*-cyanobenzamide or dibromobenze can also be used as starting materials since these compounds leads to the *in situ* formation of the actual precursors for the cyclotetramerization process which are phthalonitrile and diiminoisoindoles.

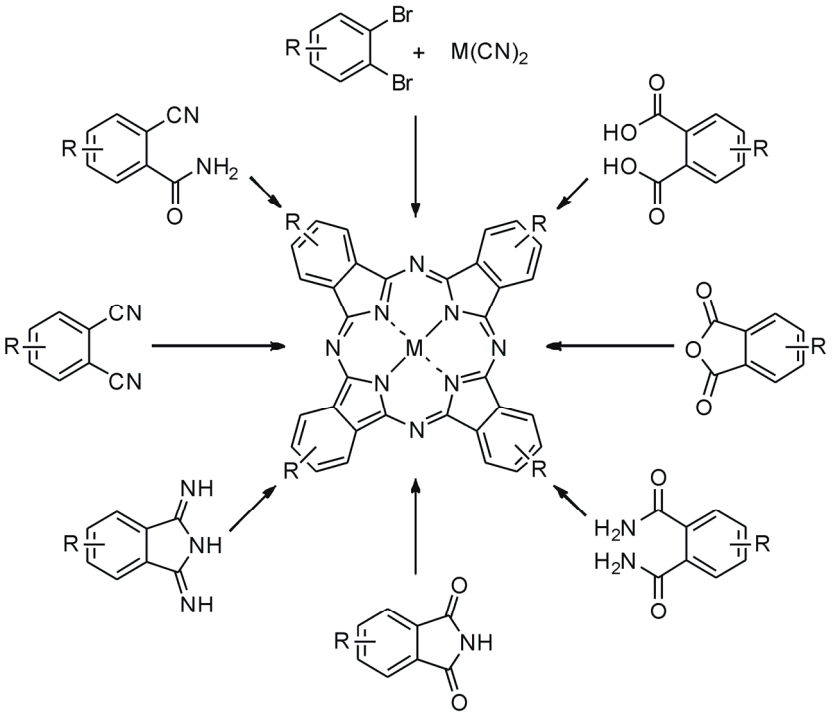

Figure 1.5 Different synthetic routes to form MPcs.

Phthalonitriles are the most useful precursors yielding phthalocyanine complexes in good yields. They are transformed into phthalocyanines via a metal template assisted cyclotetramerization reaction which generally involves elevated temperatures in either a melt of reagents or in a high boiling point solvent in the presence of a metal source. The macrocyclization can be also accomplished by refluxing phthalonitriles in 1-pentanol or another similar alcohol in the presence of an organic base such as DBU, piperidine or cyclohexylamine. The use of strong organic bases permits the reaction to proceed under milder conditions by acting as an electron acceptor. This promotes the formation of the alcoholate that reacts with the dinitrile cyano groups forming an alkoxyisoindoline which is rapidly cyclized to form the phthalocyanine. The use of precursors like phthalic anhydrides and phthalimides requires the presence of a nitrogen source such as urea and a catalyst such as ammonium molybdate in order to form the macrocycle.

The mechanism of the phthalocyanine formation was studied by Christie *et al.*[12]. They studied the reaction of phthalonitrile with a range of copper salts producing thermally stable non-volatile products that were analyzed by differential scanning calorimetry (DSC) and infrared spectra (IR). The results obtained provided qualitative information for the elucidation of the reaction mechanism. It was proposed that in the first step of the reaction, the counter ion of the metal (II) cation or an alkoxide in a basic solution (X) nucleophilically attacks the dinitrile carbon of the phthalonitrile forming an anionic species (Figure 1.6). This reaction sequence is supported by the report published by Borodkin[13] in which they isolated and characterized the sodium salts of these proposed anionic species from the reaction of phthalonitrile with sodium methanolate under mild conditions. After cyclization to form an isoindoline intermediate it attacks another dinitrile molecule to form a dimeric complex that undergoes another cyclization in the next step. The cyclization process is accomplished by combining two dimeric complexes and is favored by the metal template effect. The elimination of X and the transfer of two electrons results in the formation of the final phthalocyanine macrocycle. In the case where the reactant is a metal in its elemental form they suggested that the two electrons are taken from the metal allowing the elimination of X^- to form the very stable 18 π-electron metal phthalocyanine.

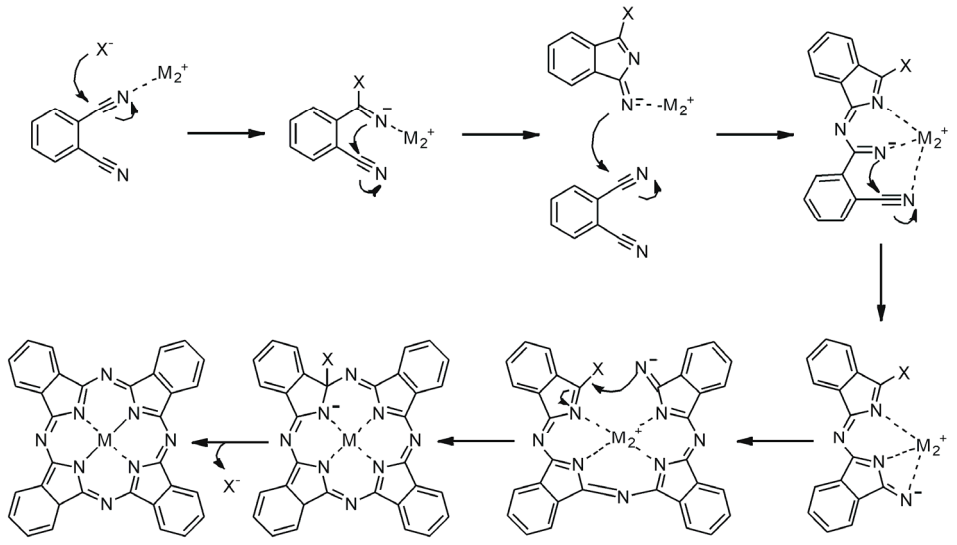

Figure 1.6 Proposed mechanism for the tetramerization reaction to form a phthalocyanine

1.2.1 Synthesis of symmetrically substituted phthalocyanines

Generally, the reaction conditions for preparing substituted phthalocyanines are softer than those employed in the synthesis of the unsubstituted derivatives. The increase in solubility of substituted precursors allows the use of a wide variety of solvents which solve the problem of the thermal instability of these starting materials. The synthesis of symmetrically substituted metal-free phthalocyanines is usually carried out using 1,3-diiminoisoindolines or phthalonitriles with a basic catalyst such as 1,8-diazabicyclo[5.4.0]undec-7-ene (DBU) in the presence of an alcohol. Lithium alkoxides are also used with phthalonitriles producing lithium phthalocyanines that can be easily demetalated by acid treatment.

Tetrasubstituted phthalocyanines

Tetrasubstituted Pcs are widely described in the literature. They are produced in the tetramerization reaction of 3- and 4-substituted phthalonitriles and are obtained as mixtures of four structural isomers. If the existence of electronic and steric effects than can modify the statistical distribution is neglected, then a 1:1:2:4 ratio of the isomers with D_{2h}:C_{4h}:C_{2v}:C_s symmetry are obtained (Figure 1.7). In the cyclotetramerization reaction of 3-substituted phthalonitriles the close spatial proximity of substituents in the resulting Pc core and the existence of energetically disfavored steric interactions between them can be exploited to control the regioselectivity of the reaction. Thus, Pcs with C_{4h} symmetry are selectively[14] produced when 3-substituted phthalonitriles are used as starting materials.

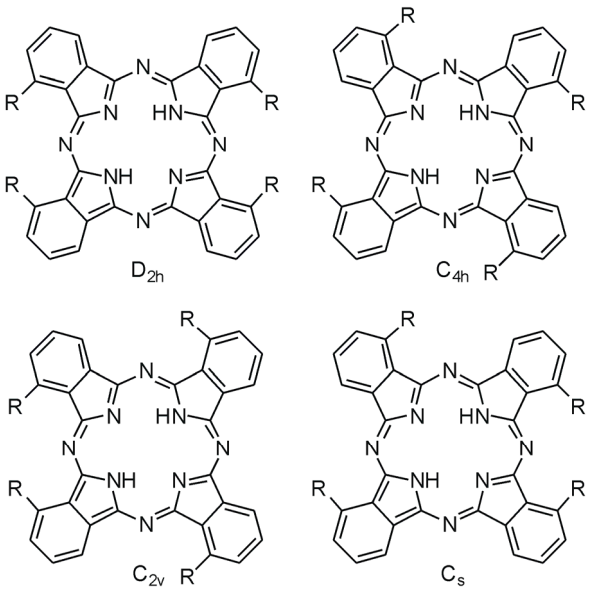

Figure 1.7 Four possible constitutonal isomers of tetrasubstituted phthalocyanines

Octasubstituted Phthalocyanines

Octasubstitued phthalocyanines can be prepared either with substituents located at the nonperipheral or the peripheral position. Most of them are obtained as symmetrical compounds that contain two substituents in each isoindole unit. Unlike the previously discussed tetrasubstituted phthalocyanines, octasubstituted compounds exist as a single D_{4h} or C_{3v} symmetry isomer because of their symmetric nature. Similarly to the tetra-alkylsubstituted phthalocyanines, the presence of bulky or long chain alkyl substitutents results in an increase in solubility of these complexes in a variety of non-polar solvents. Phthalocyanines with eight substituents at the sterically demanding positions (1,4,8,11,15,18,22,25) can be formed even with bulky substituents, however the yields of the cyclotetramerization reaction are lower in comparison with phthalocyanines substituted in other positions.[15] In some cases, the steric hindrance does not allow the cyclization and thus phthalocyanines cannot be obtained.

1.2.2 Synthesis of non-symmetrically substituted phthalocyanines

The preparation of unsymmetrically substituted phthalocyanines is more challenging mainly due to purification difficulties. The different established methods for their synthesis are outlined in this section.

Statistical cyclotetramerization

The strategy that is most widely used consists in performing the cyclotetramerization reaction using a statistical mixture of two precursors: A and B. For example, to obtain mainly the AAAB isomer, the condensation requires the use of three equivalents of precursor A with one equivalent of precursor B. Nevertheless, this method is expected to afford a mixture of compounds, namely, AAAA, AAAB, ABAB, AABB, ABBB and BBBB, where each differently substituted precursor unit is represented by the letters A or B (Figure 1.8). Although it might be expected that the stoichiometry control of the reactants

should play a role in the product distribution, reality shows that in general the symmetrical Pc derived from the isoindole unit used in excess prevails in the mixture, in the case at hand the regioisomer AAAA. The asymmetric introduction of substituents often provides solubility enhancement of the macrocycle due to reduced aggregation.

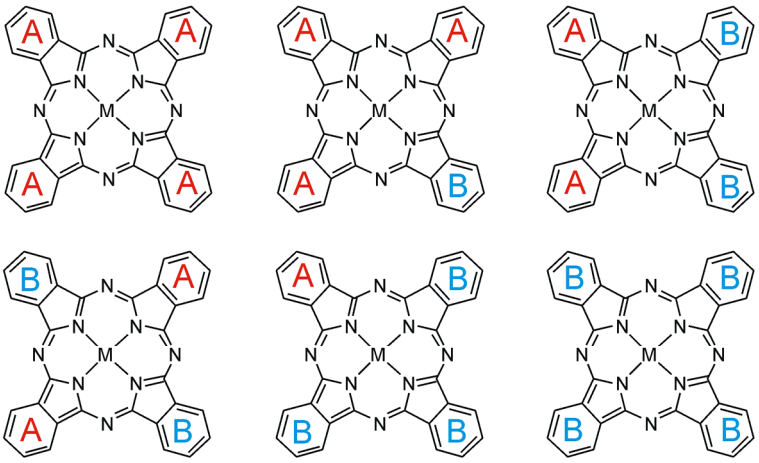

Figure 1.8 Mixture of phthalocyanines obtained using the statistical cyclotetramerization method with two different functionalized phthalonitriles A and B.

Ring expansion reaction

Another strategy used to prepare unsymmetrical A_3B Pcs is based on the ring-expansion reaction experienced by a subphthalocyanine in the presence of diiminoisoindolines (Figure 1.9).[16] Subphthalocyanines were synthesized for the first time in 1972 and they are small homologs of Pcs composed by three isoindole units and containing a boron atom in the center. Subphthalocyanines are macrocyclic complexes featuring an aromatic delocalized 14 π-electron system and a cone-shaped structure.

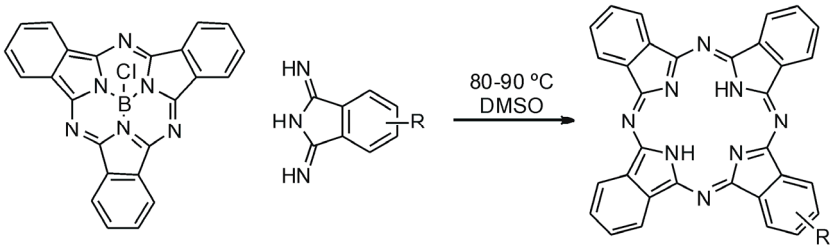

Figure 1.9 Selective synthesis of an A_3B macrocycle by ring expansion of a subphthalocyanine

However, recent reports indicate that the ring enlargement reaction is not always selective due to the opening and breaking of the subphthalocyanine ring takes place leading to a mixture of all the possible statistical Pc products. Moreover, the difficulty in the preparation and purification of subphthalocyanines and the restricted number of functional groups that can support the strong reaction conditions employed in their synthesis drastically limits the use of this methodology.

Solid-phase synthesis

The synthesis of Pcs with AAAB symmetry, which is based on the use of a polymeric support, was developed by Leznoff and coworkers as an alternative methodology.[17] This methodology consists in the covalent attachment of a 1,3-diiminoisoindoline or a phthalonitrile to an insoluble polymer followed by reaction with an excess of a different but soluble diiminoisoindoline (Figure 1.10). After removal of the symmetrical Pc formed in solution, the desired A_3B-Pc is cleaved from the polymer support by acid treatment. This approach is limited to phthalonitriles or diiminoisoindolines bearing substituents that can easily react with the polymer.

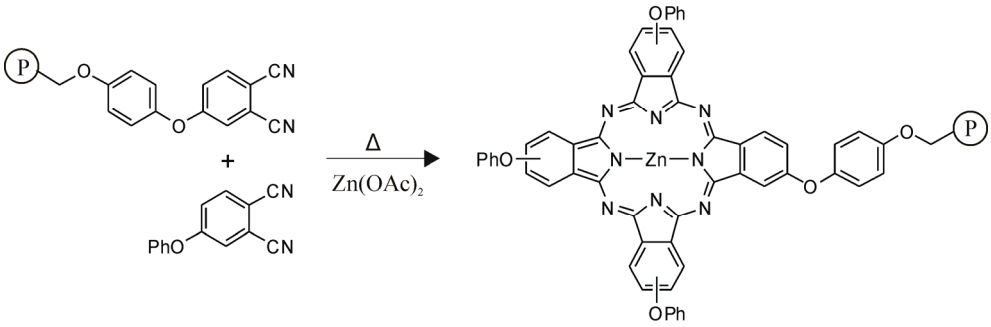

Figure 1.10 Synthetic methodology developed by Leznoff based on the use of polymeric support. The polymer is represented by the letter P.

Cross-condensation reaction

As the chromatographic separation of the C_{2v} and D_{2h} isomers of the A_2B_2 system is usually not possible, Young *et al.*[18] developed a selective method to prepare a particular isomer. The condensation of a 1,3-diiminoisoindoline derivative with 1,3,3-trichloroisoindolenine in 1:1 molar ratio was reported as an efficient method to obtain phthalocyanines with face-to-face identically substituted isoindoles, via reductive coupling of the chloro compound and the diiminoisoindoline derivative (Figure 1.11).

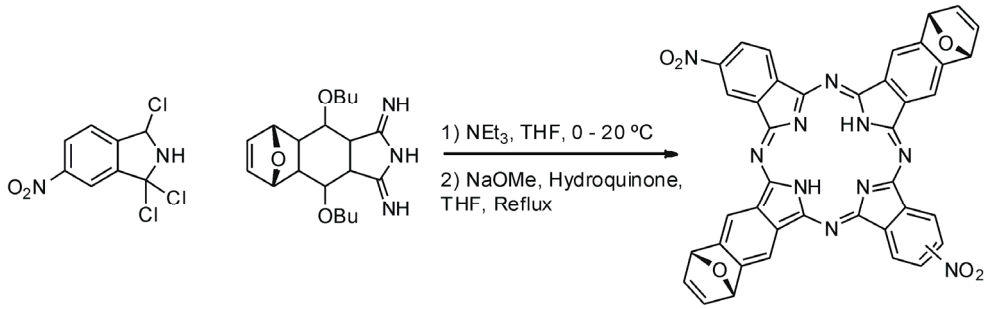

Figure 1.11 Synthetic scheme for the synthesis of ABAB phthalocyanines by cross-condensation reaction

Phthalocyanines with this ABAB substitution pattern are also obtained by combining a phthalonitrile or 1,3-diiminoisoindoline that cannot be involved in a self-condensation reaction due to steric reasons, namely, the presence of bulky groups at the 3,6-positions, with a non-substituted isoindole. Thus, only Pcs isomers that do not present bulky substituents in close proximity are formed and the ABAB isomer is easily isolated.

1.3 Structural variations of phthalocyanines

Several modifications can be made over the Pc ring to obtain Pc analogs. The most common structural changes that provide Pc-related compounds are the extension or contraction of the π-system by variation of the number of isoindole units, and the formal substitution of some of the isoindole moieties by another heteroaromatic ring (Figure 1.12). Derivatives containing extended π-systems are naphthalocyanines, anthracenocyanines and phenanthrenocyanines which are obtained by cyclotetramerization of the corresponding dinitrile precursor.[19]

Another Pc analog obtained by formal variation of the number of isoindole units is the superphthalocyanine (SuperPcs), which can be prepared by treatment of phthalonitrile with anhydrous uranyl chloride. The first superphthalocyanine was synthesized in 1964[20] by heating at 170ºC a DMF solution containing phthalonitrile and anhydrous UO_2Cl_2 and its structure was confirmed by X-ray crystallography in 1975.[21] X-ray structural analysis revealed a structure extremely distorted from planarity, probably because of steric strain within the macrocycle. For this reason, even peripherally unsubstituted SuperPcs show higher solubility than normal MPcs.[22] It is worth noting that SuperPcs undergo ring-contraction in the presence of transition metals to yield Pcs.[23]

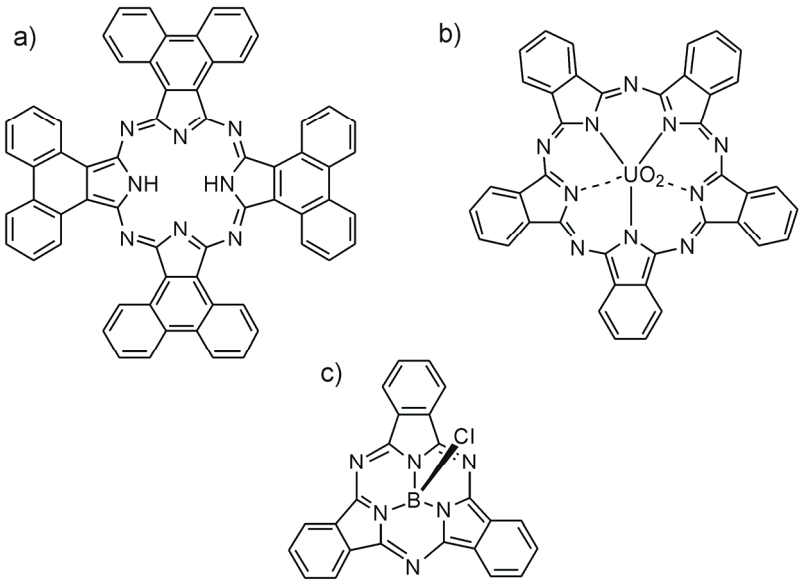

Figure 1.12 Chemical structures of a) phenanthrenocyanine b) superphthalocyanine c) subphthalocyanine

Pc derivatives containing contracted porphyrinoid species are called subphthalocyanines (SubPcs). The serendipitous discovery of SubPcs was made in 1972 by Meller and coworkers[24] and its X-ray structure was resolved two years later.[25] These compounds possess a particular macrocyclic ring formed by the arrangement of three isoindole units linked together by three aza-bridges. This contracted macrocycle presents an aromatic delocalized 14 π-electron system and adopt a nonplanar C_{3v} cone-shaped conformation. The condensation reaction of phthalonitrile in the presence of boron trichloride in chloronaphthalene at 200 ºC yielded the formation of a SubPc instead of the expected cyclotetramerization product. SubPcs containing another central atom have not been described, but derivatives containing different axial substituents depending on the boron reactant employed are known. Contrary to Pcs, unsubstituted SubPcs are slightly soluble in organic solvents

1.4 Phthalocyanine properties

Phthalocyanines are thermally stable, *e.g.* the substituted Pcs decompose at temperatures above 600ºC and are relatively stable against acids and alkalis. Due to their planar π-system they experience strong π-π interactions resulting in their practical insolubility in most common organic solvents.

1.4.1 Absorption spectral properties

The extensively conjugated aromatic system of the Pcs generates intense bands in their absorption spectra. Pcs absorb radiation corresponding to visible light and have a high optical stability, reason why Pcs have been traditionally used as dyes and pigments in the textile industry and paintings. New applications in distinct fields are continuously found taking advantage of their high extinction coefficient and photophysical characteristics.

The absorption spectra of MPc complexes consists of an intense and often well-resolved absorption band in the visible region at wavelengths between 650 to 670 nm, called Q band and a generally weaker band near 340 nm called the Soret or B band (Figure 1.13). The high molar absorptivity of ~10^5 $L \cdot mol^{-1} \cdot cm^{-1}$ of the Q band is the origin of the depth green or blue color of Pc dyes.

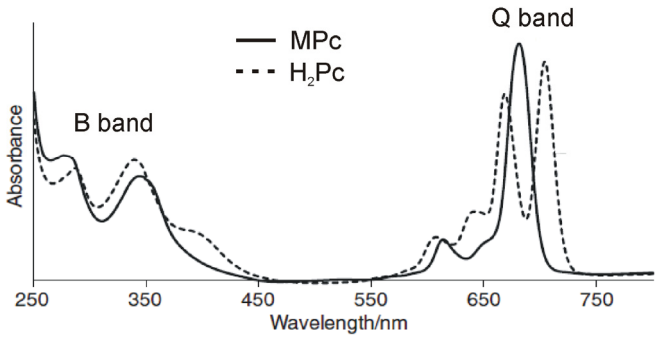

Figure 1.13 Typical absorption spectra of a metal-free and metallated phthalocyanines

Unmetallated Pcs show a D_{2h} symmetry and usually presents a split in the Q-band as a result of their lower symmetry. On the other hand, the incorporation of a metal ion inside the central cavity of a symmetrical Pc affects the system in such a way that increases the symmetry to D_{4h} and the planarity is maintained. Thus, they exhibit a single absorption peak for the Q-band in the absorption spectra. This is because the introduction of a metal ion reduces the electron density. The Q band is associated to π-π* HOMO-LUMO doubly degenerated transition of the ground state of a_{1u} symmetry to the first excited state which is of e_g symmetry. The position of the absorption bands in Pcs (particularly the Q band) is affected by the central metal atom, axial ligation, solvents, peripheral and non-peripheral substitution, aggregation and by the extension of the conjugation. Q band shifts in the range of 100 nm can be found by the replacement of the central metal atom which are attributed to changes of the electronic structure within the molecule. Pc with closed-shell metal, *e.g.*, lithium(I), magnesium(II), or zinc(II) show λ_{max} values around 670 nm. On the other hand, Pcs with open-shell metal ions such as iron(II), cobalt(II), or ruthenium(II), have Q bands blue-shifted with λ_{max} values around 630 nm. The relative geometry of the Pcs upon aggregation determines its spectroscopic behavior. As a result of the orientation within the oligomeric species, different tilt angles have been measured between the polarization axis of monomer and the line connecting the molecular centers between two Pcs. Tilt angles in the range of 90 to 54.7º are found in the so-called *H*-type aggregates and they exhibit a blue-shifted Q band in their absorption spectra. On the other hand, values of tilt angle lower than 54.7º lead to the so-called *J*-type aggregates which show a red-shifted Q band in their absorption spectra.

1.4.2 Supramolecular organization of phthalocyanines

The self-organizing properties of Pcs are mainly determined by the strong π-π interactions between the extended aromatic rings, and can be tuned with structural modifications. The overlap between the π-orbitals within a well-organized stack of Pc molecules may result in unusual uni-dimensional materials. The suitable choice of the substituents and the central metal atom assist in the formation of multiple and highly ordered condensed phases. In many cases, the type of supramolecular architecture formed can be predicted and it will determine the final properties of the material.[26] The most important organized structures formed by Pcs are the following:

Crystals

Pcs are relatively rigid molecules with very few, if any, options for conformational flexibility. In the crystal lattice, however, the molecules of Pc can be packed in different arrangements, giving rise to different polymorphs. The definition of Barth says "Polymorphism includes every possible difference encountered in the crystalline lattice of a substance of constant chemical composition excepting homogeneous deformations".[27] Pcs are organized into two kinds of polymorphic crystals: the α form and the more thermodynamically stable β crystalline form (Figure 1.14). The main difference between them is the magnitude of the angle between the axis of symmetry of the macrocycle and the axis formed by the columnar arrangement.

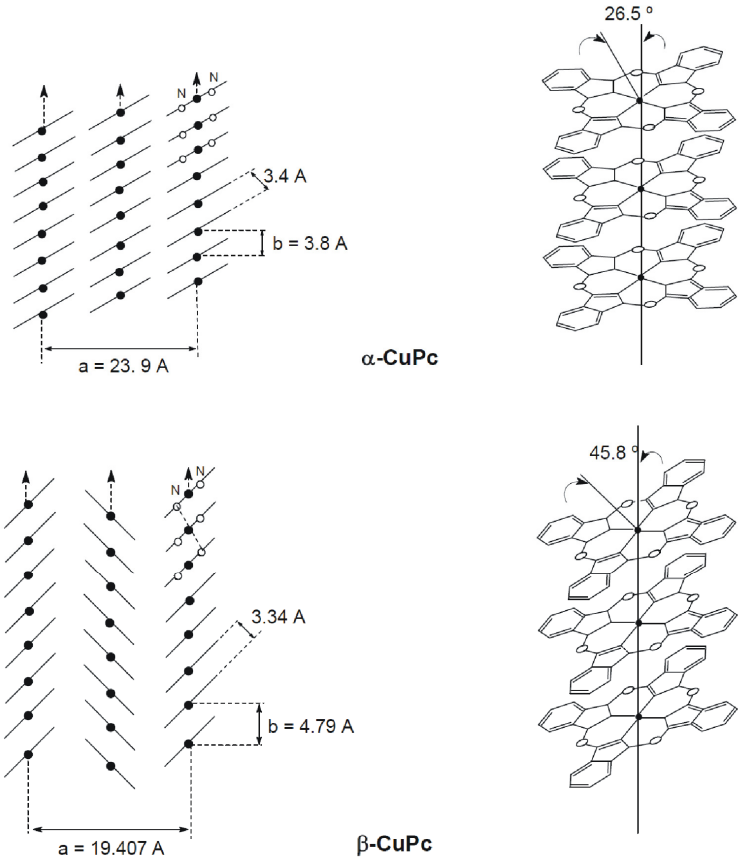

Figure 1.14 α and β polymorphic crystalline forms of CuPc

Liquid crystals

Pcs are included in the group of metallomesogens which can be defined as metal-containing liquid crystals. These kinds of mesogens are of great interest in the area of molecular materials because they combine the intrinsic organization and processability properties of organic mesogens with the physical properties associated with the metal atoms.

In general, Pcs and porphyrazines substituted with long flexible hydrocarbon side chains form so-called discotic mesophases at elevated temperatures. The first mesogenic Pc was synthesized by Piechocki *et al*. in 1982 and consisted in a peripheral octa(alkoxymethyl) substituted Pc.[28] Following this report, a wide variety of Pcs and porphyrins, including molecules substituted with eight linear alkyl,[29] alkoxymethyl,[30] and alkoxy chains[31] forming a well-defined mesophase have been described. The discotic molecules were stacked in columns with a hexagonal arrangement and intracolumnar distances close to the van der Waals radii of the aromatic macrocycles (Figure 1.15).

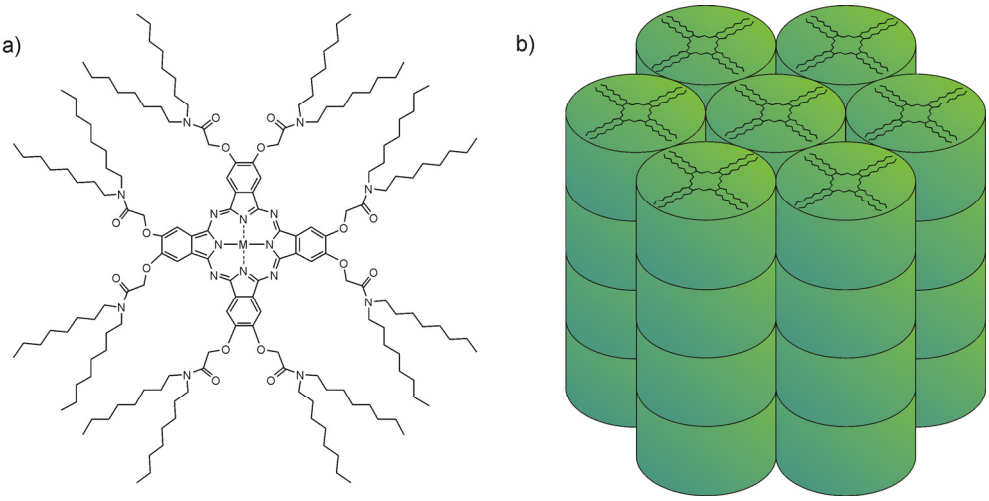

Figure 1.15 a) Example of a mesogenic phthalocyanine and b) schematic representation of the one-dimensional stacks of Pc units

The temperature range of the mesophases is fairly dependent on the length of the hydrocarbon chains and the central metal atom. Few Pcs are known to be liquid crystalline at room temperature.[32] Most of them, are functionalized with a branched hydrocarbon chain, which probably introduce disorder and hence a decrease in the transition temperature. The property of being liquid crystalline at ambient temperature may play an important role for some applications, *e.g*. in the construction of Langmuir-Blodgett (LB) films.

Cofacial polymers

The central atom of the Pc plays a key role in the Pc cofacially oriented polymers, since the polymerization occurs through the bridging ligands that connect two central metal atoms, in the so-called "shish-kebab" architecture.[33,34] Nolte *et al.* reported an interesting supramolecular chemistry found in a Pc to which four benzo crown ether moieties were attached (Figure 1.16).[35] The peripheral aromatic rings of the Pc were each di-substituted with chiral alkoxy tails. When a chloroform solution of this Pc was heated and then cooled slowly, strong aggregation of the molecules was observed. Transition electron micrographs (TEM) images showed the formation of helical long fibers structures with clockwise staggered orientation. These structures, in turn, self-assembled to form coiled-coil aggregates with left-handed helicity and with nanometer diameter and micrometer length. The addition of potassium ions to the crown ether Pc fibers resulted in the formation of fibers with almost no helical structure as can be seen in the TEM image. The disappearance of helicity can be explained by assuming that the metal ions are located dynamically in, or between, the crown ether rings. In this way, the transfer of chirality is blocked because the Pcs are forced to adopt an eclipsed conformation. These tunable chiral materials have potential for optoelectronic applications and as components in sensor devices, for example, for the detection of alkali metal ions.

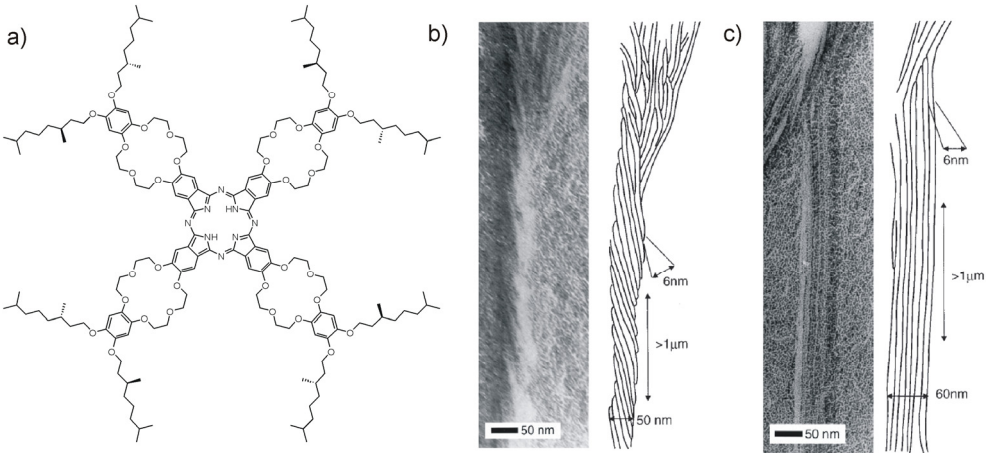

Figure 1.16 a) Chemical structure of Nolte's crown ether Pc b) TEM image of the crown ether Pc showing left-handed coiled-coil aggregates in chloroform and a schematic representation of the helices, and c) TEM image el the non-helical rods formed by the ether crown Pc in presence of KCl in chloroform and a schematic representation of the rods

Thin films

The most direct way to incorporate Pcs in electronic devices is probably using thin films, which can be prepared by vacuum sublimation, polymeric matrix scattering or spin-coating. Highly ordered Pc films have been prepared by the Langmuir-Blodgett technique and by self-assembly of thiol-substituted macrocycles onto a gold surface.

Nanostructures on surfaces

Pcs can self-organize on surfaces giving rise to nanowires and nanoribbon structures, among others, by organic vapor-phase deposition. The nature of the nanostructures was found to depend on the type of substrate and the deposition conditions. On metals and semiconductors, phthalocyanines prefer to lie flat on the surface and grow in a layer-island mode. This section will be explored in more detailed in Chapter 4

1.4.3 Semiconducting and conduction properties of metallophthalocyanines

Many papers and reviews have been published during the last two decades about the conducting properties of Pcs.[36,37] The conductivity behavior found in MPc systems arises either from the intrinsic properties of a particular Pc or from the supramolecular level organization of the molecules which allows an extended orbital overlap along the conducting pathway.

Intrinsic Molecular Semiconductors

Intrinsic molecular semiconductors are characterized by a small band gap and a given density of highly mobile intrinsic charge carriers. The density of the charge carriers in the solid state is estimated from the value of the redox potentials in solution. Organic compounds, including conjugated polymers, are not usually prepared in a pure enough state to observe their intrinsic electrical properties.

The conducting properties of bis(phthalocyanato)lutetium ($LuPc_2$) and lithium monophthalocyanine (LiPc) were studied in detail by Maitrot *et al.* in 1987.[38] They found that the intrinsic conducting properties of these MPs were related to the radical nature of the compounds. Detailed electrochemical studies were carried out, which allowed the determination of the redox potentials. Single crystals of $LuPc_2$ showed a conductivity of 6×10^{-5} $S \cdot cm^{-1}$ with a thermal activation energy of conduction of 0.64 eV that falls in the same order of magnitude as the difference in the redox potentials of the oxidized and reduced species. In the case of LiPc, electrochemical studies pointed out a ΔE_{redox} larger than the one obtained for $LuPc_2$ and thus, the intrinsic conductivity is expected to be smaller due to the lower density of charge carriers. On the contrary, the conductivity measured in LiPc crystals was two orders of magnitude higher (2×10^{-3} $S \cdot cm^{-1}$) than $LuPc_2$ with a thermal activation of conduction four times lower than the difference of the redox potentials obtained in solution. The explanation of these facts lies on the large energy of interaction between the individual units in the crystal. Both Pc derivatives have been used for the

preparation of gas sensor devices based on conductivity measurements.[48] In the case of $LuPc_2$, the gas sensed gradually oxidises the $LuPc_2$ to $LuPc_2^+$ increasing the conductivity and thus evidencing the presence of the gas in the media. Low concentrations of gases such as NO_2, O_2 or NH_3 were measured using this conductivity-based device build up with Pc thin films. On the other hand, divalent MPcs such as CoPc or NiPc, act as insulators with conductivities lower than 10^{-12} $S \cdot cm^{-1}$. This can be explained by the large thermal activation energy found in this compound, which fall in the range of 2 mV.

Organized Phthalocyanines

As mention before, Pcs can be organized in columns at supramolecular level due co facial stacking. This columnar geometry enables the electron delocalization along the main axis of the column through π-π overlapping giving rise to conducting properties. MPc, however, crystallize very seldom in the stacked arrangement and this organization does not allow an overlap of the π orbitals and, hence there is no formation of a conduction band. To overcome this problem, different methods were developed for organizing MPcs and achieving semiconducting properties. The best are chemical methods like oxidative doping and physical methods such as the preparation of discotic liquid crystals and organized LB films.

Pcs have electron-donor properties and can be readily doped with electron-acceptors to give columnar semiconductors. The conductivity is enhanced by small dopant molecules that can fit into the lattice of the columnar arrangement.[39] The oxidative doping of MPc with iodine results in a highly increased conductivity of the polycrystalline samples. As an example, undoped NiPc shows a powder conductivity of 10^{-11} $S \cdot cm^{-1}$, whereas doped NiIPc exhibit a powder conductivity of 0.7 $S \cdot cm^{-1}$.[40,41]

Pc axially substituted with cyano groups, $M(Pc)(CN)_2$, have shown conductivities of 120 $S \cdot cm^{-1}$ when they are converted in partially oxidized salts by electro crystallization.[42] Hanack and coworkers developed a method called “shish kebab” approach for the assembly

of Pcs in a stacked structures.[34] This method involves the formation of coordination polymers of type $[MPc(L)]_n$, where the macrocycles are linked together by biaxially metal-bonded bridging ligands. The powder conductivities of most of the bridged Pc transition metal complexes are low and in the range of 10^{-7} – 10^{-6} $S \cdot cm^{-1}$. However, they can be doped either chemically, *i.e.* with iodine, or electrochemically with BF^{4-}, PF^{6-} or ClO^{4-}, which leads to good semiconducting properties in the range of 10^{-5} – 10^{-1} $S \cdot cm^{-1}$.

1.4.4 Magnetic properties of metallophthalocyanines

MPcs with divalent transition metal ion can form planar molecules arranged in columnar stacks with different tilt angles and interplanar distances. In such circumstances, complexes can be coupled by exchange interactions leading to a ferromagnetic ordering below a transition temperature. Understanding of magnetism of *d*-MPc complexes requires consideration on both intrinsic molecular properties, which depend on the *d*-electronic configuration of the metal, and intermolecular magnetic interactions depending on the crystal structure.

The first and most studied Pc-based ferromagnet is β-polymorphic manganese (II) phthalocyanine (β-MnPc).[43] In this polymorph, the two pyrrole nitrogen atoms of the Pc core lie exactly above or below the Mn center of the Pc neighbour ring. The distance between these axially located nitrogen atoms and Mn atom is 3.4 Å, which is sufficiently short to provide a possible pathway for magnetic exchange interactions. Magnetic susceptibility at high temperatures was measured and followed the Curie-Weiss law. At temperatures below about 20 K the susceptibility deviates from the Curie-Weiss law and reaches a constant maximum value below 7 K.[44] The ferromagnetic behavior is understood qualitatively in terms of the electronic configuration and the 90º superexchange interaction between nearest neighboring Mn atoms via the nitrogen of the Pc ring, resulting in the ordering of Mn^{2+} with $S = 3/2$ state.[45] In 2002, Evangelisti *et al*. reported the ferromagnet-like behavior of a FePc in its meta-stable α-polymorph.[46] They showed that in the α-FePc,

Fe(II) moments are strongly coupled into ferromagnetic chains, with the weak interchain coupling leading to a canted, soft molecular ferromagnet below 10 K.

A breakthrough in the field occurred when Ishikawa *et al*. reported in 2003 the magnetic properties of a lanthanide bis(phthalocyanine) complex.[53] It was demonstrated that $TbPc_2$, in which two phthalocyanine rings are encapsulating a single lanthanide ion in the trivalent state, showed magnetic properties at the single molecule level. The temperature ranges in which the slow relaxation of the magnetization was observed were significantly higher than the 3*d* transition-metal clusters. The magnetic properties of these complexes will be reviewed in detail in Chapter 3.

1.5 Applications of phthalocyanines

Since their discovery and identification, phthalocyanines have been extensively used as dyes and pigments in paint, printing, textile and paper industries due to their blue-green color and their high chemical and thermal stabilities. Approximately 25% of all artificial organic pigments are phthalocyanine derivatives.[47] High-tech applications have been found using phthalocyanines in several fields such as electrophotography, inkjet printing and photo conducting agents in photocopying devices. In addition to traditional applications as dyes and pigments their novelty is rapidly growing in other fields were they are used as gas sensors[48], photovoltaic cells[49,50], liquid crystals[51,52], molecular magnets[53], non-linear optics[54] and as photosensitizers for photodynamic therapy of cancer.[55,56] Most of these applications are related to their high chemical and thermal stability, which, in turn, is closely related to the electrochemical properties of Pc compounds. The electrochemical and spectroscopic properties of Pc derivatives can be tuned by either varying the central metal atom; changing the size of the π-conjugated system of Pcs; or alternating the type, number, and positions of the substituents on the macrocyclic ligands. The possibility of incorporation about 70 different metal atoms into the Pc ring offers additional features to optimize their physical properties. Additionally, their thermal stability makes them promising candidates to be incorporated into devices. A brief overview in selected Pcs applications is given below.

1.5.1 Photosensitizer in photodynamic therapy

Photodynamic therapy (PDT) is a rapidly advancing modality for cancer treatment.[57] It involves the destruction or damage of living structures by exposure of tissues to a photosensitizer drug, followed by irradiation with light of an appropriate wavelength (optimal tissue penetration is in the range of 630-800 nm).[58] PDT can be used to selectively destroy cancer tissue without harming surrounding cells by directing the light beam to the target area. The destruction of living tissues is ascribed to reactive oxygen species. Two main photo oxidation pathways are possible. Type I involves the formation of reactive

oxygen species (ROS) by the light-activated photosensitizer meanwhile the direct reaction with molecular oxygen to form highly active singlet oxygen is referred to type II. To achieve optimal efficacy a photosensitizer should fulfill several requirement such as high absorbance at wavelengths > 600 nm, low tendency to aggregate to achieve maximal yield of singlet oxygen, and possess favorable intracellular localization properties.[59] Phthalocyanines are excellent candidates to be used as photosensitizer due to their high molecular absorption at high wavelengths, lack of dark toxicity and chemical stability.[60] Aluminum phthalocyanine (AlPc),[61] zinc-phthalocyanine (ZnPc) and silicon phthalocyanines (SiPc)[62] have been used as photosensitizers for PDT (Figure 1.17). These compounds often show aggregation in aqueous media however they can be substituted with bulky or charged groups at the periphery of the Pc ring to prevent stacking of the hydrophobic macrocycles.

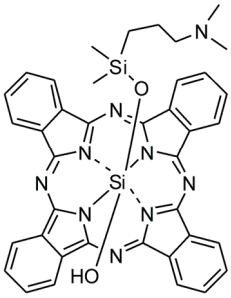

Figure 1.17 Structural formula of a axially substituted silicon phthalocyanine-based photosensitizer known as Pc_4

Additionally, the axial derivatization of tri- or tetravalent metal atoms like aluminium(III) or silicon (IV) allows solubility in aqueous media due to the steric shielding of the Pc core. An axially substituted SiPc is known as one of the most potent Pc-based photosensitizer and has been used in clinical trials.[63]

1.5.2 Non-linear optics

Non-linear optics (NLO) is a branch of optics that studies the interaction of light with matter in the regime where the response of the material to the applied electromagnetic field is non-linear in the amplitude of the field. Generally, optical limiting is a non-linear effect consisting of a decrease in the sample transmittance under high intensity irradiation which can be provided by laser sources modifying the optical properties of the material. Light waves can then interact with each other and this interaction results in the generation of optical fields at new frequencies, including optical harmonics of incident radiation or sum (or difference) frequency signals. In the early stage, research work was focused on inorganic materials but recently, the use of organic materials for non-linear optical application has grown in interest. They offer several advantages over inorganic materials, such as fast response times, large non-linearity and easy and economic processability to prepare films. Moreover, it has been suggested that asymmetrically substituted Pcs with suitable donor/acceptor groups able to exhibit efficient intramolecular charge transfer should exhibit interesting NLO responses.[64] Organic materials for non-linear optics are typically based on a highly polarizable π-conjugated system. For this reason, phthalocyanines, with their extended two-dimensional π-electron delocalization, have been widely studied with regard to their non-linear optical properties.

1.5.3 Catalytic applications of phthalocyanines

MPcs are very attractive as catalysts not only because of structural analogy with porphyrin complexes, which are widely used by nature in the active sites of enzymes responsible for catalytic aerobic oxidations, reduction and transport of dioxygen, but also due to their accessibility in terms of cost and large scale preparation as well as their chemical and thermal stability.

MPcs have been used as catalyst in different chemical reactions, such as oxidations of olefins,[65] phenols[66] and alcohols,[67] C-C bond formation[68] and in reduction reactions.[69] One of the most important applications of MPcs as catalysts is the Merox process. This large-

scale industrial process involves the catalytic oxidation of mercaptans in the presence of sulfonated cobalt Pcs to remove a major part of sulfur from petrol. The catalytic properties of MPcs depend on the metal and the structure of the complex which can be tuned by appropriate structural modifications.

MPc as catalyst in oxidation reactions

Numerous industrially important products can be obtained by the oxidation of olefins which make this chemical transformation a very interesting reaction. Selective oxidation of double bonds provides epoxides and diols, whereas the oxidation of allylic positions leads to the formation of allylic alcohols and ketones. The important goal is, therefore, to obtain either epoxides or products of allylic oxidation with high selectivity. An example of oxidation of olefins catalyzed by MPcs was published in 1993 by Weber *et al*.[65] The authors reported the aerobic oxidation of olefins catalyzed by μ-oxo dimeric $(Pc^tBu_4Fe)_2O$ and $(Pc^tBu_4Mn)_2O$ complexes in the presence of molecular oxygen. The oxidation of 1-hexene, cyclohexene, and cycloheptene afforded epoxides (12-29% yield), allylic alcohols (27-45% yield), and ketones (30-45% yield) with turnover numbers (TONs) of 120 and 80, 520 and 580, 120 and 100 for $(Pc^tBu_4Fe)_2O$ and $(Pc^tBu_4Mn)_2O$, respectively.

Another important application of MPcs is their use as catalyst in the oxidation of phenols. Selective oxidation of phenols to quinones is the key step in the preparation of many vitamins and valuable synthetic precursors. Quinones are powerful intermediates in organic synthesis and show biological activity since quinone fragments often occur within the molecular frameworks of natural products. Oxidative coupling of phenols affords bisphenol derivatives. The oxidation of 2,3,6-trimethylphenol (TMP) with potassium peroxymonosulfate ($KHSO_5$) catalyzed by iron and cobalt phthalocyanine tetrasulfonates, [FePcTS] and [CoPcTS], in a methanol-water mixture at room temperature was investigated by Türk *et al*.[66] The authors claimed that the [FePcTS] catalyzed oxidation reaction produced quantitative yield of 2,3,5-trimethylbenzoquinone (TQM) after 5 min using an oxidant:substrate:catalyst ratio of 1200:300:1. The high selectivity to TMQ

formation was explained by quenching of radicals by MeOH used as solvent in an 8:2 mixture with water. When cobalt phthalocyanine tetrasulfonate [CoPcTS] was employed as catalyst instead of [FePcTS], a slower reaction rate for the oxidation of TQM was observed and the product was obtained in a 49% yield. In both reactions, $KHSO_5$ was introduced into the reaction mixture by using oxone which is a solid consisting of a 2:1:1 mixture of $KHSO_5$, $KHSO_4$ and K_2SO_4.

The catalytic activity of MPcs in the oxidation of alcohols has also been proved. Zhdankin *et al.* reported in 2008 the oxidation of alcohols catalyzed by a Fe(III) phthalocyanine in the presence of hypervalent iodine (V) reagents.[67] It was proved that the $(Pc^tBu_4Fe)_2O$ catalyst in combination with esters of iodoxybenzoic acid performed oxidation of primary and secondary alcohols to carbonyl compounds (Figure 1.18). The reaction showed an especially high selectivity with benzylic alcohols yielding the corresponding aldehydes and ketones in 91-95% isolated yields.

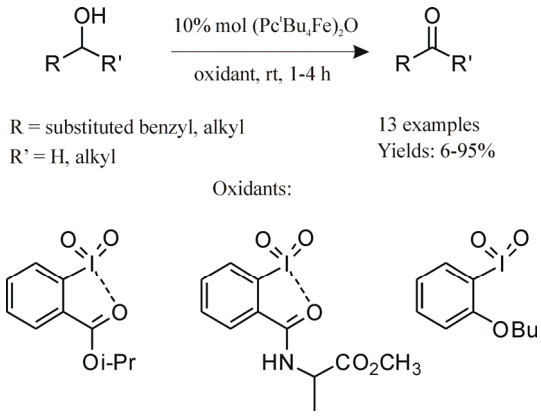

Figure 1.18 Oxidation of alcohols catalyzed by $(Pc^tBu_4Fe)_2O$. Image adapted from reference[67]

MPc as catalyst in C-C bond formation reactions

The formation of C-C bonds is typically associated with the noble metal catalysts (Pd, Rh, Ru, etc). Heck and Suzuki reactions are catalyzed by "ligandless" Pd species released in the reaction solution from homogeneous and heterogeneous catalysts. Irreversible precipitation of Pd black provokes a drop of the catalytic activity. To overcome this problem a controlled and reversible release of Pd from macrocyclic complexes was proposed which should lead to high C-C coupling activity. In this context, Köhler *et al.* reported in 2010 the superior catalytic activity of PdPc in the Suzuki coupling of aryl bromides with phenylboronic acid compared with PdTPP and Robson-type Pd bimetallic complexes (Figure 1.19 a).[70] In the same work, the Heck coupling reaction of styrene with aryl halides catalyzed by PdPc was also performed (Figure 1.19 b). The reaction showed better performance compared with the one using PdTPP as catalyst but inferior to a Pd bimetallic complex.

The replacement of expensive and toxic catalysts with more available and nontoxic complexes in the C-C bond formation reaction was successfully achieved by Taniguchi *et al*.[68] The oxidative addition of alkoxycarbonyl radicals derived from different carbamates to α-methylstyrene was performed in the presence of 10 mol % of FePc to afford 47-82% yields of addition products (Figure 1.19 c). Noteworthy, simple iron salts, $FeCl_3$ and $Fe(NO_3)_3$, gave low product yields. The scope of this method was tested in the reaction of methyl carbamate with 13 different olefins. Isolated product yields ranging from 21 to 81% were obtained being 2-arylpropenes with conjugated double bonds especially suitable substrates. This iron-catalyzed reaction of alkoxycarbonyl radicals presents several advantages such as: 1) many carbamate precursors of alkoxycarbonyl radicals are stable solids and readily available; 2) the reaction is environmentally friendly, since the iron catalyst has low toxicity and is inexpensive, and 3) the experimental procedure is very simple and safe.

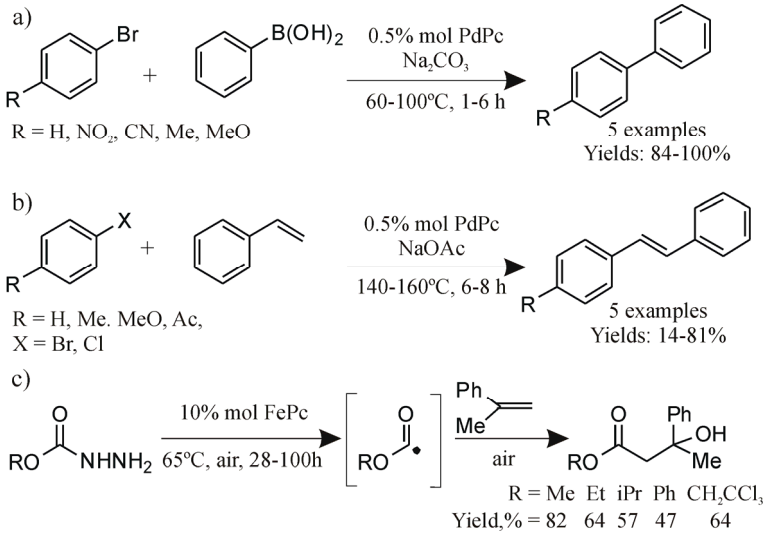

Figure 1.19 a) Formation of biaryls by Suzuki coupling b) Heck coupling of styrene with aryl halides and c) oxidative addition of alkoxycarbonyl radicals to α-methylstyrene

MPc as catalyst in reduction reactions

The application of MPcs for reductive transformations has received less attention compared with the oxidation reactions. Kudrik *et al.* reported in 2002 the catalytic activity of cobalt (II) tetrasulphophthalocyanine, CoPcTS, in the reduction reaction of sodium nitrite with sodium dithionite in aqueous alkaline solution.[69] This reaction is important since denitrification plays an important role in the biogeochemical nitrogen cycle. The authors demonstrated that CoPcTS was shown to be an efficient catalyst for the reduction of nitrite and nitrate by $Na_2S_2O_4$. Two features of the MPc-catalyzed reduction of nitro compounds are particularly useful: 1) the possibility of converting nitro compounds to N-heterocycles in a one-pot process with reduction and condensation steps and 2) the possibility of reduction of nitro functions in the presence of many sensitive functionalities without the need to protect them.[71] The advantage of using phthalocyanines as catalyst in the reduction reactions is the use of unsubstituted MPcs, which are cheap and readily available on a large scale. On the other hand, the catalytic properties of MPcs can be tuned

by the introduction of appropriate substituents that might lead to catalytic systems with novel reactivity and improved catalytic activity.

1.6 Thesis Goals

In this work we will show the use of tetrapyrrole macrocycles in the formation of lanthanide double-decker complexes. These complexes are known to show interesting magnetic properties. We will measure the magnetic properties of the newly formed complexes and evaluate the possibility of introducing such complexes onto surfaces.

In Chapter 2 we investigate the dimerization process of an enantiopure zinc phthalocyanine in solution by means of UV-vis experiments and variable temperature ^{1}H NMR experiments. Moreover, the coordination of quinuclidine to the zinc center is also studied at two different concentrations in order to determine accurate binding constant and the stoichiometries of the corresponding species formed in the complexation process.

In Chapter 3 we present the preparation and characterization of new single-molecule magnets using lanthanides and tetrapyrrole macrocycles as ligands. The single-molecule magnet behavior of the different complexes will be tested by magnetic susceptibility measurements. Additionally, different functionalized phthalocyanines will be synthesized in order to used them in the synthesis of lanthanide bis(phthalocyanine) complexes. The resulting double-decker compounds will be characterized and their magnetic properties measured. The aim of this chapter is the preparation of new single-molecule magnets with better processability in order to incorporate them into nanostructures and thereby allow the study and manipulation of individual single-molecule magnets.

In Chapter 4 we show a comprehensive scanning tunneling microscopy (STM) study of the adsorption, self-assembly, chemical and electronic properties of the free base octaethyltetraazaporphyrine, and two single-molecule magnet derivatives on different metallic surfaces.

1.7 References

[1] Ostrowski, S.; Mikus, A.; Lopuszynska, B. "Synthesis of highly substituted meso-tetraarylporphyrins". *Tetrahedron* **2004**, *60*, 11951.

[2] Woodward, R. B.; Ayer, W. A.; Beaton, J. M.; Bickelhaupt, F.; Bonnett, R.; Buchschacher, P.; Closs, G. L.; Dutler, H.; Hannah, J.; Hauck, F. P.; Ito, S.; Langemann, A.; Legoff, E.; Leimgruber, W.; Lwowski, W.; Sauer, J.; Valenta, Z.; Volz, H. "The Total Synthesis of Chlorophyll". *J. Am. Chem. Soc.* **1960**, *82*, 3800.

[3] Braun, A.; Tcherniac, J. "The products of the action of acet-anhydride on phthalamide.". *Ber. Dtsch. Chem. Ges.* **1907**, *40*, 2709.

[4] Linstead, R. P. "Phthalocyanines part I A new type of synthetic colouring matters". *J. Chem. Soc.* **1934**, 1016.

[5] Robertson, J. M. "An X-ray study of the phthalocyanines - Part II Quantitative structure determination of the metal-free compound". *J. Chem. Soc.* **1936**, 1195.

[6] Schmid, G.; Witke, E.; Schlick, U.; Knecht, S.; Hanack, M. "Substituent Effects in Soluble Phthalocyaninatoiron (II) Complexes". *J. Mater. Chem.* **1995**, *5*, 855.

[7] Vacus, J.; Doppelt, P.; Simon, J.; Memetzidis, G. "Towards Nanometer-Scale Gratings - Synthesis and Characterization of Dodecyloxy-Substituted Platinum Phthalocyanines". *J. Mater. Chem.* **1992**, *2*, 1065.

[8] Fernandez, D. A.; Dicelio, L. E.; Awruch, J. "Synthesis and Properties of 2 New N-Alkyl Substituted Phthalocyanines". *J. Heterocycl. Chem.* **1995**, *32*, 519.

[9] Gurol, I.; Ahsen, V.; Bekaroglu, O. "Synthesis of Tetraalkylthio-Substituted Phthalocyanines and Their Complexation with Ag(I) and Pd(Ii)". *J. Chem. Soc., Dalton Trans.* **1994**, 497.

[10] Masilela, N.; Nyokong, T. "The synthesis and photophysical properties of water soluble tetrasulfonated, octacarboxylated and quaternised 2,(3)-tetra-(2 pyridiloxy) Ga phthalocyanines". *Dyes Pigm.* **2010**, *84*, 242.

[11] Barrett, P. A.; Dent, C. E.; Linstead, R. P. "Phthalocyanines Part VII Phthalocyanine as a co-ordinating group - A general investigation of the Metallic derivatives". *J. Chem. Soc.* **1936**, 1719.

[12] Christie, R. M.; Deans, D. D. "An Investigation into the Mechanism of the Phthalonitrile Route to Copper Phthalocyanines Using Differential Scanning Calorimetry". *J. Chem. Soc., Perkin Trans. 2* **1989**, 193.

[13] Borodkin, V. F. *Zh. Prikl. Khim*., **1958**, *31*, 813.

[14] Leznoff, C. C.; Hu, M. G.; Mcarthur, C. R.; Qin, Y. N.; Vanlier, J. E. "The Syntheses of 2,9,16,23-Tetrahydroxyphthalocyanines and 1,8,15,22-Tetrahydroxyphthalocyanines". *Can. J. Chem.* **1994**, *72*, 1990.

[15] Rihter, B. D.; Kenney, M. E.; Ford, W. E.; Rodgers, M. A. J. "Synthesis and Photoproperties of Diamagnetic Octabutoxyphthalocyanines with Deep Red Optical Absorbency". *J. Am. Chem. Soc.* **1990**, *112*, 8064.

[16] Kobayashi, N.; Kondo, R.; Nakajima, S.; Osa, T. "New Route to Unsymmetrical Phthalocyanine Analogs by the Use of Structurally Distorted Subphthalocyanines". *J. Am. Chem. Soc.* **1990**, *112*, 9640.

[17] Leznoff, C. C.; Hall, T. W. "The synthesis of a soluble, unsymmetrical phthalocyanine on a polymer support". *Tetrahedron Lett.* **1982**, *23*, 3023.

[18] Young, J. G.; Onyebuagu, W. "Synthesis and Characterization of Di-Disubstituted Phthalocyanines". *J. Org. Chem.* **1990**, *55*, 2155.

[19] Bedworth, P. V.; Perry, J. W.; Marder, S. R. "The synthesis of a symmetrically substituted alpha-octa(isopentoxy)anthralocyanine". *Chem. Commun.* **1997**, 1353.

[20] Bloor, J. E.; Schlabitz, J.; Walden, C. C.; Demerdac, A. "Organic Complexes of Uranium. Synthesis and Spectrum of Uranyl Phthalocyanine". *Can. J. Chem.* **1964**, *42*, 2201.

[21] Day, V. W.; Marks, T. J.; Wachter, W. A. "Large Metal Ion-Centered Template Reactions - Uranyl Complex of Cyclopentakis(2-Iminoisoindoline)". *J. Am. Chem. Soc.* **1975**, *97*, 4519.

[22] Cuellar, E. A.; Marks, T. J. "Synthesis and Characterization of Metallo and Metal-Free Octaalkylphthalocyanines and Uranyl Decaalkylsuperphthalocyanines". *Inorg. Chem.* **1981**, *20*, 3766.

[23] Marks, T. J.; Stojakovic, D. R. "Large Metal Ion-Centered Template Reactions - Chemical and Spectral Studies of Superphthalocyanine Dioxocyclopentakis(1-Iminoisoindolinato)Uranium(Vi) and Its Derivatives". *J. Am. Chem. Soc.* **1978**, *100*, 1695.

[24] Meller, A.; Ossko, A. "Phthalocyaninartige Bor-Komplex". *Monatsh. Chem.* **1972**, *103*, 150.

[25] Kietaibl, H. "Crystal and Molecular-Structure of a New Phthalocyanine-Like Boron Complex". *Monatsh. Chem.* **1974**, *105*, 405.

[26] vanNostrum, C. F.; Nolte, R. J. M. "Functional supramolecular materials: Self-assembly of phthalocyanines and porphyrazines". *Chem. Commun.* **1996**, 2385.

[27] Barth, T. F. W. "Polymorphic phenomena and crystal struciure". *Am. J. Sci.* **1934**, *27*, 273.

[28] Piechocki, C.; Simon, J.; Skoulios, A.; Guillon, D.; Weber, P. "Discotic Mesophases Obtained from Substituted Metallophthalocyanines - toward Liquid-Crystalline One-Dimensional Conductors". *J. Am. Chem. Soc.* **1982**, *104*, 5245.

[29] Engel, M. K.; Bassoul, P.; Bosio, L.; Lehmann, H.; Hanack, M.; Simon, J. "Mesomorphic Molecular Materials - Influence of Chain-Length on the Structural-Properties of Octa-Alkyl Substituted Phthalocyanines". *Liq. Cryst.* **1993**, *15*, 709.

[30] Hanack, M.; Beck, A.; Lehmann, H. "Syntheses of Liquid-Crystalline Phthalocyanines". *Synthesis-Stuttgart* **1987**, 703.

[31] Vanderpol, J. F.; Neeleman, E.; Zwikker, J. W.; Nolte, R. J. M.; Drenth, W.; Aerts, J.; Visser, R.; Picken, S. J. "Homologous Series of Liquid-Crystalline Metal Free and Copper Octa-Normal-Alkoxyphthalocyanines". *Liq. Cryst.* **1989**, *6*, 577.

[32] Lelievre, D.; Bosio, L.; Simon, J.; Andre, J. J.; Bensebaa, F. "Dimeric Substituted Copper Phthalocyanine Liquid-Crystals - Synthesis, Characterization and Magnetic-Properties". *J. Am. Chem. Soc.* **1992**, *114*, 4475.

[33] Kobayashi, N. "Dimers, trimers and oligomers of phthalocyanines and related compounds". *Coord. Chem. Rev.* **2002**, *227*, 129.

[34] Hanack, M. "Handbook of organic conducting molecules and polymers". **1997**, *1*

[35] Engelkamp, H.; Middelbeek, S.; Nolte, R. J. M. "Self-assembly of disk-shaped molecules to coiled-coil aggregates with tunable helicity". *Science* **1999**, *284*, 785.

[36] Craciun, M. F.; Rogge, S.; den Boer, M. J. L.; Margadonna, S.; Prassides, K.; Iwasa, Y.; Morpurgo, A. F. "Electronic Transport through Electron-Doped Metal Phthalocyanine Materials". *Adv. Mater. (Weinheim, Ger.)* **2006**, *18*, 320.

[37] Claessens, C. G.; Hahn, U.; Torres, T. "Phthalocyanines: From outstanding electronic properties to emerging applications". *The Chemical Record* **2008**, *8*, 75.

[38] Turek, P.; Petit, P.; Andre, J. J.; Simon, J.; Even, R.; Boudjema, B.; Guillaud, G.; Maitrot, M. "A new series of molecular semiconductors: phthalocyanine radicals". *J. Am. Chem. Soc.* **1987**, *109*, 5119.

[39] Marks, T. J. "Interfaces between Molecular and Polymeric Metals - Electrically Conductive, Structure-Enforced Assemblies of Metallomacrocycles". *Angew. Chem. Int. Ed.* **1990**, *29*, 857.

[40] Schramm, C. J.; Scaringe, R. P.; Stojakovic, D. R.; Hoffman, B. M.; Ibers, J. A.; Marks, T. J. "Chemical, Spectral, Structural, and Charge Transport-Properties of the Molecular-Metals Produced by Iodination of Nickel Phthalocyanine". *J. Am. Chem. Soc.* **1980**, *102*, 6702.

[41] Pace, L. J.; Martinsen, J.; Ulman, A.; Hoffman, B. M.; Ibers, J. A. "Conductive Molecular-Crystals - Structural, Magnetic, and Charge-Transport Properties of (5,10,15,20-Tetramethylporphyrinato)Nickel(Ii) Iodide". *J. Am. Chem. Soc.* **1983**, *105*, 2612.

[42] Hasegawa, H.; Naito, T.; Inabe, T.; Akutagawa, T.; Nakamura, T. "A highly conducting partially oxidized salt of axially substituted phthalocyanine. Structure and physical properties of $TPP[Co(Pc)(CN)_2]_2$ {TPP=tetraphenylphosphonium, $[Co(Pc)(CN)_2]$=dicyano(phthalocyaninato)cobalt(III)}". *J. Mater. Chem.* **1998**, *8*, 1567.

[43] Lever, A. B. P. "Magnetic Behaviour of Transition-Metal Phthalocyanines". *J. Chem. Soc.* **1965**, 1821.

[44] Miyoshi, H.; Ohyanish.H; Deguchi, Y. "Magnetic Properties of Manganese (II) Phthalocyanine". *Bull. Chem. Soc. Jpn.* **1973**, *46*, 2724.

[45] Mitra, S.; Gregson, A. K.; Hatfield, W. E.; Weller, R. R. "Single-Crystal Magnetic Study on Ferromagnetic Manganese (II) Phthalocyaninate". *Inorg. Chem.* **1983**, *22*, 1729.

[46] Evangelisti, M.; Bartolome, J.; de Jongh, L. J.; Filoti, G. "Magnetic properties of alpha-iron(II) phthalocyanine". *Phys. Rev. B,* **2002**, *66*.

[47] Löbbert, G. "Phthalocyanines". *Ullmann's Encyclopedia of Industrial Chemistry* **2000**.

[48] Guillaud, G.; Simon, J.; Germain, J. P. "Metallophthalocyanines - Gas sensors, resistors and field effect transistors". *Coord. Chem. Rev.* **1998**, *178*, 1433.

[49] Loi, M. A.; Denk, P.; Hoppe, H.; Neugebauer, H.; Winder, C.; Meissner, D.; Brabec, C.; Sariciftci, N. S.; Gouloumis, A.; Vazquez, P.; Torres, T. "Long-lived photoinduced charge separation for solar cell applications in phthalocyanine-fulleropyrrolidine dyad thin films". *J. Mater. Chem.* **2003**, *13*, 700.

[50] Guldi, D. M.; Gouloumis, A.; Vazquez, P.; Torres, T. "Charge-transfer states in strongly coupled phthalocyanine fullerene ensembles". *Chem. Commun. (Cambridge, U. K.)* **2002**, 2056.

[51] Gursel, Y. H.; Senkal, B. F.; Kandaz, M.; Yakuphanoglu, F. "Synthesis and liquid crystal properties of phthalocyanine bearing a star polytetrahydrofuran moiety". *Polyhedron* **2009**, *28*, 1490.

[52] Durmus, M.; Yesilot, S.; Ahsen, V. "Separation and mesogenic properties of tetraalkoxy-substituted phthalocyanine isomers". *New J. Chem.* **2006**, *30*, 675.

[53] Ishikawa, N.; Sugita, M.; Ishikawa, T.; Koshihara, S.; Kaizu, Y. "Lanthanide double-decker complexes functioning as magnets at the single-molecular level". *J. Am. Chem. Soc.* **2003**, *125*, 8694.

[54] Chen, Y.; Hanack, M.; Blau, W. J.; Dini, D.; Liu, Y.; Lin, Y.; Bai, J. R. "Soluble axially substituted phthalocyanines: Synthesis and nonlinear optical response". *J. Mater. Sci.* **2006**, *41*, 2169.

[55] Hofman, J. W.; van Zeeland, F.; Turker, S.; Talsma, H.; Lambrechts, S. A. G.; Sakharov, D. V.; Hennink, W. E.; van Nostrum, C. F. "Peripheral and axial substitution of phthalocyanines with solketal groups: Synthesis and in vitro evaluation for photodynamic therapy". *J. Med. Chem.* **2007**, *50*, 1485.

[56] Kolarova, H.; Nevrelova, P.; Bajgar, R.; Hrova, D.; Kejlova, K.; Strnad, M. "In vitro photodynamic therapy on melanoma cell lines with phthalocyanine". *Toxicol. in Vitro* **2007**, *21*, 249.

[57] Ackroyd, R.; Kelty, C.; Brown, N.; Reed, M. "The history of photodetection and photodynamic therapy". *Photochem. Photobiol.* **2001**, *74*, 656.

[58] Bonnett, R. "Progress with heterocyclic photosensitizers for the photodynamic therapy (PDT) of tumours". *J. Heterocycl. Chem.* **2002**, *39*, 455.

[59] Castano, A. P.; Demidova, T. N.; Hamblin, M. R. "Mechanisms in photodynamic therapy: part one-photosensitizers, photochemistry and cellular localization". *Photodiagnosis and Photodynamic Therapy* **2004**, *1*, 279.

[60] Ali, H.; van Lier, J. E. "Metal complexes as photo- and radiosensitizers". *Chem. Rev. (Washington, DC, U. S.)* **1999**, *99*, 2379.

[61] Brasseur, N.; Ouellet, R.; La Madeleine, C.; van Lier, J. E. "Water-soluble aluminium phthalocyanine-polymer conjugates for PDT: photodynamic activities and pharmacokinetics in tumour-bearing mice". *Br. J. Cancer* **1999**, *80*, 1533.

[62] Lo, P. C.; Huang, J. D.; Cheng, D. Y. Y.; Chan, E. Y. M.; Fong, W. P.; Ko, W. H.; Ng, D. K. P. "New amphiphilic silicon (IV) phthalocyanines as efficient Photosensitizers for photodynamic therapy: Synthesis, photophysical properties, and in vitro photodynamic activities". *Chemistry-a European Journal* **2004**, *10*, 4831.

[63] Allen, C. M.; Sharman, W. M.; Van Lier, J. E. "Current status of phthalocyanines in the photodynamic therapy of cancer". *J. Porphyrins Phthalocyanines* **2001**, *5*, 161.

[64] Li, D. Q.; Ratner, M. A.; Marks, T. J. "Molecular and Macromolecular Nonlinear Optical-Materials - Probing Architecture Electronic-Structure Frequency Doubling Relationships Via an Scf-Lcao Meci -Pi Electron Formalism". *J. Am. Chem. Soc.* **1988**, *110*, 1707.

[65] Weber, L.; Grosche, M.; Hennig, H.; Haufe, G. "Oxygenation of Alkenes with Phthalocyaninato Manganese(Iii) and Iron(Iii) Complexes and Dioxygen". *J. Mol. Catal.* **1993**, *78*, L9.

[66] Cimen, Y.; Turk, H. "Oxidation of 2,3,6-trimethylphenol with potassium peroxymonosulfate catalyzed by iron and cobalt phthalocyanine tetrasulfonates in a methanol-water mixture". *Applied Catalysis a-General* **2008**, *340*, 52.

[67] Geraskin, I. M.; Luedtke, M. W.; Neu, H. M.; Nemykin, V. N.; Zhdankin, V. V. "Organic iodine(V) compounds as terminal oxidants in iron(III) phthalocyanine catalyzed oxidation of alcohols". *Tetrahedron Lett.* **2008**, *49*, 7410.

[68] Taniguchi, T.; Sugiura, Y.; Zaimoku, H.; Ishibashi, H. "Iron-Catalyzed Oxidative Addition of Alkoxycarbonyl Radicals to Alkenes with Carbazates and Air". *Angewandte Chemie-International Edition* **2010**, *49*, 10154.

[69] Kudrik, E. V.; Makarov, S. V.; Zahl, A.; van Eldik, R. "Kinetics and mechanism of the cobalt phthalocyanine catalyzed reduction of nitrite and nitrate by dithionite in aqueous solution". *Inorg. Chem.* **2003**, *42*, 618.

[70] Rohlich, C.; Kohler, K. "Macrocyclic Palladium(II) Complexes in C-C Coupling Reactions: Efficient Catalysis by Controlled Temporary Release of Active Species". *Adv. Synth. Catal.* **2010**, *352*, 2263.

[71] Eckert, H. "Selective Reduction of the Nitro to the Amino Functional-Group by Means of the Phthalocyaninecobalt (I) Anion - Synthesis of N-Heterocycles and Alkaloids". *Angew. Chem. Int. Ed.* **1981**, *20*, 208.

UNIVERSITAT ROVIRA I VIRGILI
SYNTHESIS OF TETRA-AZAPORPHYRINS, PHTHALOCYANINES AND LANTHANIDE DOUBLE-DECKER SANDWICH COMPLEXES
Nelson Giménez Agulló

Chapter 2

Study of the Coordination of Quinuclidine to a Chiral Zinc Phthalocyanine Dimer

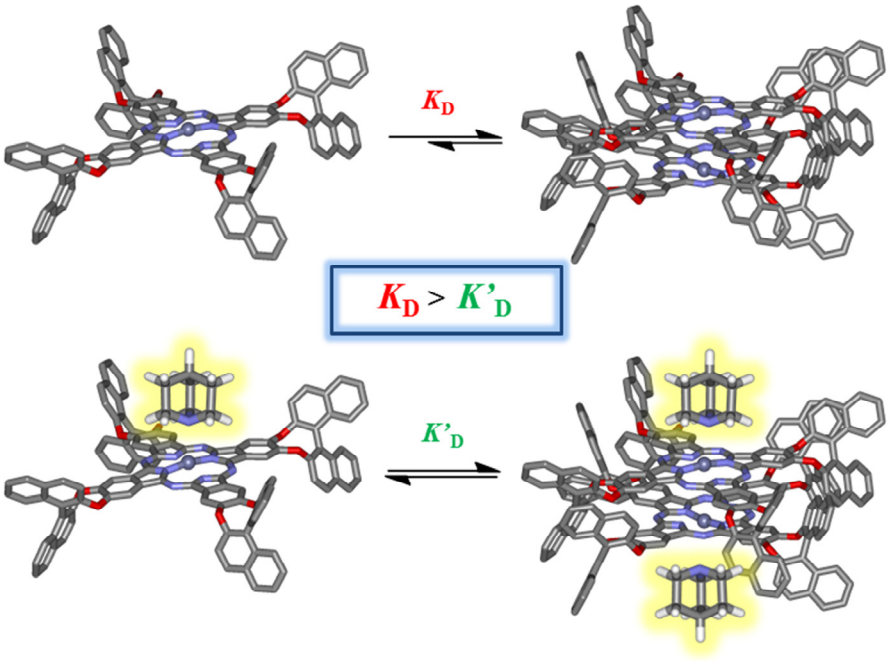

*Part of this Chapter is accepted to be published in *Journal of Porphyrins and Phthalocyanines*

UNIVERSITAT ROVIRA I VIRGILI
SYNTHESIS OF TETRA-AZAPORPHYRINS, PHTHALOCYANINES AND LANTHANIDE DOUBLE-DECKER SANDWICH COMPLEXES
Nelson Giménez Agulló

2.1 Introduction

Phthalocyanines (Pc) and their metallated derivatives have attracted general attention due to their interesting physical, electronic and optical properties. Of particular interest to this work is their tendency to aggregate by stablishing intermolecular π-π stacking interactions. This ability provides Pcs with the capacity to self-assemble into complex supramolecular systems featuring new properties that are not present in the individual entities. The molecular aggregation of Pcs usually leads to one-dimensional nanostructures such as, nanoribons[1] or nanofibers[2] with interest in the field of functional materials. In recent years, the exceptional properties featured by the Pcs and their aggregates have found application in multiple fields that cover from gas sensors,[3] molecular magnets,[4] photovoltaic cells,[5] photosensitizers for photodynamic therapy,[6,7] to non-linear optical materials.[8]

2.1.1 Chiral phthalocyanines

Up to date, a large number of different substituted Pcs have been synthesized and their aggregation properties reported.[9] However, the number of reports dealing with chiral Pcs is scarce.[10,11] The unique optical and magnetic properties of chiral porphyrinoids make them interesting candidates for several applications including chiral recognition,[12] chiral memory,[13] and asymmetric catalysis.[14] Different approaches have been used for their synthesis leading to three diverse groups of optically active Pcs: 1) Pcs substituted with alkyl chains that contain a stereogenic carbon,[15] 2) Pcs substituted with optically active components[16] and 3) Pcs displaying supramolecular asymmetry.[17] The most widely used synthetic approach consists on the introduction of chiral residues into the macrocycle's periphery.

Pc substituted with alkyl chains that contain a stereogenic center

The decoration of the phthalocyanine ring with alkyl chains that contain a stereogenic center is the strategy most widely used to build chiral phthalocyanines as mentioned above. This methodology allows the formation of optically active phthalocyanines and simplifies the purification since the precursors used are enantiomerically pure. Symmetrically octasubstituted chiral phthalocyanines are usually prepared by cyclotetramerization of a chiral dinitrile precursor. These compounds present mesogenic behavior, giving rise to different types of columnar mesophases. Nolte *et al*. reported a chiral phthalocyanine containing branched aliphatic tails derived from (*S*)-citronellol shown in Figure 2.1.[15] This compound was shown to form a chiral columnar mesophase in which each phthalocyanine ring is tilted and gradually rotating along the stacking axis.

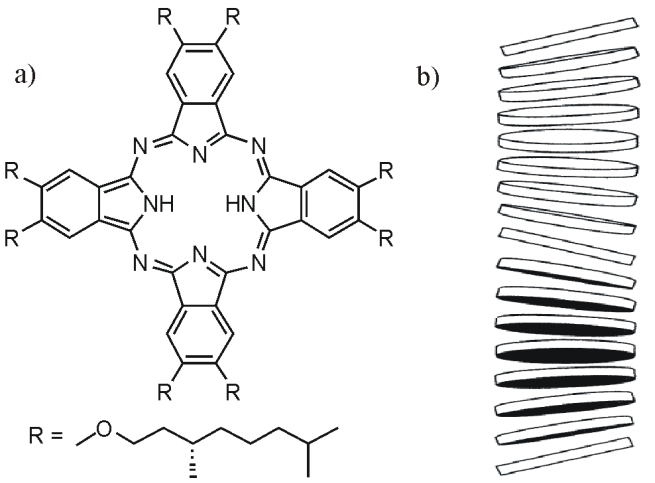

Figure 2.1 a) Molecular structure of a phthalocyanine substituted with alkyl chains containing a sterogenic center and b) Schematic cartoon of the columnar mesophase showing the stacking arrangement of phthalocyanine rings.

Pcs substituted with optically active components

Another methodology for chiral phthalocyanine formation resides in the use of optically active molecules. The substitution of the phthalocyanine with binaphtyl moieties have been reported to produce chiral phthalocyanines in relative good yields.[16] An important property of these compounds is that they do not racemice under general phthalocyanine synthesis conditions allowing the preparation of enantiopure phthalocyanine derivatives. A nice example of preparation of a chiral phthalocyanine substituted with optically active moieties was reported by Kobayashi in 1998 (Figure 2.2).[18] The reaction of enantiopure and commercially available (*S*)- or (*R*)-2,2'-dihydroxy-1,1'-binaphtyl (BINOL) and 3-nitrophthalonitrile yielded the phthalocyanine precursor which was then converted by tetracyclization into the final chiral phthalocyanine in 30-36% yield.

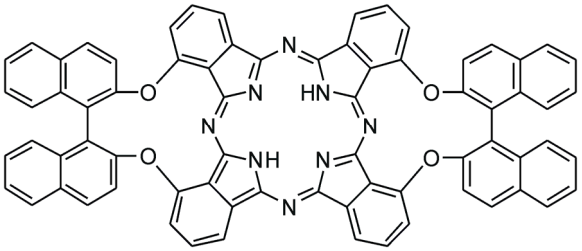

Figure 2.2 Line-drawing molecular structure of a phthalocyanine substituted with two optically active binaphtyl substituents described by Kobayashi.

Pcs displaying supramolecular asymmetry

Metal phthalocyanines (MPc) are planar D_{4h} or C_{4v} molecules and they are achiral when unsubstituted. However, optically active phthalocyanines can be prepared by considering the position of peripheral substituent groups and the deformation of the Pc skeleton. This can be accomplished even using not optically active substituents and such Pcs are said to be intrinsically optically active. Phthalocyanines displaying supramolecular asymmetry can be prepared by the introduction of an axial ligand to one side of the tetrasubstituted MPc

plane, leading to a mixture of right-handed and left-handed conformers. An example of supramolecular asymmetry in phthalocyanines was reported by Kobayashi *et al*. in 2009 (Figure 2.3).[17] Inherently chiral oxovanadium(IV) phthalocyanine (VOPc) with single-handed rotation was prepared by cyclic tetramerization of 3-hexyloxyphthalonitrile followed by metal insertion reaction with V_2O_5. The two enantiomers of the VOPc were successfully separated by chiral HPLC chromatographic techniques and showed circular dichroism (CD) spectra of opposite signs.

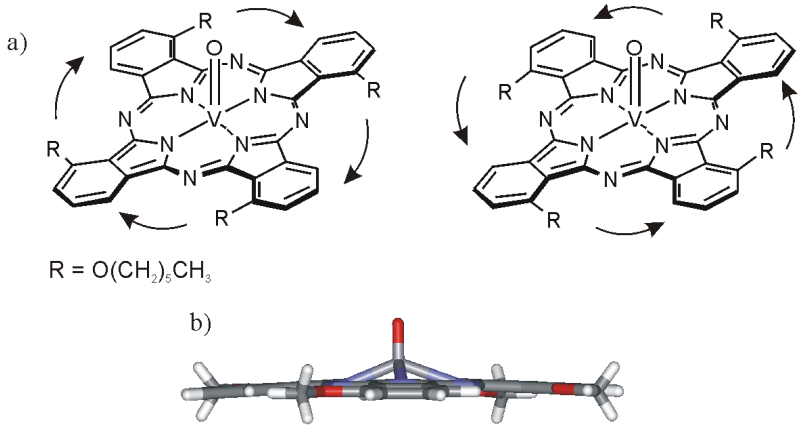

Figure 2.3 a) Chemical structures of the two enantiomers of VOPc displaying supramolecular asymmetry. b) Side view of the MM3 energy minimized structure of a VOPc model in which the metal center bows the planarity of the macrocycle giving rise to supramolecular asymmetry.

2.1.2 Phthalocyanine metal coordination chemistry

Metal coordination bonds have been extensively used to direct the self-assembly of large supramolecular architectures. In this context, transition-metal porphyrins have been amply exploited as acceptor building blocks since the central metal atom possesses at least one axial site available for coordination.[19,20] The formation of coordination bonds is a simple strategy to self-assemble metalloporphyrin monomers to form large supramolecular architectures. In turn, the use of metallophthalocyanines as acceptor ligands is very attractive not only due to their analogous structure with porphyrin complexes but also due

to their higher chemical and thermal stability. Some works regarding the coordination of amino ligands to several Zn(II) phthalocyanines have been published in literature.[21,22,23] However, in these reports the determination of accurate binding constants for the corresponding complexes was not addressed in detail.

2.2 Objectives

The aim of this Chapter is the study of the dimerization process of an enantiopure zinc phthalocyanine in solution in order to calculate the dimerization constant. Considering that the accurate assessment of the dimerization constant is crucial for the calculation of its speciation (monomer/dimer) in solution at any concentration, we decided to investigate the dimerization equilibria of the enantiopure zinc phthalocyanine in chloroform using dilution UV-vis experiments and variable temperature ^{1}H NMR.

Additionally, the coordination of an amine (quinuclidine) to the enantiopure zinc phthalocyanine will be also studied at two different concentrations using UV-vis and ^{1}H NMR titrations experiments. The determination of accurate binding constants for the corresponding complexes will be addressed in detail.

2.3 Results and Discussion

2.3.1. Synthesis of Zn-1

Chiral phthalocyanine **Zn-1** (Figure 2.4) was described in 2012 by Jiang and coworkers.[24] It constitutes a nice example of building an enantiomerically pure Pc through peripheral decoration with chiral binaphtyl units. It was described that **Zn-1** formed dimeric aggregates held together through multiple cooperative π-π interactions. The existence of **Zn-1** as discrete dimeric entities (i.e. [**Zn-1**]$_2$) featuring a face-to-face supramolecular structure was demonstrated in the solid state by X-ray diffraction of single crystals and in solution using ^{1}H NMR spectroscopy.

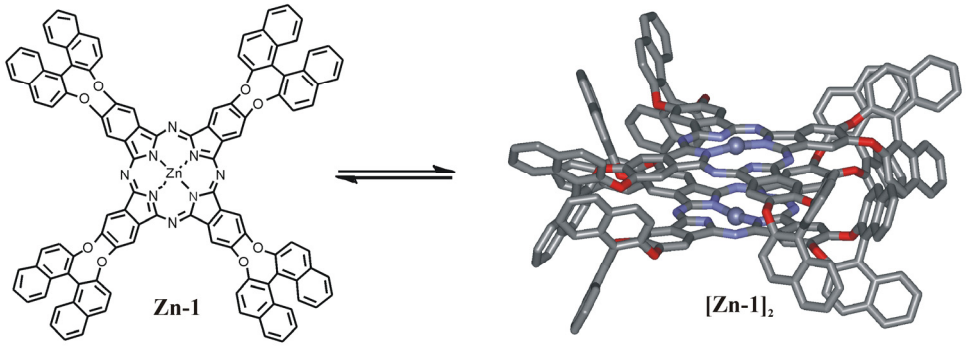

Figure 2.4 Dimerization equilibrium of the chiral zinc phthalocyanine **Zn-1**. The structure of **Zn-1** monomer is shown as line-drawing structure and the dimer [**Zn-1**]$_2$ as MM3 energy minimized structure (protons are omitted for clarity).

Chiral phthalocyanines (*R*)- and (*S*)-**Zn-1** and the enantiomerically pure *(R)*- and *(S)*-dinitriles precursors were synthesized following reported procedures (Scheme 2.1).[24,25] The preparation of the enantiomerically pure precursors for the phthalocyanine formation was accomplished by reaction of commercial and enantiomerically pure (*R*)- or (*S*)-1-1'-Bi-2-naphtol (BINOL) with dry DMF solution of 4,5-dichlorophthalonitrile and K_2CO_3 (Scheme 2.1). The circular dichroism (CD) spectra of the prepared dinitriles, not reported in the

original paper, showed, as expected, bisignated CD spectra due to the exciton coupling between the chromophores (naphthyls) present in the molecule.

The enantiopure dinitriles were refluxed in separated hexanol solutions in the presence of $Zn(OAc)_2$ and DBU to yield the (*R*)-**Zn-1** and (*S*)-**Zn-1.**[26] Enantiopure **Zn-1** was isolated in acceptable yields (39-45 %) after silica column chromatography purification of the reaction crude using CH_2Cl_2:THF (100:2) as eluent mixture. As expected, both enantiomers presented identical ^{1}H NMR and UV-vis spectra that were in agreement with the ones previously reported by Jiang and co-workers.[23]

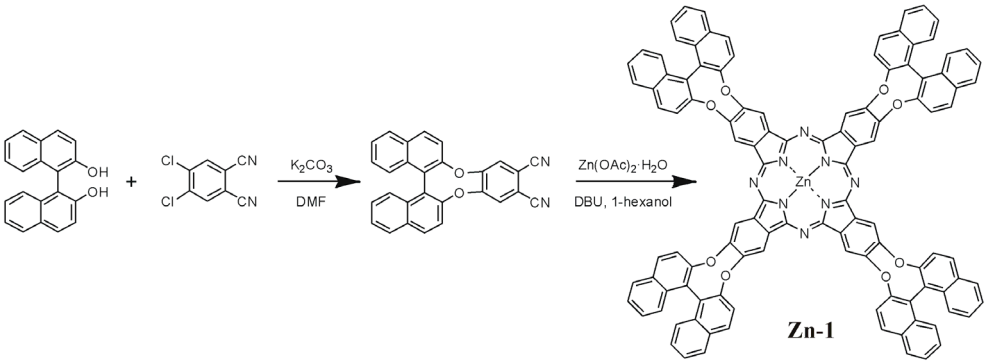

Scheme 2.1 Reaction procedure used for the synthesis of (*R*)- and (*S*)-enantiomers of **Zn-1**

2.3.2. Thermodynamic characterization of the dimerization process of Zn-1

The ^{1}H NMR spectrum of (*R*)-**Zn-1** displayed two singlets resonating at 9.29 and 7.83 ppm assigned to the aromatic protons of the isoindole units and two sets of six signals appearing in the range of 8.72 to 6.79 ppm corresponding to the aromatic protons of the peripheral binaphtyl moieties. This observation was in agreement with the described π-π dimerization experienced by (*R*)-**Zn-1** at 1 mM concentration, that assigns a C_4 symmetry of the monomer in the dimeric assembly [(*R*)-**Zn-1**]$_2$ [27] The ^{1}H NMR spectrum recorded for a more diluted sample of (*R*)-**Zn-1** in $CDCl_3$ solution (5×10^{-4} M) resulted in the emergence of a new set of proton signals that was attributed to the monomeric species, (*R*)-**Zn-1**, featuring D_4 symmetry. In the (*R*)-**Zn-1** monomer the protons from the isoindole units appear as a singlet at 9.43 ppm. Moreover, the protons corresponding to the peripheral binaphthyl substituents produce a single set of six signals between 8.17-7.36 ppm owing to the symmetry increase for the monomer. A dimerization constant value of $K_D = 7.3 \times 10^3$ M^{-1} in $CDCl_3$ was previously reported by Jiang *et al*. This constant value was calculated using the integral areas of the proton signals assigned to the monomer and the dimer.

Considering that the accurate assessment of the dimerization constant for enantiopure **Zn-1** was crucial for the calculation of its speciation (monomer/dimer) in solution at any concentration, we decided to investigate the dimerization equilibria of **Zn-1** in chloroform using dilution UV-vis experiments.

The aggregation of zinc-phthalocyanines is known to occur in solution even at the low concentrations used to register their UV-vis spectra.[24] The UV-vis spectrum of enantiopure **Zn-1** in $CHCl_3$ solution at a 10^{-6} M concentration displayed the typical absorption bands of a metallated phthalocyanine (i.e. Soret band with maximum at 350 nm, and an intense Q-band centered at 680 nm together with two weak shoulders with maxima at 616 and 647 nm). The absorption band corresponding to the binaphtyl moieties was centered at 280 nm. UV-vis dilution studies of enantiopure **Zn-1** dissolved in chloroform in a concentration range of 10^{-5} to 10^{-6} M returned an absorption spectra that did not show significant changes in the epsilon scale. This result evidenced that in the used range of concentrations

enantiopure **Zn-1** existed in solution as a unique species, most likely the monomer considering the previously reported K_D value. Conversely, the UV-vis spectra acquired in a range of more concentrated solutions of enantiopure **Zn-1** (1×10^{-5} M to 1.24×10^{-4} M) showed a non-linear relationship between concentration and molar extinction coefficient values. Upon increasing the concentration of enantiopure **Zn-1**, the UV-vis spectrum (epsilon scale) displayed a small increment in the intensity of the bands centered at 617 and 647 nm, while the band at 680 nm decreased in intensity (Figure 2.5). This observation suggested the formation of aggregates in solution induced by π-π stacking interactions.[24]

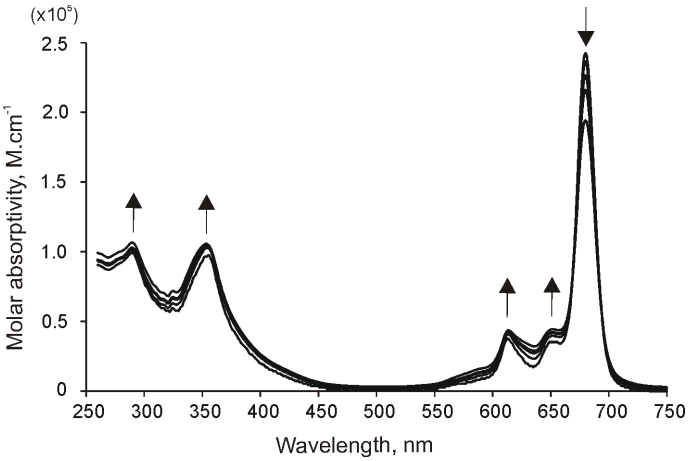

Figure 2.5 UV-Vis spectra of **Zn-1** at different concentrations (1×10^{-5} M to 1.24×10^{-4} M) in chloroform recorded during the dilution experiment.

We performed the mathematical analysis of the UV-vis dilution data using a simple theoretical dimerization model. The fit of the experimental data to the model was good and returned a value of $K_D = 5.17 \times 10^3$ M^{-1} for the dimerization constant (Figure 2.6).

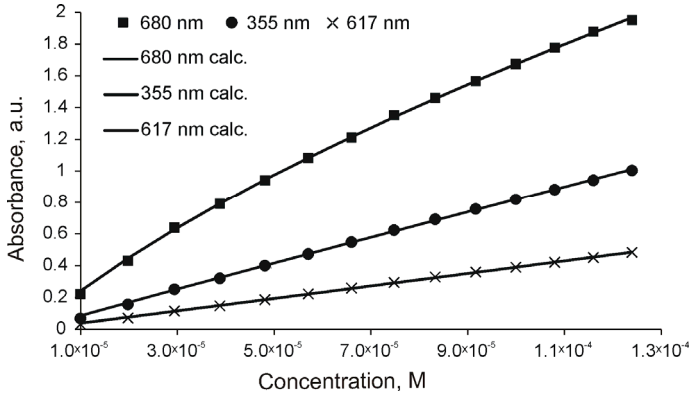

Figure 2.6 Fit of the experimental data at 355, 617 and 680 nm obtained from the UV-vis dilution experiments of **Zn-1** (1×10^{-5} M to 1.24×10^{-4} M in chloroform) to the calculated theoretical dimerization model for **Zn-1**

It is worthy to note that the magnitude of the calculated K_D should allow the observation of monomeric and dimeric species in the ^{1}H NMR spectra at the working concentration range (2 mM). The observation of a single species (dimer) in the ^{1}H NMR spectra at this concentration indicated that the dimerization constant value was underestimated. Probably, the low amount of dimer present in solution in the range of concentrations covered for the UV-vis dilution experiments (i.e. less than 20%) complicated the determination of an accurate value (Figure 2.7). However, the high absorptivity displayed by enantiopure **Zn-1** did not allow us to acquire UV-vis spectra at higher concentrations. In view of these limitations and considering the results obtained by NMR spectroscopy, we simply estimated a value of $K_D > 10^4$ M^{-1} for the dimerization process. Our estimate is close but larger than the value reported by Jiang *et al*. using ^{1}H NMR spectroscopy.

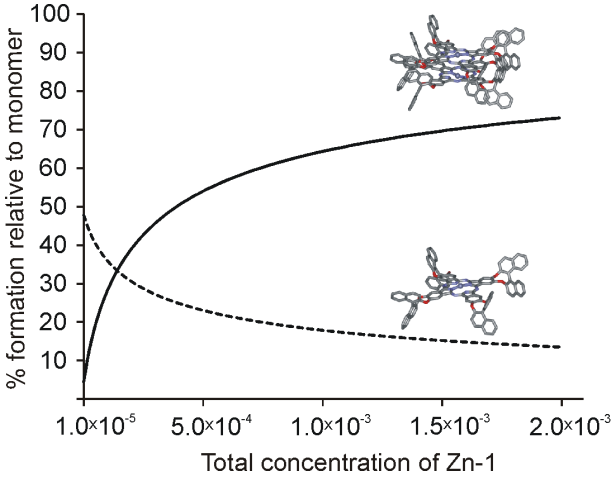

Figure 2.7 Speciation profile of the dimerization process of **Zn-1** in the concentration range of 1×10^{-5} M to 2×10^{-3} M calculated considering a dimerization constant of $K_D = 10^4$ M^{-1}

The reasons why the aggregation of enantiomerically pure **Zn-1** stops at the dimeric state are unknown for us. However, the analysis of the diffraction data of single crystals obtained from a $CHCl_3$ solution of enantiopure **Zn-1** previously described by Jiang and co-workers also revealed the exclusive presence of dimeric aggregates in the solid state.[24] Analogous results were obtained in the solid state for the enantiopure free base phthalocyanine **H_2-1.**[25]

Surprisingly, contrary to the sharp and well-defined signals observed in ^{1}H NMR spectra of enantiomerically pure samples of (*R*)- and (*S*)-**Zn-1** in $CDCl_3$, an equimolar mixture of (*R*)- and (*S*)-**Zn-1** in $CDCl_3$ solution, that is racemic **Zn-1**, did not produce observable proton signals when analyzed using ^{1}H NMR spectroscopy. This result suggested that in the racemic mixture the aggregation process does not stop at the dimeric state but continues with the formation of higher order colloidal aggregates that are not detectable by ^{1}H NMR spectroscopy.

Dynamic Light Scattering (DLS) experiments were performed on 0.1 mM $CHCl_3$ solutions of enantiomerically pure (*S*)-**Zn-1** and of an equimolar mixture of (*R*)- and (*S*)-

Zn-1 gave an average radii of 1.71 nm and 337.4 nm, respectively (Figure 2.8). These results demonstrated that in the racemic mixture of (*R*)- and (*S*)-**Zn-1** aggregates of bigger dimensions are formed compared to the enantiomerically pure solutions.

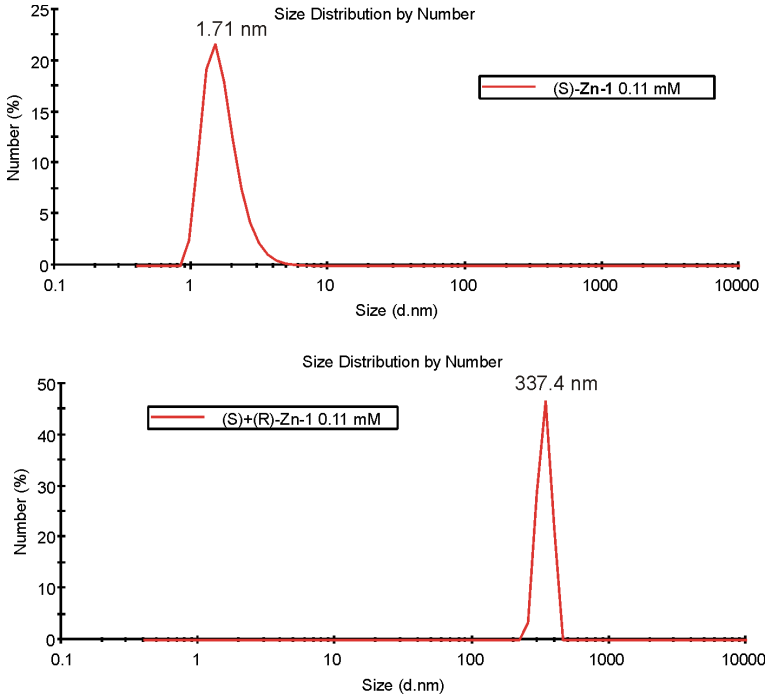

Figure 2.8 Dynamic Light Scattering (DLS) experiments on 0.1 mM $CHCl_3$ solutions of enantiomerically pure (*S*)-**Zn-1** and of an equimolar mixture of (*R*)- and (*S*)-**Zn-1**

According to the magnitude of the estimated dimerization constant, the ^{1}H NMR spectrum of a 2mM solution of enantiopure **Zn-1** displayed a number of proton signals in agreement with the C_4 symmetry of [**Zn-1**]$_2$ in a dimeric species. We performed a Diffusion-Ordered SpectroscopY (DOSY) experiment[28] using the above solution and determined a diffusion constant of $3.51 \pm 0.06 \times 10^{-10}$ m^2/s for the [**Zn-1**]$_2$ dimer. Using the Stokes-Einstein equation we derived a hydrodynamic radius of 11.7 Å for the [**Zn-1**]$_2$ dimer, which agrees well with the dimensions of the dimer estimated from simple molecular modelling studies (Figure 2.9).

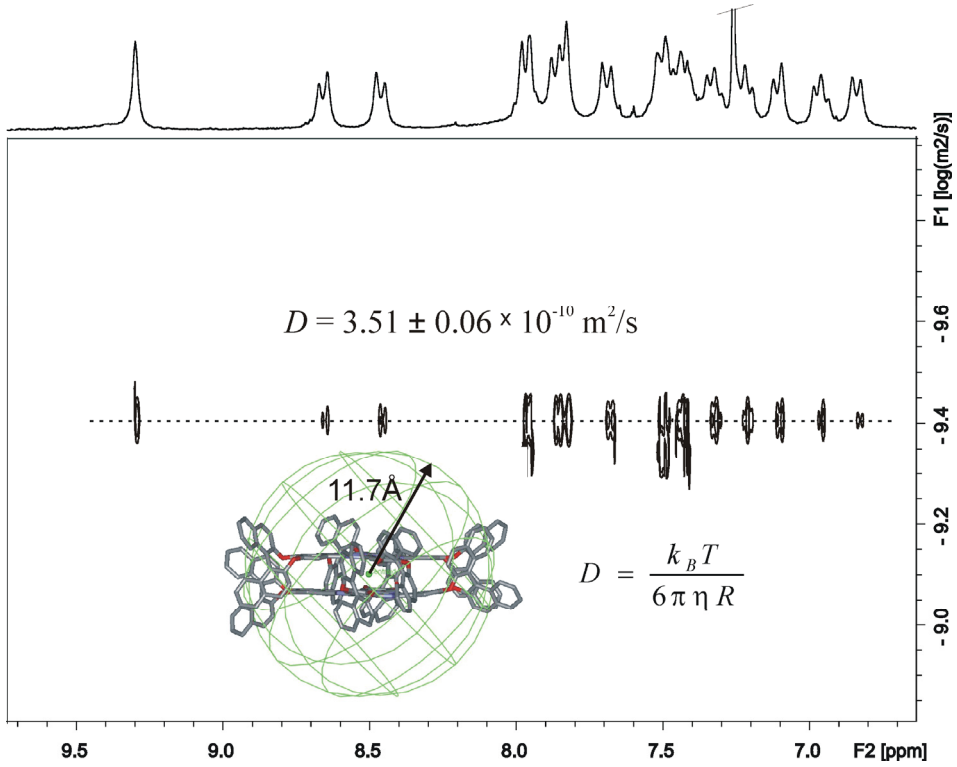

Figure 2.9 Left: ^{1}H NMR DOSY spectra of a 2 mM solution of **Zn-1** in chloroform showing the presence of a single species in solution. Right: MM3 energy minimized structure of dimer **[Zn-1]$_2$** with a sphere centered on it with a radius of 11.7 Å that corresponded to the one determined form the DOSY experiment using the Stokes-Einstein equation.

The dimerization process of enantiopure **Zn-1** was also investigated in solution by means of variable temperature ^{1}H NMR experiments. As stated above, at 298 K, the ^{1}H NMR spectrum of a 2 mM solution of enantiopure **Zn-1** in chloroform displayed two singlets at 9.30 and 7.83 ppm corresponding to the chemically non-equivalent H_a protons in the isoindole units of **Zn-1** in the [**Zn-1**]$_2$ dimer (Figure 2.10). Lowering the temperature to 263 K resulted in the appearance of a new signal at 9.43 ppm that was assigned to the chemically-equivalent isoindole H_a protons of the monomer **Zn-1**. Further lowering of temperature induced an increase in the signal resonating at 9.43 ppm, corresponding to the monomer, at the expenses of those attributed to the [**Zn-1**]$_2$ dimer. At 223 K, the proton

signals corresponding to the monomer were the only ones observable in the ^{1}H NMR spectrum.

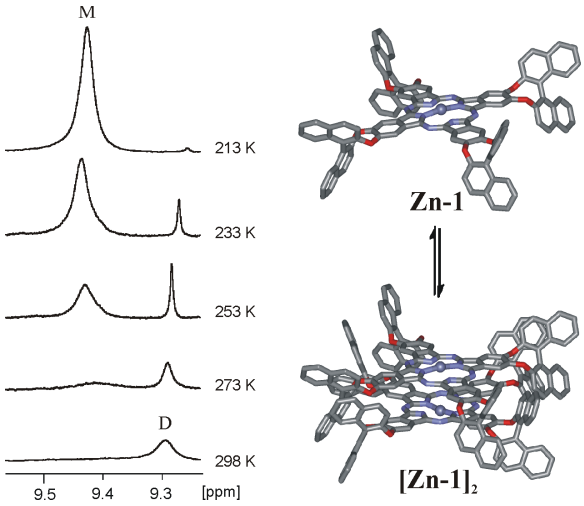

Figure 2.10 Left: Selected region of the variable temperature ^{1}H NMR spectra of a 2 mM chloroform solution of **Zn-1** showing the proton signal corresponding to the isoindole unit of the monomer (M) and one of the two isoindole protons displayed by the dimer (D). Right: MM3 energy minimized structures of the monomeric and dimeric species of **Zn-1**.

These results suggested that the monomer is favored at low temperatures while the dimer is favored on increasing the temperature. This was not an expected result; typically dimerization is favored at low temperatures.

The thermodynamic signature for the dimerization process was obtained from a van't Hoff plot (see experimental section for more details). The linear fit of the experimental data was good and allowed the calculation of the values of the thermodynamic contributions to the dimerization as ΔH = 8.25 kcal·mol^{-1} and ΔS = 42.1 cal·mol^{-1}·K^{-1}, corresponding to a ΔG = -4.28 kcal·mol^{-1} at 298 K (Figure 2.11).

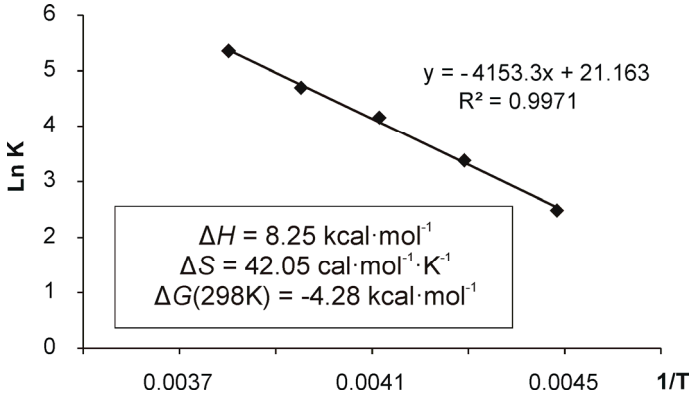

Figure 2.11 Van't Hoff plot and calculated thermodynamic parameters for the dimerization process of **Zn-1** in $CDCl_3$. Temperature range used: 263 K to 233 K. Calculation was based on the integral values of the ^1H NMR signals at 9.43 ppm (monomer) and 9.29 ppm (dimer)

The obtained thermodynamic parameters indicated that the dimerization process is endothermic and driven exclusively by entropy. This result may appear counterintuitive if one thinks that dimeric species are more ordered and both vibrationally and conformationally more constrained than the monomer. However, we can rationalize the obtained result by considering the solvation/desolvation processes that are involved with the dimerization equilibrium. The formation of the dimer [**Zn-1**]$_2$ is associated with a substantial reduction of the Pc's surface that is accessible to the solvent. In other words, upon dimerization a non-defined number of ordered solvent molecules that solvated one of the monomer's faces must be released to the bulk solution. The dimerization process definitively produces a gain in entropy when considering the solvent molecules. This large gain in entropy compensates the enthalpic cost of the dimerization process that is associated with a lower enthalpy for the π-π interactions of the dimer than for the solvated monomers. When the temperature is increased the released solvent molecules pay for the energetic cost of the dimerization process which is enthalpically unfavorable. This is translated in the observed increase of the dimerization equilibrium constant at higher temperatures. Entropy-driven dimerization processes in organic solvents are uncommon but have been observed for other systems such as Cram's velcrands[29] and Rebek's molecular capsules.[30]

2.3.3. Solution studies of quinuclidine binding to Zn-1

The binding of quinuclidine **2** to enantiopure **Zn-1** was studied by means of UV-vis and ^{1}H NMR spectroscopy. The concentration of **Zn-1** used to perform the binding studies plays an important role in determining its distribution into monomeric and dimeric species.[31] The coordination of quinuclidine to enantiopure **Zn-1** was first probed by UV-vis titration experiments using a 4×10^{-6} M chloroform solution of **Zn-1**. From the dimerization studies, one can derive that under these diluted conditions **Zn-1** exists in solution exclusively as a monomer. The addition of increasing amounts of quinuclidine to a 4 μM solution of enantiopure **Zn-1** resulted in a gradual diminution of the Soret band centered at 355 nm and the concomitant appearance of a red-shifted band with maximum at 362 nm (Figure 2.12). This 7 nm red-shift is associated with the axial coordination of the quinuclidine ligand to the Zn center of **Zn-1** to form a 1:1 complex, as typically observed for Zn-porphyrins.[32] Moreover, the titration spectra provided a clear isosbestic point centered at 361 nm. This observation suggested the presence of a single equilibrium involving two colored species in solution. Based on previously reported coordination studies using Zn-porphyrins, we assigned the two species to free **Zn-1** and the 1:1 complex **2•Zn-1** having one molecule of quinuclidine axially coordinated to the zinc metal center. The analysis of the experimental titration data using a theoretical 1:1 binding isotherm gave a good fit and returned an association constant value of K(**2•Zn-1**) = 1.69×10^6 M^{-1} for the **2•Zn-1** complex (Figure 2.12). This value is two orders of magnitude larger than the one measured for coordination complexes of quinuclidine with zinc-porphyrins.[33] Most likely, the Lewis acidity of the zinc(II) metal center is increased in the Pc derivatives compared to their porphyrin analogues provoking the strengthening of the coordination bonds.

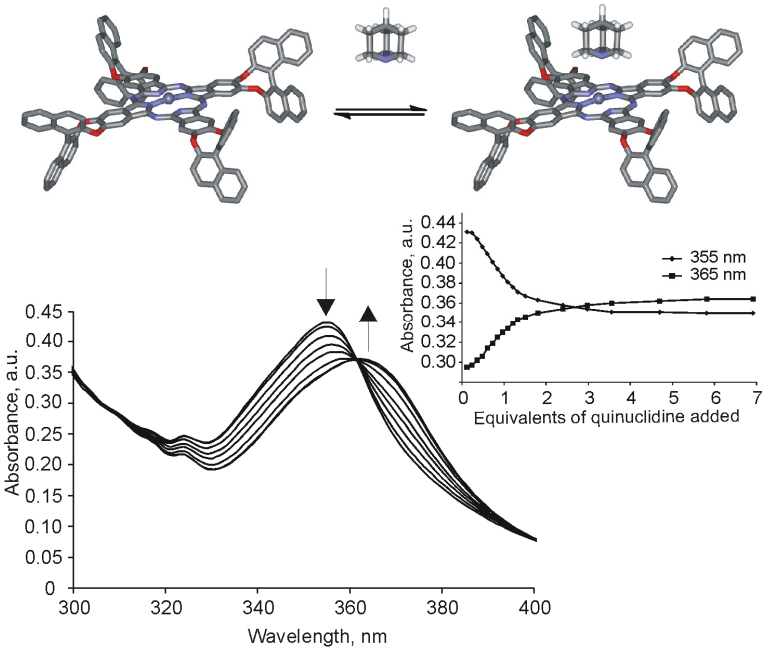

Figure 2.12 MM3 energy minimized structures representing the quinuclidine coordination to the **Zn-1** monomer (top) and UV-vis titration spectra (Soret region) of **Zn-1** with increasing amounts of quinuclidine in chloroform at 298K (from 0 to 7 eq) (bottom). The concentration of the zinc-phthalocyanine was maintained constant throughout the titration (4×10^{-6} M). Inset: Fit of the experimental data at 355 and 365 nm to the calculated theoretical 1:1 binding isotherm.

When the binding process of quinuclidine with enantiopure **Zn-1** was studied using ^{1}H NMR spectroscopy complexes of larger stoichiometry than the simple 1:1 were detected. At NMR concentration ([**Zn-1**] ~ 2×10^{-3} M) and room temperature, enantiopure **Zn-1** is exclusively present in solution as the dimer [**Zn-1**]$_2$ (Figure 2.13 a). The addition of 0.3 equiv of quinuclidine to a 2 mM $CDCl_3$ solution of **Zn-1** resulted in the emergence of a new singlet (H_a') in the downfield region of the ^{1}H NMR spectrum (Figure 2.13 b). This new singlet emerging at 9.13 ppm was attributed to isoindole aromatic protons of **Zn-1** in a coordination complex of unknown stoichiometry. Concomitantly, three new signals appeared in the upfield region of the ^{1}H NMR spectrum. These signals resonated at -2.85, -0.7, and 0 ppm and were assigned to the H_1', H_2' and H_3' protons of bound quinuclidine. The notable upfield shift experienced by the quinuclidine protons compared to their

chemical shifts in the free ligand ($\Delta\delta$ = -5.7, -2.2 and -1.7 ppm for the H_1, H_2 and H_3, respectively), pointed to the formation of an axially coordinated complex between quinuclidine and **Zn-1**. The protons of the bound quinuclidine experienced a large upfield shift induced by the ring-current that was more evident for the α-quinuclidine protons (H_1') due to its close proximity to the Pc π-system.

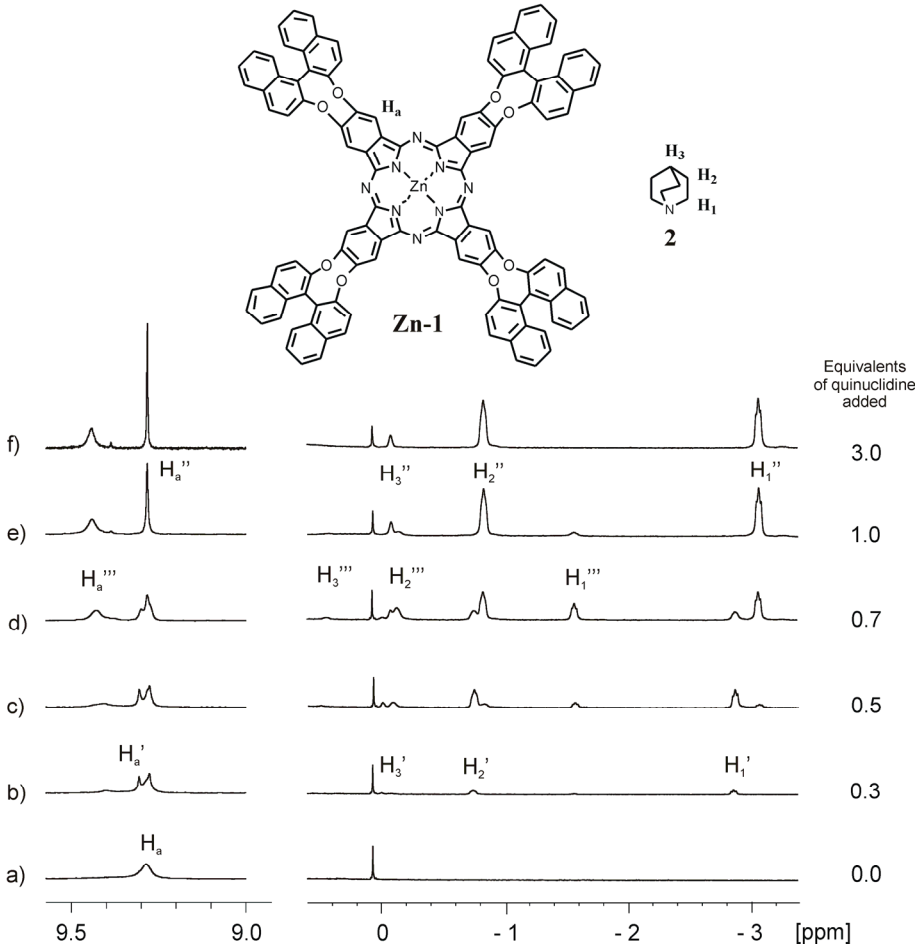

Figure 2.13 Selected regions of the ^{1}H NMR spectrum recorded during a titration of **Zn-1** with increasing amounts of quinuclidine **2** displaying the progressive formation of the 2:1, 2:2 and 1:1 complexes. ([**Zn-1**] = $2 \cdot 10^{-3}$ M, $CDCl_3$, 400 MHz). Primed letter corresponded to 1:2 complex **2**•[**Zn-1**]$_2$, doubly primed to the 2:2 complex **2**$_2$•[**Zn-1**]$_2$, and triply primed to the 1:1 complex **2**•[**Zn-1**].

Taken together, these observations suggested the initial formation of a 2:1 complex **2•[Zn-1]$_2$**, in which one quinuclidine molecule is bound to one of two faces of the [**Zn-1$_2$**] dimer. Addition of incremental amounts of **2** (up to 0.5 equiv) provoked a decrease in the intensity of the proton signals assigned to the initially formed 2:1 complex. Simultaneously, a new broad signal resonating at 9.29 ppm (H_a'') emerged and a new set of three signals for bound quinuclidine, resonating at -3.06, -0.83 and -0.08 ppm, and assigned as H_1'', H_2'' and H_3'', appeared (Figure 2.13 c). We attributed this new set of signals to the formation of a 2:2 complex **2$_2$•[Zn-1]$_2$** having one quinuclidine axially coordinated in each one of the two faces of the [**Zn-1$_2$**] dimer. A further increase in the quinuclidine concentration gradually shifted the equilibrium towards the preferential formation of the 2:2 complex. Nonetheless, in the presence of 0.7 equiv of quinuclidine (Figure 2.13 d) a third set of signals for the bound ligand emerged (-1.6, -0.1 and 0.4 ppm, H_1''', H_2''' and H_3''', respectively) in the upfield region of the spectrum together with a new broad aromatic signal resonating at 9.43 ppm (H_a'''). The downfield shift of this aromatic signal suggested that the newly formed complex should have a 1:1 stoichiometry (**2•Zn-1**). We have observed an analogous downfield shift of the isoindole protons in the **Zn-1** monomer. The emergent **2•Zn-1** complex will result from the dissociation of the previously formed 2:2 complex, whose concentration had increased (Figure 2.14).

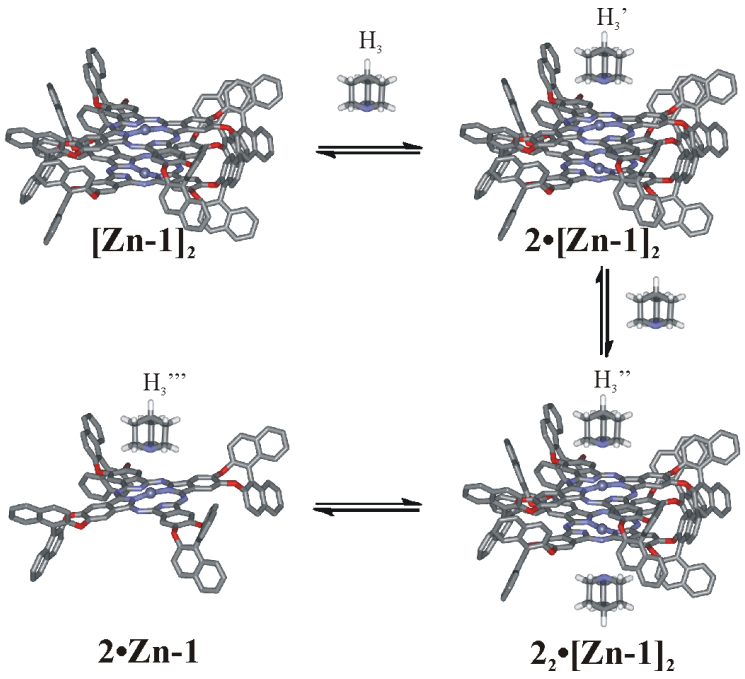

Figure 2.14 Binding model used to rationalize the binding of quinuclidine **2** to the **[Zn-1]$_2$**. MM3 energy minimized structures are shown for the species involved.

The simulated speciation profile for the quinuclidine binding to enantiopure **Zn-1** at millimolar concentration, considering dimerization constants for **Zn-1** and **2•Zn-1** as K_D = 10^4 M^{-1} and K_D = 0.6 × 10^3 M^{-1} (*vide infra*), respectively, and a microscopic binding constant value of K = 1.69 × 10^6 M^{-1} for the interaction of quinuclidine with enantiopure **Zn-1** in any of its stoichiometric states, was in complete agreement with the results obtained in the above ^{1}H NMR titration (Figure 2.15)

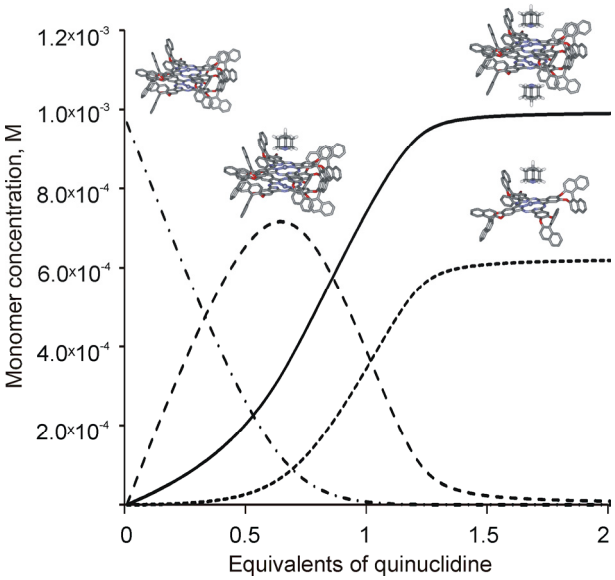

Figure 2.15 Speciation profile of the quinuclidine:**Zn-1** binding process at mM concentration. The speciation was simulated considering dimerization constants for **Zn-1** and **2•Zn-1** as K_D = 10^4 M^{-1} and K_D = 0.6 × 10^3 M^{-1}, respectively, and a microscopic binding constant value of K = 1.69 × 10^6 M^{-1} for the interaction of quinuclidine with enantiopure **Zn-1** in any of its stoichiometric states.

The addition of more than 1 equiv of quinuclidine to the solution, provoked the selective disappearance of the quinuclidine signals assigned to the 1:1 complex but not to those of the parent 2:2 complex (Figure 2.13 f). In contrast, the proton signals corresponding to the isoindole units in the 1:1 and the 2:2 complex did not experience noticeable changes. These observations together with the lack of well-defined proton signals in the ^{1}H NMR spectra of mixture for free quinuclidine added in excess, suggested the existence of a chemical exchange process that was intermediate on the chemical shift timescale between the 1:1, **2•Zn-1,** complex and free quinuclidine. The differences in the exchange kinetics observed for free quinuclidine and bound quinuclidine in the 1:1, **2•Zn-1,** (intermediate) or the 2:2, **2_2•[Zn-1]$_2$,** (slow) complexes suggested that they were involved in exchange mechanisms with different energy barriers (Figure 2.16).

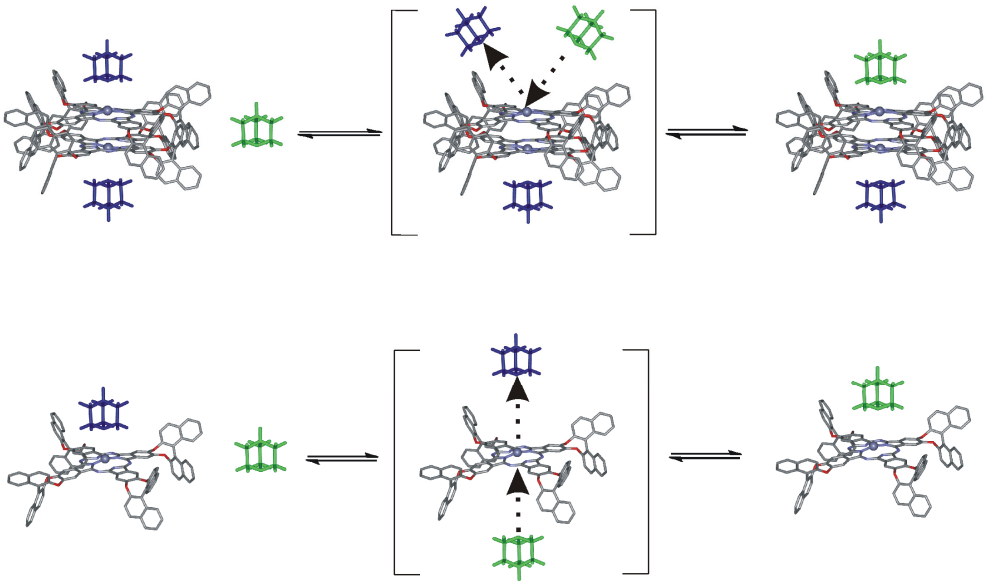

Figure 2.16 a) Proposed "dissociative-like" mechanism for the ligand exchange in the 2:2 complex and b) proposed "associative-like" mechanism for the ligand exchange in the 1:1 complex.

We hypothesize that in the 2:2 complex the exchange of bound quinuclidine implies the complete cleavage of the Zn(II)···N coordination bond prior to the exchange with the free ligand (i.e. "dissociative-like" ligand exchange mechanism). Conversely, in a 1:1 complex the face opposite to the bound ligand is available for the entrance of the exchange partner. Most likely, the approach of the incoming quinuclidine occurs synchronously to the departure of the one leaving. Thus, the ligand exchange occurs through an "associative-like" mechanism. The energy barrier for the "dissociative-like" exchange (2:2 complex) should be higher compared to the "associative-like" one (1:1) because the former requires the complete cleavage of the coordination bond prior to the exchange. This translates into the slow exchange process on the ^{1}H NMR timescale observed for the free/bound quinuclidine in the 2:2, $\mathbf{2_2 \bullet [Zn\text{-}1]_2}$, complex. Likewise, the lower energy barrier that might be associated with the ligand exchange in the 1:1, **2•Zn-1,** complex would explain the intermediate rate on the ^{1}H NMR timescale observed for exchange process of the free/bound quinuclidine in this complex.

In order to reduce the exchange rate of quinuclidine in the 1:1, **2•Zn-1**, complex we performed variable temperature ^{1}H NMR experiments using a 2 mM $CDCl_3$ solution of **Zn-1** in the presence of a large excess of quinuclidine (Figure 2.17).

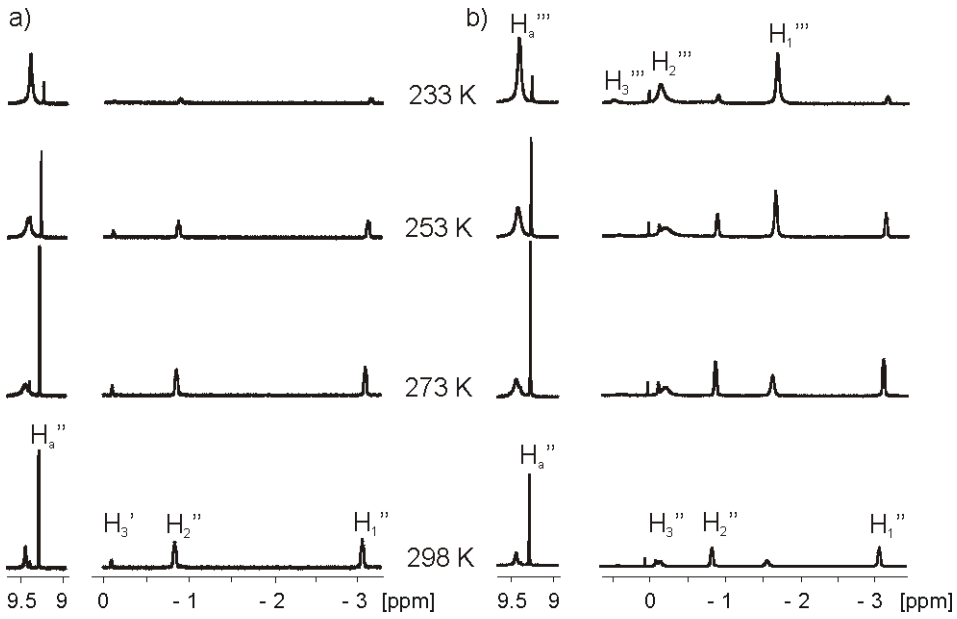

Figure 2.17 a) Selected regions of the variable temperature ^{1}H NMR spectra of a 2 mM solution of **Zn-1** with 3 equiv of quinuclidine in $CDCl_3$. b) Selected regions of the variable temperature ^{1}H NMR spectra of a 2 mM sample of **Zn-1** with 0.8 equiv of quinuclidine in $CDCl_3$.

Unfortunately, we were not able to observe separate proton signals for free and bound quinuclidine in the solution containing the 1:1, **2•Zn-1**, complex even at 213 K. The only significant change we observed in the variable temperature ^{1}H NMR spectra was the decrease in intensity of the proton signals corresponding to the 2:2, $\mathbf{2_2•[Zn\text{-}1]_2}$, complex and the concomitant increase of the ones corresponding to the 1:1 complex. This observation indicated that at lower temperatures the 1:1 ↔ 2:2 equilibrium was shifted towards the formation of the 1:1, **2•Zn-1**, complex whereas at higher temperatures the π-aggregation was favored. This result was in complete agreement with the previous findings made for the variable temperature study of the dimerization process of **Zn-1**.

We observed that at room temperature the ^{1}H NMR spectrum of a $CDCl_3$ solution containing 2 mM enantiopure **Zn-1** and 3 equiv of **2** showed proton signals for dimeric and monomeric coordinated species (2:2 and 1:1 complexes, respectively). This observation indicated a reduction in the dimerization affinity for the coordinated monomer compared to the non-coordinated counterpart. Using the values of the integral areas of the most downfield shifted proton signals of the **2•Zn-1** and **[2•Zn-1]$_2$** complexes we calculated a dimerization constant value of K_D (**[2•Zn-1]$_2$**)= 0.6×10^3 M^{-1} at 298 K for the enantiopure **2$_2$•[Zn-1]$_2$** complex. This value is indeed lower than our estimate for the dimerization constant of free **Zn-1** ($K_D > 10^4$ M^{-1}, *vide supra*) and Jiang's reported value ($K_D = 7.3 \times 10^3$ M^{-1}). The strength of π-π interactions responsible for the dimer formation is reduced upon coordination of the axial ligand. Probably, the complexation of quinuclidine to the Zn(II) metal center of the **Zn-1** Pc distorted its planarity resulting in weaker π-π interactions between the two coordinated monomers in the dimer.[34] We also determined the thermodynamic signature of the dimerization process for axially coordinated **2•Zn-1** complex as ΔH = 7.90 kcal·mol^{-1} and ΔS = 39.41 cal·mol^{-1}·K^{-1} using a van't Hoff plot constructed in the same way that the previous dimerization equilibria.

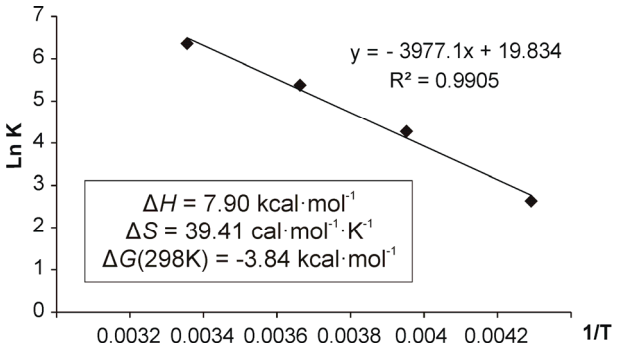

Figure 2.18 Van't Hoff plot and calculated thermodynamic parameters for the 1:1 ↔ 2:2 dimerization process for the axially coordinated quinuclidine **2** to **Zn-1** in $CDCl_3$. Temperature range used: 263 K to 223 K. Calculation was based on the integral values of the ^{1}H NMR signals at 9.43 ppm (monomer) and 9.29 ppm (dimer)

Not surprisingly, these values are very similar to the ones determined for the non-coordinated **Zn-1** counterpart

As expected, separated $CDCl_3$ solutions of enantiomerically pure complexes (*R*) and (*S*)-[**Zn-1**] containing an excess of quinuclidine ligand (3 equiv) displayed identical ^{1}H NMR spectra that showed the diagnostic proton signals for the chiral monomer and the corresponding chiral dimer. Remarkably, the ^{1}H NMR spectrum of a solution containing racemic **Zn-1** and 3 equiv of **2** displayed an additional set of proton signals. This was especially visible in the upfield region of the spectrum (Figure 2.19 b). We assigned the new set of signals to quinuclidine protons in the *meso*-dimer $\mathbf{2_2}\bullet$[(*R*,*S*)-**Zn-1**]$_2$. Simple integration of the signals corresponding to the homo ($\mathbf{2_2}\bullet$(*R*,*R*)-[**Zn-1**]$_2$, $\mathbf{2_2}\bullet$(*S*,*S*)-[**Zn-1**]$_2$) and hetero dimeric complexes ($\mathbf{2_2}\bullet$[(*R*,*S*)-**Zn-1**]$_2$) allowed the calculation of an equilibrium constant value for the self-sorting process of the chiral homodimers into the *meso*-heterodimer as $K_{ss} = 4$. This value coincides with the statistical estimate indicating that all dimers are isoenergetic and the self-sorting process of racemic **2•Zn-1** complexes into dimers does not show signs of chiral discrimination (self-recognition or self-discrimination).

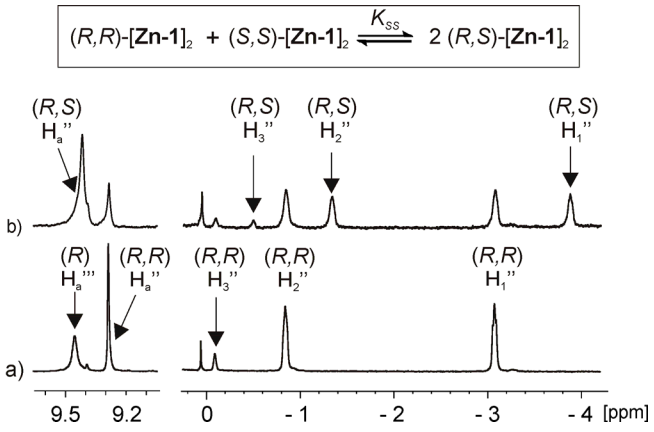

Figure 2.19 a) Selected regions of the ^{1}H NMR spectrum of (*R*)-**Zn-1** with 3 equiv of quinuclidine and b) Selected regions of the ^{1}H NMR spectrum of the equimolar mixture of (*R*) and (*S*)-**Zn-1** with 3 equiv of quinuclidine.

2.4 Conclusions

The dimerization process of enantiopure **Zn-1** was studied using UV-vis dilution experiments and variable temperature ^{1}H NMR experiments. Unexpectedly, we found that the dimerization process was favored at high temperatures. The calculated thermodynamic contributions of the dimerization process revealed that it is entropy-driven and enthalpically opposed. We rationalized these results considering the solvation/desolvation processes that are involved in the dimerization equilibria.

The coordination of quinuclidine **2** to enantiopure **Zn-1** was studied at two different concentrations using UV-vis and ^{1}H NMR titrations. At micromolar concentration, enantiopure **Zn-1** is exclusively present in solution as a monomer and formed simple 1:1 **2•Zn-1** complexes. The calculated association constant for the **2•Zn-1** complex is larger than 10^6 M^{-1}. This value is two orders of magnitude higher than the ones typically reported for the coordination of **2** with Zn-porphyrins. At millimolar concentration, enantiopure **Zn-1** is present in solution mainly as a dimer. The incremental addition of quinuclidine to mM solutions of enantiopure **Zn-1**, produced quinuclidine:**Zn-1** complexes of larger stoichiometry than the simple 1:1. Using ^{1}H NMR spectroscopy, it was possible to demonstrate the formation of 1:2 (**2•[Zn-1]$_2$**) and 2:2 (**2$_2$•[Zn-1]$_2$**) complexes in addition to the known 1:1 (**2•Zn-1**) complex. We measured a reduction in the dimerization constant value of the coordinated enantiopure monomer **2•Zn-1** compared to the parent uncoordinated metallo-phthalocyanine **Zn-1**. Most likely, the axial coordination of quinuclidine to the Zn(II) metal centers bows the planarity of the Pc weakening the π-π interactions responsible for dimer **2$_2$•[Zn-1]$_2$** formation. The addition of an excess of quinuclidine to a millimolar solution of enantiopure **Zn-1** induced the selective disappearance of the quinuclidine signals assigned to the 1:1 complex. The protons of the quinuclidine in the 2:2 complex remained unaltered. This observation prompted us to propose a different exchange mechanism between free and bound quinuclidine in the two complexes. The dissimilar kinetics observed on the NMR chemical shift timescale for the two exchange processes are related to different energy barriers for them (dissociative exchange and associative exchange).

Finally, we demonstrated that the dimerization of racemic **Zn-1** (equimolar mixture of (*R*)- and (*S*)-**Zn-1)** produced large oligomers. Remarkably, when the dimerization study of racemic **Zn-1** was performed in solution containing an excess of quinuclidine, we observed the assembly of both the chiral homodimers and the *meso*-heterodimer. The ratio of the dimers coincided with the expected statistical estimate assuming isoenergetic species, indicating a lack of chiral discrimination in the self-sorting process of racemic (*R,S*)-**2•Zn-1** into dimers.

2.5 Experimental Section

2.5.1 General information and instrumentation

^{1}H NMR spectra were recorded on a Bruker Avance 400 (400 MHz for ^{1}H NMR spectroscopy), or a Bruker Avance 500 (500 MHz for ^{1}H NMR spectroscopy) ultrashield spectrometer. The deuterated solvents (Aldrich) used are indicated and chemical shifts are given in ppm. For $CDCl_3$, the peaks were referenced relative to the solvent residual peak δ_H = 7.26 ppm. High-resolution mass spectra were obtained using a Bruker Autoflex MALDI-TOF mass spectrometer. Thin-layer chromatography (TLC) and flash column chromatography were performed with DC-aufolien Kieselgel 60 F_{254} (Merck) and Scharlab 60 silica gel, respectively. UV-vis measurements were carried out using a Shimadzu UV-2410PC spectrophotometer equipped with a photomultiplier detector, double-beam optics, and D2 and W light sources and using a 1 mm path cell for the dimerization studies.

2.5.2 Materials

All commercial solvents and chemicals were of reagent grade quality and were used without further purification. Dry DMF was acquired form a Solvent Purification System MBraun SPS-800. Deuterated chloroform and chloroform were deacidified by passing through a short column of aluminum oxide 90 active, neutral (Merck).

2.5.3 Synthetic procedures

Preparation of (R)- and (S)-benzo[b]dinaphtho[2,1-e:1',2'-g][1,4]-dioxocine-5,6 dicarbonitrile

A mixture of (*R*)/(*S*)- 1-1'-Bi-2-naphtol (1.0 g, 3.49 mmol), 4,5-dichlorophthalonitrile (0.688 g, 3.49 mmol) and potassium carbonate (1.931 g, 13.97 mmol) in dry DMF (10 mL) was stirred at 80ºC for 6 h under argon atmosphere. After reaction time the mixture was poured onto water (50 mL) and extracted with $CHCl_3$ (20 mL × 3). The combined organic phases were then washed with water (50 mL × 2), dried over Na_2SO_4, filtered and

concentrated under reduced pressure. The yellowish crude was purified by silica gel column cromatography using CH_2Cl_2:Hexane (1:1) as eluent mixture. Evaporation of the solvent followed by recrystallization from $CHCl_3$ and MeOH gave 0.980 g of white crystals of the desired product in 69% yield.

^{1}H NMR (400 MHz, $CDCl_3$, Me_4Si): 7.39-7.44 (m, 4H), 7.47-7.57 (m, 4H), 7.71 (s, 2H), 7.98 (d, J = 8.25 Hz, 2H), 8.36 (d, J = 8.81 Hz, 2H)
^{1}H NMR spectrum of this compound is in agreement with that reported in the literature[25]

Preparation of (R)- and (S)-phthalocyanato zinc (Zn-1)

A mixture of enantiomerically pure (*R*) or (*S*)-benzo[b]dinaphtho[2,1-e:1',2'-g][1,4]dioxocine-5,6-dicarbonitrile (200 mg, 0.489 mmol), $Zn(OAc)_2 \cdot 2H_2O$ (22.4 mg, 0.122 mmol) and DBU (0.05 mL) were refluxed at 160 ºC in 1-hexanol (2 mL) for 4 h. After reaction time the mixture was cooled at room temperature, the volatiles were removed under reduced pressure and the crude was purified by silica gel column chromatography using CH_2Cl_2:THF (100:2) as eluent mixture. The solvent of the collected fractions was evaporated in vacuum to yield 52 mg of the (*R*)-enantiomer as a green powder (25%).

^{1}H NMR (400 MHz; $CDCl_3$; Me_4Si): δ_H, ppm: 6.84 (1H, d, J = 8.46 Hz), 6.96 (1H, t, J = 7.58 Hz), 7.11 (1H, d, J = 8.46 Hz), 7.20 (1H, t, J = 7.58), 7.32 (1H, t, J = 7.58 Hz), 7.44 (1H, t, J = 7.58 Hz), 7.50 (1H, d, J = 8.46 Hz), 7.69 (1H, d, J = 8.46 Hz), 7.83 (1H, s), 7.87 (1H, d, J = 8.46 Hz), 7.97 (1H, d, J = 8.46), 8.46 (1H, d, 8.46 Hz), 8.66 (1H, d, 8.46 Hz), 9.30 (1H, s).
HRMS (MALDI+): 1704.3527 m/z (calcd. for $[M]^{\cdot+}$ 1704.3513).
^{1}H NMR data are in complete agreement with those reported in the literature.[23]

2.5.4 Titrations and data analysis

^{1}H NMR and UV-vis titrations were performed by addition of incremental amounts of a solution containing the ligand to a solution of the **Zn-1** in either a 5 mm NMR tube or a 1 cm path quartz cuvette by using microliter syringes. After each addition the sample mixture was hand shacked and the spectrum recorded. In both types of titration experiments, **Zn-1** was present in the ligand solution at the same concentration than that in the NMR tube or cuvette to avoid dilution effects. UV-vis dilution studies of **Zn-1** were performed in a 0.1 cm path quartz cuvette. Deacidified chloroform and deacidified deuterated chloroform were used as solvent for the UV-vis and ^{1}H NMR titration, respectively. UV-vis spectrophotometric titrations were analyzed by fitting the whole series of spectra at 1 nm intervals by using the software ReactLab Equilibria 1.1 from Jplus Consulting Pty Ltd (8 Windsor Road, East Fremantle, WA 6158, Australia).

2.5.5 Van't Hoff plots

Dimerization of ***[Zn-1]***

To assess the thermodynamic signature for the dimerization process of **[Zn-1]**, we first determined the integral areas of the isoindole aromatic protons for both, the dimer and monomer at all temperatures where the signals were integrable.

	263 K	**253 K**	**243 K**	**233 K**	**223 K**
DIMER (9.29 ppm)	1	1	1	1	1
MONOMER (9.43 ppm)	1.826	3.041	4.746	9.455	21.806

Table 2.1 Integral values of the ^{1}H NMR signals at 9.29 ppm (dimer) and 9.43 ppm (monomer)

The ratio between dimer and monomer was calculated integrating both signals along the range of temperatures measured. The integral values were then normalized having into account that the dimer possesses two signals for the isoindole protons (9.29 and 7.83 ppm) that integrates for 8 protons each one. On the other hand, the monomer only displays one signal at 9.43 ppm that integrates for 8 protons.

	263 K	253 K	243 K	233 K	223 K
DIMER (9.29 ppm)	0.125	0.125	0.125	0.125	0.125
MONOMER (9.43 ppm)	0.22825	0.380125	0.59325	1.181875	2.72575

Table 2.2 Normalized integral values of the ^{1}H NMR signals at 9.29 ppm (dimer) and 9.43 ppm (monomer)

From the normalized ratios of the dimer/monomer we obtained the molar fraction values for each species.

$$\chi_{dimer} = \frac{I_{dimer}}{I_{dimer} + I_{monomer}} \qquad \chi_{monomer} = \frac{I_{monomer}}{I_{monomer} + I_{dimer}}$$

Multiplying these fractions by initial concentrations and having into account that in the dimer there are 2 monomers associated, we obtained their equilibria concentrations at each temperature measured.

$$[dimer] = \frac{\chi_{dimer}}{2} \cdot C_T \qquad [monomer] = \chi_{monomer} \cdot C_T$$

Using the formula below, we calculated an equilibria constant for each temperature:

$$K_{eq} = \frac{[dimer]}{[monomer]^2}$$

	263 K	253 K	243 K	233 K	223 K
χ dimer	0.3538	0.2474	0.1740	0.0956	0.0438
χ monomer	0.6461	0.7525	0.8259	0.9043	0.9561
[dimer] (M)	3.54×10^{-4}	2.47×10^{-4}	1.74×10^{-4}	9.56×10^{-5}	4.38×10^{-5}
[monomer] (M)	1.29×10^{-3}	1.51×10^{-3}	1.65×10^{-3}	1.81×10^{-3}	1.91×10^{-3}
K_{eq} (K)	576.621	216.049	71.660	13.850	3.237

Table 2.3 Calculated molar fraction values, partial concentrations and equilibrium constants at the temperature range from 263 K to 223 K.

By plotting the calculated equilibria constants *vs* the inverse of temperature we constructed the van't Hoff plot (Figure 2.11) and from the linear fit we determined the intercept and the slope.

To calculate the enthalpy (ΔH), the entropy (ΔS) and the free energy (ΔG) of the dimerization process, we combined equation for the Gibbs free energy : $\Delta G = \Delta H - T\,\Delta S$, with Gibbs free energy isotherm equation : $\Delta G = \mathrm{RT}\cdot\ln(K_{eq})$, where R is a gas constant (1.987 $\mathrm{cal\cdot mol^{-1}\cdot K^{-1}}$). This gave us the following equation:

$$\ln(K_{eq}) = -\frac{\Delta H}{\mathrm{RT}} + \frac{\Delta S}{\mathrm{R}}$$

from this equation we could calculate the values of

$\Delta H = -\,\mathrm{R} \times \text{slope} = -1.987\ \mathrm{cal\cdot mol^{-1}\cdot K^{-1}} \times (-4153.3\ \mathrm{K}) = 8.25\ \mathrm{kcal\cdot mol^{-1}}$

$\Delta S = \mathrm{R} \times \text{intercept} = -1.987\ \mathrm{cal\cdot mol^{-1}\cdot K^{-1}} \times 21.163 = 42.1\ \mathrm{cal\cdot mol^{-1}\cdot K^{-1}}$

at room temperature (298 K) we have : $\Delta G(298\ \mathrm{K}) = \Delta H - 298\ \Delta S$

$\Delta G(298\ \mathrm{K}) = 8.25 - 298 \times 0.0421 = -4.28\ \mathrm{kcal\cdot mol^{-1}}$

*Dimerization of **2•Zn-1***

To assess the thermodynamic signature for the dimerization process for the enantiopure and axially coordinated **2•Zn-1** complex we first determined integral area values for both, the dimer and monomer at all temperatures where the signals were integrable.

	298 K	273 K	253 K	233 K	213 K
DIMER (9.29 ppm)	1	1	1	1	1
MONOMER (9.43 ppm)	0.91	1.8	4.3	19	78.212

Table 2.4 Integral values of the ^{1}H NMR signals at 9.29 ppm (dimer) and 9.43 ppm (monomer)

The ratio between dimer and monomer was calculated integrating both signals along the range of temperatures measured. The integral values were then normalized having into account that the dimer possesses two signals for the isoindole protons (9.29 and 7.83 ppm) that integrates for 8 protons each one. On the other hand, the monomer only displays one signal at 9.43 ppm that integrates for 8 protons.

	298 K	273 K	253 K	233 K	213 K
DIMER (9.29 ppm)	0.125	0.125	0.125	0.125	0.125
MONOMER (9.43 ppm)	0.11375	0.225	0.5375	2.375	9.7765

Table 2.5 Normalized integral values of the ^{1}H NMR signals at 9.29 ppm (dimer) and 9.43 ppm (monomer)

From the normalized ratios of the dimer/monomer we obtained the molar fraction values for each species.

$$\chi_{dimer} = \frac{I_{dimer}}{I_{dimer} + I_{monomer}} \qquad \chi_{monomer} = \frac{I_{monomer}}{I_{monomer} + I_{dimer}}$$

Multiplying these fractions to initial concentration (2 mM) and having into account that in the dimer there are 2 monomers associated, we obtained their equilibria concentrations at each temperature measured.

$$[dimer] = \frac{\chi\ dimer}{2} \cdot C_T \qquad [monomer] = \chi\ monomer\ \cdot C_T$$

Using the formula below, we calculated an equilibria constant for each temperature:

$$K_{eq} = \frac{[dimer]}{[monomer]^2}$$

	298 K	**273 K**	**253 K**	**233 K**	**213 K**
χ dimer	0.5235	0.3571	0.1886	0.05	0.0126
χ monomer	0.4764	0.6428	0.8113	0.95	0.9873
[dimer] (M)	5.24×10^{-4}	3.57×10^{-4}	1.89×10^{-4}	5.00×10^{-5}	1.26×10^{-5}
[monomer] (M)	9.53×10^{-4}	1.29×10^{-3}	1.62×10^{-3}	1.90×10^{-3}	1.97×10^{-3}
K_{eq} (K)	576.621	216.049	71.660	13.850	3.237

Table 2.6 Calculated molar fraction values, partial concentrations and equilibrium constants at the temperature range from 298 K to 213 K.

By plotting the calculated equilibria constants *vs* the inverse of temperature we constructed the van't Hoff plot and from the linear fit we determined the intercept and the slope.

To calculate the enthalpy (ΔH), the entropy (ΔS) and the free energy (ΔG) of the dimerization process for the enantiopure and axially coordinated **2•[Zn-1]** complex, we combined equation for the Gibbs free energy : $\Delta G = \Delta H - T\,\Delta S$, with Gibbs free energy isotherm equation : $\Delta G = RT \cdot \ln(K_{eq})$, where R is a gas constant (1.987 $cal \cdot mol^{-1} \cdot K^{-1}$). This gave us the following equation:

$$\ln(K_{eq}) = -\frac{\Delta H}{RT} + \frac{\Delta S}{R}$$

from this equation we could calculate the values of

ΔH = – R × slope = –1.987 cal·mol^{-1}·K^{-1} × (– 3977.1 K) = 7.90 kcal·mol^{-1}

ΔS = R × intercept = –1.987 cal·mol^{-1}·K^{-1} × 19.834 = 39.41 cal·mol^{-1}·K^{-1}

at room temperature (298 K) we have : ΔG(298 K) = ΔH – 298 ΔS

ΔG(298 K) = 7.90 – 298 × 0.03941 = – 3.84 kcal·mol^{-1}

2.6 References and notes

[1] Tong, W. Y.; Djurisic, A. B.; Xie, M. H.; Ng, A. C. M.; Cheung, K. Y.; Chan, W. K.; Leung, Y. H.; Lin, H. W.; Gwo, S. "Metal phthalocyanine nanoribbons and nanowires". *J. Phys. Chem. B* **2006**, *110*, 17406.

[2] Duzhko, V.; Singer, K. D. "Self-assembled fibers of a discotic phthalocyanine derivative: internal structure, tailoring of geometry, and alignment by a direct current electric field". *J. Phys. Chem. C.* **2007**, *111*, 27.

[3] Guillaud, G.; Simon, J.; Germain, J. P. "Metallophthalocyanines - Gas sensors, resistors and field effect transistors". *Coord. Chem. Rev.* **1998**, *178*, 1433.

[4] Ishikawa, N.; Sugita, M.; Ishikawa, T.; Koshihara, S.; Kaizu, Y. "Lanthanide double-decker complexes functioning as magnets at the single-molecular level". *J. Am. Chem. Soc.* **2003**, *125*, 8694.

[5] Loi, M. A.; Denk, P.; Hoppe, H.; Neugebauer, H.; Winder, C.; Meissner, D.; Brabec, C.; Sariciftci, N. S.; Gouloumis, A.; Vazquez, P.; Torres, T. "Long-lived photoinduced charge separation for solar cell applications in phthalocyanine-fulleropyrrolidine dyad thin films". *J. Mater. Chem.* **2003**, *13*, 700.

[6] Hofman, J. W.; van Zeeland, F.; Turker, S.; Talsma, H.; Lambrechts, S. A. G.; Sakharov, D. V.; Hennink, W. E.; van Nostrum, C. F. "Peripheral and axial substitution of phthalocyanines with solketal groups: synthesis and in vitro evaluation for photodynamic therapy". *J. Med. Chem.* **2007**, *50*, 1485.

[7] Kolarova, H.; Nevrelova, P.; Bajgar, R.; Hrova, D.; Kejlova, K.; Strnad, M. "In vitro photodynamic therapy on melanoma cell lines with phthalocyanine". *Toxicol. in Vitro* **2007**, *21*, 249.

[8] de la Torre, G.; Vazquez, P.; Agullo-Lopez, F.; Torres, T. "Phthalocyanines and related compounds: organic targets for nonlinear optical applications". *J. Mater. Chem.* **1998**, *8*, 1671.

[9] Nemykin, V. N.; Lukyanets, E. A. "Synthesis of substituted phthalocyanines". *Arkivoc* **2010**, 136.

[10] Kobayashi, N. "Optically active phthalocyanines". *Coord. Chem. Rev.* **2001**, *219*, 99.

[11] Kimura, M.; Kuroda, T.; Ohta, K.; Hanabusa, K.; Shirai, H.; Kobayashi, N. "Self-organization of hydrogen-bonded optically active phthalocyanine dimers". *Langmuir* **2003**, *19*, 4825.

[12] Hembury, G. A.; Borovkov, V. V.; Inoue, Y. "Chirality-sensing supramolecular systems". *Chem. Rev.* **2008**, *108*, 1.

[13] Furusho, Y.; Kimura, T.; Mizuno, Y.; Aida, T. "Chirality-memory molecule: A D-2-symmetric fully substituted porphyrin as a conceptually new chirality sensor". *J. Am. Chem. Soc.* **1997**, *119*, 5267.

[14] Lu, H. J.; Zhang, X. P. "Catalytic C-H functionalization by metalloporphyrins: recent developments and future directions". *Chem. Soc. Rev.* **2011**, *40*, 1899.

[15] Vannostrum, C. F.; Bosman, A. W.; Gelinck, G. H.; Picken, S. J.; Schouten, P. G.; Warman, J. M.; Schouten, A. J.; Nolte, R. J. M. "Evidence of a chiral superstructure in the discotic mesophase of an optically-active phthalocyanine". *J. Chem. Soc., Chem. Commun.* **1993**, 1120.

[16] Kobayashi, N.; Kobayashi, Y.; Osa, T. "Optically-active phthalocyanines and their circular-dichroism". *J. Am. Chem. Soc.* **1993**, *115*, 10994.

[17] Kobayashi, N.; Narita, F.; Ishii, K.; Muranaka, A. "Optically active oxo(phthalocyaninato)vanadium (IV) with geometric asymmetry: synthesis and correlation between the circular dichroism sign and conformation". *Chem-Eur. J.* **2009**, *15*, 10173.

[18] Kobayashi, N. "Optically active 'adjacent' type non-centrosymmetrically substituted phthalocyanines". *Chem. Commun.* **1998**, 487.

[19] Hunter, C. A.; Meah, M. N.; Sanders, J. K. M. "DABCO metalloporphyrin binding - ternary complexes, host guest chemistry, and the measurement of pi-pi-interactions". *J. Am. Chem. Soc.* **1990**, *112*, 5773.

[20] Taylor, P. N.; Anderson, H. L. "Cooperative self-assembly of double-strand conjugated porphyrin ladders". *J. Am. Chem. Soc.* **1999**, *121*, 11538.

[21] Liu, C. H. J.; Lu, W. C. "Optical amine sensor based on metallophthalocyanine". *J. Chin. Inst. Chem. Eng.* **2007**, *38*, 483.

[22] Przybyl, B.; Janczak, J. "Structural characterisation and DFT calculations of three new complexes of zinc phthalocyanine with n-alkylamines". *Dyes Pigm.* **2014**, *100*, 247.

[23] D'Souza, F.; Ito, O. "Supramolecular donor-acceptor hybrids of porphyrins/phthalocyanines with fullerenes/carbon nanotubes: electron transfer, sensing, switching, and catalytic applications". *Chem. Commun.* **2009**, 4913.

[24] Wang, K.; Qi, D. D.; Wang, H. L.; Cao, W.; Li, W. J.; Jiang, J. Z. "A chiral phthalocyanine dimer with well-defined supramolecular symmetry based on pi-pi interactions". *Chem-Eur. J.* **2012**, *18*, 15948.

[25] Wang, K.; Wang, H. L.; Mack, J.; Li, W. J.; Kobayashi, N.; Jiang, J. Z. "Chiral phthalocyanine with unambiguous absolute molecular structures for both enantiomers". *Acta Chim. Sinica.* **2012**, *70*, 1791.

[26] The absolute configuration of all the BINOL units is the same, all-(*R*)-**Zn-1** or all-(*S*)-**Zn-1**.

[27] The chemical exchange of the monomers within the dimeric species is slow on the ^{1}H NMR timescale.

[28] Johnson, C. S. "Diffusion ordered nuclear magnetic resonance spectroscopy: principles and applications". *Prog. Nucl. Magn. Reson. Spectrosc.* **1999**, *34*, 203.

[29] Cram, D. J.; Choi, H. J.; Bryant, J. A.; Knobler, C. B. "Host-guest complexation. 62. Solvophobic and entropic driving forces for forming velcraplexes, which are 4-fold, lock-key dimers in organic media". *J. Am. Chem. Soc.* **1992**, *114*, 7748.

[30] Kang, J. M.; Rebek, J. "Entropically driven binding in a self-assembling molecular capsule". *Nature* **1996**, *382*, 239.

[31] Chi, X. L.; Guerin, A. J.; Haycock, R. A.; Hunter, C. A.; Sarson, L. D. "Self-assembly of macrocyclic porphyrin oligomers". *J. Chem. Soc., Chem. Commun.* **1995**, 2567.

[32] Hunter, C. A.; Sanders, J. K. M.; Stone, A. J. "Exciton coupling in porphyrin dimers". *Chem. Phys.* **1989**, *133*, 395.

[33] Ballester, P.; Costa, A.; Castilla, A. M.; Deya, P. M.; Frontera, A.; Gomila, R. M.; Hunter, C. A. "DABCO-directed self-assembly of bisporphyrins (DABCO=1,4-diazabicyclo[2.2.2]octane)". *Chem-Eur. J.* **2005**, *11*, 2196.

[34] Andryushkevich, S. O.; Birin, K. P.; Gorbunova, Y. G.; Tsivadze, A. Y. "Complexes of Zinc(II) tetra-(15-crown-5)-phthalocyaninate with axially coordinates N-donor ligands as

potential components of photosensitive materials of telecommunication range". *Prot. Met. Phys. Chem. Surf.,* **2011**, *47*, 494.

Chapter 3

Lanthanide-based single-molecule magnets with tetrapyrrolic ligands

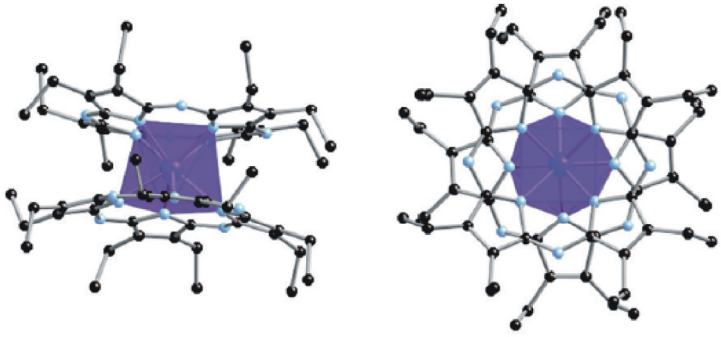

*Part of this Chapter was published in: *Chem. Eur. J.* **2014**, *20*, 12817-12825

UNIVERSITAT ROVIRA I VIRGILI
SYNTHESIS OF TETRA-AZAPORPHYRINS, PHTHALOCYANINES AND LANTHANIDE DOUBLE-DECKER SANDWICH COMPLEXES
Nelson Giménez Agulló

3.1 Introduction

3.1.1. Lanthanides

Lanthanides (Ln) are strictly defined as the 14 elements following lanthanum (La). They are part of the family of rare earths, which also includes scandium (Sc) and yttrium (Y) due to their chemical similarities. Lanthanides present 4*f* electrons in the valence band, strongly shielded by the occupied $5s^1$ and $5p^6$ orbitals. They exhibit the extended Xe core electronic configuration [Xe]$4f^n 5d^0 6s^2$ (n=1-14), with some exceptions. In their most stable ionic configuration (Ln^{+3}), electrons are moved first form the 6*s* and 5*d* orbitals having [Xe]$4f^n$ electronic configuration. In addition, the weak overlap of *d* orbitals with the orbitals of the ligands in the lanthanide contraction contributes to the prevalence of the ionic character in the lanthanide metal-organic complexes. Due to this fact, several of their chemical characteristics are in contrast with the *d*-block elements where the external *d* orbitals are sequentially occupied.

Since the effect of the 4*f* electrons on the chemical properties is negligible, the most stable oxidation state for lanthanides is +3 (Ln^{+3}). Generally, the two outer 6*s* electrons and one taken form the 4*f* sub-shell are removed from the ground state in order to obtain the +3 oxidation configuration. Nevertheless, there are some exceptions where, apart from the 6*s* electrons, one electron is taken form the 5*d* sub-shell to maintain the higher stability of empty, half- and fully-filled 4*f* sub-shell. This is the case of Ce^{+4}, Gd^{+3} and Lu^{+3}. The +2 and +4 oxidation states are only formed by elements that can maintain the 4*f* sub-shell empty, half-filled or fully-filled. On the other hand, Eu^{+2} and Yb^{+2} are the most stable di-positive configurations having half-filled and fully-filled the 4*f* sub-shell, respectively.

An important feature of the lanthanides is the so-called lanthanide contraction, in which the 5*s* and 5*p* orbitals penetrate the 4*f* sub-shell. This means that the 4*f* orbital is not shielded from the increasing nuclear charge, which causes the atomic radius of the atom to decrease continuously throughout the series.

Lanthanides have the largest atomic magnetic moment of all elements. Their local 4*f* moments are primarily responsible for their magnetism whereby a multitude of magnetic structures due to the 4*f*-4*f* coupling exist, producing long-range magnetic order. Moreover, lanthanides present a strong spin-orbit coupling being especially used as single molecular magnets (SMMs) due to the large spin and unquenched orbital angular momentum interesting for spintronics and future applications like quantum computing, high-density information storage or magnetic refrigeration.

Lanthanide elements have a growing variety of applications in modern technology. They have been extensively used due to their catalytic, magnetic and luminescence properties resulting in the development of numerous important applications in particular in the field of bio-imaging as fluorescent probe for fluoro-immunoassays as well as contrast agents for medical magnetic resonance imaging,[1] biotechnology,[2] telecommunications,[3] corrosion inhibitors[4] and therapeutic applications.[5]

3.1.2. Lanthanide-phthalocyanine complexes

Sandwich-type metal complexes of tetrapyrolic macrocycles have been known since 1936, with the first synthesis of a tin(IV) bis(phthalocyanine) by Linstead and co-workers.[6] The complex was formed through the coordination of two phthalocyanine units acting as ligands of a central tin ion, $Sn(Pc)_2$. The complex was characterized by elemental analysis. However, the detailed molecular structure remained unsolved until the structure elucidation of the actinoids homologs $Th(Pc)_2$ and $U(Pc)_2$ was described by Lux *et al*. in 1968.[7] These two later complexes displayed a sandwich-type double-decker structure formed by the tetrapositively charged central metal ion that coordinates to two dinegatively charged phthalocyanine anions in a distorted square-antiprism geometry. In 1970 Kirin and Moskalev postulated[8] that a necessary condition for the formation of sandwich-like bisphthalocyanine metal complexes $M(Pc)_2$ is that the radius of the phthalocyanine coordination space between the four internal nitrogen atoms should exceed the covalent radius of the metal and in addition, the metal oxidation state must not be less than +3. Large number of metal ions, including all trivalent lanthanides, scandium and yttrium, and

tetravalent cerium cannot fit into the central cavity of a phthalocyanine ring due to the fact that the ionic radii of the Ln^{+3}, Sc^{3+}, Y^{3+} and Ce^{+4} ions exceed the "coordination space" of the dinegative quadridentate phthalocyanine ligand. In 1971 Kasuga *et al*. described the synthesis of a Neodynium double-decker complex with phthalocyanine ligands. Due to the trivalent nature of lanthanides (Ln^{3+}), researchers hypothesized about the formation of a $Nb^{III}(Pc)_2H$ species. However, in 1980, Tsutsui and co-workers reported the solid state structure of the complex using X-ray diffraction of a single crystal.[9] The structure of the complex consisted in a sandwich-type geometry, $Nd(Pc)_2$, where the trivalent Neodynium ions are located in the central position created by two parallel but staggered phthalocyanine ligands. The absence of the proton in the solid-state structure of the complex indicated that the coordination of the lanthanide (III) ion takes place with a negatively double charged $(Pc)^{-2}$ unit and one unit of $(Pc)^{-1}$ that is a radical anion.

Three general subgroups of the lanthanide phthalocyanine derivatives are known: lanthanide monophthalocyanines or 1:1 complexes, lanthanide bis(phthalocyanines) or 1:2 complexes and dilanthanide tris(phthalocyanine) or 2:3 complexes (Figure 3.1).

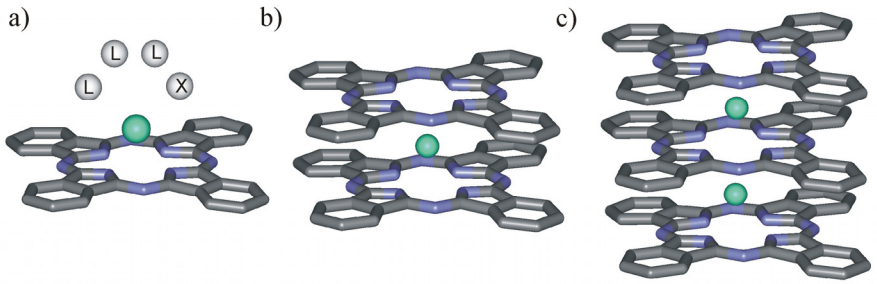

Figure 3.1 Schematic representation of the different lanthanide phthalocyanine derivatives: a) lanthanide monophthalocyanine or 1:1 complex, X represents a monoanionic ligand and L a neutral ligand b) lanthanide bis(phthalocyanine) or 1:2 complex and c) dilanthanide tris(phthalocyanine) or 2:3 complex.

For the monophthalocyanine type, $[Ln^{3+}Pc^{2-}X^{-}]$, the Ln^{3+} is coordinated to one dianionic tetradentate phthalocyanine ligand and through the other face is coordinated to axial ligands which are monoanionic and either mono- or bi-dentate. In order to complete the coordination sphere which is often 8, other neutral ligand or solvent molecule can

coordinate the lanthanide ion. Effective solvation of lanthanide ion during the reaction, which prevents the formation of sandwich complexes, is a condition to success in the synthesis of lanthanide monophthalocyanines.

The lanthanide bis(phthalocyanine) or 1:2 complexes, often called double-decker or sandwich complexes consists in a trivalent lanthanide ion located in the central position created by two parallel but staggered phthalocyanine ligands. The two phthalocyanine rings can be identical or they can differ on their substituents. The former compounds are named homoleptic whereas the latter are called heteroleptic complexes. This last designation applies also for the species in which one ring is not a phthalocyanine, but rather is another tetrapyrrolic ligand.

The dilanthanide tris(phthalocyanine) or 2:3 complexes are formed by two metal cations sandwiched between three phthalocyanine rings and are often called triple-decker complexes. The term homonuclear is used when the 2:3 complex is built with the same two cations whereas structures with different metal cations are named heteronuclear triple-deckers.

In this thesis we will mainly focus in the synthesis of homoleptic 1:2 complexes using porphyrinoid ligands.

3.1.3 Synthesis of homoleptic lanthanide bis(phthalocyanine) complexes

Homoleptic bis(phthalocyanine) of transition,[10] lanthanide[11] and actinide[12] metal ions have been described in literature. There have been several reported methods for the preparation of homoleptic 1:2 lanthanide phthalocyanine complexes that can be conveniently divided into three groups depending on the initial compound used.

Template synthesis based on phthalonitrile

A straightforward but not efficient method for the preparation of lanthanide bis(phthalocyanine) complexes involves the cyclic tetramerization of solid *o*-phthalonitrile templated with a lanthanide salt (Figure 3.2, conditions a). The technical simplicity of this method makes it extensively used. The first method described to prepare 1:2 lanthanide phthalocyanine complexes was based on this approach. Kirin *et al*. reported that melting and heating up to 280-290ºC pellets composed of solid unsubstituted *o*-phthalonitrile and lanthanide acetate, $Ln(OAc)_3$ (Ln = Pr, Nd, Er, Lu, Sc and Y) yielded a mixture of green and blue species.[13] Despite the lack of a reliable analysis, the green species were tentatively identified as the 1:1:1 lanthanide phthalocyanine chloro-complexes, Ln(Pc)Cl based on their optical spectra. The blue species were identified by means of elemental analysis as the 1:2 protonated lanthanide bis(phthalocyanine) complexes, $LnH(Pc)_2$. Somewhat later, ESR, mass spectroscopy, magnetic susceptibility and X-ray crystallography techniques showed that the green complexes were neither a 1:1:1 mixed-ligand derivative, Lu(Pc)Cl nor a 1:2 protonated species. It rather was a neutral 1:2 lanthanide bis(phthalocyanine) $LuPc_2$, containing one unpaired electron associated with a monoanionic phthalocyanine due to the trivalent state of the metal center. The reported difficulties regarding the purification of the products of the solid state reaction lead to the development of solution reactions in which the cyclotetramerization of the phthalonitrile occurs using high boiling point solvents.

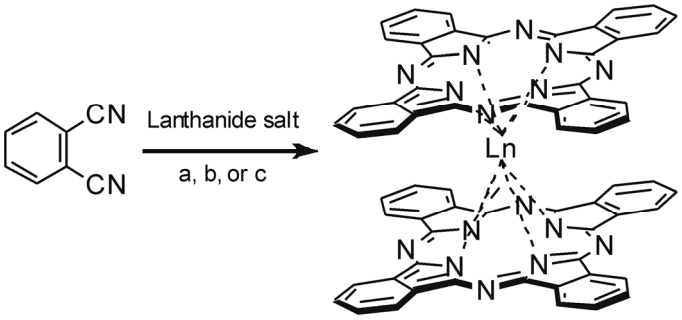

Figure 3.2 Schematic representation of the template synthesis of homoleptic double-decker based on phthalonitriles. a) 250-350ºC, 0.5-4 h; b) DBU, solvent, 130-160ºC; and c) microwave radiation (300-700 W), DBU, solvent, 5-10 min.

A large number of 1:2 lanthanide phthalocyanine complexes, especially with substituted macrocycles, have been prepared in solution by cyclic tetramerization of the corresponding *o*-phthalonitrile catalyzed by strong organic bases such as 1,8-diazabicyclo[5.4.0]undec-7-ene (DBU) in the presence of a lanthanide salt (Figure 3.2, conditions b).[14,15,16,17] This method was reported to lead better yields than the previously described method since the reaction temperature is decreased and thus, the thermal decomposition of the initial compounds is reduced.[18]

Apart from thermal fusion and solution reaction in presence of organic bases, the metallation reaction to afford double-decker structures has been initiated by microwave radiation starting from the phthalonitrile precursor in the presence of a strong base and a high-boiling point solvent (Figure 3.2, conditions c). Unsubstituted complexes $Ln(Pc)_2$ (Ln = Tb, Dy and Lu) have been prepared by irradiation (650-700 W) of a mixture of phthalonitrile with an appropriate lanthanide salt for 6-10 min affording the desired double-decker structures.[19] The use of microwave radiation reduces the reaction time from several hours to minutes and in this way, side reactions. Especially, under these conditions the formation of large amounts of free base phthalocyanine rings appeared hindered.[20]

Metallation of the free base phthalocyanine ligand

The methods of synthesis of lanthanides bis(phthalocyanine) complexes from phthalonitriles described in the previous section present some drawbacks like the low yields and difficult purification of the target products. The synthesis of double-decker lanthanide complexes using metal-free phthalocyanines is extensively used nowadays. It avoids side processes typical of template reactions and simplifies the purification process. This method is usually carried out using a previously synthesized free-base phthalocyanine in the presence of a lanthanide salt and a strong organic base. The metallation reaction only occurs under high temperatures and for that reason it is required the use of high-boiling point solvents such as 1-hexanol, 1-octanol or 1,2,4-trichlorobenzene. The stoichiometry ratio between ligand and lanthanide salt plays a crucial role in the reaction output since using an excess amount of the lanthanide salt may result in the formation of undesired triple-decker complexes.

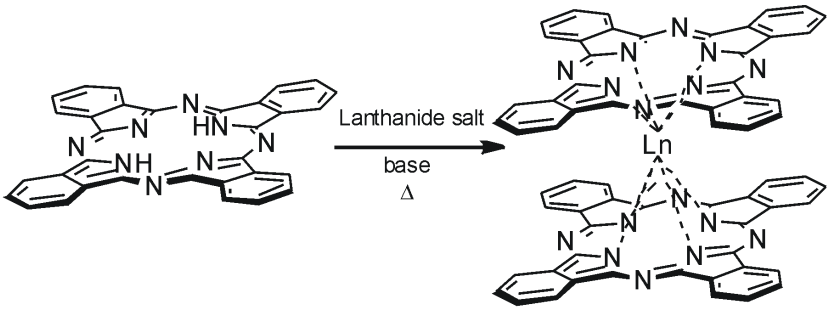

Figure 3.3 Schematic representation of the template synthesis of homoleptic double-decker using the free base phthalocyanine as starting material.

The microwave assisted metallation using free base phthalocyanines as starting material has been reported to give good yields of the desired lanthanide double-decker complexes. For example, Branzoli *et al*.[20] applied the microwave assisted (450 W) synthesis carried out in the presence of DBU, terbium acetoacetate in hexanol solution upon 10 minutes irradiation to afford terbium double-decker complex .

Note that double-decker complexes of lanthanides and other metals with porphyrins[21] and tetraazaporphyrins[22] are synthesized using only the free ligand as the starting compound. This is because the cyclization reaction of such compounds does not occur when the lanthanide double-decker conditions are used, and therefore the macrocycles cannot be formed *in situ* during the reaction.

Axial substitution at the metal ion

The direct reaction of the previously obtained lanthanide monophthalocyanine complex with a free base phthalocyanine ligand results in the formation of the corresponding sandwich 1:2 derivative and has been called "rise-by-one-story" method. This method is used mainly for the synthesis of heteroleptic mixed-ligand complexes but, some examples of homoleptic double-decker derivatives synthesis using this method have been reported. The preparation of monophthalocyanine complexes mostly resides in the treatment of a previously formed free base phthalocyanine with butyllithium giving rise to the dianion of the macrocycle. This *in situ* generated dianion reacts with lanthanide chlorides, acetates or acetilacetonates to achieve high yields of monophthalocyanine complexes. The final reaction of the prepared monophthalocyanine with the free base phthalocyanine in the presence of DBU and using high boiling point solvents yields the desired double-decker complexes.[23] The main drawback of this method is the final separation of unreacted monophthalocyanine and the target lanthanide bis(phthalocyanine) which sometimes become challenging.

3.1.4 Properties of lanthanide-bis(phthalocyanine) complexes

Spectroscopic properties

Mass spectrometry (MS) has often been used to characterize the 1:2 lanthanide:phthalocyanine complexes. Fast atom bombardment mass spectometry (FAB) and field-ion desorption modes (FD) spectrometries were the first techniques used to characterize the complexes. Lately, desorption/ionization techniques, namely electrospray ionization (ESI) and matrix-assisted laser desorption/ionization time of flight (MALDI-ToF) spectrometries became the main routine to identify the presence of double-decker complexes.

Lanthanide bis(phthalocyanine) complexes usually do not give satisfactory ^{1}H NMR spectra because of their limited solubility in common organic solvents but mostly due to its paramagnetic nature, associated with the unpaired electron in one of the phthalocyanine rings. For this reason not many ^{1}H NMR studies of the neutral 1:2 lanthanide:phthalocyanine complexes are known. However, by adding a small amount of hydrazine hydrate as a reducing agent into deuterated solutions containing the neutral double-deckers, satisfactory ^{1}H NMR spectra can be obtained. This is because the paramagnetic neutral species are *in situ* reduced to its anionic form, $[M^{III}(Pc^{1-})Pc^{2-})]^{-}$ which is diamagnetic.

The UV-vis absorption spectra of lanthanide bis(phthalocyanine) complexes has been studied in solution, solid-films or as KBr pellets. The solvents often used for solution studies are DMF, DCM, chloroform, as well as chloroform:ethanol mixtures. Some cautions applies to the use of DMF since the neutral radical form of these 1:2 lanthanide complexes, $Ln(Pc)_2$, can be reduced by amine impurities that are often present even in reagent grade DMF. The UV-vis spectra of the $Ln(Pc)_2$ complexes is characterized by one or two broad and intense bands in the near UV (B or Soret band regions) in addition to a strong absorption band with vibrational satellites situated around 600-700 nm (Q band).

Electrochemical properties

The first description of electrochemically generated multicolor responses in solid film of a lanthanide bis(phthalocyanine) complex was given by Moskalev and Kirin in 1970. The experimental techniques used to study the electrochemical properties of the 1:2 lanthanide phthalocyanine complexes up to 1982 have been reviewed thoroughly by Nicholson.[24] Since then, formal electrode potentials for redox couples have been determined by cyclic voltammetry (CV) or differential pulse voltammetry (DPV) in non-aqueous solvents and confirmed by electrolysis at controlled potentials. The spectral properties of the different species can be determined *in situ* by spectroelectrochemistry. Lanthanide bis(phthalocyanine) complexes usually undergo a reversible ligand-based oxidation and a reversible ligand-based reduction along with some other less well-defined redox processes as revealed by cyclic voltammetry in the presence of a soluble electrolyte, such as a simple tetrabutylammonium (TBA) salt, NBu_4X (X = Br, BF_4 or PF_6).[25]

3.1.5 Applications of lanthanide-bis(phthalocyanine) complexes

The rich electron features of these double-deckers arising from the combination of the intrinsic properties of the rare earth cation with the phthalocyanine ligands has yielded several applications for these molecular materials in modern high-technology areas such as organic field-effect transistors,[26] magnetic information storage,[27] molecular machines[28] and luminescent materials.[29] Regarding magnetic properties, double-decker lanthanide complexes appear as the best candidates for the development of single-molecule magnets at high temperatures.

3.1.6 Lanthanide double-deckers as single-molecule magnets

Magnetism is an important physical phenomenon which describes the attractive and repulsive forces that some materials experience. It is present in nature, i.e. earth's magnetic field, as well as in many artificial electronic devices which are part of our everyday life. The history of magnetism dates back to earlier than 600 BC, but it was only in the twentieth century that scientist begun to develop technologies based on this understanding.

Single-Molecule Magnets (SMM)

Single-molecule magnets (SMMs) are a class of metallic compounds that show superparamagnetic behavior and/or exhibit magnetic hysteresis of purely molecular origin below a blocking temperature. These molecular materials are characterized by an isolated high-spin ground state and a high magnetic Ising anisotropy, which generates a non-negligible energy barrier that hinders the mangetization reversal by thermal activation for temperatures below the blocking temperature. Unlike bulk magnets, SMMs do not present permanent magnetization, since magnetization will eventually relax, but depending on the energy barrier, relaxation times can be over several months at low temperatures.

Since their discovery, SMMs have become a favorite subject of study for many researchers due to their enormously rich physical behavior. SMMs are for instance amongst the most complex magnetic entities that show quantum phenomena like tunneling, quantum coherence or quantum interference. It is their rich physical behavior what makes their study very difficult from an experimental point of view.

The study of SMMs started in the 1990s with the exploration of magnetism of famous Mn_{12} clusters. The determination of the ground states of those Mn_{12} clusters through alternating current susceptibility, high-field magnetization, and millimeter band EPR were the initial studies done by Gatteschi and co-workers.[30,31] Until 1993, the magnetic bistability of molecular origin is referred to explain the hysteresis effects of Mn_{12} below a blocking temperature (T_B), similar to those of bulk ferromagnets.[32] Here, the bistability is

derived from the large magnetic ground state (S) and negative anisotropy (D) of Mn_{12}, which leads to the slow relaxation of magnetization as a result of overcoming the anisotropy barrier (ΔE). Herein, U_{eff} and T_B are the two parameters to measure the success of a SMM.

Magnetic anisotropy

When the magnetic moment of an ion is free to rotate in any direction, the material is said to be isotropic in terms of magnetic response. However, the most common situation is when there are one (or more) preferred directions along the space and then, the material is said to be anisotropic. An anisotropic material always possesses at least one easy axis of the magnetization that will be denoted as the z axis. For a particle with an easy magnetization axis z, two preferred directions of the magnetic moment will be present. This can be schematized with a classical double well potential energy diagram. The magnetic moment reversal implies overcoming an energy barrier or activation energy. In the presence of an applied magnetic field, the degeneracy of the two states is removed and then, one of the two directions will be favored.

Magnetic Relaxation

The magnetic relaxation is the process that leads a magnetic system to the equilibrium and it is related to the rate at which the magnetic moment is able to overcome the energy barrier created by the anisotropy. At high temperatures, the thermal fluctuations assist the magnetic moment to visit all the possible energy configurations and thus the relaxation will be fast. On the contrary, a large anisotropy barrier will frustrate any attempt to reach thermal equilibrium. This situation is described by the Arrhenius law as followed:

$$\tau = \tau_0 e^{U/K_B T}$$

where τ is the relaxation time, that is, the time that the magnetic moment needs to change its state form one energy minima to another.

The magnetic response will be that of equilibrium for temperatures above a certain limit called blocking temperature (T_B), whereas the magnetic response will show non-equilibrium features such as hysteresis or blocking of the magnetic susceptibility for temperatures below T_B. This blocking temperature depends on the experimental time acquisition and therefore can be measured from dynamic magnetic ac susceptibility measurements.

The measurement of the ac (alternating current) magnetic susceptibility of a magnetic material provides information on its equilibrium magnetic response as well as on the magnetization dynamics.[33] The technique consists of measuring the magnetization of the sample in response to an excitation ac magnetic field. Measurements as a function of frequency and temperature enable the determination of the spin-lattice relaxation time and the superparamagnetic blocking temperature, or studying the transition between different magnetic phases. The response to an oscillatory magnetic field has two components: the component oscillating in-phase with the magnetic field, referred as the real part of the susceptibility (χ'), and the out-of-phase component also known as imaginary part of the susceptibility (χ'').

3.1.6.1 Polynuclear SMMs

The $[Mn_{12}O_{12}(CH_3COO)_{16}(H_2O)_4]\cdot 2CH_3COOH\cdot 4H_2O$ cluster structure, usually shortened as $Mn_{12}Ac$, is beyond any doubt the archetype of SMMs. This system is the first single-molecule magnet ever reported and the most studied one. It was synthesized for the first time in 1980 by T. Lis as a product of the reaction of Mn^{2+} and MnO^{4-} in the presence of acetic acid.[34] In this seminal paper the authors described the magnetic measurements performed under a dc (direct current) magnetic field and focused the observations mostly to describe the structure of the cluster. Its structure features twelve manganese ions with a central $Mn^{IV}{}_4O_4$ cubane unit surrounded by eight Mn^{III} centers connected through bridging oxo ligands (Figure 3.4).

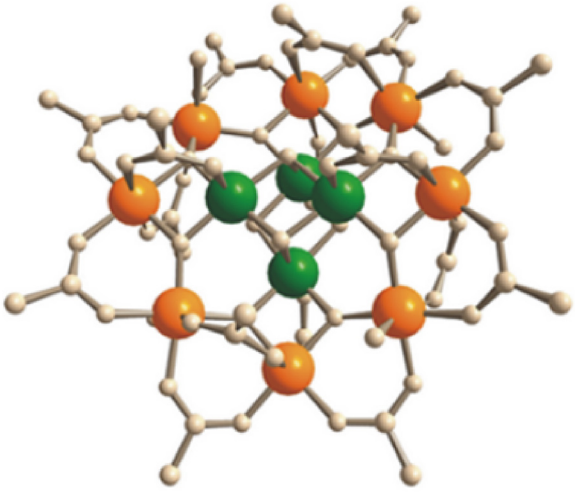

Figure 3.4 Structure of the disc-shaped cluster $[Mn_{12}O_{12}(CH_3COO)_{16}(H_2O)_4]$. Spheres represent Mn atoms: four central Mn^{IV} centers (S=3/2) and eight outer Mn^{III} centers (S=2). Image adapted from reference[30]

Not much attention was paid to this unexpected discovery until eight years later. In 1988, Boyd *et al*. presented the magnetic properties of a benzoate equivalent of the Mn_{12} cluster and conclude on the possibility to build bulk molecular magnetic materials using these clusters as building blocks.[35] It was finally in 1991 that the true magnetic nature of $Mn_{12}Ac$ was recognized.[30] The group of Gatteschi in the Laboratory for Molecular Magnetism at the University of Florence (Italy) performed ac magnetic susceptibility measurements on Mn_{12} down to 4.5 K (Figure 3.5). They could observe the onset of an imaginary component of the susceptibility in the temperature range where the spin system was expected to be in thermal equilibrium.

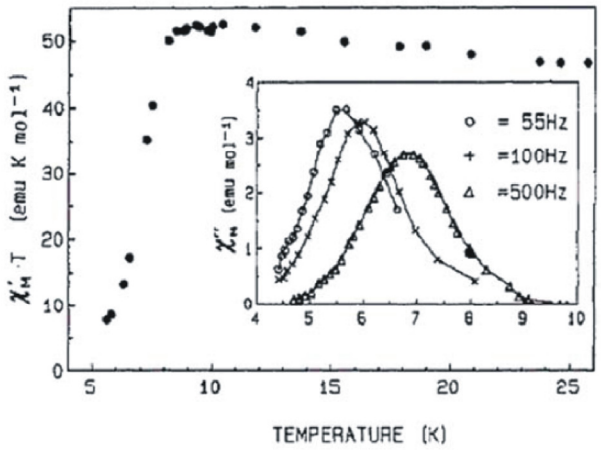

Figure 3.5 First ac magnetic susceptibility data recorded on $Mn_{12}Ac$. The inset shows the imaginary part of the magnetic susceptibility *vs* T measured at 55, 100 and 500 Hz. Image adapted from reference[30]

This phenomenon was interpreted as a thermally assisted relaxation process that becomes blocked when the experimental time is shorter than spin reversal. This polymanganese-based cluster exhibits memory effect at temperatures below 8 K and above this temperature, the thermal energy is enough to surpass the activation energy blocking the magnetization reversal. The fact that the position of the imaginary component peaks was frequency dependent allowed discarding the possibility that this was produced by a bulk magnetic ordering.

The origin of the magnet-like behavior in this polynuclear complex is the high-spin ground state stabilized by antiferromagnetic interactions between inner and outer rings of ions leading to a spin $S = \left| (8 \times 2) \ (4 \times 3/2) \right| = 10$ and the relatively high magnetic anisotropy of this ground state arising from the spin-orbit coupling and the distorted geometry of the coordination sphere of single ions. The discovery of the slow magnetic relaxation in $Mn_{12}Ac$ was only the starting point. In 1993, it was shown that the cluster exhibited magnetic hysteresis[32] of purely molecular origin since no 3D ordering could be observed in either magnetization, susceptibility of specific heat measurements (Figure 3.6).[36,37]. It was understood that these properties had a different origin than the magnetic hysteresis observed in bulk magnets. The latter is due to the motion of domain walls in a

long-range ordered magnetic material whereas the former is a property of individual molecules.

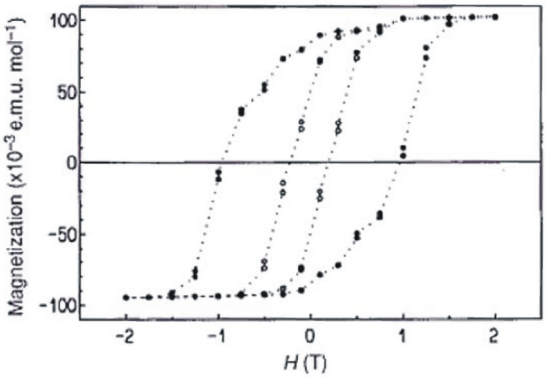

Figure 3.6 First magnetization hysteresis recorded on a polycrystalline sample of $Mn_{12}Ac$. Image adapted from reference[32]

The discovery of magnetization hysteresis in a single molecule was a breakthrough in the magnetic materials field since it was the first experimental observation that proved the possibility of making single-molecule magnets.

Inspired by the remarkable properties of Mn_{12}, many other polymetallic clusters were developed in the search for improved SMM behavior at higher blocking temperatures. A variety of Mn_{12} clusters with other ligands such us 2-hydroxymethylpyridine, 2,2'-bipyridine or 2,2'-biphenoxide, but still containing the same bridge with oxygen donor atoms were synthesized in order to evaluate the influence of the ligands in the magnetic relaxation process. These structural changes were not enough to increase its blocking temperature[38] so the strategy followed was to test the effect of replacing manganese by other metal centers bearing ground states with high spin *S* and a large axial anisotropy *D*. Beyond the chemical variants of $Mn_{12}Ac$ cluster other manganese complexes[39] have been found to behave as SMM while a few clusters formed by chromium,[40] iron,[41] and vanadium[42] also exhibited similar properties. Despite the high spin ground state that these metals present, the blocking temperature was not increased changing the metal to another transition metal. The smallest polynuclear transition metal SMMs found were those of the

Mn_2 family. These dinuclear manganese (III) Schiff base complexes allow for an easy modification of the properties by modifying the apical ligands. The ground state of those compounds was estimated to be $S = 4$ and blocking temperatures were observed in the range of 3-5 K only at 10 KHz frequencies.

A breakthrough came in 1997 with the observation of pronounced steps in its hysteresis cycle of the $Mn_{12}Ac$ complex.[43] Magnetization measurements were performed on a $Mn_{12}Ac$ single crystal at different temperatures between 1.55 K and 3.2 K, in applied magnetic field strengths up to 5 T. A staircase hysteresis loop was observed with successions of steep and flat regions at the values of H at which the resonant tunneling occurs (Figure 3.7). This phenomenon was attributed to a resonant tunneling process that occurs when levels associated to spin states on opposite sides of the anisotropy barrier coincide in energy. This was evidenced by the energy difference that separates the superposition states that would classically remain degenerated. This energy difference was experimentally determined by means of EPR and is known as tunnel splitting Δ.[44]

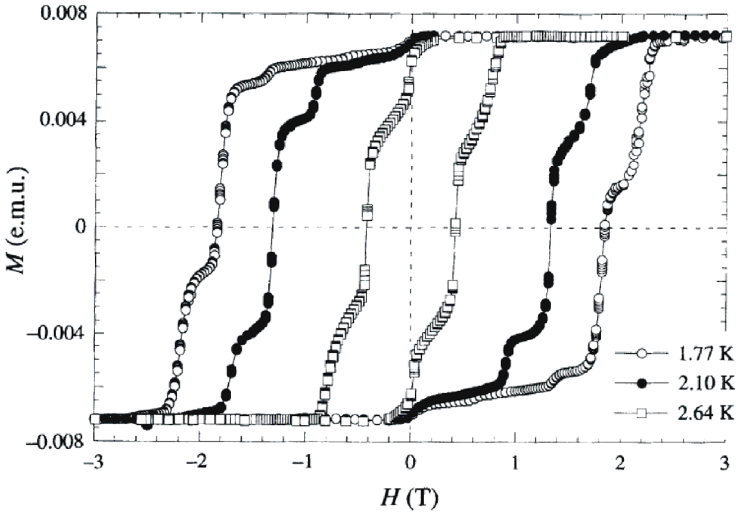

Figure 3.7 Magnetization hysteresis loops measured on a $Mn_{12}Ac$ single crystal at 1.77 K, 2.10 K and 2.64 K between magnetic fields of 5 T -5 T. Image adapted from reference[43]

In order to better understand the quantum tunneling of magnetization (QTM) phenomena we need to closely look at the energy levels diagram of the $Mn_{12}Ac$. When zero field is applied the Zeeman term is equal to zero and thus, the system presents an energy diagram like the one depicted in the left part of Figure 3.8. In this situation, the two states with quantum number S and $-S$ are equal in energy and the ground state is therefore degenerate with the two states $m_s = S$ and $m_s = -S$ equally populated.

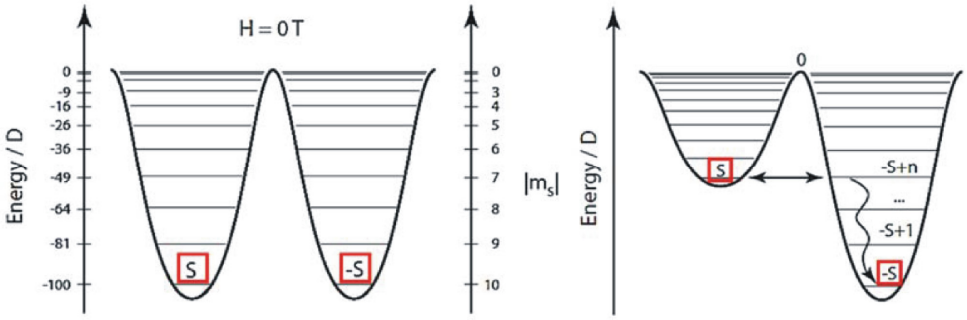

Figure 3.8 Energy diagram of $Mn_{12}Ac$ with S =10 under zero applied field (left) and applying a non-zero magnetic field component H along the easy axis (right)

On the contrary, when applying a magnetic field component H along the easy axis of magnetization, the Zeeman term is non zero and the two states become non-degenerated as can be seen in right energy diagram depicted in Figure 3.8 In this case, the energies of one well are stabilized with respect to those of the other. The relaxation can now occur in two ways:

1) Overcoming the anisotropy barrier and relaxing to the $|-S>$ state in a thermally activated process.

2) Alternatively, if the applied magnetic field along the easy axis H in such a way that the $|S>$ state coincides in energy with a $|-S + n>$ state, the resonant tunneling occurs between the two states. This process is called quantum tunneling of magnetization and is a temperature independent process.

3.1.6.2 Mononuclear SMMs

Over the past few years, molecular magnetic materials have ranged from the pioneering 2D/3D magnetic networks,[45] to 1D single-chain magnets,[46] 0D polynuclear metals[47] and finally the smallest magnet-like molecules including only one single magnetic ion, usually called single-ion magnets.[48,49] The development of the latter class of molecules, has been one of the hottest topics in magnetism research in recent years. Their simple structure compared with polynuclear complexes allow to have a better understanding for the correlation between structures and magnetic properties and further to fine-tune their single-molecule magnet properties.

In 2003, N. Ishikawa and co-workers reported the synthesis and magnetic characterization of double-decker compounds based on single lanthanide atom.[50] These sandwich-type complexes consist of two phthalocyanine rings encapsulating a single Ln ion in the trivalent state. In order to understand the magnetism of lanthanide complexes we must overview the lanthanides' electronic configuration: $[Xe]4f^n5d^16s^2$, where 4*f* orbitals are internal and thus not involved in bonding to ligands. This renders magnetic exchange between 4*f* ions very weak and makes the +3 oxidation state extremely stable. Different lanthanide atoms were studied such as Ln = Tb, Dy, Ho, Er, Tm and Yb that provide large spin states due to the strong spin-orbit coupling (J = 6, 15/2, 8, 15/2, 6 and 7/2 respectively). For single ions the energy terms are determined by strong coupling between the spin and orbital angular moments of the ions, and then split further by crystal-field effects. This strong spin-orbit coupling provides large single-ion magnetic anisotropies for 4*f* ions and has led to thermal energy barriers for the magnetization reversal, U_{eff}, that are an order of magnitude higher than those found in transition metal-based SMMs.

The consistent binding mode of the phthalocyanine macrocycles to lanthanide metal center leads to the very small deviation from the square antiprismatic symmetry in the first coordination sphere for the late lanthanide ions with smaller ion radii. Such a high symmetry was found to be favorable of an isolated ground-state doublet with large m_J value

well separated in energy from the first excited state, necessary for achieving a high-performance SMM.

In order to demonstrate the SMM behavior of the $Tb(Pc)_2$ complex, the ac magnetic susceptibility was recorded. Figure 3.9 shows ac magnetic susceptibilities as a function of temperature of polycrystalline powder sample of $[TbPc_2]^{-}\cdot TBA^{+}$. The maximum in the out-of-phase signal, typical feature of SMM behavior, was observed at 15, 32, and 40 K with ac frequencies of 10, 100 and 997 Hz, respectively. The peaks in the imaginary component for the complex appeared at much higher temperatures than those observed for the previously described SMMs. For instance, while $Mn_{12}Ac$ possess an ac magnetic susceptibility peak at 6 K at 100 Hz, $[TbPc_2]^{-}\cdot TBA^{+}$ presents an out-of-phase peak at 32 K in the same experimental conditions.

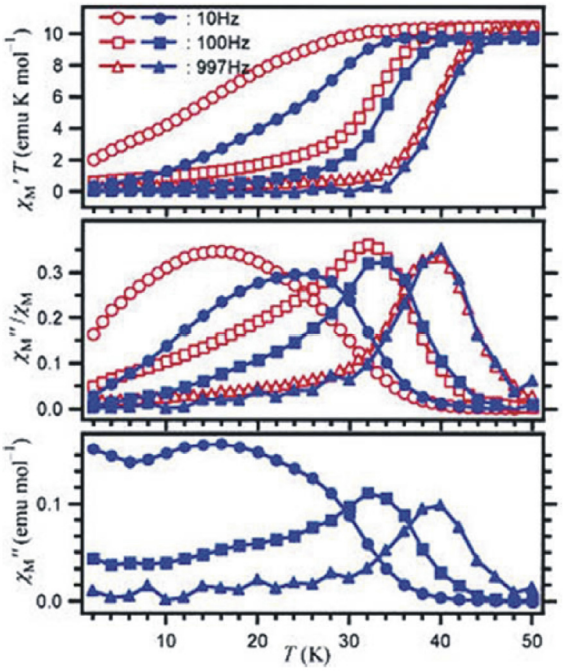

Figure 3.9 In-phase (χ') and out-of-phase (χ'') components of the ac magnetic susceptibility of $[TbPc_2]^{-}$ (open symbols) and of a 2% dilution in the diamagnetic $[YPc_2]^{-}$ complex (solid symbols). Image adapted from reference[50]

In diluted samples using diamagnetic $[YPc_2]^-\cdot TBA^+$, the χ'' peaks shift to higher temperature of the χ'' peaks clearly indicate that the slow relaxation of magnetization is purely due to intramolecular interactions.

In 2003, Ishikawa *et al*. established a new method that enabled the determination of the sublevel structures of the double-decker lanthanide complexes using a simultaneous fitting of paramagnetic NMR shifts and magnetic susceptibility data by the set of ligand field parameters from a multidimensional nonlinear minimization algorithm.[51] This method was used to evaluate the ground state energy diagrams for the $Ln(Pc)_2$ series. Figure 3.10 shows the theoretical and observed $\chi_m T$ values and paramagnetic shifts ($\Delta\delta$) of the ^{1}H NMR signal.

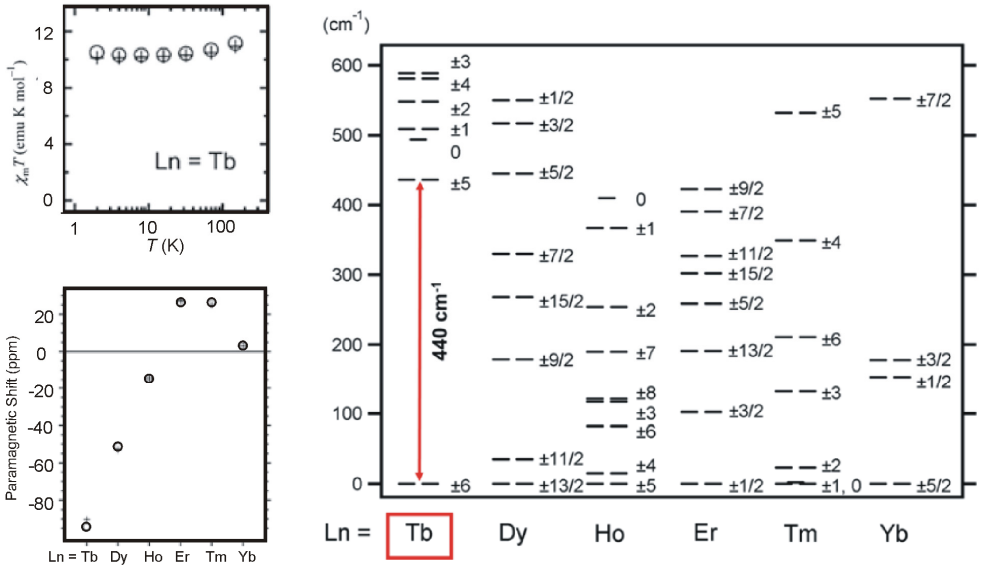

Figure 3.10 Top left: Comparison of the theoretical and experimental temperature dependence of the $\chi_m T$ values for the Tb complex. Bottom left: Theoretical and experimental paramagnetic shifts of the ^{1}H NMR signal of the α-proton on the Pc ligands. Right: Obtained energy diagram for the ground state multiplets. The *J* value indicated next to each energy level. Image adapted from reference[51]

The energy diagram for the ground state multiplets revealed that the Tb^{III}, Dy^{III}, and Ho^{III} complexes possess a well-isolated ground-state doublet with large m_J values, which are favorable for the presence of SMM behavior. In particular, the Tb complex showed a ground state with the largest m_J value and a separation of more than 400 cm^{-1} between the ground state and the first excited state. This value was in agreement with the very high effective barrier of 230 cm^{-1} experimentally measured by fitting the data to the Arrhenius law, surpassing several times that observed in the Mn_{12} SMM.

3.1.7 Applications of SMMs

The research on the properties of magnetic materials at very low temperatures has been stimulated in the last fifteen years by the observation of fascinating quantum phenomena, such as quantum tunneling of spins,[52,53,54] quantum coherence,[55,56] and quantum entanglement.[57,58] This phenomena might find application in the development of solid-state quantum information technologies and provide a direct hindsight on the quantum-to-classical transition.[59]

SMMs are materials that have important potential applications in several fields. Below the blocking temperature a SMM behaves like a magnet in the sense that, if it is magnetized by an applied magnetic field, it retains the magnetization. The strong uniaxial magnetic anisotropy exhibited by some SMMs makes them ideal candidates for high density magnetic storage applications. The ground state doublet is separated by the energy barrier created by the anisotropy, thereby stabilizing the spin orientation $\pm S$ at low temperatures. These energy levels correspond therefore to two effective spin states that can be used to store information in a binary code.[60] This goal is still out of reach, but some progress is being made. In order to have the possibility to use SMMs as information storage units, it is necessary to increase the relaxation time to significant values at accessible temperatures which implies to increase the energy barrier until very high limits.

High spin materials have also been proposed as suitable materials for low temperature magnetic refrigeration since the magnetocaloric effect (MCE) can be enhanced in these materials. MCE describes the relation between the magnetic entropy (and therefore temperature) and the applied magnetic field.

3.2 Objectives

The aim of this chapter is the preparation and characterization of new double-decker complexes that exhibit single-molecule magnets behavior using lanthanides and tetrapyrrole macrocycles as ligands within the search for novel functionalities. On one hand, we use an azaporphyrine derivative decorated with ethyl group in the β-pyrrolic positions in order to increase its solubility and processability. We also studied the functionalization of the phthalocyanine rings with bulky alkyl groups or sulfonate groups to increase solubility in organic solvents or water, respectively. Finally, we also introduced chiral groups on the phthalocyanine core in the search for combining the magnetic properties of lanthanide double deckers with optical activity.

All these different lanthanide double-deckers and their corresponding building blocks have been prepared and structurally characterized. We have also studied their physical and chemical properties, including their single-molecule magnet behavior.

3.3 Results and Discussion

3.3.1 Azaporphyrine as ligand in the lanthanide double-decker complexes

Tetraazaporphyrines (TAP) or porphyrazines are macrocyclic compounds constituted by four pyrrole units. Hence, TAPs are structurally closely related to porphyrins but differ from the latter in that the *meso*-positions connecting the pyrrole units are occupied by sp^2 nitrogen atoms instead of carbon atoms. Consequently, TAPs have the same basic 18 electron core structure than the Pcs. The synthetic methodologies for the preparation of TAPs are analogous to the ones we described above for Pcs. The main synthetic difference consists in the use of pyrrole derivatives instead of phthalyl derivatives as precursors. TPAs containing di-alkyl β-substituted pyrrole units are significantly more soluble in non-polar organic solvents than the Pcs analogs. Most likely, the alkyl substituents disrupt the aggregation behavior of the flat aromatic tetraazaporphyrin core. Thus we expected that double-decker complexes derived from TAPs will display magnetic properties similar to those of the Pc analogs described previously. However, TAPs derived double-deckers should be significantly more soluble in organic solvents.

In 2001, Barret and co-workers reported the synthesis of a series of lanthanide double-decker sandwich complexes based on tetraazaporphyrin ligands.[61] The prepared complexes showed good solubility in non-polar organic solvents. Although the potential magnetic properties of the sandwich complexes were not evaluated in the study, we hypothesized that the N_4 coordination motif provided by the tetraazaporhyrin ligands should produce a ligand field for the complexed lanthanide ions very similar to that of the phthalocyanines. Thus, the use of TAPs ligands instead of Pcs could afford single molecular magnets with improved solubility properties allowing an easier handling of the material.

3.3.1.1 Synthesis and characterization of the azaporphyrine ligand

We followed the synthesis of tetrazaporphyrin macrocycle bearing ethyl groups at all the β-positions of the pyrrole units described in 1991 by Fitzgerald and coworkers.[62] The synthesis involves treatment of the commercially available 3-hexyne **1** with one equivalent of bromine in acetic acid solution to afford the *trans*-dibromoalkene **2** (Scheme 3.1)**.**

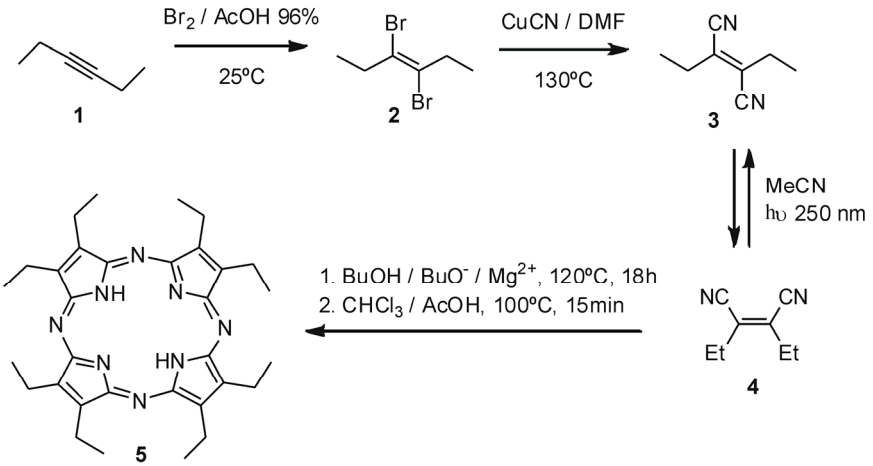

Scheme 3.1 Representation of the synthesis of OETAP based on the procedure reported by Fitzgerald

We encountered synthetic problems during the conversion of alkyne **1** to the dibromo **2**. The appearance of over brominated products was eliminated by slow dropwise addition of the bromine to the acetic acid solution containing the 3-hexyne **1**. We isolated the dibromo compound **2** as a colorless liquid in 84 % after bulb-to-bulb distillation. The ^{1}H NMR spectrum of isolated product was in complete agreement with the one reported. *trans*-Dicyano compound **3** was obtained using a slightly modified procedure of the Rosenmund-von Braun reaction described in literature. It is worthy to note, that this reaction is typically exclusively applied to aryl bromides.[63] A careful control of the reaction temperature was required to obtain good reaction yields for **3**. After refluxing for 1h a DMF solution of copper cyanide, the temperature of the mixture was carefully adjusted to 130ºC before the addition the dibromo compound **2**. After reaction workup the dicyanofumaroate **3** was isolated in 73 % yield as a liquid. The photoisomerization of **3** towards the *cis*-dicyanoalkene **4** was accomplished in 53 % yield by irradiation an acetonitrile solution at

245 nm for 24 hours. The reaction was monitored using gas chromatography. When the photostationary state was achieved the irradiation of the mixture was stopped. Longer irradiation times than the required to reach the photostationary state produced the appearance of secondary products. Both dicyano isomers, **3** and **4**, can be cyclotetramerized to yield the octaethyltetraazaporphyrin **5** (OETAP). However, the yields of the tetramerization reaction are significantly higher when maleonitrile **4** (*cis*) is used as the starting material. The cyclotetramerization reaction of **4** required the use of magnesium butoxide, which was prepared *in situ* by placing dry magnesium turnings and iodine, used to activate the magnesium, in previously dried butanol. After column chromatography purification the magnesium metallated OETAP Mg⊂**5** was isolated as a blue solid in 12 % yield. Free base **5** was obtained in quantitative yield by demetallation of the magnesium OETAP using excess of acetic acid in chloroform solution.

The ^{1}H NMR spectrum of **5** was in complement agreement with the reported spectroscopic data for this compound. The signal for the NH protons in porphyrins and aza-porphyrin is characteristic and resonates in the upfield region of the spectrum at δ = -2.36 ppm. The high upfield shift experienced by these protons is provoked by the magnetic anisotropy arising from the ring current of the aromatic aza-porphyrin system.

Single crystals suitable for X-Ray diffraction spectroscopy were obtained by slow evaporation of a THF solution containing the OETAP and helped us to confirm the identity of the macrocycle obtained.

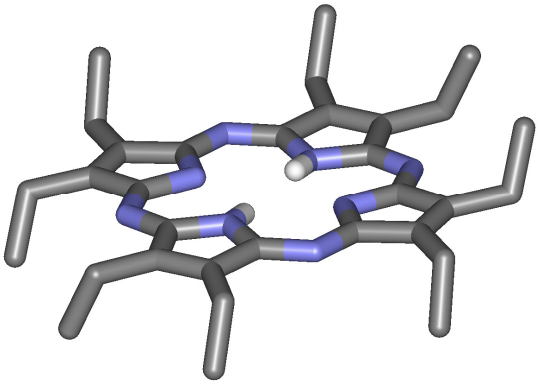

Figure 3.13 X-ray molecular structure of OETAP **5** obtained by slow evaporation of THF.

The absorption spectrum shows the typical Soret band for azaporphyrins centered at 336 nm and two intense Q bands at 624 nm 556 nm which are in agreement with the reported electronic absorption data (Figure 3.14).

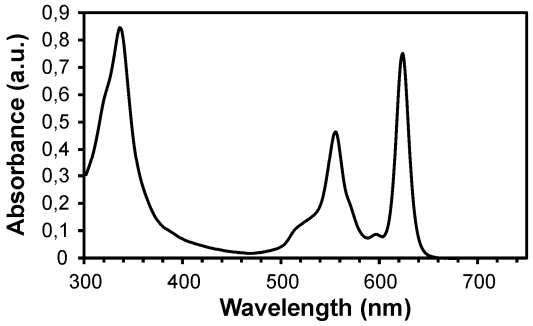

Figure 3.14 UV-vis electronic absorption spectrum of OETAP in a $1 \cdot 10^{-6}$ M CH_2Cl_2 solution showing the typical Soret band at 336 nm and two intense Q bands at 556 and 624 nm.

3.3.1.2 Synthesis and characterization of Ln(OETAP)$_2$ (Ln = Tb, Dy, Gd and Y)

The corresponding lanthanide double-decker (DD) complexes, [Ln(OETAP)$_2$] (Ln = Tb, Dy, Gd, Y), were obtained by heating OETAP in the presence of 1,8-diazabicycloundec-7-ene (DBU), the desired lanthanide acetate salt, and tetrabutylammonium (TBA) benzoate (Scheme 3.2).

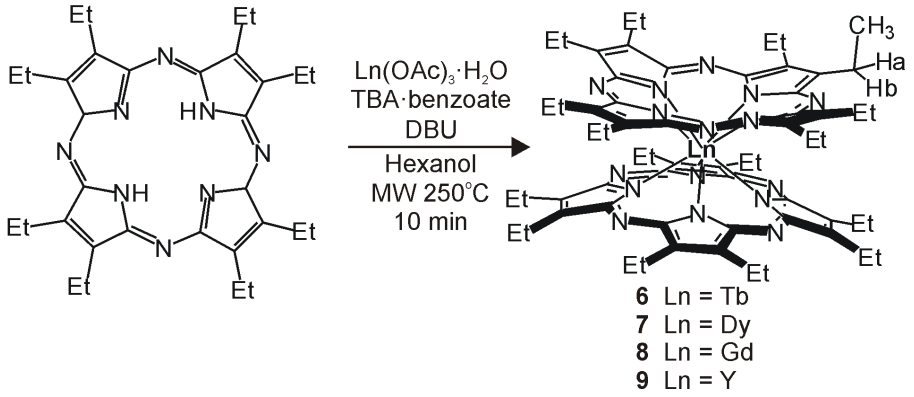

Scheme 3.2 Synthesis of neutral lanthanide double-decker complexes **6-9**

High temperature (250 ºC) was necessary, so 1-hexanol was used as the solvent, and heating was accomplished by using microwave irradiation in a sealed tube. The neutral double-decker [Ln(OETAP)$_2$] are radical species. They were isolated as blue solids after purification of the crude, first by flash chromatography on neutral alumina followed by reverse-phase semipreparative HPLC (Figure 3.15). We postulate that the neutral radical species are produced through the intermediacy of their corresponding anionic analogues, which are oxidized during work-up and purification. Indeed, when TBA·benzoate was excluded from the reaction mixture, no desired double-decker product was obtained, thus suggesting that the reaction pathway must pass through the anionic species, stabilized in solution by the TBA cations.

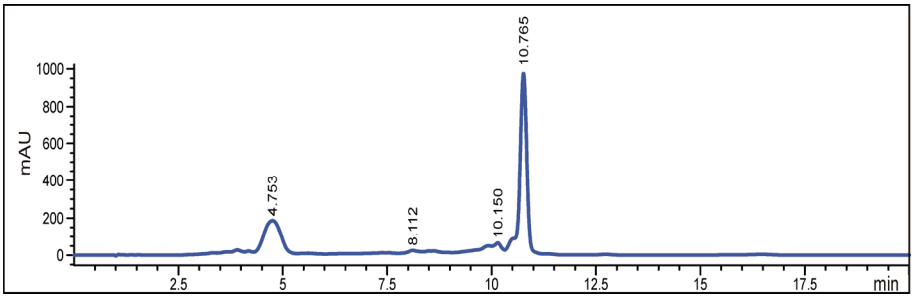

Figure 3.15 HPLC traces of complex **6** just prior to semipreparative HPLC purification. The neutral double-decker signal corresponds to the peak at 10.765 min. The peak at 4.753 min was attributed to the radical anion of the double-decker based on their UV-vis spectra.

Contrary to the Pc analogues, these DD complexes are very easy to process, as confirmed by their high solubility in organic solvents. Solutions up to 50 mM could be prepared in CH_2Cl_2. Additionally, they can be readily sublimed under relatively mild conditions, that is, 360 ºC and 10 mbar.

The MALDI-TOF mass spectra showed the expected isotopic pattern for the ion $[M+H]^+$ that corresponded to the Tb, Dy, and Gd DD complexes (**6**, **7**, and **8**, respectively). However, the yttrium DD complex **9** displayed a more complex mass spectrum. The ion peaks for $[M–e^–]^+$, $[M+H]^+$, and $[\{M+e^–\}^- + 2H]^+$ species were observed (Figure 3.16).

Owing to the presence of one unpaired electron in the radical species and/or the paramagnetic nature of some rare-earth ions, the ^{1}H NMR spectra of these neutral complexes do not produce sharp and well-resolved proton signals. Nonetheless, for the neutral species $[Tb(OETAP)_2]$ and $[Dy(OETAP)_2]$, it was possible to observe proton signals in their ^{1}H NMR spectra (Figure 3.17). Both spectra differ significantly from that of the starting OETAP. The ^{1}H NMR spectrum of OETAP features three sharp and well-defined signals: one broad singlet at δ = –2.36 ppm that is assigned to the two NH protons, one triplet that resonates at δ = 1.86 ppm for the 24 CH_3 protons, and one quartet centered at δ = 3.95 ppm that corresponds to the 16 CH_2 methylene protons. In contrast, these two

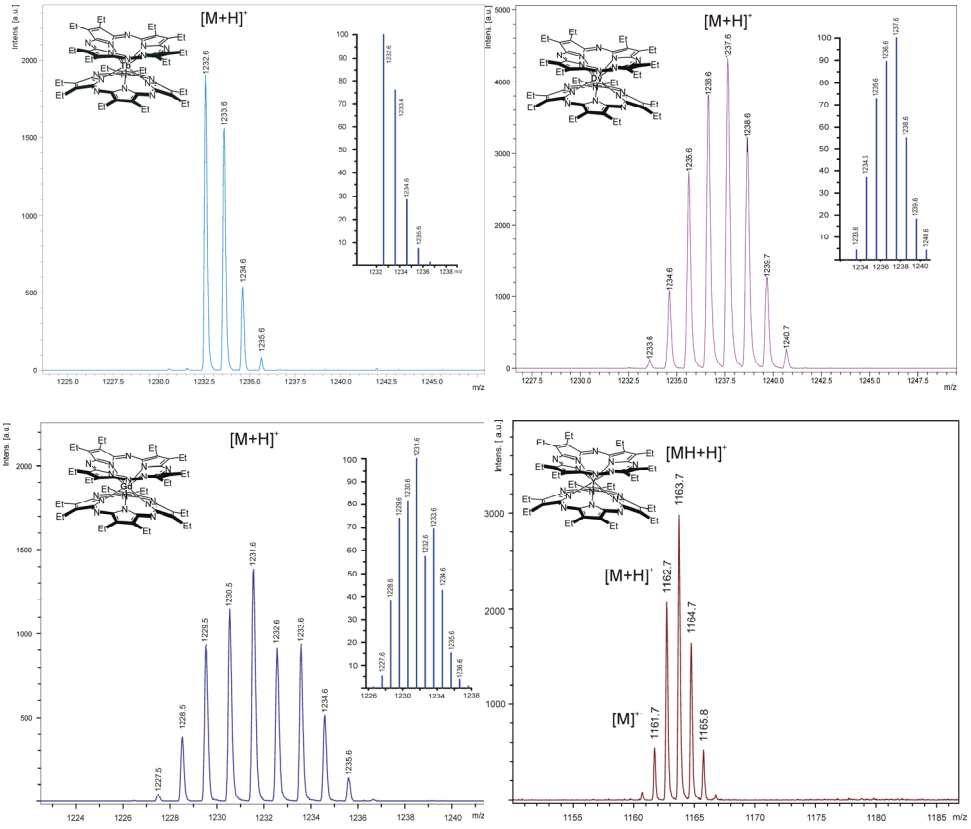

Figure 3.16 Experimental MALDI-TOF mass spectrum and simulated isotopic pattern (inset) for [M+H]+ of **6**-**8**. In the case of **9** a cluster of the ion-peaks corresponding to $[M–e^–]^+$, $[M+H]^+$ and $[MH+H]^+$ species is observed. In all cases the used ionization method was matrix-assisted laser desorption/ionization (MALDI) with positive ion mode detection and using trans-2-[3-(4-tert-Butylphenyl)-2-methyl-2-propenylidene]malononitrile as matrix. The samples were prepared using as solvent mixture methanol and dichloromethane.

sandwich complexes exhibit ^{1}H NMR spectra that display three broad signals that are shifted highly upfield and integrate with a 3:1:1 ratio. The paramagnetic nature of the Tb and Dy DD complexes causes their proton signals to appear at unconventional chemical shifts. These signals are spread over a much larger range (between δ = –20 and –80 ppm) than usually observed for the protons in diamagnetic organic compounds. For the Tb DD complex, the protons of the CH_3 groups appear at δ = –27.1 ppm (isotropic shift, $\Delta\delta$ = –

25.3 ppm). Notably, the protons of the methylene groups appear as two separate signals that resonate at δ = –60.4 and –75.4 ppm. This is because, in the double-decker complex, the two faces of the OETAP ligands are not identical. This symmetry reduction renders protons Ha and Hb chemically nonequivalent. The observation of two separate signals for the methylene protons helps to confirm the double-decker structure of these two complexes. The Gd DD also showed the expected three signals in the upfield region of the ^{1}H NMR spectrum. However, in this particular case the signals had very low intensities.

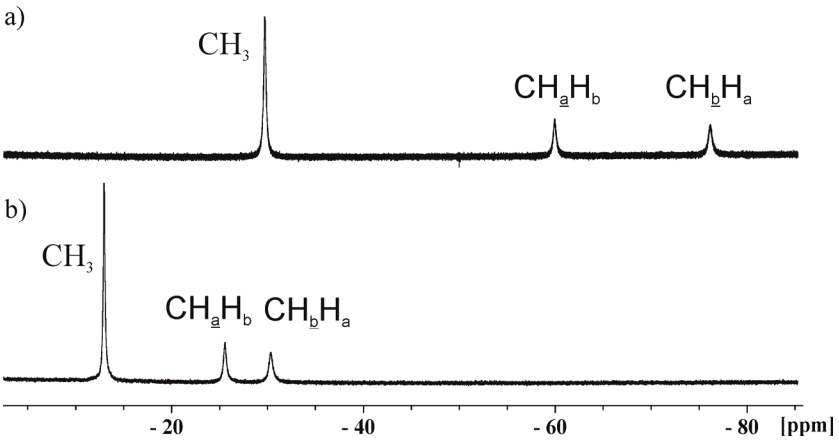

Figure 3.17 a) Selected region of the ^{1}H NMR spectra of **6** in $CDCl_3$ recorded at 298 K and b) Selected region of the ^{1}H NMR spectra of **7** in $CDCl_3$ recorded at 298 K.

The ^{1}H NMR spectrum of the neutral yttrium double-decker complex did not display any observable signals. Hydrazine hydrate was added to the solution of the neutral complex to induce the *in situ* formation of the anionic counterpart $[Y^{III}(OETAP^{2-})_2]^-$. The anionic complex does not contain unpaired electrons. Subsequently, the ^{1}H NMR spectrum expected for $[Y^{III}(OETAP^{2-})_2]^-$ was revealed and displayed signals at standard chemical-shift values. The ^{1}H-^{1}H COSY NMR spectrum of Y DD clearly shows the presence of cross-peaks owing to the scalar coupling between the protons of the methyl CH_3 group and the two chemically nonequivalent methylene protons. Similar hydrazine reduction of DD complexes **6**–**8** induced reduced changes in the shape and chemical-shift values of the

proton signals. The anionic counterparts of the DD complexes **6–8** are still paramagnetic owing to the presence of unpaired electron spins in the molecular orbitals at the metal center.

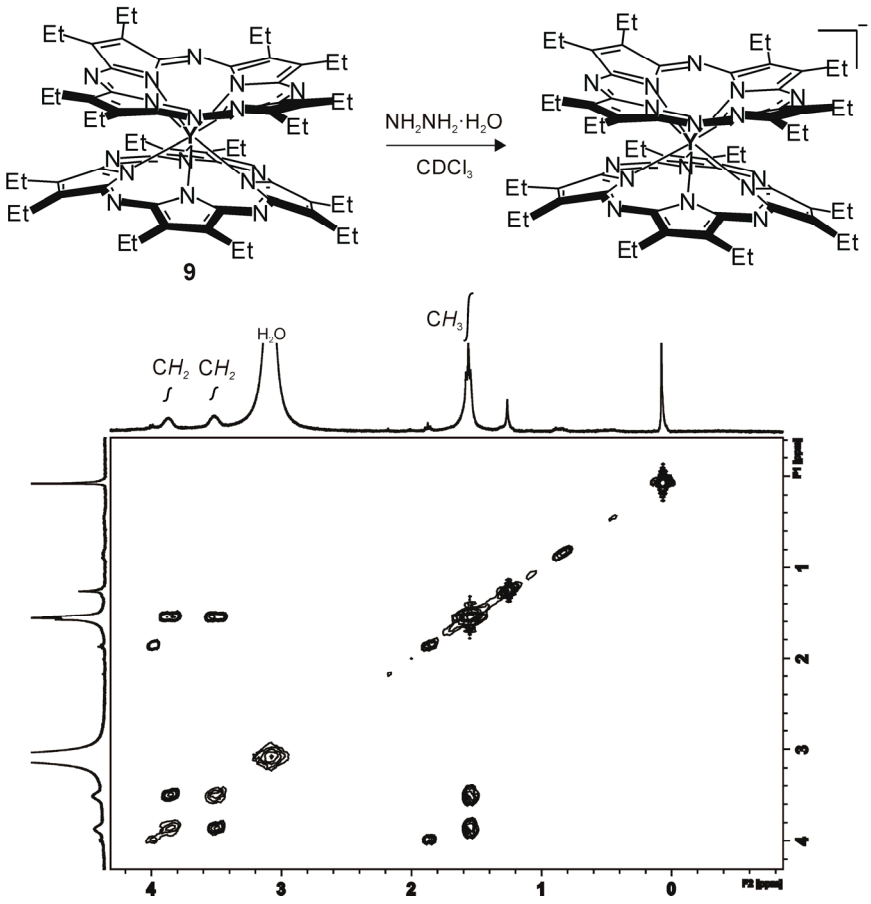

Figure 3.18 Reduction of neutral DD **9** to the anionic complex $[Y(OETAP)_2]^-$ with hydrazine hydrate in $CDCl_3$. ^1H–^1H COSY NMR spectra of the *in situ* formed anionic complex $[Y(OETAP)_2]^-$ in $CDCl_3$ at 298 K.

The cyclic voltammograms (CV) of the solutions of DD complexes in dichloromethane show two quasi-reversible one-electron redox processes (Figure 3.19). Most likely, both electron-transfer processes are ligand-centered. By analogy with the $[Ln(Pc)_2]$ complexes,

we assign the first redox wave to the oxidation of the anionic species $[Ln(OETAP)_2]^-$ that yields the neutral mono-radical double-decker, $[Ln(OETAP)_2]^0$, and the second wave to the one-electron oxidation process that gives a formal diradical cationic species $[Ln(OETAP)_2]^+$. These experiments demonstrate the high stability of these DD complexes in solution, regardless of their oxidation state. The measured redox potentials are almost identical for all four of the double-decker complexes supporting their ligand-based character.

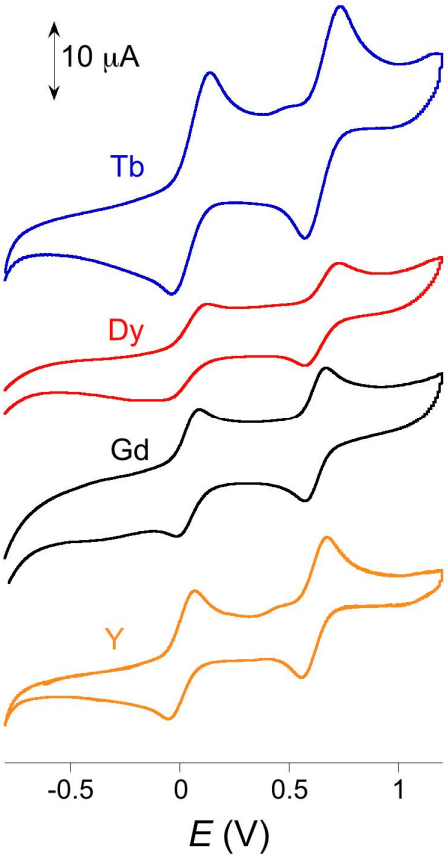

Figure 3.19 Cyclic voltammograms for compounds **6-9** in CH_2Cl_2 solution containing $TBA^+PF_6^-$ as electrolyte. The reported potentials are referenced to Ag/AgCl electrode

It is well known that DD complexes display significant changes in their UV absorption spectra depending on the formal oxidation state. We investigated the

spectroelectrochemical behavior of **6**–**8** to identify the spectroscopic features of the charged species in dichloromethane (Figure 3.20). The spectra of the neutral species show the typical features of the DD lanthanide complexes, a Soret band and only one Q band. The anionic $[Ln(OETAP)_2]^-$ complexes were generated by applying a potential of –0.7 V to a solution of the neutral species in methylene chloride. The UV-vis spectra showed an overall increase in extinction coefficients, a bathochromic shift of the S band, and a new weak absorption centered at about 400 nm. The cationic $[Ln(OETAP)_2]^+$ species were generated by applying a +1.2 V potential (versus Ag/AgCl reference electrode). These species display a hypsochromic shift, an increase in intensity of the Soret band, and a significant decrease in intensity of the band centered at 595 nm.

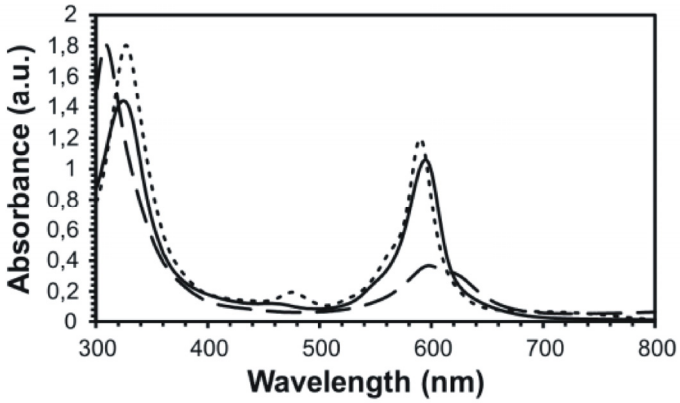

Figure 3.20 Spectroelectrochemistry experiment showing the UV-vis absorption spectra of the three different species of **6** in CH_2Cl_2 solution: anionic (····) and cationic species (– –) derived from neural (—) complex

Good-quality single crystals of **6** were obtained by slow evaporation of a THF/methanol solution. The neutral $[Tb(OETAP)_2]$ molecule (Figure 3.21) crystallizes in the tetragonal space group $P4_2/n$ and forms layers on the *ab* plane. In the layers, adjacent molecules appear perpendicular to each other with respect to the mean plane of the organic ligands. This arrangement yields very long intralayer Tb···Tb distances (over 10.8 Å). The Tb···Tb interlayer distances are larger (over 15 Å). There are no close contacts between molecules, and therefore good magnetic isolation is expected. The shortest intralayer contacts occur

between terminal CH_3 moieties and adjacent non-coordinating N atoms (C···N = 4.2(1) Å), whereas the shortest interlayer contacts involve two terminal CH_3 groups (C···C = 3.95(2) Å).

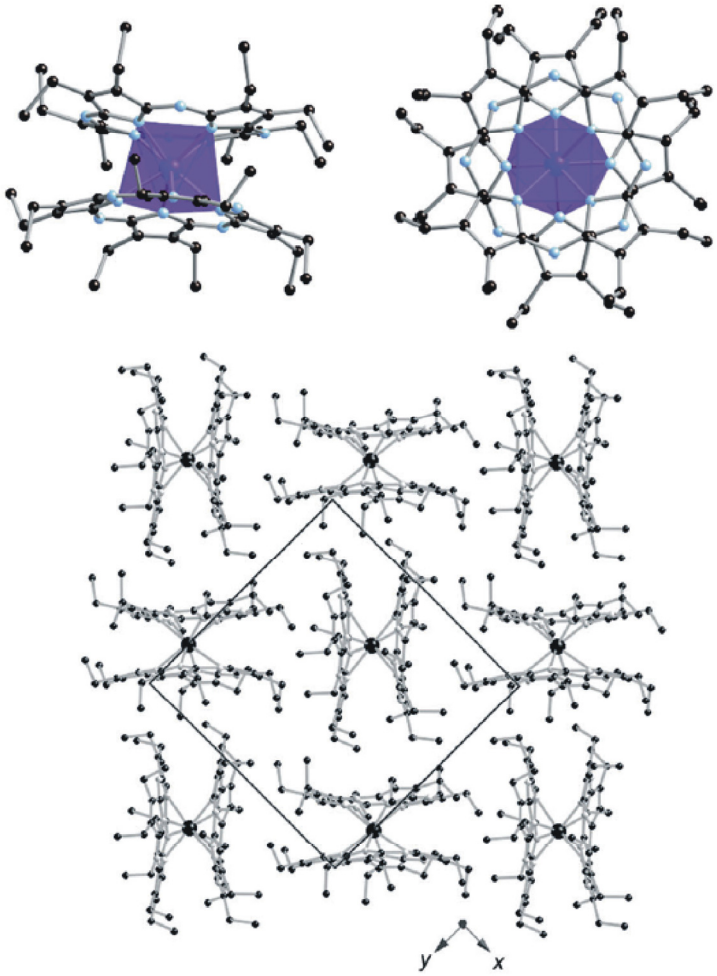

Figure 3.21 Two different views of the molecular structure of the [Tb(OETAP)$_2$] complex showing the square antiprism coordination of the Tb^{3+} centers (top) and representation of the crystal structure of **6** on the *ab* plane (bottom)

The central Tb^{3+} ions possess a regular square antiprismatic coordination with local D_{4d} symmetry. Bond lengths are in the 2.35–2.45 Å range, and the ligands appear staggered

with respect to each other, with a displacement close to 45º. Despite its high symmetry, the complex exists in a variety of conformations in the crystal lattice. The ethyl groups are randomly oriented between the upward and downward configurations with respect to the sandwich core and show some slight disorder in their orientation. However, in a given complex, adjacent ethyl groups on separate OETAP ligands orient themselves in the same direction, probably to limit steric repulsion. Thus, if one ethyl group points towards the metal ion, the adjacent ethyl group attached to the other OETAP ligand points away from the metal.

Compounds **6** and **7** are isostructural, as confirmed by X-ray powder diffraction (Figure 3.22). The isolated Gd and Y DD complexes **7** and **8** are also neutral molecular species, according to NMR spectroscopy, electrochemistry, and mass spectrometry. However, on the basis of X-ray powder diffraction data, they crystallize in a different space group from that determined for the Tb and Dy complexes **6** and **7** (Figure 3.23). Unfortunately, we did not obtain suitable single crystals of these two compounds to determine their structure and packing in the solid state.

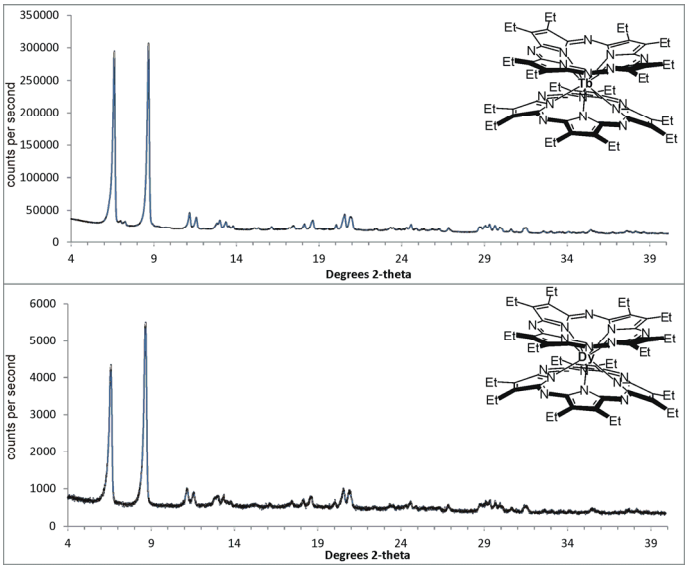

Figure 3.22 X-ray diffraction powder pattern for **6** and **7**

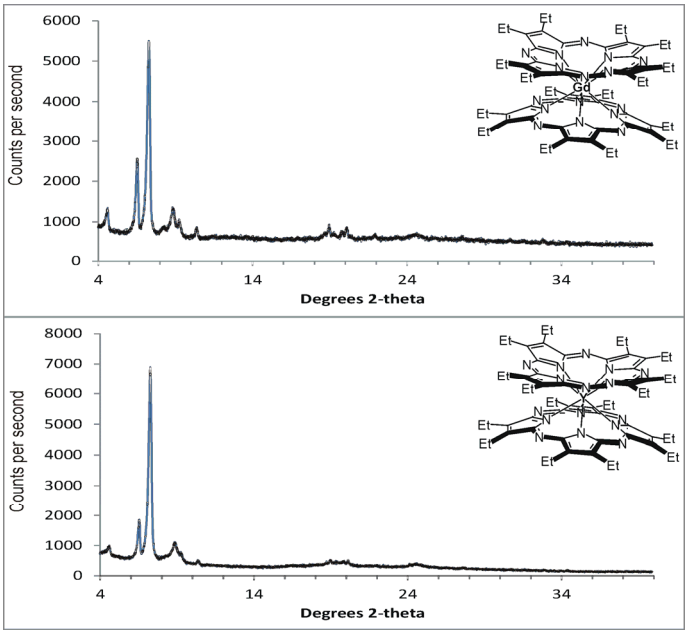

Figure 3.23 X-ray diffraction powder pattern for **8** and **9**

dc magnetic susceptibility was measured for compounds **6**–**8** under an applied field of 0.1 T (Figure 3.24) after field cooling and also after zero-field cooling (ZFC). At room temperature we found that $\chi_m T$ values were in good agreement with the typical magnetic moment expected in complexes of these lanthanides: 12.96 emu·K·mol^{-1} for Tb, 12.57 emu·K·mol^{-1} for Dy, and 7.80 emu·K·mol^{-1} for Gd. The contribution of the radical centered on the organic ligand to the overall magnetic moment of the complex was negligible. As the temperature was lowered, $\chi_m T$ slowly decreased to 10.91 emu·K·mol^{-1} for **6** and 8.80 emu·K·mol^{-1} for **7** owing to the strong spin–orbit coupling that affects Tb^{3+} (ground term $^7F_6$) and Dy^{3+} (ground term $^6H_{15/2}$). On the contrary, **8** maintains a constant $\chi_m T$ value in good agreement with that expected for only a spin $S = 7/2$ contribution (7.875 emu·K·mol^{-1}, $g = 2$) since the Gd^{3+} ground electronic state is an isotropic $^8S_{7/2}$ term. There are no significant deviations in these trends, not even at very low T, thus suggesting negligible intermolecular magnetic interactions in the crystal packing. In all samples, the

ZFC data confirmed no irreversibility, thereby discounting the appearance of long range ordering.

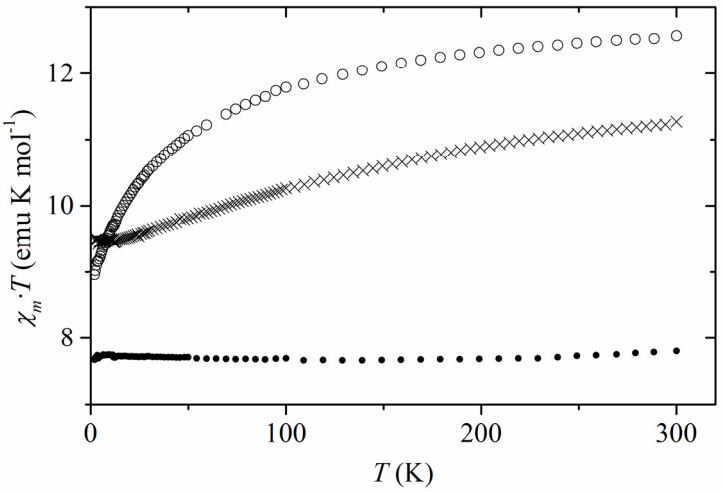

Figure 3.24 dc magnetic data for compounds **6** (×), **7** (○) and **8** (●)

The thermal dependence of the alternating current (ac) magnetic susceptibility of compound **6** shows a non-zero out of- phase susceptibility (χ_m'') below 50 K that is related to a decay of the in-phase χ_m'T product (Figure 3.25). Both features show clear frequency-dependent behavior that suggests superparamagnetic behavior. In addition, a second relaxation phenomenon with small frequency dependence appears below 10 K as suggested by the onset of a fast increase in χ_m''.

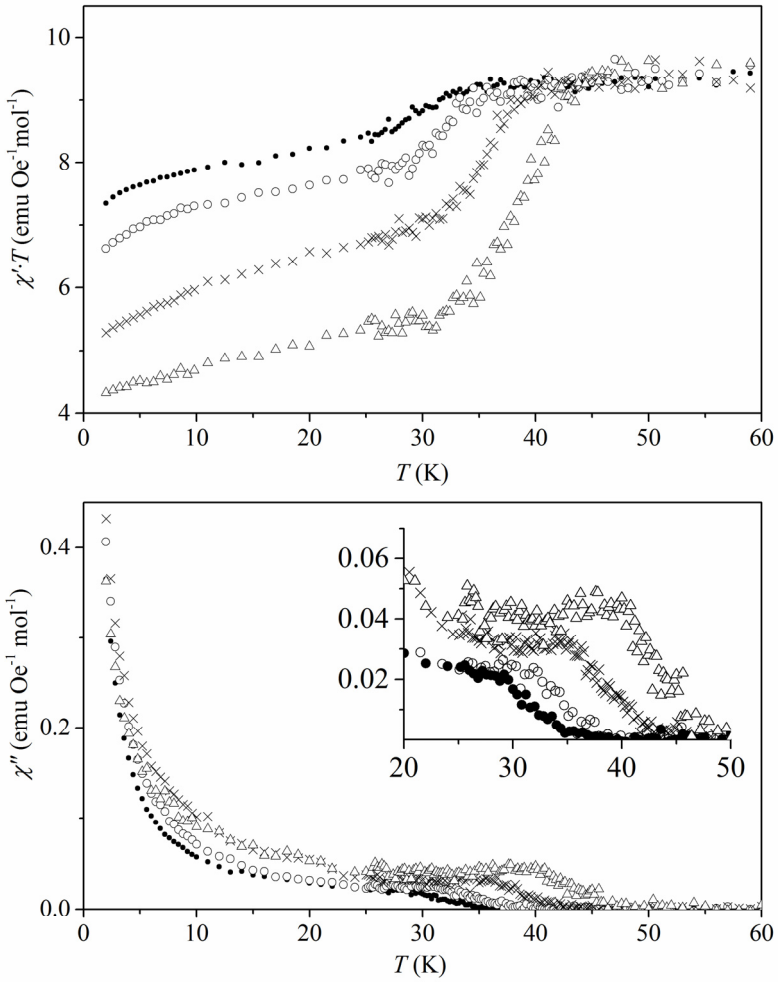

Figure 3.25 Top: In-phase ac susceptibilities for **6** at 3 (●), 13 (○), 133 (×) and 1030 Hz (Δ). Bottom: Out-of-phase ac susceptibilities for **6** at 3 (●), 13 (○), 133 (×) and 1030 Hz (Δ). Inset: Detail of the out-of-phase signal

The superparamagnetic relaxation time was extracted from the exponential fitting of the relaxation time and the energy barrier (Figure 3.26). We found ΔE = (383 ± 37) K and a characteristic time equal to $\tau_0 = (1.3 \pm 1.3) \times 10^{-8}$ s. Since quantum tunneling is known to affect the relaxation time of SMMs, we also carried out the same ac measurements under an applied dc field of H_{dc} = 0.1 T. The good agreement between the data obtained in the absence or presence of the dc field (ΔE = (376 ± 51) K and a characteristic time equal to τ_0

= (1.3 ± 1.8) × 10^{-8} s) suggests that tunneling is not contributing to the superparamagnetic relaxation above 10 K.

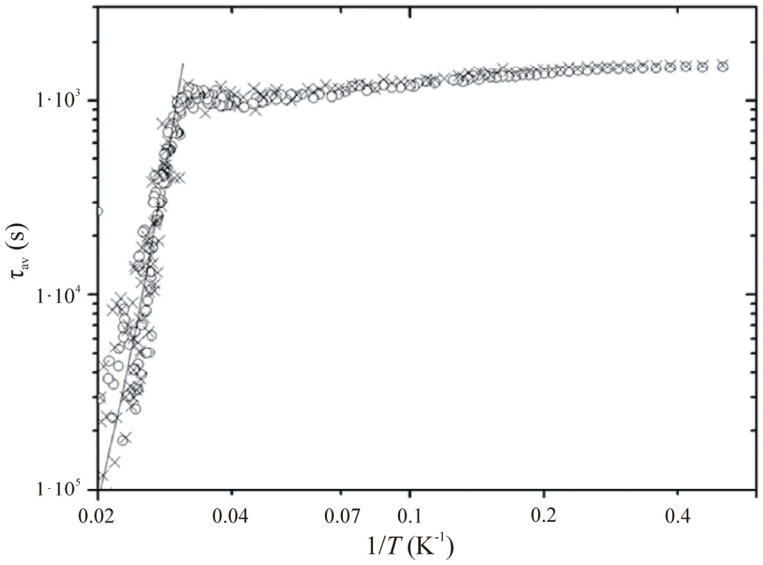

Figure 3.26 Average magnetic relaxation time (τ_{av}) for **6** versus the reciprocal temperature at 13 Hz and zero field (×) or 0.1 T (○). The continuous line corresponds to the best Arrhenius fit used to determine the activation energy

The ac data for **7** show similar behavior although at lower temperatures. A weak out-of-phase signal appears below 20 K, superimposed with another crescent signal at lower temperatures (Figure 3.27).

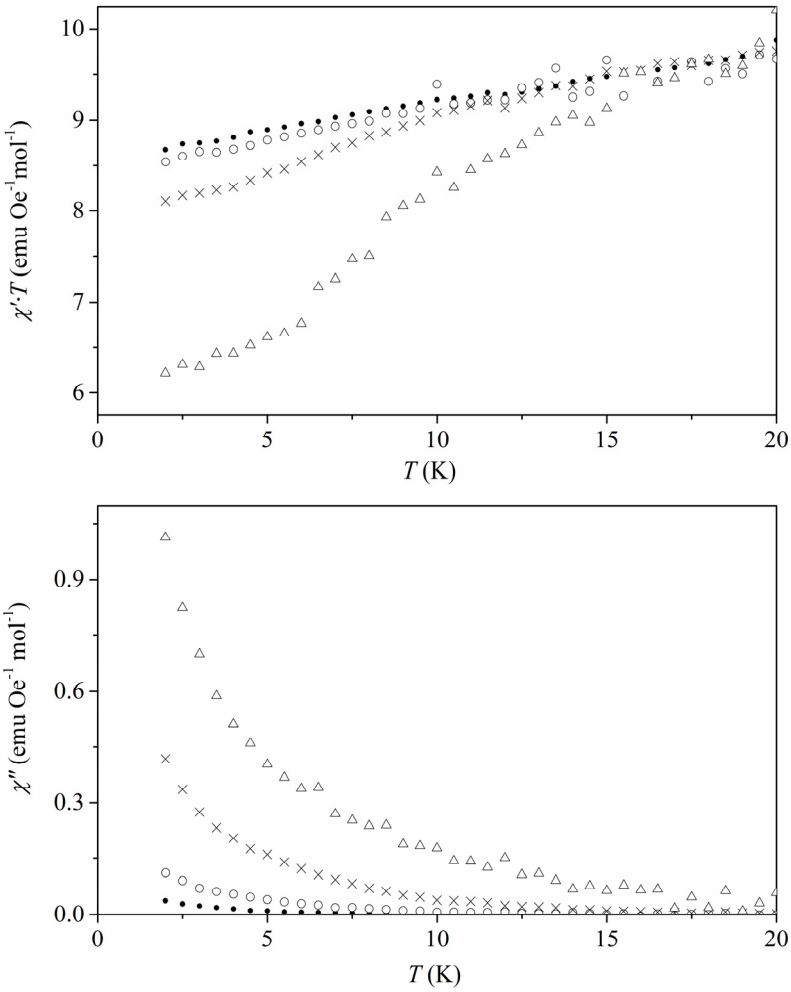

Figure 3.27 Top: In-phase ac susceptibilities for **7** at 3 (●), 13 (○), 133 (×) and 1030 Hz (Δ). Bottom: Out-of-phase ac susceptibilities for **7** at 3 (●), 13 (○), 133 (×) and 1030 Hz (Δ).

To observe the anomaly more clearly, the dynamic response was measured under different applied fields (Figure 3.28). As the field strength is increased, the peak in χ_m'' becomes more apparent, and the blocked signal decomposes into two peaks. The second peak could be due to small amounts of the reduced $[Dy(OETAP)_2]^-$ species present in the

sample. The reduced anionic species is expected to have a lower energy barrier; however, the presence of other dynamic phenomena in the crystal lattice cannot be discarded.

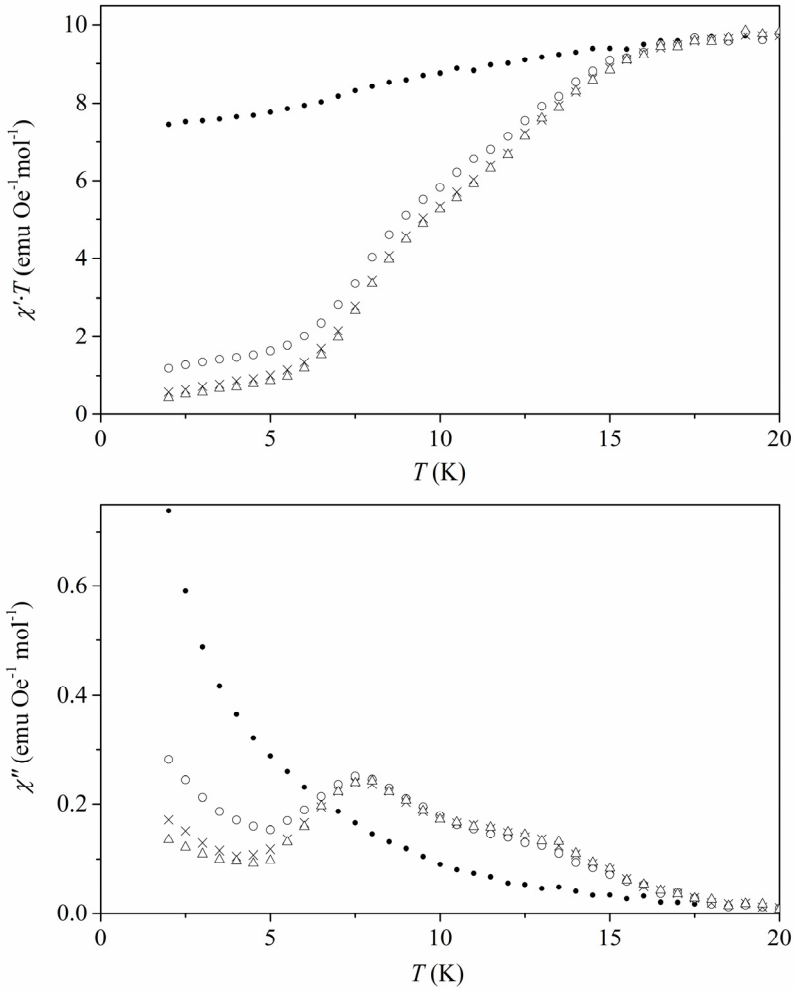

Figure 3.28 Magnetic data (ac) for **7**. Left: Temperature dependence of the in-phase ac magnetic susceptibility measured with a frequency of 523 Hz at different magnetic field applied: 0 (●), 500 (○), 1000 (×) and 1500 Oe (Δ). Right: Out-of-phase ac magnetic susceptibilities measured at 523 Hz at different fields: 0 (●), 500 (○), 1000 (×) and 1500 Oe (Δ).

The superparamagnetic relaxation time was extracted from the exponential fitting of the relaxation time and the energy barrier. From the superparamagnetic relaxation at 0 T (184 Hz) we estimate an activation energy ΔE=(32 ± 3) K and a characteristic τ_0 = (1.4 ± 0.4) × 10^{-6} s.

We also obtained EPR spectra for compounds **6** and **9** (Figure 3.29). At room temperature, the EPR spectrum of **9** shows the typical signal for an S = 1/2 radical species, and is centered at g = 1.99. This is a direct proof of the presence of an organic radical in these neutral complexes. In the case of the complex with paramagnetic Tb **6**, the intensity of this signal is severely reduced. This indicates that the unpaired electron in the organic framework is indeed coupled with the paramagnetic Ln center.

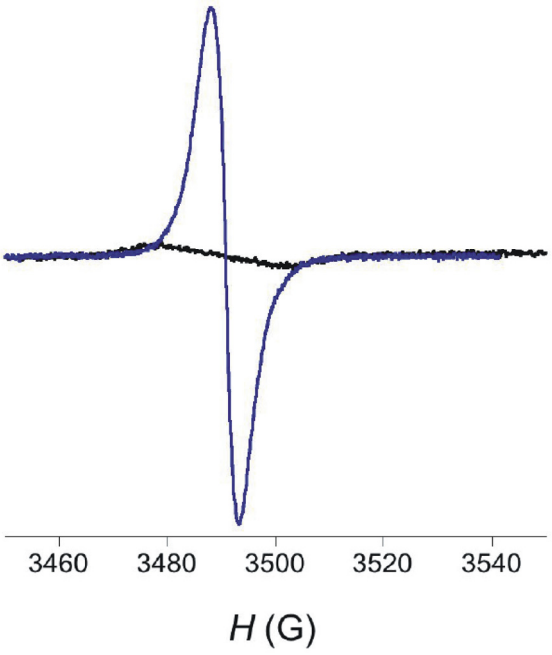

Figure 3.29 Solid state X-band EPR spectra of compound **6** (black line) and **9** (blue line) recorded at room temperature.

3.3.2 Functionalized phthalocyanines as ligands in the lanthanide double-decker complexes

3.3.2.1 Synthesis and characterization of Tb(^{t}BuPc)$_2$

To increase the scope of DD complexes we synthesized additional tetrapyrrolic ligands based on functionalized phthalocyanine scaffolds. Since it is widely known that Pcs possess low solubility in organic solvents, we decided to prepare a *tert*-butyl tetrasubstituted Pc in order to gain solubility in these solvents. The tetramerization reaction of the commercially available 4-(*tert*-butyl)phthalonitrile **10** using lithium methoxide in 1-hexanol yielded the desired phthalocyanine **11** in 12 % yield. Remarkably, when the same reaction was performed with magnesium, iodine in dry butanol followed by treatment with sulfuric acid Pc **11** was obtained in a 43% yield (Scheme 3.3).

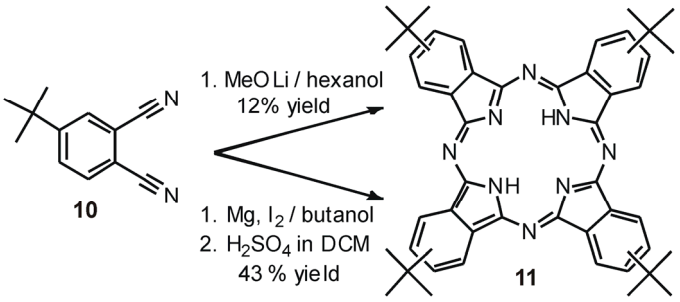

Scheme 3.3 Two different synthetic routes to produce *tert*-butyl substituted phthalocyanine **11**

Due to the formation of different isomers in the cyclization reaction, the ^{1}H NMR spectrum of the isolated **11** showed three sets of signals in the aromatic region resonating as multiplets and integrating for the 12 protons attributed to the isoindole moieties. The signals corresponding to the four *tert*-butyl groups and the NH resonating at -2.45 ppm were also detected. The high upfield shift experienced by these protons is provoked by the magnetic anisotropy arising from the ring current of the aromatic Pc system.

The corresponding [Tb(^{t}BuPc)$_2$] double-decker complex was obtained by heating **11** in the presence of 1,8-diazabicycloundec-7-ene (DBU), terbium acetate, and tetrabutylammonium (TBA) benzoate.

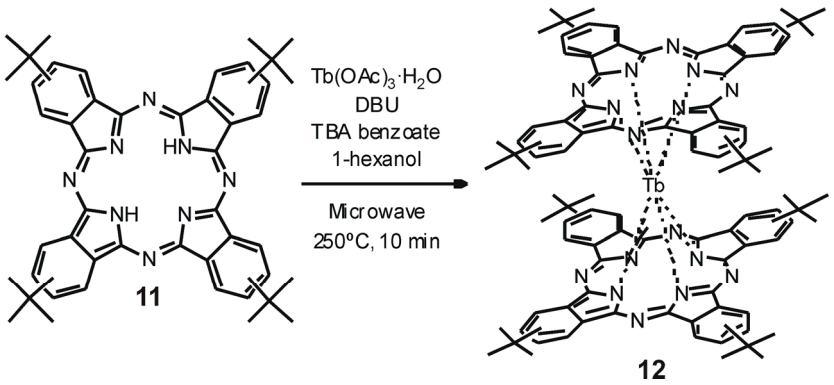

Scheme 3.4 Pc metallation reaction conditions to form double-decker sandwich **12**

The metallation reaction of **11** affording double-decker sandwich [Tb(**11**)$_2$] was accomplished by heating in a microwave reactor at 250 ºC a mixture of phthalocyanine **11,** terbium acetate, DBU, and *n*-tetrabutylammonium benzoate dissolved in 1-hexanol (Scheme 3.4). After column chromatography purification we were able to remove the non-reacted starting material and isolate the pure desired product **12**.

The MALDI-TOF mass spectra of complex **12** showed an isotopic cluster due to the formation of the radical cation [$M^{+\bullet}$]. It can be seen that the isotopic distribution pattern is in good agreement with the corresponding simulated pattern (Figure 3.30).

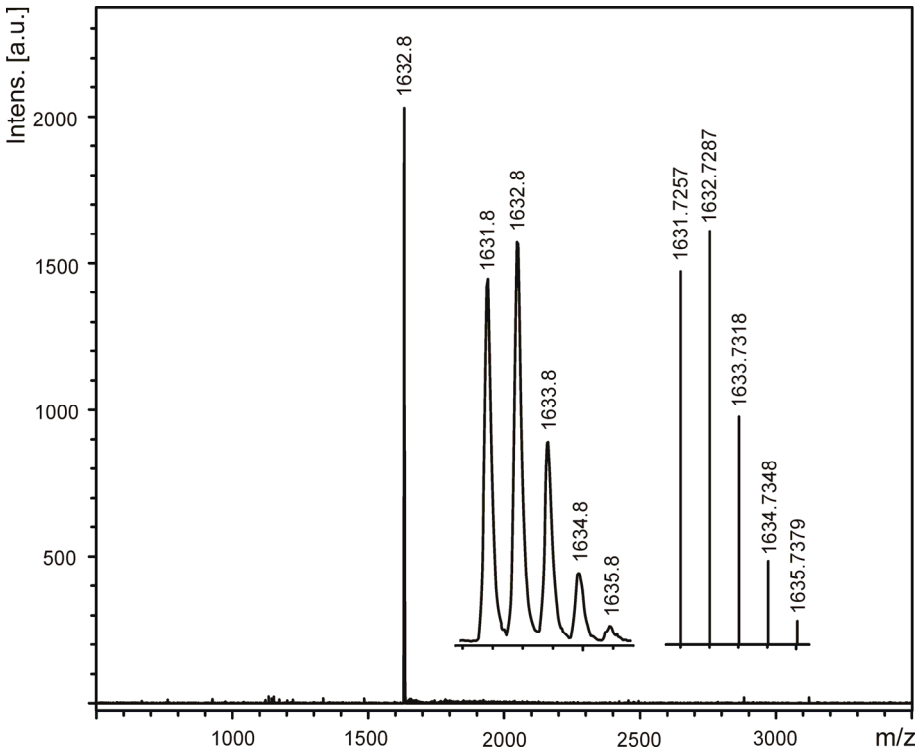

Figure 3.30 Experimental MALDI-TOF mass spectrum and simulated isotopic pattern (inset) for [$M^{+\bullet}$] of **12**. The used ionization method was matrix-assisted laser desorption/ionization (MALDI) with positive ion mode detection and using *trans*-2-[3-(4-tert-Butylphenyl)-2-methyl-2-propenylidene]malononitrile as matrix. The samples were prepared using dichloromethane as solvent.

Figure 3.31 displays the UV-vis spectrum of Tb⊂**11**$_2$ in dichloromethane solution. The Soret bands appeared at 325 nm and 348 nm, and two Q absorption bands were observed, with the strongest at 674 nm and the weakest one at 607 nm.

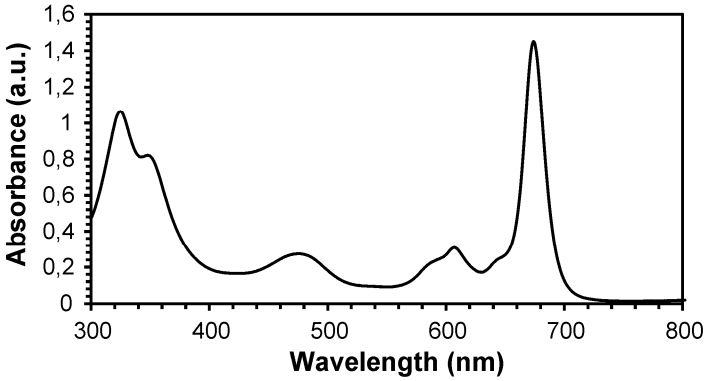

Figure 3.31 UV-vis electronic absorption spectra of Tb(^{t}BuPc)$_2$ in CH_2Cl_2 solution showing the typical Soret band at 325 and 348 nm and two Q bands with the strongest at 647 nm and the weak one at 607 nm.

Complex [Tb(**11**)$_2$] (**12**) is also expected to be electro-active due to the known redox properties of the Pc ligands. Figure 3.32 shows the cyclic voltammogram of [Tb(**11**)$_2$]. Two reversible one-electron redox processes were detected with half-wave potentials centered at $E_{1/2}$ = 399 and -54 mV, respectively. Most likely, both electron transfer processes are centered at the ligands. We assigned the redox wave at 399 mV to the one-electron oxidation process that converts the neutral mono-radical double-decker, [Tb(**11**)$_2$], into a formal diradical cationic species [Tb(**11**)$_2$]$^+$. On the other hand, the electron wave at -54 mV must correspond to the reduction of the neutral double-decker radical to the anionic species [Tb(**11**)$_2$]$^-$.

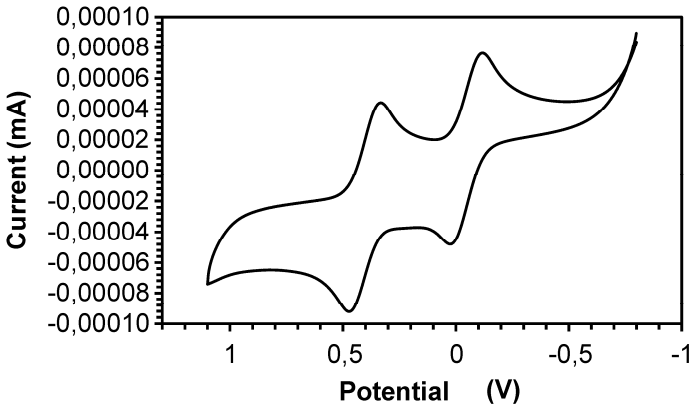

Figure 3.32 Cyclic voltammograms for compound **12** in CH_2Cl_2 solution containing $TBA^+PF_6^-$ as electrolyte. The reported potentials are referenced to Ag/AgCl electrode

We also investigated the spectroelectrochemical behavior of [Tb(**11**)$_2$] to identify the spectroscopic features of the radical anion [Tb(**11**)$_2$]$^-$ and the cation [Tb(**11**)$_2$]$^+$ upon electrochemical reduction and oxidation of the former, respectively (Figure 3.33). Application of a potential of -0.8 V to a green methylene chloride solution of [Tb(**11**)$_2$] afforded a blue solution of the radical anion [Tb(**11**)$_2$]$^-$ with the consequent change in the UV-Vis spectrum (increase and bathochromic shift of the bands at 325 nm and 674 nm). The electrochemical reoxidation of the anion to the neutral radical [Tb(**11**)$_2$] proceeded uneventfully when a potential of 0.1 V is applied to the solution above. Conversion of the neutral radical to the cationic species [Tb(**11**)$_2$]$^+$ was achieved applying a positive potential of +1.1 V. This red solution displays a distinguished UV-vis spectrum with a hypsochromic shift and increase in intensity of the Soret band and a bathochromic shift of the band at 674 nm. Electrochemical reduction of [Tb(**11**)$_2$]$^+$ by applying a potential of 0.1 V produced the neutral radical. The results obtained in the spectroelectrochemical experiments testify the high stability of the different oxidation states of the double-decker complexes.

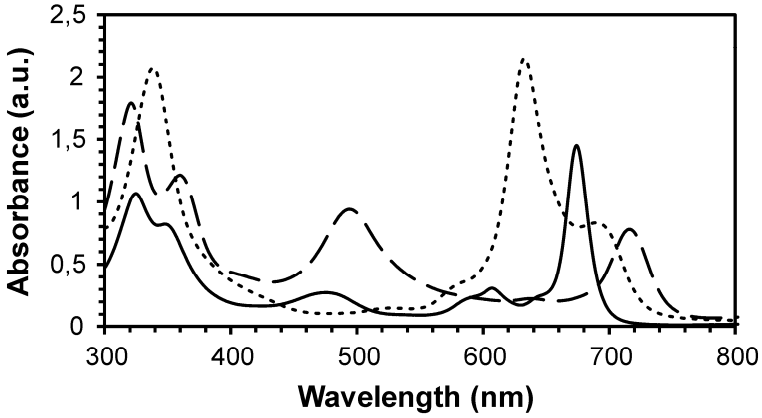

Figure 3.33 Spectroelectrochemistry experiments of **12** showing the UV-vis absorption spectra of the three different species in solution: neutral (—), anionic (····) and cationic species (– –)

3.3.2.2 Synthesis of lanthanide double-deckers functionalized with sulfonate groups

Sulfonated phthalocyanines can be synthesized via two general methods. The Weber-Busch synthesis,[64] also known as template or condensation synthesis, involves the condensation of 4-sulfophthalic acid in the presence of urea, nitrobenzene, cobalt chloride salt and ammonium molybdate as catalyst at 170 – 190 ºC. This method leads to isomeric mixtures, though all the molecules produced are presumably tetrasulfonated with one sulfonic acid group per peripheral ring. However, to the extent that the parent sulfophthalic acid is contaminated with phthalic acid with more than one sulfonic acid on the aromatic ring, the phthalocyanine product will have more than four sulfonic acid substituents. Even though starting the synthesis with a sulfonated phthalic acid with the sulfonic acid at the 4-position of the ring, different phthalocyanine isomers are formed in the cyclization reaction. This is due to the fact that the sulfonic acid can be found at either the 4- or 5- position of each of the four isoindole rings, giving a total of four isomers. Sulfonated phthalocyanines are prone to aggregation, even at low concentrations which hinders the separation of the different isomers produced in their formation.

Alternatively, a second synthesis method involves the "direct sulfonation" of an already formed phthalocyanine ring.[65] The parent macrocycle is prepared in a first step, most commonly by heating phthalic acid in the presence of urea and nitrobenzene and then treated with oleum or sulfuric acid. This method sulfonates predominately at the 4(5)-position of the isoindole unit, but it may also sulfonate other sites such as the 3(6)-position. This direct sulfonation methodology gives a difficult-to-separate mixture of the mono-, di-, tri-, and tetrasulfonate

In order to obtain sulfonated phthalocyanines, we first tested the reactions conditions reported by Torres *et al*.[66] The condensation of potassium 4-sulfonatophthalate and phthalic anhydride in a 1:1 ratio was carried out in the presence of $Zn(OAc)_2$, ammonium chloride and ammonium molybdate as catalyst using melted urea as solvent. Unfortunately, this reaction conditions gave a very difficult-to-separate mixture of products in very low yield.

In order to synthesize a sulfonated Pc-TAP hybrid we decided to prepare the phthalonitrile **16** containing a protected sulfonate group to be used as precursor in the synthesis of the macrocycle. Compound **16** was synthesized following a described procedure detailed in Scheme 3.5.[67] Sulfonamides are made from sulfonyl chloride and amines, and they are used as protecting groups of amines. The cleavage of sulphonamides often requires harsh conditions (i.e. the use of concentrated acid at high temperature or the treatment with reducing agents). During these treatments the sulfonic acid residue is often degraded. In the reported procedure for the synthesis of **16** a pyrrole is used as protecting group of the sulfonic acid. Interestingly to us, the sulphonic acid group can be released using mild conditions.

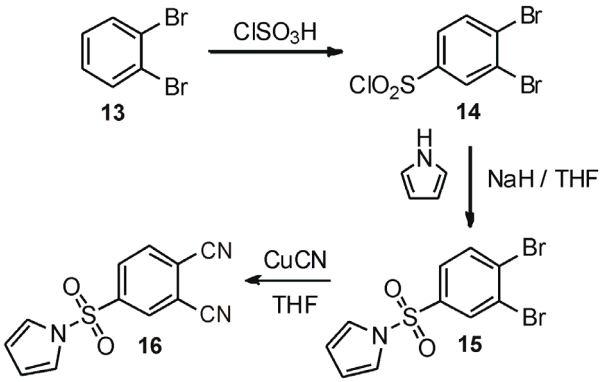

Scheme 3.5 Synthesis of precursor **16** for the Pc-TAP hybrid formation

First, treatment of 1,2-dibromobenzene **13** with chlorosulfonic acid afforded pure 3,4-dibromobenzenesulfonyl chloride **14** after purification by distillation. In the next step, freshly distilled pyrrole was firstly treated with NaH in THF solution to form the sodium derivative, which then reacted with **14** at room temperature to give 1-(3,4-dibromophenylsulfonyl)pyrrole **15**. The dibromosulfonamide **15** was readily converted via Rosenmund – von Braun reaction using CuCN in DMF to the desired phthalocyanine precursor 1-(3,4-dicyanophenylsulfonyl)pyrrole **16**.

Compound **16** and **4** were used as precursors for the formation of the A_3B-type phthalocyanine **17** (Scheme 3.6). The cyclization reaction was performed using a 3:1 statistical mixture of reactants in 1-butanol solution containing magnesium butoxide. The reaction crude was treated with acetic acid to induce demetallation and formation of the free-base Pc-TAP hybrid. Column chromatography purification allowed the isolation of OETAP **5** and the monosulfonamide hybrid ligand **17.**

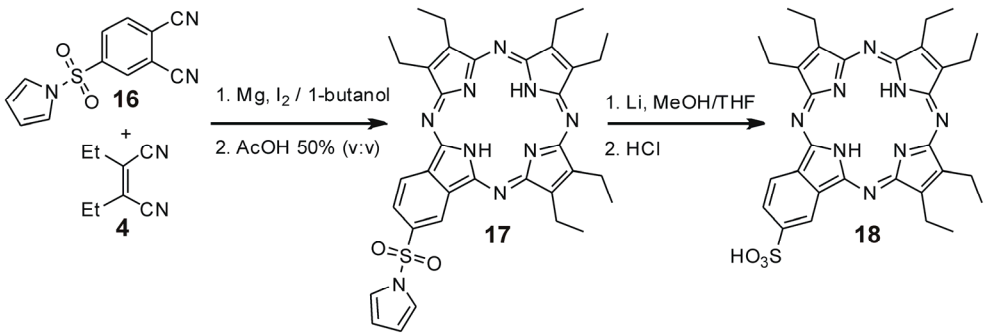

Scheme 3.6 Synthesis of the monosulfonated TAP-Pc hybrid **18**

The detection of signals corresponding to the pyrrole protons in the ^{1}H NMR spectrum of **17** indicated that the sulfonamide group survived the demetallation conditions. As expected, three sharp aromatic signals were observed. The characteristic signal for the NH protons of the azaporphyrin macrocycle was detected in the high upfield region of the spectrum. Finally, the sulfonamide group was removed by reaction of the monosulfonamide hybrid **17** with lithium followed by hydrochloric acid treatment to yield the desired monosulfonate TAP-Pc hybrid **18**.

In the same way, tetrasubstituted Pcs with sulfonamide groups were obtained by cyclotetramerization of the precursor **16** in 1-butanol solution containing magnesium butoxide. The reaction crude was treated with acetic acid to induce demetallation and formation of the free-base which was purified by silica column chromatography. As expected, the reaction output was a mixture of four different constitutional isomers. The deprotection of the sulfonamide groups to yield the desired tetrasulfonated phthalocyanine

20 was successfully achieved by reaction of lithium in a methanol:tetrahydrofurane solution of **19** followed by hydrochloric acid treatment (Scheme 3.7).

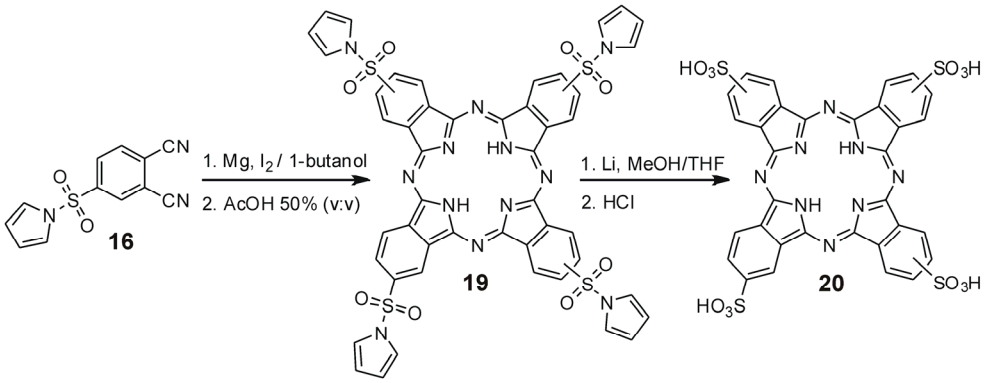

Scheme 3.7 Synthesis of tetrasulfonate substituted phthalocyanine **20**

The ^{1}H NMR spectrum of **20** in *d*-DMSO, clearly displayed three different multiplet signals for the aromatic protons that were in agreement with the reported spectroscopic data for this compound. It is worth noting that these signals appeared as multiplets due to the different isomers formed during the cyclization reaction.

All the metallation attempts using macrocycles **17**, **18**, **19** and **20** and $Ln(OAc)_3 \cdot H_2O$ lanthanide salts (Ln = Tb and Y) did not produce the desired double-decker sandwich complexes. However, when sulfonamide substituted dinitrile **16** was used as starting material, the cyclization in the presence of the corresponding lanthanide salt produced the corresponding $[Ln(Pc)_2]$ double-decker complex **21**. The metallation reaction affording double-decker sandwich **21** was accomplished by heating at 160 ºC a mixture of sulfonamide substituted dinitrile **16,** the corresponding lanthanide acetate salt and DBU dissolved in 1-hexanol (Scheme 3.8). After column chromatography purification we were able to remove the non-reacted starting material and isolate the pure desired products **21** and **22** in 12 and 14 % yields for the terbium and yttrium derivatives respectively.

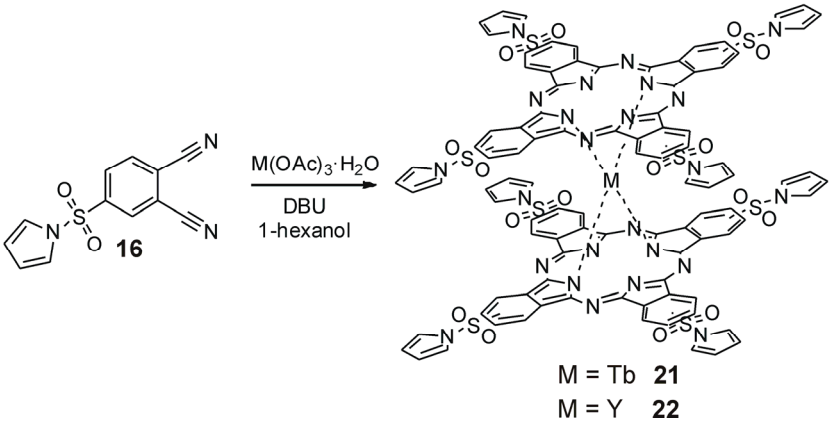

Scheme 3.8 Double-decker sandwich reaction conditions to form **21** and **22**

The MALDI-TOF mass spectra of complexes **21** and **22** showed an isotopic cluster due to the formation of the radical cation [$M^{+\bullet}$]. It can be seen that the isotopic distribution patterns are in good agreement with the corresponding simulated patterns (Figure 3.34).

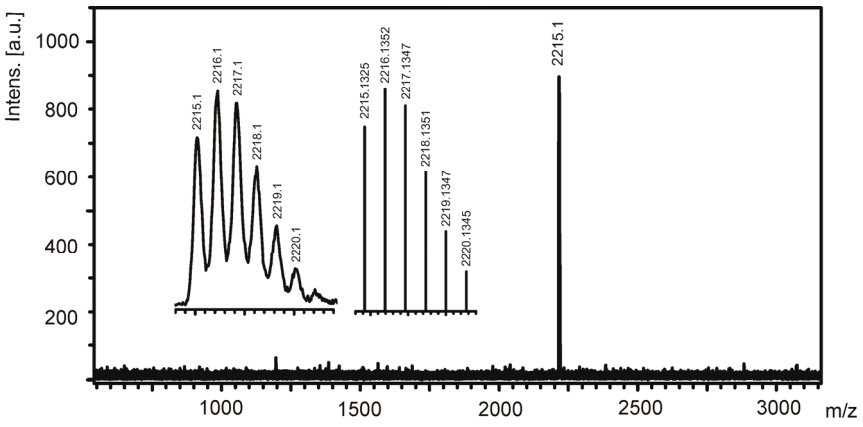

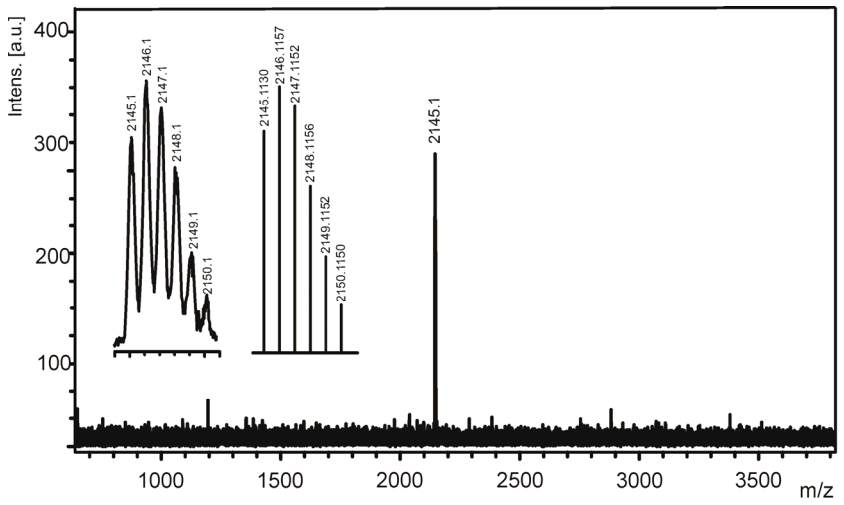

Figure 3.34 Experimental MALDI-TOF mass spectrum and simulated isotopic pattern (inset) for [$M^{+\bullet}$] of **21** and **22**. The used ionization method was matrix-assisted laser desorption/ionization (MALDI) with positive ion mode detection and using trans-2-[3-(4-tert-Butylphenyl)-2-methyl-2-propenylidene]malononitrile as matrix. The samples were prepared using as solvent mixture methanol and dichloromethane.

The final deprotection of the sulfonamide to afford the desired sulfonated terbium double-decker was achieved by treatment of **21** with lithium methoxide in THF-MeOH solution (Scheme 3.9).

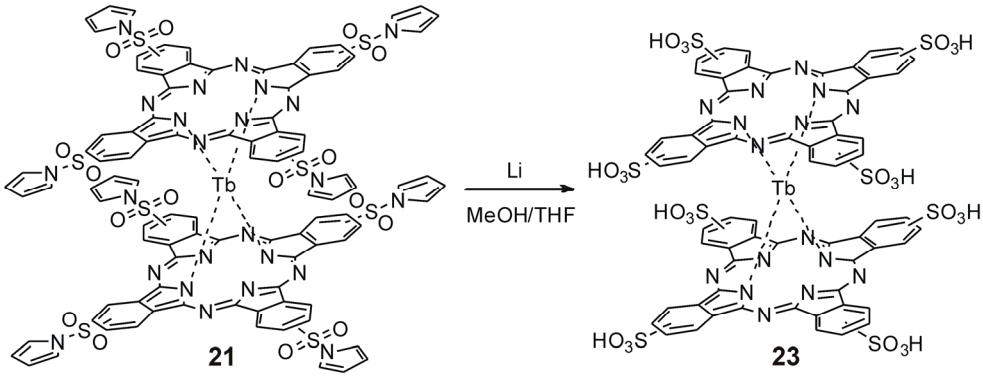

Scheme 3.9 Deprotection of sulfonamide groups to achieve terbium sulfonate double-decker sandwich **23**

The MALDI-TOF mass spectra in negative mode of complex **23** showed an isotopic cluster due to the formation of the radical anion [$M^{-\bullet}$]. It can be seen that the isotopic distribution patterns are in good agreement with the corresponding simulated patterns (Figure 3.35).

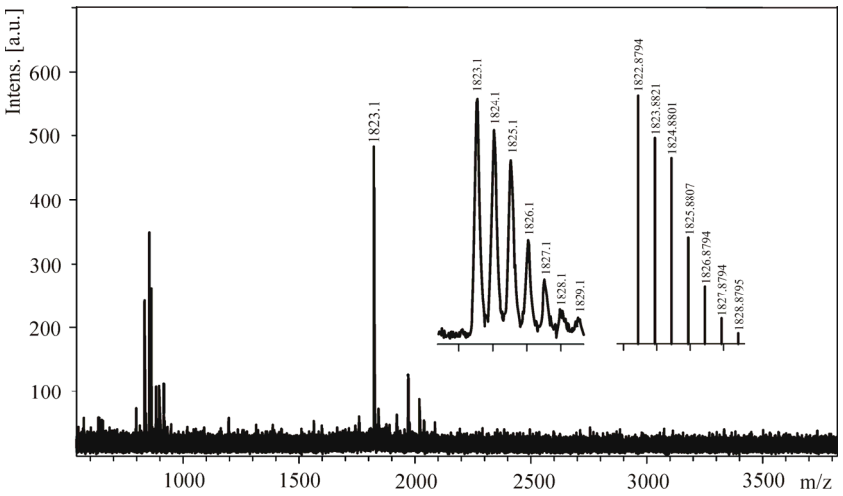

Figure 3.35 Experimental MALDI-TOF mass spectrum and simulated isotopic pattern (inset) for [$M^{-\bullet}$] of **23**. The used ionization method was matrix-assisted laser desorption/ionization (MALDI) with negative ion mode detection and using 2,5-dihydroxybenzoic acid in methanol as matrix. The samples were prepared using water as solvent.

The single-molecule magnet behavior of sulfonated double-decker derivative **23** was studied. Figure 3.36 shows the result of ac susceptibility measurements on a powder sample of homoleptic neutral Tb^{III}bis(phthalocyanine) **23** in different ac magnetic-field frequencies. The thermal dependence of the ac magnetic susceptibility of compound **23** shows a non-zero out-of-phase susceptibility (χ_m'') below 50 K that is related to a decay of the in-phase $\chi'T$ product. Both features clearly show frequency-dependent susceptibilities that suggests superparamagnetic behavior typical in single-molecule magnets.

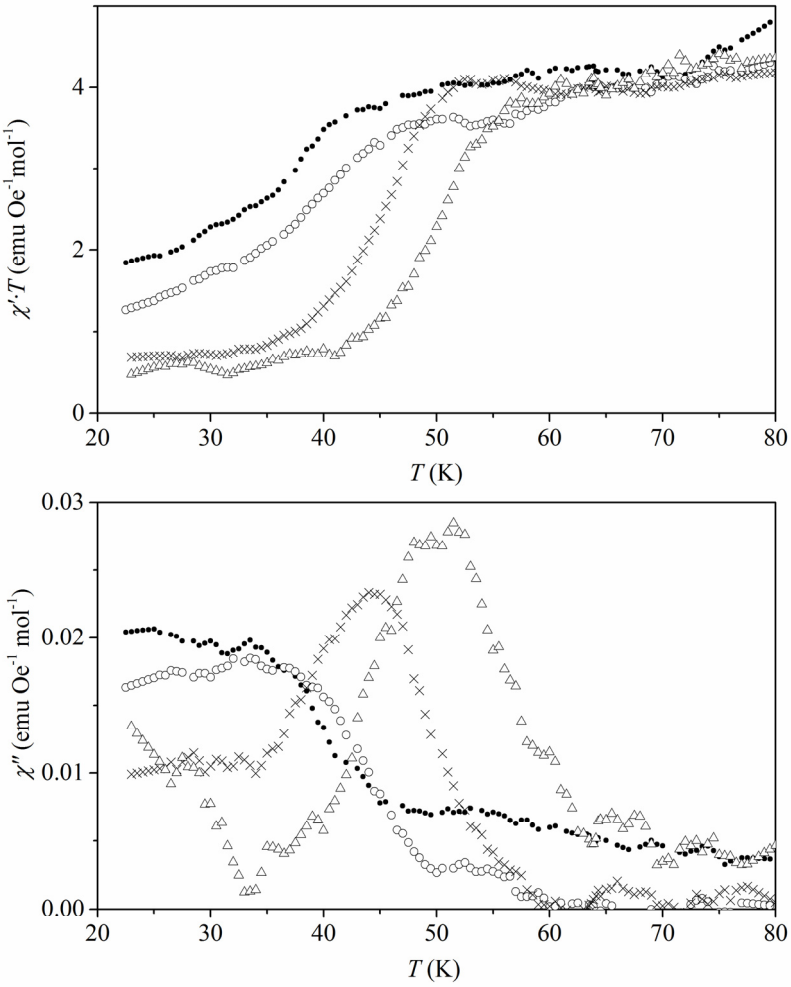

Figure 3.36 Top: In-phase ac susceptibilities for **23** at 3 (●), 13 (○), 133 (×) and 1030 Hz (Δ). Bottom: Out-of-phase ac susceptibilities for **23** at 3 (●), 13 (○), 133 (×) and 1030 Hz (Δ).

3.3.2.3 Synthesis of a terbium double-decker functionalized with chiral substituents

With the view to create novel single-molecule magnets based on chiral sandwich-type phthalocyanine rare earth complexes, we prepared *D*- and *L*-enantiomers of homoleptic bis(phthalocyanine) terbium double-deckers. Specifically, a chiral phthalocyanine substituted with 4 menthol units at the peripheral position of the phthalocyanine ligand was used. The first step for the phthalonitrile precursor synthesis consists on the reaction of the commercially available 4-nitrophthalimide **24** with concentrated aqueous ammonium hydroxide solution to yield 4-nitrophthalamide **25**.[68] In our hands, the reaction for the formation of 4-nitrophthalonitrile **26** did not work when the described synthetic procedure was used.[69] For this reason, alternative conditions were tested. The treatment of a DMF solution of **25** with thionyl chloride afforded the desired product **26** in excellent yield. The synthesis of the menthol substituted phthalonitrile **28** was accomplished following an established synthetic procedure.[70] Commercially and enantiomerically pure menthol **27** and 4-nitrophthalonitrile **26** were treated with potassium carbonate in DMF solution at 80ºC to produce the desired phthalocyanine precursor **28** in 24% yield after silica gel chromatography purification (Scheme 3.10).

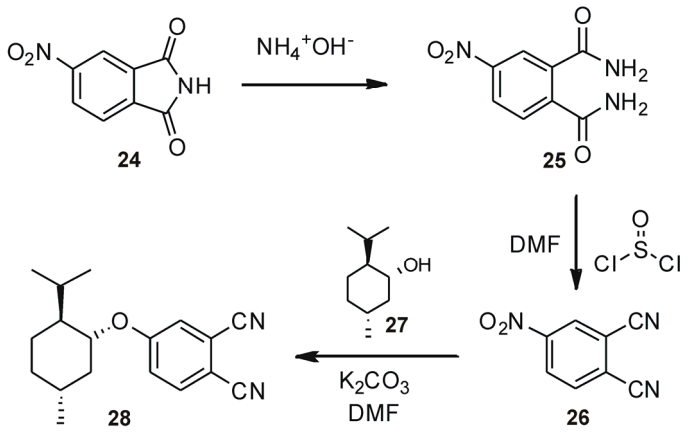

Scheme 3.10 Synthetic route to prepare menthol-substituted dinitrile precursor **28**

The cyclic tetramerization of enantiomerically pure phthalonitrile precursor **28** was accomplished by metal template reaction using magnesium butoxide (prepared *in situ* by placing dry magnesium turnings and iodine in previously dried butanol) followed by demetallation by treatment with sulfuric acid to yield the two enantiomers of the free base chiral phthalocyanine **29** (Scheme 3.11)

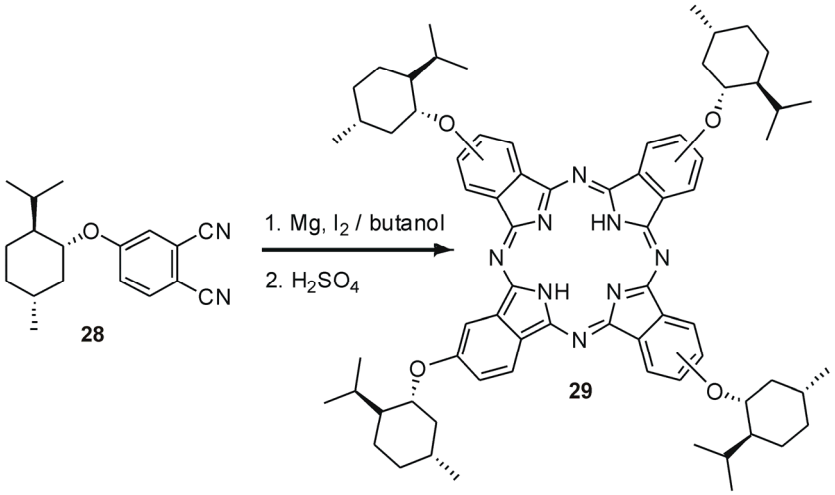

Scheme 3.11 Cyclization reaction conditions to form chiral phthalocyanine **29**

It is worth noting that due to the random location at the peripheral positions of the phthalocyanine ring of four 2-isopropyl-5-methylcyclohexoxyl substituents, both enantiomers are actually a mixture of constitutional stereoisomers with different molecular symmetry.

The ^{1}H NMR spectra of **29** in chloroform solution showed the expected three aromatic signals from the isoindole moieties of the phthalocyanine ring and the aliphatic signals belonging to the menthol units. Those ^{1}H NMR signals appeared as a multiplet signals probably due to the formation of the four possible constitutional isomers during the reaction. Additionally, the diagnostic signal of the NH core of the phthalocyanine ring was detected in the upfield region of the ^{1}H NMR spectrum (-0.87 ppm) due to the ring-current effect of the aromatic macrocycle.

The chiral phthalocyanine **29** was also characterized by means of MALDI-TOF mass spectroscopy. Clear signals for the molecular ion [$M^{+\bullet}$] were observed with an isotopic pattern that closely resembled the simulated one.

Both (*D)* and (*L)* enantiomers of the target homoleptic bis(phthalocyanine) terbium double-decker complex **30**, were synthesized from the metal free derivative **29** in the presence of terbium acetate, tetrabutylammonium benzoate and DBU in hexanol solution under microwave radiation (250 ºC) for 10 minutes. After column chromatography purification the products were obtained in 19 % yield.

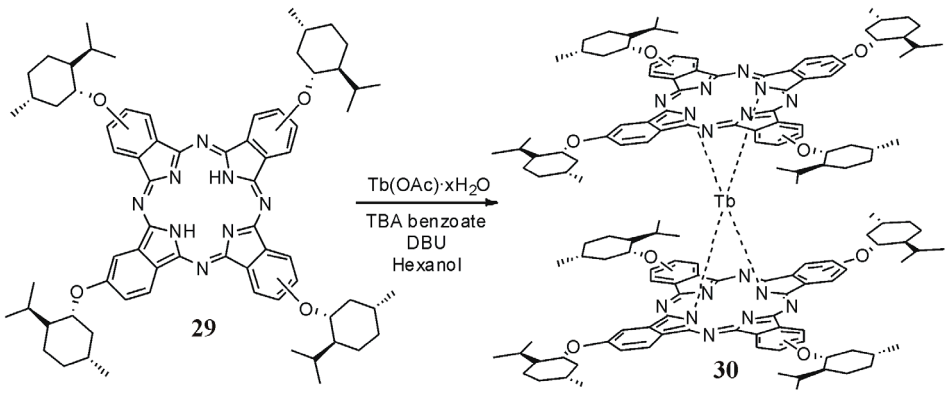

Scheme 3.12 Reaction conditions to produce double-decker **30**

Unfortunately no clear ^{1}H NMR signals were detected for compound **30** in chloroform solution, even after the *in situ* reduction of the neutral double-decker using hydrazine hydrate. The anionic counterparts of the double-decker complex are still paramagnetic owing to the presence of unpaired electron spins in the molecular orbitals at the metal center which may result in the observation of broad NMR signals.

Compound **30** was characterized by MALDI-TOF mass spectroscopic method. The mass spectra clearly showed intense signal for the molecular ion [$M^{+\bullet}$] with an isotopic pattern that closely resembled the simulated one as exemplified in the spectrum of **30** shown in Figure 3.37.

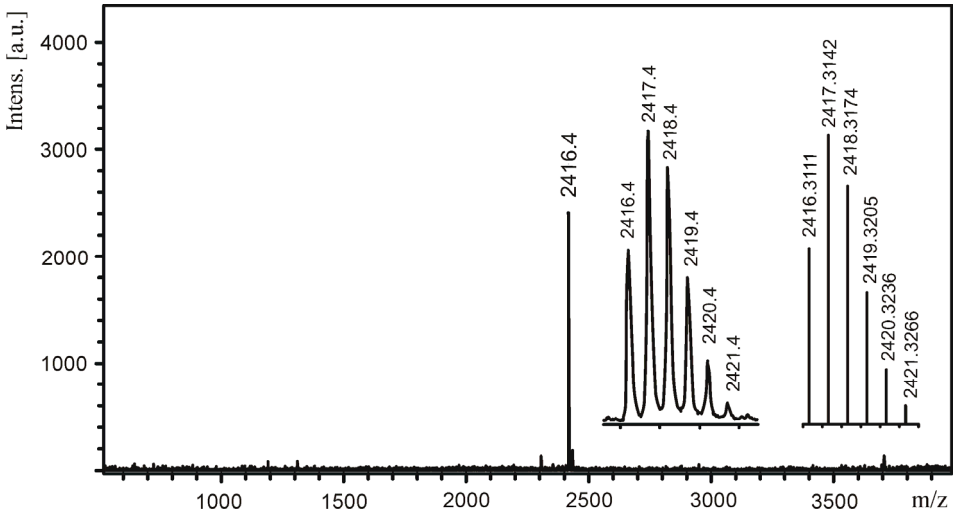

Figure 3.37 Experimental MALDI-TOF mass spectrum and simulated isotopic pattern (inset) for [$M^{+\bullet}$] of **30**. The used ionization method was matrix-assisted laser desorption/ionization (MALDI) with positive ion mode detection and using trans-2-[3-(4-tert-Butylphenyl)-2-methyl-2-propenylidene]malononitrile as matrix. The samples were prepared using dichloromethane as solvent.

The monomeric metal-free (*L*)- and (*D*)-**29** (H_2Pc) showed no CD signal in the whole electronic absorption region due to the lack of effective asymmetrical perturbation of the chiral menthol units.[71] However, the two enantiomerically pure double-deckers prepared, (*L*)- and (*D*)-**30**, displayed bisignated CD spectra in dichloromethane solution, as can be seen in Figure 3.38. Perfect mirror CD signals were observed along the Soret and Q absorption regions of the phthalocyanine ligand. The CD signal observed implied the effective chiral information transfer from the peripheral chiral menthol side chains to the phthalocyanine chromophore at the molecular level.

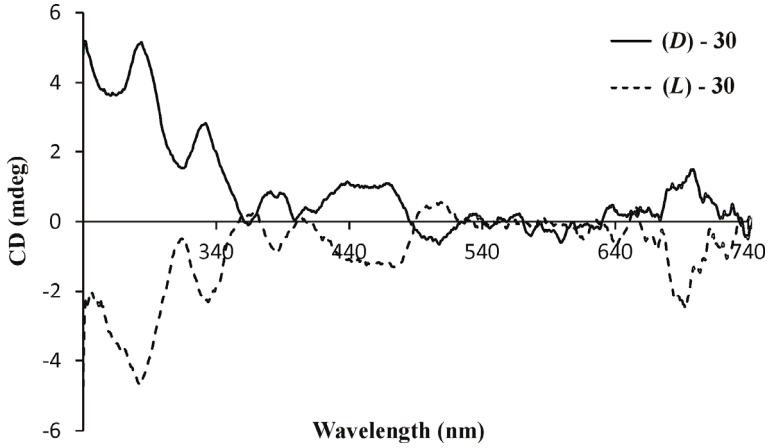

Figure 3.38 Circular dichroism (CD) spectra of the Soret and Q absorption regions along the whole absorption spectrum of enantiomers (*L*)-**30** and (*D*)-**30** in dichloromethane solution showing perfect mirror images

The electrochemical behavior of the homoleptic bis(phthalocyanine) terbium double-decker **30** was investigated by cyclic voltammetry (CV) in CH_2Cl_2 solution (Figure 3.39). Two reversible one-electron redox processes are detected with half-wave potentials centered at $E_{1/2}$ = 334 and -92 mV, respectively. All the processes can be attributed to the successive removal or addition of one electron to the ligand-based orbitals, as the oxidation state of the central Tb^{3+} metal atom in the double-decker complex does not change. We assigned the redox wave at 334 mV to the one-electron oxidation process that converts the neutral mono-radical double-decker, [Tb(**29**)$_2$], into a formal diradical cationic species [Tb(**29**)$_2$]$^+$. On the other hand, the electron wave at -92 mV must correspond to the reduction of the neutral double-decker radical to the anion species [Tb(**29**)$_2$]$^-$.

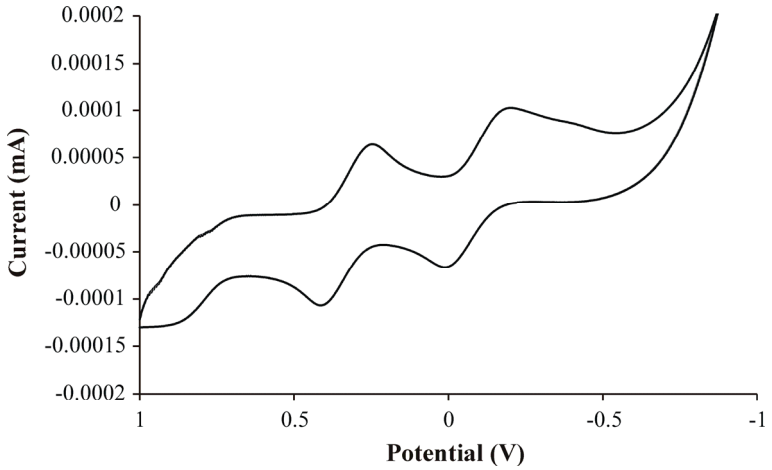

Figure 3.39 Cyclic voltammograms for compound **30** in CH_2Cl_2 solution containing $TBA^+PF_6^-$ as electrolyte showing the two reversible one-electron redox processes. The reported potentials are referenced to Ag/AgCl electrode

We also investigated the spectroelectrochemical behavior of [Tb(**29**)$_2$] to identify the spectroscopic features of the radical anion [Tb(**29**)$_2$]$^-$ and the cation [Tb(**29**)$_2$]$^+$ upon electrochemical reduction and oxidation of the former, respectively (Figure 3.40). Application of a potential of -0.8 V to a green methylene chloride solution of [Tb(**29**)$_2$] afforded the formation of the radical anion [Tb(**29**)$_2$]$^-$ with the consequent change in the UV-Vis spectrum (increase and bathochromic shift of the Soret bands and a decrease in intensity of the Q band centered at 685 nm). The electrochemical reoxidation of the anion to the neutral radical [Tb(**29**)$_2$] proceeded uneventfully when a potential of 100 mV was applied to the solution above. Conversion of the neutral radical to the cation species [Tb(**29**)$_2$]$^+$ was achieved applying a positive potential of +0.8 V. The methylene chloride solution of the radical cation displayed a distinguished UV-vis spectrum with an increase in intensity of the Soret bands centered at 331 and 361 nm, and the appearance of a new absorption band centered at 474 nm. Electrochemical reduction of [Tb(**29**)$_2$]$^+$ by applying a potential of 0.1 V regenerated the neutral radical. The results obtained in the spectroelectrochemical experiments testify the high stability of the different oxidation states of the double-decker complex.

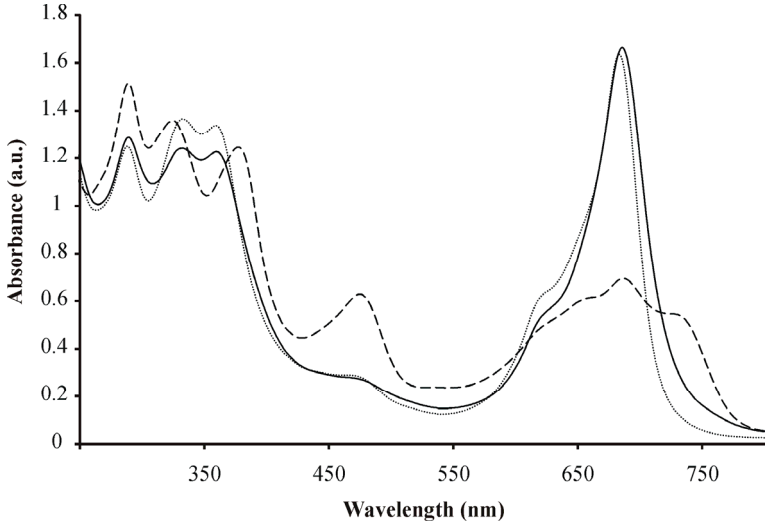

Figure 3.40 Spectroelectrochemistry experiments of **30** showing the UV-vis absorption spectra of the three different species in solution: neutral (—), anionic (····) and cationic species (– –)

Alternating current magnetic-susceptibility measurements were performed on a powdered sample of compound **30** in different ac magnetic-field frequencies (Figure 3.41). There is a clear frequency-dependent out-of-phase signal (χ'') at low temperatures. A maximum was observed at frequencies from 13 to 1030 Hz in the out-of-phase signal when the temperature decreases. This maximum has a notable temperature dependence and varies from 48 K at a frequency of 1030 Hz to 35 K at 13 Hz. Below this frequency, the maximum becomes a shoulder, owing to a sharp increase in χ'' at low temperatures, which corresponds to the region in which the quantum-tunneling effects become dominant.

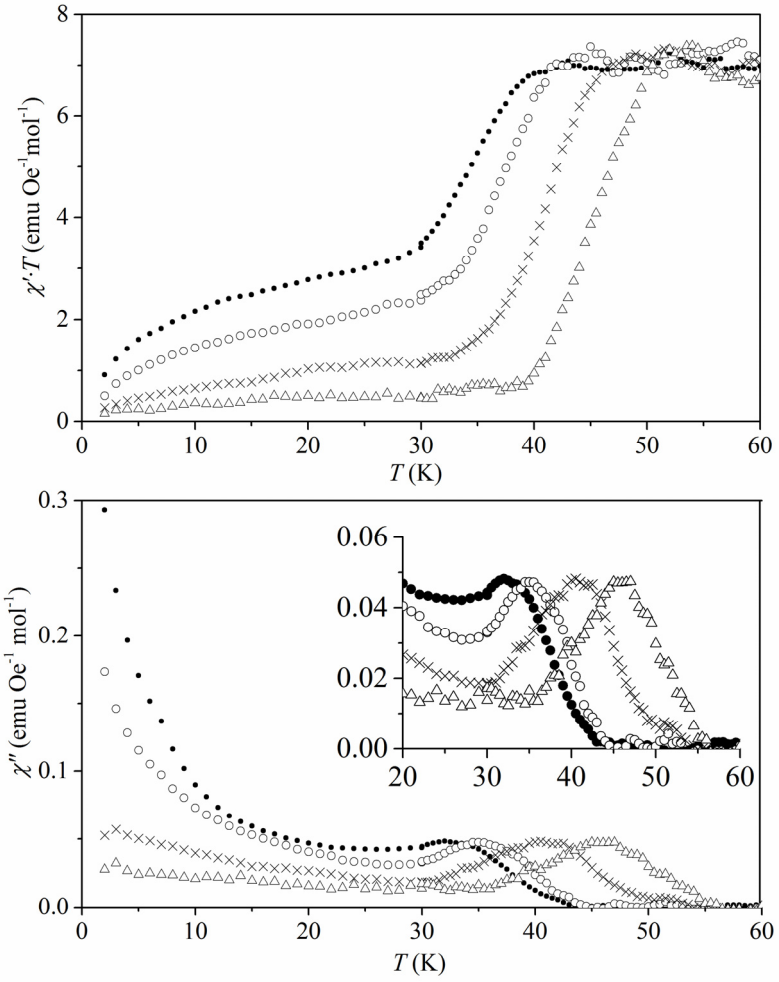

Figure 3.41 Top: In-phase ac susceptibilities for **30** at 3 (●), 13 (○), 133 (×) and 1030 Hz (Δ). Bottom: Out-of-phase ac susceptibilities for **30** at 3 (●), 13 (○), 133 (×) and 1030 Hz (Δ).

3.4 Conclusions

In conclusion, we have prepared and characterized a new family of neutral double-decker complexes by means of the combination of a tetraazaporphyrin and lanthanides. Similarly to the series of phthalocyanine analogs, the D_{4d} symmetry promoted by the $(N_4)_2$ coordination geometry induced single-molecule magnet behavior in the Tb and Dy derivatives, with blocking temperatures very close to those of their phthalocyanine counterparts. Notably, the synthesized complexes feature very high activation energies of magnetization reversal, as determined by magnetic data.

These double-decker complexes, in contrast with their phthalocyanine counterparts, are highly soluble in nonpolar organic solvents and they can be conveniently sublimed under relatively mild conditions. This easy processing opens the way for the incorporation of these single-molecule magnets into nanostructures through typical procedures such as dip coating, spin coating, and ultra-high vacuum techniques, thereby allowing the study and manipulation of individual single-molecule magnets.

On the other hand, we have synthesized and characterized different lanthanide double-decker complexes using functionalized phthalocyanines as ligands. Firstly, a terbium bis(phthalocyanine) complex decorated with *tert*-butyl groups in the peripheral positions of each phthalocyanine ring was prepared. This functionalization provides better solubility of the resulting complex in common organic solvents. Secondly, double-decker complexes functionalized with sulfonate groups were successfully synthesized and characterized. This functionality provides solubility of the newly prepared complexes in aqueous media. Finally, chiral menthol moieties were used to functionalize the phthalocyanine ligand prior the metallation reaction to afford the final terbium double-decker structure. This complex will be used to study in the future the synergy between magnetic and optical properties such as the magneto chiral dichroism effect. The single-molecule magnet behavior of the newly prepared complexes has been proved by means of magnetic susceptibility measurements showing blocking temperatures close to the previously described $TbPc_2$ unfunctionalized derivatives.

3.5 Experimental section

3.5.1 General information and instrumentation

^{1}H NMR spectra were recorded using a Bruker Avance 300 (300 MHz for ^{1}H NMR spectroscopy), a Bruker Avance 400 (400 MHz for ^{1}H NMR spectroscopy), or a Bruker Avance 500 (500 MHz for ^{1}H NMR spectroscopy) ultrashield spectrometer. The deuterated solvents (Aldrich) used are indicated and chemical shifts are given in ppm. For $CDCl_3$ the peaks were referenced relative to the solvent residual peak δ_H = 7.26 ppm and δ_C = 77.0 ppm. All NMR *J* values are given in Hz. Mass spectra were obtained on an Autoflex Bruker Daltonics MALDI-TOF Mass Spectrometer. Flash column chromatography was performed with Silica gel Scharlab60 or Aluminium oxide 90 active neutral (active stage I) 70-230 mesh. High-resolution mass spectra were obtained using a Bruker Autoflex MALDI-TOF mass spectrometer. HPLC analysis was performed with an Agilent 1100 series HPLC equipped with a Waters Sunfire C18 (5µm 4.6x100mm) column using a diode array detector with single wavelength detection at 300 nm. HPLC semipreparative purification was carried out using a Delta 600 Waters Semi-preparative HPLC equipped with a Waters Sunfire Prep C18 OBD (5µm 19x100mm) column and a Waters 2487 UVVIS detector recording at 300 nm. UV/Vis measurements were carried out using a Shimadzu UV-2410PC spectrophotometer equipped with a photomultiplier detector, double-beam optics, and D2 and W light sources. Cyclic voltammetry (CV) experiments and control potential electrolysis were performed using a BASi Epsilon potentiostat connected to a C3 standard electrochemical cell that consisted of a Pt gauche working electrode, a Pt wire counter electrode, and a Ag/AgCl reference electrode. Circular Dichroism spectra measurements were carried out on an Applied Photophysics Chirascan Circular Dichroism spectrometer equipped with a photomultiplier detector, dual polarizing prism design monochromator, photo-elastic modulator (PEM) and 150W Xenon light source. Magnetic susceptibility measurements (dc and ac) on grained single crystals were performed using a Quantum Design MPMS-XL-7·SQUID magnetometer in the 2–300 K range under an applied direct current (dc) magnetic field between 0 and 7 T, and under an applied alternative current (ac) magnetic field of 3.9×10^{-4} T with frequencies between 1 and 1500 Hz. Pascal's constants

were used to estimate the diamagnetic corrections for the compounds. Powder X-ray diffraction (PXRD) data were collected using a D8 Advance Series 2q/q powder diffractometer at room temperature. EPR measurements in the solid state were performed at the Unitat de Mesures Magnètiques (Universitat de Barcelona) and registered at the X-band (9.4 GHz) frequency using a Bruker ESP-300E spectrometer at room temperature.

Single crystals were mounted on a tip of a Kapton cryoloop immersed in perfluoropolyether as protecting oil for manipulation. Crystal data was collected using an Apex DUO Kappa 4-axis goniometer equipped with an APPEX 2 4K CCD area detector, a Microfocus Source E025 IuS using Mo_{Ka} radiation (λ = 0.71073 Å), a Quazar MX multilayer Optics as monochromator and a Cryostream 700 plus low-temperature device (T = 100 K) from Oxford Cryosystems. Crystal structure determination was carried out using a Bruker–Nonius diffractometer equipped with an APPEX 2 4K CCD area detector, a FR591 rotating anode with Mo_{Ka} radiation, Montel mirrors as monochromator, and a Cryostream 700 plus low-temperature device from Oxford Cryosystems. Full-sphere data collection was used with ω and ϕ scans.

All solvents were obtained from commercial sources and used without further purification with the exception of THF, which was distilled from blue ketyl (sodium and benzophenone), DMF that was dried over 4 Å MS; and $CHCl_3$ that was dried over $CaCl_2$ and distilled. All used reagents were commercially available and used as received.

3.5.2 Synthetic procedures

Synthesis of (E)-3,4-dibromohex-3-ene (2)

Bromine (9.41 ml, 183 mmol) in 60 ml of acetic acid (96%) was added dropwise using a dropping funnel into a stirred solution of 3-hexyne (15 g, 183 mmol) in 60 ml of acetic acid (96%). The reaction mixture turned brown when a drop of bromine was added and after a few seconds it decolored. After the addition the reaction mixture was poured into water (80 ml), extracted with pentane (3 x 50 ml), washed with $NaHCO_3$ (2 x 50 ml) and dried with $MgSO_4$. The solvent was removed on the rotary evaporator to give 37.8123 g of a non-color liquid. Purification of the reaction crude was accomplished using a regular distillation apparatus (60ºC, 3mbar) to isolate the pure product in a 84 % yield.

^{1}H NMR (300 MHz, $CDCl_3$, 25 ºC) δ (ppm) 2.67 (q, J = 7.3 Hz, 4H, $C\underline{H}_2CH_3$) 1.11 (t, J = 7.3 Hz, 6H, CH_3),
^{1}H NMR spectrum of this compound is in agreement with that reported in the literature[62]

Synthesis of 2,3-diethylfumaronitrile (3)

A 250 ml twin-neck round bottom flask, fitted with a magnetic stirred and a condenser was dried and argon purged. Once water was removed, Cooper (I) cyanide (18.51 g, 207 mmol, 2.5 eq) was dissolved in freshly dry DMF (85 ml). The stirred mixture was heated to reflux (153ºC) for 1 h and then allowed to cool to r.t. under argon atmosphere. Then, when the temperature of the oil bath was stabilized at 130ºC, (E)-3,4-dibromohex-3-ene (20 g, 83 mmol) was added and heated for 18 h. Temperature control is critical in this reaction because heating t the reflux temperature causes catastrophic decreases in yield. The cooled mixture was poured into 6M aq. NH_3 (600 ml); the resulting deep blue solution was stirred for 1 h and then vacuum filtered. The precipitate was washed with Et_2O (3 x 50 ml) and the filtrate was extracted with Et_2O (3 x 100 ml). All the ether portions were combined, washed once with water (100 ml), once brine (100 ml), dried with $MgSO_4$, filtered and concentrated under reduced pressure to give 9.96 g of crude. The desired product was purified via

distillation using a glass oven (120ºC, 6mbar, 30 r.p.m) obtaining 8.1 g of pure product (73% yield)

^{1}H NMR (300 MHz, 25 ºC) δ (ppm) 2.56 (q, *J* = 7.5 Hz, 4H, $C\underline{H}_2CH_3$) 1.21 (t, *J* = 7.5 Hz**,** 6H, CH_3)
^{1}H NMR spectrum of this compound is in agreement with that reported in the literature[62]

Synthesis of 2,3-diethylmaleonitrile (4)

2,3-diethylfumaronitrile (4.7 g, 35.1 mmol) was dissolved in 80 ml of acetonitrile. The solution was bubbled degassed with argon for 10 min. and then poured into a Rayonet photochemical chamber reactor using a cannula. The photoreactor was equipped with 254 nm lamps and the reaction mixture was stirred and irradiated for 24 h and then the solvent was removed under reduced pressure. The desired product was distilled off using a glass oven (70ºC, 6mbar, 30 r.p.m.) and then the remaining starting material was recovered at (120ºC, 6mbar, 30 r.p.m.). The product was obtained in a 53% yield.

^{1}H NMR (300 MHz, $CDCl_3$, 25 ºC) δ (ppm) 2.39 (q, *J* = 7.5 Hz, 4H, $C\underline{H}_2CH_3$), 1.22 (t, *J* = 7.5 Hz, 6H, CH_3)
^{1}H NMR spectrum of this compound is in agreement with that reported in the literature[62]

Synthesis of Octaethyltetraazaporphyrin (OETAP) (5)

To a dried twin-neck round bottom flask equipped with a condenser, magnesium (0.453 g, 18.66 mmol, 1 eq) and iodine (2.368 g, 9.33 mmol, 0.5 eq) were refluxed under argon atmosphere in dry butanol (25 ml). Once all magnesium metal was consumed, the solution was allowed to cool to r.t. and then 2,3-diethylmaleonitrile (2.5 g, 18.66 mmol, 1 eq) was added and heated back to the reflux temperature for 18 h. The cooled solution was dissolved in ethanol (200 ml) and then water (800 ml) was added and the resulting precipitate was collected by vacuum filtration using polycarbonate membrane filters. This precipitate was extracted with chloroform (200 ml) using a Soxhlet extractor for 24h. Removal of the solvent followed by column chromatography of the resulting residue using CH_2Cl_2/Et_2O (10:1) as eluent afforded crude magnesium octaethyltetraazaporphyrin (0.487

g). Removal of magnesium from the extract octaethyltetrazaporphyrin is accomplished by heating at reflux temperature (65ºC) in a $CHCl_3$/AcOH (20:1) solution (210 ml) for 15 min. The cooled violet solution is poured into water (200 ml) which is made basic by the addition of NaOH pellets. The organic layer is separated, washed once with 5% NaOH (50 ml), dried (Na_2SO_4) and filtered. The tetraazaporphyrin is adsorbed onto silica gel by suspending silica gel in the filtrate and removing the solvent on a rotary evaporator. The coated silica gel is loaded onto a silica gel column and eluted with CH_2Cl_2/hexane (1:1). The solvents were removed under reduced pressure to give 267 mg of the pure product (12% yield)

^{1}H NMR (300 MHz, $CDCl_3$, 25 ºC) δ (ppm) 3.97 (q, *J* = 7.6 Hz, 16H, $C\underline{H}_2CH_3$), 1.86 (t, *J* = 7.6 Hz, 24H, CH_3), -2.36 (s, 2H, NH)
UV-vis (CH_2Cl_2): λ_{max} (nm) (logε) = 336 (4.9), 556 (4.6), 598 (3.9), 624 (4.9).
MALDI-TOF MS: calcd: 538.35 m/z, found: 538.4 m/z
IR $\tilde{\nu}$ (cm^{-1}) 3296 s; 2962 s; 2929 s; 2868 s; 1460 s.
All the spectroscopic data of this compound are in agreement with those reported in the literature.[62]

Synthesis of [Tb(OETAP)$_2$] (6)

A solution of octaethyltetraazaporphyrin (20.00 mg, 0.037 mmol, 2 equiv) in hexanol (2 mL) was added to a microwave vial. $Tb(OAc)_3 \cdot H_2O$ (6.60 mg, 0.02 mmol, 1 equiv), tetrabutylammonium benzoate (6.75 mg, 0.02 mmol, 1 equiv), and DBU (0.1 mL, 0.67 mmol) were added to the purple solution. The tube was sealed and the reaction mixture was heated to 250ºC in a Biotage Initiation Microwave Synthesizer for 10 min. The solvent was partially removed under reduced pressure, and then the blue crude material was dissolved in freshly distilled dichloromethane (10 mL) and washed once with citric acid solution (30 mL) and once with water (30 mL). The organic layer was separated, dried with Na_2SO_4, filtered, and concentrated on a rotary evaporator. This crude material was passed through a neutral alumina column with CH_2Cl_2 (collecting the blue fraction) before proceeding with the HPLC purification. A solution (10 $mg \cdot mL^{-1}$) of the blue fraction was prepared using

THF/H_2O (60:40) and then filtered through a 0.45 mm pore size filter. This solution (1 mL) was manually injected at a 10 mLmin_1 flow rate to a Delta 600 Waters semipreparative HPLC, with a Waters Sunfire Prep C18 OBD (5 µm, 19 × 199 mm) column. The elution was performed with a linear gradient THF/H_2O 50:50 to THF/H_2O 80:20 for 7 min, and then the 80:20 mixture was maintained for seven additional minutes. The peak at 12.5 min corresponded to the pure desired product, which was isolated in 31% yield after solvent evaporation.

^{1}H NMR (300 MHz, $CDCl_3$, 25ºC): δ = –27.1 (s, 48H; CH_2CH_3), –60.4 (s, 16H; $CH_aCH_bCH_3$), –75.4 ppm (s, 16H; $CH_aCH_bCH_3$)
UV/Vis (CH_2Cl_2): λmax = 322, 595 nm
MALDI-TOF MS: *m/z* (%): 1232.6 $[M+H]^+$ (100).

Synthesis of [Dy(OETAP)$_2$] (7)

A solution of octaethyltetraazaporphyrin (20.00 mg, 0.037 mmol, 2 equiv) in hexanol (2 mL) was added to a microwave vial. $Dy(OAc)_3 \cdot H_2O$ (6.70 mg, 0.02 mmol, 1 equiv), tetrabutylammonium benzoate (6.75 mg, 0.02 mmol, 1 equiv), and DBU (0.1 mL, 0.67 mmol) were added to the purple solution. The tube was sealed and the reaction mixture was heated to 250ºC in a Biotage Initiation Microwave Synthesizer for 10 min. The solvent was partially removed under reduced pressure, and then the blue crude material was dissolved in freshly distilled dichloromethane (10 mL) and washed once with citric acid solution (30 mL) and once with water (30 mL). The organic layer was separated, dried with Na_2SO_4, filtered, and concentrated on a rotary evaporator. After semipreparative HPLC separation using the exact same chromatographic conditions as for **6**, the pure product was obtained in 36% yield.

^{1}H NMR (300 MHz, $CDCl_3$, 25ºC): δ = –13 (s, 48H; CH_2CH_3), –26 (s, 16H; $CH_aCH_bCH_3$), –32 ppm (s, 16H; $CH_aCH_bCH_3$)

MALDI-TOF MS: *m/z* (%): 1237.6 $[M+H]^+$ (100).

Synthesis of [Gd(OETAP)$_2$] (8)

A solution of octaethyltetraazaporphyrin (20.00 mg, 0.037 mmol, 2 equiv) in hexanol (2 mL) was added to a microwave vial. $Gd(OAc)_3 \cdot H_2O$ (6.65 mg, 0.02 mmol, 1 equiv), tetrabutylammonium benzoate (6.75 mg, 0.02 mmol, 1 equiv), and DBU (0.1 mL, 0.67 mmol) were added to the purple solution. The tube was sealed and the reaction mixture was heated to 250ºC in a Biotage Initiation Microwave Synthesizer for 10 min. The solvent was partially removed under reduced pressure, and then the blue crude material was dissolved in freshly distilled dichloromethane (10 mL) and washed once with citric acid solution (30 mL) and once with water (30 mL). The organic layer was separated, dried with Na_2SO_4, filtered, and concentrated on a rotary evaporator. After semipreparative HPLC separation using the exact same chromatographic conditions as for **6**, the pure product was obtained in 39% yield.

MALDI-TOF MS: *m/z* (%): 1231.8 $[M+H]^+$ (100).

Synthesis of [Y(OETAP)$_2$] (9)

A solution of octaethyltetraazaporphyrin (20.00 mg, 0.037 mmol, 2 equiv) in hexanol (2 mL) was added to a microwave vial. $Y(OAc)_3 \cdot H_2O$ (6.6 mg, 0.02 mmol, 1 equiv), tetrabutylammonium benzoate (6.75 mg, 0.02 mmol, 1 equiv), and DBU (0.1 mL, 0.67 mmol) were added to the purple solution. The tube was sealed and the reaction mixture was heated to 250ºC in a Biotage Initiation Microwave Synthesizer for 10 min. The solvent was partially removed under reduced pressure, and then the blue crude material was dissolved in freshly distilled dichloromethane (10 mL) and washed once with citric acid solution (30 mL) and once with water (30 mL). The organic layer was separated, dried with Na_2SO_4, filtered, and concentrated on a rotary evaporator. After semipreparative HPLC separation using the exact same chromatographic conditions as for **6**, the product could be further purified by recrystallization from acetonitrile and was obtained in 63% yield.

MALDI-TOF MS: *m/z*: 1161.6 $[M-e^-]+$, 1162.6 $[M+H]^+$, 1163.6 $[\{Y(OETAP^{2-})_2 + e^-\}^- + 2H]^+$.

Synthesis of tetrakis(t-butyl)-phthalocyanine (11)

To a dried 5 mL round bottom flask equipped with a condenser, Mg (14 mg), dry butanol (2 ml) and I_2 (69 mg) were added. This mixture is heated at reflux (120ºC) under Ar until all the Mg metal was consumed. Then the reaction mixture was cooled down and 100 mg of 4-(tert-butyl)phthalonitrile were added. The reaction was left refluxing for 18 h. The crude reaction was dissolved in 10 mL of MeOH and then 15 mL of water were added. The solid obtained was filtered through a syntered filter (nº 4) and washed with water. The precipitate was dissolved in DCM, dried with sodium sulphate, and concentrated. The reaction crude was dissolved in DCM (10 mL) and 10 drops of H_2SO_4 95-97% were added stirring for 10 min. Then it was washed with water, sodium hydrogen carbonate saturated solution, dried with Na_2SO_4 and concentrated. Column chromatography with DCM afforded pure product in 43 % yield.

^{1}H NMR (300 MHz, $CDCl_3$, 25 ºC) δ (ppm) 9.29-8.83 (m, 8H), 8.22-8.09 (m, 4H), 1.90-1.82 (m, 36H), -2.10 (s, 2H).
MALDI-TOF MS: calcd. 738.42 m/z, found 738.5 m/z

Synthesis of $Tb(Pc)_2$ [Pc = tetrakis(t-butyl)-phthalocyanine] (12)

Tetrakis(t-butyl)-phthalocyanine (15 mg, 0.02 mmol, 2 eq), $Tb(OAc)_3 \cdot H_2O$ (9.19 mg, 0.001 mmol, 1 eq), tetrabutylmmonium benzoate (3.69 mg, 0.001 mmol, 1 eq), DBU (0.1 ml) were dissolved in hexanol (2 ml) into a microwave vial. The reaction mixture was heated to 250ºC in a Biotage Initiation Microwave Synthesizer for 10 min. The solvent was partially removed under reduced pressure and then the crude was dissolved in methanol (5 ml) and water (20 ml) was added. The precipitate was filtered through a funnel with glass frit nº3 and washed with water, dried with Na_2SO_4 and concentrated on a rotary evaporator.

Silica column chromatography was used to purify the compound using a mixture of CH_2Cl_2:hexane (1:1) as eluent to recover the starting material and then the eluent mixture was changed to CH_2Cl_2:Hexane (5:1) to obtain the desired pure green product in 48 % yield.

MALDI-TOF MS: calcd. 1632.73 m/z, found 1632.8 m/z
UV/Vis (CH_2Cl_2): λmax = 325, 348, 674 nm

Synthesis of 3,4-dibromobenzenesulfonyl chloride (14)

A solution (-10ºC) of 1,2-dibromobenzene (10.1 g, 42.4 mmol) and freshly dry $CHCl_3$ (30 ml) was cooled to -10ºC using an ice-NaCl bath. Chlorosulfonic acid (15 g) was added over a period of 20 minutes. The light brown solution was stirred at room temperature for 20 h and the reaction mixture turned red during this period. Then, the solution was refluxed for 1h and some precipitate appeared. After cooling to room temperature, the vigorously stirred reaction mixture was poured onto crushed ice (100 g). The aqueous and organic layers were separated and the former was washed with dichloromethane (100 x 2 ml). The combined organic layers were washed with aqueous $NaHCO_3$ (10%, 75 ml) followed by water until neutral pH. After drying over $MgSO_4$ and evaporating the solvent orange oil was obtained. Vacuum distillation (130ºC/5 mbar) afforded 10.2 g of a colorless liquid (71 % yield)

^{1}H NMR (300 MHz, $CDCl_3$, 25 ºC) δ (ppm) 8.26 (d, *J* = 2.11 Hz, 1H), 7.89 (d, *J* = 8.65 Hz, 1H), 7.82 (dd, *J* = 8.65, 2.11, Hz, 1H)
^{1}H NMR spectrum of this compound is in agreement with that reported in the literature[67]

Synthesis of 1-(3,4-dibromophenylsulfonyl)pyrrole (15)

NaH (789 mg, 60% oil dispersion) was poured into a round bottom flask and washed several times with hexane under argon atmosphere. Then, the flask was cooled to 0ºC using an ice bath and fresh distilled pyrrole (1.214 mg) and dry THF (25 ml) were added. After

10 minutes, 3,4-dibromobenzenesulfonyl chloride (5.5 g) was added over 30 minutes period. After stirring at room temperature overnight, the brown reaction mixture was carefully poured into saturated NH_4Cl solution (150 ml) placed in an ice bath. Ether (150 ml) was added and the aqueous layer was washed with ether (120 ml). The combined organic layers were washed with saturated NH_4Cl until neutral pH. After drying over $MgSO_4$ and evaporating the solvent, the crude was recrystallized from ethanol to give 4.5 g of colorless crystalline needles (75 % yield)

^{1}H NMR (300 MHz, $CDCl_3$, 25 ºC) δ (ppm) 8.07 (d, *J* = 2.11 Hz, 1H), 7.74 (d, *J* = 8.62 Hz, 1H), 7.60 (dd, *J* = 8.62, 2.11 Hz, 1H), 7.13 (t, *J* = 2.25 Hz, 2H), 6.34 (t, *J* = 2.25 Hz, 2H),
^{1}H NMR spectrum of this compound is in agreement with that reported in the literature[67]

Synthesis of 1-(3,4-dicyanophenylsulfonyl)pyrrole (16)

In a dry 25 ml two-neck round bottom flask fitted with a magnetic stirrer and a condenser, cooper cyanide (0.613 g, 6.85 mmol) was dissolved in dry DMF (6 ml). The stirred mixture was heated to reflux for 2 h. and then allowed to cool to room temperature. Then, 1-(3,4-dibromophenylsulfonyl)pyrrole (1 g, 2.74 mmol) was added when the temperature of the oil bath was stabilized at 130ºC, and the reaction mixture was heated for 5 h. The crude was cooled to room temperature and then dichloromethane (100 ml) were added and a fine insoluble powder started to precipitate (overnight). After filtration and evaporation of the solvent, the desired product was purified by flash column chromatography using a mixture of dichloromethane:hexane (2:1). Removal of the solvent gave 281 mg of the product (39 % yield)

^{1}H NMR (300 MHz, $CDCl_3$, 25 ºC) δ (ppm) 8.23 (dd, *J* = 1.82, 0.58 Hz, 1H), 8.16 (dd, *J* = 8.20, 1.82 Hz, 1H), 7.97 (dd, *J* = 8.20, 0.58 Hz, 1H), 7.16 (t, *J* = 2.29 Hz, 2H), 6.42 (t, *J* = 2.29 Hz, 2H),
^{1}H NMR spectrum of this compound is in agreement with that reported in the literature[67]

Synthesis of 9,10,16,17,23,24-Hexakis-(ethyl)-2-(1-pyrrolylsulfonyl)-phthalocyanine (17)

To a dry 50 ml two-neck round bottom flask fitted with a magnetic stirred and a condenser, magnesium (181 mg, 7.45 mmol) and iodine (189 mg, 0.745 mmol) were refluxed in dry 1-butanol for 3 h. Once all the magnesium was dissolved the reaction mixture was allowed to cool to room temperature and then 2,3-diethylmaleonitrile (200 mg, 1.491 mmol) and 1-(3,4-dicyanophenylsulfonyl)pyrrole (77 mg, 0.298 mmol) were added and it was refluxed for 5h. When the reaction was finished, the solvent was removed under reduced pressure in a rotary evaporator. Aqueous acetic acid solution (5ml, 50% v/v) was added and stirred at room temperature for 30 minutes. The precipitate was filtered off using a sintered filter nº3 and washed thoroughly with water:methanol (4:1) solution. The crude was dissolved in dichloromethane, suspended in 1 g of silica gel and solvent removed. DCM was passed through the suspended crude and then it was dried using Na_2SO_4 and concentrated. The desired product was purified by silica column chromatography using a mixture of hexane:dichloromethane in a 3:2 ratio isolating first the symmetrical OETAP **5** and then the desired product. After removal of the solvent 27 mg of the product were obtained (11 % yield).

^{1}H NMR (300 MHz, $CDCl_3$, 25 ºC) δ (ppm) 9.59 (d, *J* = 1.46 Hz, 1H), 9.04 (d, *J* = 7.84 Hz, 1H), 8.48 (dd, *J* = 7.84, 1.46 Hz, 1H), 7.59 (t, *J* = 2.29 Hz, 2H), 6.50 (t, *J* = 2.29 Hz, 2H), 3.89-3.69 (m, 12H, $C\underline{H}_2CH_3$), 1.80-1.67 (m, 18H, $CH_2C\underline{H}_3$), -2.99 (s, 2H, NH).
ESI-TOF MS: calcd. 661.29 m/z, found 660.3 m/z $[M-H]^+$

Synthesis of 9,10,16,17,23,24-Hexakis-(ethyl)-phthalocyanine-2-sulfonic acid (18)

Small pieces of metal lithium (40 mg) were dissolved in a mixture of methanol (2 mL) and THF (2 mL). 9,10,16,17,23,24-Hexakis-(ethyl)-2-(1-pyrrolylsulfonyl)-phthalocyanine (20 mg) was added and the resulting solution was refluxed for 20h. After reaction time, solvent was removed under reduced pressure. The residue was treated with aqueous HCl (36%, 3mL) and centrifuge three times and then washed with methanol to give 15 mg of the desired product (81% yield)

Synthesis of 2(3),9(10),16(17),23(24)-tetrakis-(1-pyrrolylsulfonyl)-phthalocyanine (19)

To a dry 25 ml two-neck round bottom flask fitted with a magnetic stirred and a condenser, magnesium (7.56 mg, 0.31 mmol) and iodine (39.5 mg, 0.15 mmol) were refluxed in 2 mL of dry 1-butanol for 3 h. Once all the magnesium was dissolved the reaction mixture was allowed to cool to room temperature and then 1-(3,4-dicyanophenylsulfonyl)pyrrole (80 mg, 0.31 mmol) was added and the reaction was refluxed for 8h. When the reaction was finished, the solvent was removed under reduced pressure in a rotary evaporator. Aqueous acetic acid solution (5 mL, 50% v/v) was added and stirred at room temperature for 30 minutes. The precipitate was filtered off using a syntered filter nº3 and washed thoroughly with water:methanol (4:1) solution. The precipitate was purified by silica column chromatography using dichloromethane with 5 % of tetrahydrofurane as eluent mixture. After removal of the solvent 10 mg of the product were obtained (12 % yield).

^{1}H NMR (300 MHz, $CDCl_3$, 25 ºC) δ (ppm) 8.29 (d, *J* = 1.46 Hz, 1H), 8.24 (dd, *J* = 7.84, 1.46 Hz, 1H), 7.99 (d, *J* = 7.84 Hz, 1H), 7.18 (t, *J* = 2.29 Hz, 2H), 6.36 (t, *J* = 2.29 Hz, 2H)
ESI-TOF MS: calcd. 1030.12 m/z, found 1029.3 m/z $[M-H]^+$

Synthesis of 2(3),9(10),16(17),23(24)-phthalocyanine tetrasulfonic acid (20)

Small pieces of metal lithium (40 mg) were dissolved in a mixture of methanol (2 mL) and THF (2 mL). 2(3),9(10),16(17),23(24)-tetrakis-(1-pyrrolylsulfonyl)-phthalocyanine (20 mg) was added and the resulting solution was refluxed for 20h. After reaction time, solvent was removed under reduced pressure. The residue was treated with aqueous HCl (36%, 3mL) and centrifuge three times and then washed with methanol to give 14 mg of the desired product (86 % yield)

Synthesis of $Tb(Pc)_2$ [Pc = 2(3),9(10),16(17),23(24)-tetrakis-(1-pyrrolylsulfonyl)-phthalocyanine] (21)

1-(3,4-dicyanophenylsulfonyl)pyrrole (100 mg, 0.39 mmol), $Tb(OAc)_3 \cdot H_2O$ (22 mg, 0.06 mmol) and DBU (0.1 mL) were dissolved in hexanol (2 mL) in a dry 10 mL Schlenk flask. The reaction mixture was refluxed at 160ºC under argon atmosphere for 6 hours. After reaction time, the solvent was removed under reduced pressure. The crude was purified by silica column chromatography using dichloromethane:tetrahydrofurane 2:1 as eluent mixture. After removal of the solvent 13 mg of the product were obtained (12 % yield).

MALDI-TOF MS: *m/z*: 2215.1 [$M^{+\bullet}$] (100)

Synthesis of $Y(Pc)_2$ [Pc = 2(3),9(10),16(17),23(24)-tetrakis-(1-pyrrolylsulfonyl)-phthalocyanine] (22)

1-(3,4-dicyanophenylsulfonyl)pyrrole (100 mg, 0.39 mmol), $Y(OAc)_3 \cdot H_2O$ (17.6 mg, 0.06 mmol) and DBU (0.1 mL) were dissolved in hexanol (2 mL) in a dry 10 mL Schlenk flask. The reaction mixture was refluxed at 160ºC under argon atmosphere for 6 hours. After reaction time, the solvent was removed under reduced pressure. The crude was purified by silica column chromatography using dichloromethane:tetrahydrofurane 2:1 as eluent mixture. After removal of the solvent 15 mg of the product were obtained (14 % yield).

MALDI-TOF MS: *m/z*: 2145.1 [$M^{+\bullet}$] (100)

Synthesis of $Tb(Pc)_2$ [Pc = 2(3),9(10),16(17),23(24)-phthalocyanine tetrasulfonic acid] (23)

Small pieces of metal lithium (40 mg) were dissolved in a mixture of methanol (2 mL) and THF (2 mL). $Tb(Pc)_2$ [Pc = 2(3),9(10),16(17),23(24)-tetrakis-(1-pyrrolylsulfonyl)-

phthalocyanine] (20 mg) was added and the resulting solution was refluxed for 17 h. After reaction time, solvent was removed under reduced pressure. The residue was treated with aqueous HCl (36%, 3mL) and centrifuge three times and then washed with methanol to give 13 mg of the desired product (79 % yield)

MALDI-TOF MS: *m/z*: 1823.1 [$M^{-\bullet}$]

Synthesis of 4-nitrophthalamide (25)

1 g of 5-nitrophthalimide **11** (5.22 mmol) was dissolved in 100 ml of concentrated aqueous NH_4OH solution. The reaction mixture was stirred at room temperature for 24 hours. When the reaction finished, the desired product was filtered, washed with cold water and dried with an air flow to give a colorless powder (74% yield).

Synthesis of 4-nitrophthalonitrile (26)

In a dry 25 ml round bottom flask, thionyl chloride (0.510 ml, 7.03 mmol) was added dropwise into 5 ml of dry DMF. The temperature was kept below 5ºC during the addition and the reaction mixture was stirred for 10 minutes. 4-nitrophtalamide (300 mg, 1.434 mmol) was added in portions over a period of 10 minutes at this temperature and it was stirred for 2 hours while allowed to warm to room temperature. After this, the reaction mixture was poured into 15 ml of vigorously stirred ice. The product was collected by vacuum filtration and washed with 30 ml of water and 30 ml of sodium carbonate solution. The white powder was air dried at 50 ºC to give 465 mg of the desired product (80 % yield).

^{1}H NMR (300 MHz, $CDCl_3$, 25 ºC) δ (ppm) 8.66 (d, J = 2.25 Hz, 1H), 8.59 (dd, J = 8.23, 2.25 Hz, 1H), 8.07 (d, J = 8.23 Hz, 1H)
^{1}H NMR spectrum of this compound is in agreement with that reported in the literature[69]

Synthesis of (L) or (D)-2-isopropyl-5-methylcyclohexyl)oxy)phthalonitrile (28)

(*L*) or (*D*)-2-isopropyl-5-methylcyclohexan-1-ol (903 mg, 5.78 mmol), 4-nitrophthalonitrile (500 mg, 2.89 mmol) and potassium carbonate (960 mg, 6.95 mmol) were stirred in 15 ml of dry DMF at 80ºC for 2 days. The reaction mixture which turned orange/yellow was cooled down to room temperature. Then it was poured into 30 mL of ice and the aqueous layer was extracted with ethyl acetate. After being dried over anhydrous Na_2SO_4, the organic layer was evaporated and the residue was purified by silica gel chromatography with 1:8 v/v ethyl acetate:hexane as eluent, giving 198 mg of the desired product in 24% yield

^{1}H NMR (400 MHz; $CDCl_3$; Me_4Si): δ_H, ppm: 7.67 (d, J = 8.6 Hz, 1H), 7.22 (d, J = 2.5 Hz, 1H), 7.15 (dd, J = 8.6, 2.5 Hz, 1H), 4.14 (td, J = 10.6, 4.2 Hz, 1H), 2.12-2.01 (m, 2H), 1.80-1.72 (m, 2H), 1.63-1.45 (m, 2H), 1.14-1.01 (m, 2H), 0.98 (d, J = 6.8 Hz, 3H), 0.91 (d, J = 6.8 Hz, 3H), 0.96-0.92 (m, 1H), 0.74 (d, J = 6.8 Hz, 3H)
^{1}H NMR spectrum of this compound is in agreement with that reported in the literature[70]

Synthesis of (L)- and (D)-2(3),9(10),16(17),23(24)-tetrakis-(2-isopropyl-5-methylcyclohexoxyl)phthalocyanine (29)

To a dry two-neck 25 ml two-neck round bottom flask fitted with a magnetic stirred and a condenser, magnesium (34.4 mg, 1.416 mmol) and iodine (44.9 mg, 0.177 mmol) were refluxed in 2.5 mL of dry 1-butanol for 3 h. Once all the magnesium was dissolved the reaction mixture was allowed to cool to room temperature and then (*L*) or (*D*)-2-isopropyl-5-methylcyclohexyl)oxy)phthalonitrile (100 mg, 0.354 mmol) was added and it was refluxed for 6.5 h. When the reaction was finished, the solvent was removed under reduced pressure in a rotary evaporator. The green fraction was dissolved in 10 mL of dichloromethane and 10 drops of H_2SO_4 were added and the mixture stirred for 20 min. The brown reaction mixture was poured into 50 ml of ice and then the green color appeared again. Dichloromethane was added and the organic layer was neutralized with $NaHCO_3$,

water, dried over sodium sulfate and concentrated to give 130 mg of a green crude. The desired product was purified by silica column chromatography using dichloromethane as eluent. After removal of the solvent 16 mg of the product were obtained (15 % yield).

^{1}H NMR (400 MHz; $CDCl_3$; Me_4Si): δ_H, ppm: 9.29-9.09 (m, 4H), 8.90-8.77 (m, 4H), 7.78-7.65 (m, 4H), 4.82-4.63 (m 4H), 2.73-2.45 (m, 8H), 1.93-1.77 (m, 16H), 1.14-1.08 (m, 24H), 1.06-0.97 (m, 12H), 0.92-0.77 (m, 12H), -0.87 (s, 2H)
MALDI-TOF MS: *m/z*: 1130.8 [$M^{+\bullet}$] (100)

Synthesis of (L) and (D)-Tb(Pc)$_2$ [Pc = 2(3),9(10),16(17),23(24)-tetrakis-(2-isopropyl-5-methylcyclohexoxyl)phthalocyanine] **(30)**

A solution of (*L*)- or (*D*)-2(3),9(10),16(17),23(24)-tetrakis-(2-isopropyl-5-methylcyclohexoxyl)phthalocyanine (20.00 mg, 0.02 mmol, 2 equiv) in hexanol (2 mL) was added to a microwave vial. $Tb(OAc)_3 \cdot H_2O$ (2.81 mg, 0.01 mmol, 1 equiv), tetrabutylammonium benzoate (3.04 mg, 0.01 mmol, 1 equiv), and DBU (0.1 mL) were added to the green solution. The tube was sealed and the reaction mixture was heated to 250ºC in a Biotage Initiation Microwave Synthesizer for 10 min. The solvent was removed under reduced pressure. The residue was subjected to chromatography on a silica gel column using dichloromethane:hexane 4:1 as eluent mixture. After removal of the solvent 8 mg of the product were obtained (19 % yield).

MALDI-TOF MS: *m/z*: 2416.4 [$M^{+\bullet}$] (100)

3.6 References

[1] Bottrill, M.; Nicholas, L. K.; Long, N. J. "Lanthanides in magnetic resonance imaging". *Chem. Soc. Rev.* **2006**, *35*, 557.

[2] Dosev, D.; Nichkova, M.; Kennedy, I. M. "Inorganic lanthanide nanophosphors in biotechnology". *J. Nanosci. Nanotechnol.* **2008**, *8*, 1052.

[3] Bunzli, J. C. G.; Eliseeva, S. V. "Lanthanide NIR luminescence for telecommunications, bioanalyses and solar energy conversion". *J. Rare Earths* **2010**, *28*, 824.

[4] Bethencourt, M.; Botana, F. J.; Calvino, J. J.; Marcos, M.; Rodriguez-Chacon, M. A. "Lanthanide compounds as environmentally-friendly corrosion inhibitors of aluminium alloys: A review". *Corros. Sci.* **1998**, *40*, 1803.

[5] Fricker, S. P. "The therapeutic application of lanthanides". *Chem. Soc. Rev.* **2006**, *35*, 524.

[6] Barrett, P. A.; Dent, C. E.; Linstead, R. P. "Phthalocyanines Part VII Phthalocyanine as a co-ordinating group - A general investigation of the Metallic derivatives". *J. Chem. Soc.* **1936**, 1719.

[7] Lux, F.; Dempf, D.; Graw, D. "Diphthalocyaninato-Thorium(4) and -Uranium(4)". *Angew. Chem., Int. Ed.* **1968**, *7*, 819.

[8] Kirin, I. S.; Moskalev, P. N. "Scandium Complexes with Phthalocyanine". *Zh. Neorg. Khim.* **1971**, *16*, 3179.

[9] Kasuga, K.; Tsutsui, M.; Petterson, R. C.; Tatsumi, K.; Vanopdenbosch, N.; Pepe, G.; Meyer, E. F. "Structure of "Bis(Phthalocyaninato)Neodymium(III)". *J. Am. Chem. Soc.* **1980**, *102*, 4835.

[10] Donzello, M. P.; Ercolani, C.; Chiesi-Villa, A.; Rizzoli, C. "One step forward to "stapled" bis(phthalocyanine) metal complexes: Synthesis, characterization, and redox properties of bis(phthalocyaninato)niobium(IV). ". *Inorg. Chem.* **1998**, *37*, 1347.

[11] Moussavi, M.; Decian, A.; Fischer, J.; Weiss, R. "Synthesis, Structure, and Spectroscopic Properties of the Reduced and Reduced Protonated Forms of Lutetium Diphthalocyanine". *Inorg. Chem.* **1988**, *27*, 1287.

[12] Gieren, A.; Hoppe, W. "X-Ray Crystal Structure Analysis of Bisphthalocyaninatouranium(IV)". *J. Chem. Soc. D. Chem. Comm.* **1971**, 413.

[13] Kirin, I. S.; Moskalev, P. N.; Maskashev. Y. A. *Zh. Neorg. Khim*. **1965**, *10*, 1951

[14] Decian, A.; Moussavi, M.; Fischer, J.; Weiss, R. "Synthesis, Structure, and Spectroscopic and Magnetic-Properties of Lutetium(III) Phthalocyanine Derivatives - $LuPc_2 \cdot CH_2Cl_2$ and $[LuPc(OAc)(H_2O)_2].H_2O \cdot 2CH_3OH$". *Inorg. Chem.* **1985**, *24*, 3162.

[15] Toupance, T.; Ahsen, V.; Simon, J. "Ione-Electronics - Crown-Ether Substituted Lutetium Bisphthalocyanines". *Journal of the Chemical Society-Chemical Communications* **1994**, 75.

[16] Nyokong, T.; Furuya, F.; Kobayashi, N.; Du, D. M.; Liu, W.; Jiang, J. Z. "Comparative spectroscopic and electrochemical properties of bis(octakis(dodecylthio)naphthalocyaninato)europium(III) and bis(tetra-tert-butylnaphthalocyaninato)europium(III) complexes". *Inorg. Chem.* **2000**, *39*, 128.

[17] Sleven, J.; Gorller-Walrand, C.; Binnemans, K. "Synthesis, spectral and mesomorphic properties of octa-alkoxy substituted phthalocyanine ligands and lanthanide complexes". *Materials Science & Engineering C-Biomimetic and Supramolecular Systems* **2001**, *18*, 229.

[18] Lapkina, L. A.; Niskanen, E.; Ronkkomaki, H.; Larchenko, V. E.; Popov, K. I.; Tsivadze, A. Y. "Synthesis and characterization of sandwich-type gadolinium and ytterbium crown ether-substituted phthalocyanines". *J. Porphyrins Phthalocyanines* **2000**, *4*, 587.

[19] Kogan, E. G.; Ivanov, A. V.; Tomilova, L. G.; Zefirov, N. S. "Synthesis of mono- and bisphthalocyanine complexes using microwave irradiation". *Mendeleev Commun.* **2002**, 54.

[20] Branzoli, F.; Carretta, P.; Filibian, M.; Zoppellaro, G.; Graf, M. J.; Galan-Mascaros, J. R.; Fuhr, O.; Brink, S.; Ruben, M. "Spin Dynamics in the Negatively Charged Terbium (III) Bis-phthalocyaninato Complex ". *J. Am. Chem. Soc.* **2009**, *131*, 7934.

[21] Buchler, J. W.; Decian, A.; Fischer, J.; Kihnbotulinski, M.; Paulus, H.; Weiss, R. "Metal-Complexes with Tetrapyrrole Ligands .40. Cerium(Iv) Bis(Octaethylporphyrinate) and Dicerium(Iii) Tris(Octaethylporphyrinate) - Parents of a New Family of Lanthanoid Double-Decker and Triple-Decker Molecules". *J. Am. Chem. Soc.* **1986**, *108*, 3652.

[22] Montalban, A. G.; Michel, S. L. J.; Baum, S. M.; Vesper, B. J.; White, A. J. P.; Williams, D. J.; Barrett, A. G. M.; Hoffman, B. M. "Lanthanide porphyrazine sandwich complexes:

synthetic, structural and spectroscopic investigations". *J. Chem. Soc., Dalton Trans.* **2001**, 3269.

[23] Chabach, D.; Tahiri, M.; Decian, A.; Fischer, J.; Weiss, R.; Bibout, M. E. "Tervalent-Metal Porphyrin-Phthalocyanine Heteroleptic Sandwich-Type Complexes - Synthesis, Structure, and Spectroscopic Characterization of Their Neutral, Singly-Oxidized, and Singly-Reduced States". *J. Am. Chem. Soc.* **1995**, *117*, 8548.

[24] Nicholson, M. M. "Lanthanide Diphthalocyanines - Electrochemistry and Display Applications". *Ind. End. Chem. Prod. Rd.* **1982**, *21*, 261.

[25] Guyon, F.; Pondaven, A.; Guenot, P.; Lher, M. "Bis(2,3-Naphthalocyaninato)Lutetium(III) and (2,3-Naphthalocyaninato)(Phthalocyaninato)Lutetium(Iii) Complexes - Synthesis, Spectroscopic Characterization, and Electrochemistry". *Inorg. Chem.* **1994**, *33*, 4787.

[26] Gao, Y. N.; Ma, P.; Chen, Y. L.; Zhang, Y.; Bian, Y. Z.; Li, X. Y.; Jiang, J. Z.; Ma, C. Q. "Design, Synthesis, Characterization, and OFET Properties of Amphiphilic Heteroleptic Tris(phthalocyaninato) Europium(III) Complexes. The Effect of Crown Ether Hydrophilic Substituents". *Inorg. Chem.* **2009**, *48*, 45.

[27] Liu, Z. M.; Yasseri, A. A.; Lindsey, J. S.; Bocian, D. F. "Molecular memories that survive silicon device processing and real-world operation". *Science* **2003**, *302*, 1543.

[28] Takami, T.; Ye, T.; Pathem, B. K.; Arnold, D. P.; Sugiura, K.; Bian, Y. Z.; Jiang, J. Z.; Weiss, P. S. "Manipulating Double-Decker Molecules at the Liquid-Solid Interface". *J. Am. Chem. Soc.* **2010**, *132*, 16460.

[29] Shinoda, S.; Noguchi, T.; Ikeda, M.; Habata, Y.; Tsukube, H. "Luminescent double-decker type guanine octets with trivalent lanthanide cations: in situ self-assembling and stability evaluation in homogeneous organic media". *J. Inclusion Phenom. Macrocyclic Chem.* **2011**, *71*, 523.

[30] Caneschi, A.; Gatteschi, D.; Sessoli, R.; Barra, A. L.; Brunel, L. C.; Guillot, M. "Alternating-Current Susceptibility, High-Field Magnetization, and Millimeter Band Epr Evidence for a Ground S = 10 State in $[Mn_{12}O_{12}(CH_3COO)_{16}(H_2O)_4]\cdot 2CH_3COOH\cdot 4H_2O$". *J. Am. Chem. Soc.* **1991**, *113*, 5873.

[31] Sessoli, R.; Tsai, H. L.; Schake, A. R.; Wang, S. Y.; Vincent, J. B.; Folting, K.; Gatteschi, D.; Christou, G.; Hendrickson, D. N. "High-Spin Molecules - $[Mn_{12}O_{12}(O_2Cr)_{16}(H_2O)_4]$". *J. Am. Chem. Soc.* **1993**, *115*, 1804.

[32] Sessoli, R.; Gatteschi, D.; Caneschi, A.; Novak, M. A. "Magnetic Bistability in a Metal-Ion Cluster". *Nature* **1993**, *365*, 141.

[33] De Haas, W. J.; Du Pre, F. K. "Paramagnetic relaxation in iron ammonium alum at low temperatures". *Physica* **1938**, *5*, 501.

[34] Lis, T. "Preparation, Structure, and Magnetic-Properties of a Dodecanuclear Mixed-Valence Manganese Carboxylate". *Acta Crystallographica Section B-Structural Science* **1980**, *36*, 2042.

[35] Boyd, P. D. W.; Li, Q. Y.; Vincent, J. B.; Folting, K.; Chang, H. R.; Streib, W. E.; Huffman, J. C.; Christou, G.; Hendrickson, D. N. "Potential Building-Blocks for Molecular Ferromagnets - $[Mn_{12}O_{12}(O_2CPh)_{16}(H_2O)_4]$ with a S=14 Ground-State". *J. Am. Chem. Soc.* **1988**, *110*, 8537.

[36] Sessoli, R.; Tsai, H. L.; Schake, A. R.; Wang, S. Y.; Vincent, J. B.; Folting, K.; Gatteschi, D.; Christou, G.; Hendrickson, D. N. "High-Spin Molecules - $[Mn_{12}O_{12}(O_2Cr)_{16}(H_2O)_4]$". *J. Am. Chem. Soc.* **1993**, *115*, 1804.

[37] Thomas, L.; Lionti, F.; Ballou, R.; Gatteschi, D.; Sessoli, R.; Barbara, B. "Macroscopic quantum tunnelling of magnetization in a single crystal of nanomagnets". *Nature* **1996**, *383*, 145.

[38] Soler, M.; Artus, P.; Folting, K.; Huffman, J. C.; Hendrickson, D. N.; Christou, G. "Single-molecule magnets: Preparation and properties of mixed-carboxylate complexes $[Mn_{12}O_{12}(O_2Cr)_8(O_2Cr\ ')_8(H_2O)_4]$". *Inorg. Chem.* **2001**, *40*, 4902.

[39] Brechin, E. K.; Yoo, J.; Nakano, M.; Huffman, J. C.; Hendrickson, D. N.; Christou, G. "A new class of single-molecule magnets: mixed-valent $[Mn(O_2CMe)_2(Hpdm)_6][ClO_4]_2$ with an S=8 ground state". *Chem. Commun. (Cambridge, U. K.)* **1999**, 783.

[40] Ferlay, S.; Mallah, T.; Ouahes, R.; Veillet, P.; Verdaguer, M. "A chromium-vanadyl ferrimagnetic molecule-based magnet: Structure, magnetism, and orbital interpretation". *Inorg. Chem.* **1999**, *38*, 229.

[41] Taft, K. L.; Papaefthymiou, G. C.; Lippard, S. J. "A Mixed-Valent Polyiron Oxo Complex That Models the Biomineralization of the Ferritin Core". *Science* **1993**, *259*, 1302.

[42] Castro, S. L.; Sun, Z. M.; Grant, C. M.; Bollinger, J. C.; Hendrickson, D. N.; Christou, G. "Single-molecule magnets: Tetranuclear vanadium(III) complexes with a butterfly structure and an S=3 ground state". *J. Am. Chem. Soc.* **1998**, *120*, 2365.

[43] Hernandez, J. M.; Zhang, X. X.; Luis, F.; Tejada, J.; Friedman, J. R.; Sarachik, M. P.; Ziolo, R. "Evidence for resonant tunneling of magnetization in Mn-12 acetate complex". *Physical Review B* **1997**, *55*, 5858.

[44] Luis, F.; Mettes, F. L.; Tejada, J.; Gatteschi, D.; de Jongh, L. J. "Observation of quantum coherence in mesoscopic molecular magnets". *Physical Review Letters* **2000**, *85*, 4377.

[45] Miller, J. S. "Magnetically ordered molecule-based materials". *Chem. Soc. Rev.* **2011**, *40*, 3266.

[46] Sun, H. L.; Wang, Z. M.; Gao, S. "Strategies towards single-chain magnets". *Coord. Chem. Rev.* **2010**, *254*, 1081.

[47] Christou, G.; Gatteschi, D.; Hendrickson, D. N.; Sessoli, R. "Single-molecule magnets". *Mrs Bulletin* **2000**, *25*, 66.

[48] Jiang, S. D.; Wang, B. W.; Su, G.; Wang, Z. M.; Gao, S. "A Mononuclear Dysprosium Complex Featuring Single-Molecule-Magnet Behavior". *Angew. Chem., Int. Ed.* **2010**, *49*, 7448.

[49] Feltham, H. L. C.; Brooker, S. "Review of purely 4f and mixed-metal nd-4f single-molecule magnets containing only one lanthanide ion". *Coord. Chem. Rev.* **2014**, *276*, 1.

[50] Ishikawa, N.; Sugita, M.; Ishikawa, T.; Koshihara, S.; Kaizu, Y. "Lanthanide double-decker complexes functioning as magnets at the single-molecular level". *J. Am. Chem. Soc.* **2003**, *125*, 8694.

[51] Ishikawa, N.; Sugita, M.; Okubo, T.; Tanaka, N.; Lino, T.; Kaizu, Y. "Determination of ligand-field parameters and f-electronic structures of double-decker bis(phthalocyaninato) lanthanide complexes". *Inorg. Chem.* **2003**, *42*, 2440.

[52] Hernandez, J. M.; Zhang, X. X.; Luis, F.; Bartolome, J.; Tejada, J.; Ziolo, R. "Field tuning of thermally activated magnetic quantum tunnelling in Mn-12-Ac molecules". *Europhysics Letters* **1996**, *35*, 301.

[53] Friedman, J. R.; Sarachik, M. P.; Tejada, J.; Ziolo, R. "Macroscopic measurement of resonant magnetization tunneling in high-spin molecules". *Physical Review Letters* **1996**, *76*, 3830.

[54] Thomas, L.; Lionti, F.; Ballou, R.; Gatteschi, D.; Sessoli, R.; Barbara, B. "Macroscopic quantum tunnelling of magnetization in a single crystal of nanomagnets". *Nature* **1996**, *383*, 145.

[55] Awschalom, D. D.; Smyth, J. F.; Grinstein, G.; Divincenzo, D. P.; Loss, D. "Macroscopic Quantum Tunneling in Magnetic Proteins". *Physical Review Letters* **1992**, *68*, 3092.

[56] Bertaina, S.; Gambarelli, S.; Mitra, T.; Tsukerblat, B.; Muller, A.; Barbara, B. "Quantum oscillations in a molecular magnet". *Nature* **2008**, *453*, 203.

[57] Ghosh, S.; Parthasarathy, R.; Rosenbaum, T. F.; Aeppli, G. "Coherent spin oscillations in a disordered magnet". *Science* **2002**, *296*, 2195.

[58] Timco, G. A.; Carretta, S.; Troiani, F.; Tuna, F.; Pritchard, R. J.; Muryn, C. A.; McInnes, E. J. L.; Ghirri, A.; Candini, A.; Santini, P.; Amoretti, G.; Affronte, M.; Winpenny, R. E. P. "Engineering the coupling between molecular spin qubits by coordination chemistry". *Nat. Nanotechnol.* **2009**, *4*, 173.

[59] Tejada, J.; Chudnovsky, E. M.; del Barco, E.; Hernandez, J. M.; Spiller, T. P. "Magnetic qubits as hardware for quantum computers". *Nanotechnology* **2001**, *12*, 181.

[60] Affronte, M. "Molecular nanomagnets for information technologies". *J. Mater. Chem.* **2009**, *19*, 1731.

[61] Montalban, A. G.; Michel, S. L. J.; Baum, S. M.; Vesper, B. J.; White, A. J. P.; Williams, D. J.; Barrett, A. G. M.; Hoffman, B. M. "Lanthanide porphyrazine sandwich complexes: synthetic, structural and spectroscopic investigations". *J. Chem. Soc., Dalton Trans.* **2001**, 3269.

[62] Fitzgerald, J.; Taylor, W.; Owen, H. "Facile synthesis of substituted fumaronitriles and maleonitriles - Precursors to soluble tetraazaporphyrins". *Synthesis-Stuttgart* **1991**, 686.

[63] Mowry, D. T. "The Preparation of Nitriles". *Chem. Rev. (Washington, DC, U. S.)* **1948**, *42*, 189.

[64] Weber, J. H.; Busch, D. H. "Complexes Derived from Strong Field Ligands .19. Magnetic Properties of Transition Metal Derivatives of 4,4',4",4"'-Tetrasulfophthalocyanine". *Inorg. Chem.* **1965**, *4*, 469.

[65] Linstead, R. P.; Weiss, F. T. "Phthalocyanines and Related Compounds .20. Further Investigations on Tetrabenzporphin and Allied Substances". *J. Chem. Soc.* **1950**, 2975.

[66] Ryan, J. W.; Anaya-Plaza, E.; de la Escosura, A.; Torres, T.; Palomares, E. "Small molecule solar cells based on a series of water-soluble zinc phthalocyanine donors". *Chem. Commun. (Cambridge, U. K.)* **2012**, *48*, 6094.

[67] Li, Z. P.; van Lier, J.; Leznoff, C. C. "Heterocyclic aromatic amide protecting groups for aryl and phthalocyaninesulfonic acids". *Canadian Journal of Chemistry-Revue Canadienne De Chimie* **1999**, *77*, 138.

[68] Aranyos, V.; Castano, A. M.; Grennberg, H. "An application of the stille coupling for the preparation of arylated phthalonitriles and phthalocyanines". *Acta Chem. Scand.* **1999**, *53*, 714.

[69] Young, J. G.; Onyebuagu, W. "Synthesis and Characterization of Di-Disubstituted Phthalocyanines". *J. Org. Chem.* **1990**, *55*, 2155.

[70] de Oliveira, K. T.; de Assis, F. F.; Ribeiro, A. O.; Neri, C. R.; Fernandes, A. U.; Baptista, M. S.; Lopes, N. P.; Serra, O. A.; Iamamoto, Y. "Synthesis of Phthalocyanines-ALA Conjugates: Water-Soluble Compounds with Low Aggregation". *J. Org. Chem.* **2009**, *74*, 7962.

[71] Lv, W.; Zhu, P. H.; Bian, Y. Z.; Ma, C. Q.; Zhang, X. M.; Jiang, J. Z. "Optically Active Homoleptic Bis(phthalocyaninato) Rare Earth Double-Decker Complexes Bearing Peripheral Chiral Menthol Moieties: Effect of pi-pi Interaction on the Chiral Information Transfer at the Molecular Level". *Inorg. Chem.* **2010**, *49*, 6628.

Chapter 4

On surface chemistry of octaethyltetraazaporphyrine and lanthanide double-decker derivatives

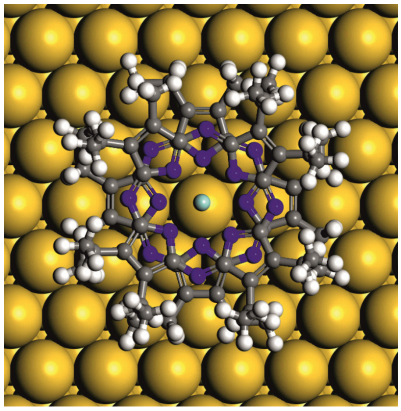

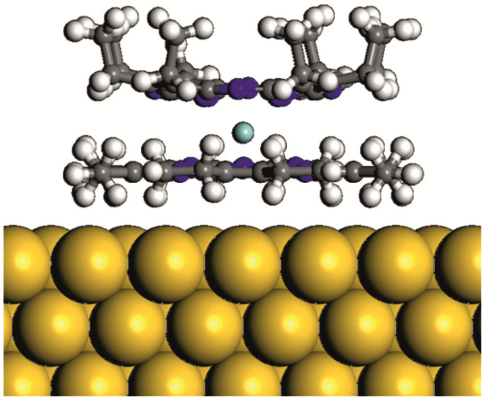

*Part of this Chapter was published in: *Nat. Commun*. 7:11002 doi:10.1038/ncomms11002

UNIVERSITAT ROVIRA I VIRGILI
SYNTHESIS OF TETRA-AZAPORPHYRINS, PHTHALOCYANINES AND LANTHANIDE DOUBLE-DECKER SANDWICH COMPLEXES
Nelson Giménez Agulló

4.1 Introduction

4.1.1 Scanning tunneling microscopy

Scanning tunneling microscopy (STM) was invented by Binnig and Rohrer in the early 1980s at the IBM Zurich Research Laboratory.[1,2] It was the first instrument capable of directly obtaining images of solid surfaces with atomic resolution. In 1986, Binnig and Rohrer received the Nobel Prize in Physics for the discovery of the STM. By integrating scanning capacity into vacuum tunneling capability, STM enables the imaging of surfaces of conducting samples and the study of their local electronic properties down to atomic levels. STM is a technique that exploits the tunnel phenomena and is based on the displacement of a metallic sharp tip onto a conductive surface and the measurement of the current that flows between both electrodes. This current arises from electrons that tunnel between tip and surface due to an applied bias V_{bias} and depends exponentially on the vacuum gap width between the tip and the surface, which are separated a distance of a few angstroms resulting in an overlap of their electronic wave functions.

Now a day, STM is an instrument not only used to *see* individual atoms by imaging, but also used to *touch* and *take* the atoms or to *hear* their vibrations by means of manipulation.[3] In this perspective, STM can be considered as the *eyes*, *hands* and *ears* of the scientists connecting our macroscopic world to the atomic and nanoscopic scale.

The essential components of an STM include a sharp probing tip, a piezoelectric scanning unit (which controls the vertical and lateral movement of the tip), a coarse positioning unit (used to bring the tip-sample separation to within the tunneling range), a vibration isolation stage and a set of electronics which detects the small tunneling current and drives the coarse positioning.

Tunneling effect

Quantum mechanics explains the behavior of matter at the nanoscale. One of its foundational concepts is the "wave-particle duality", which postulates that all particles exhibit both wave and particle properties. The tunnel effect is a consequence of this concept. A tunneling current occurs when electrons move through a region in which the potential energy is higher than the total energy of the electrons. Classically, an electron can never be inside such a region because negative kinetic energy is not allowed according to Newtonian mechanics. However, on the scale of the order of 10 Å, Newtonian concepts fail and quantum concepts dominate the scene. The quantum rules make it possible for an electron to move from one classically allowed region to the other through a classically forbidden region. This phenomenon is called electron tunneling. According to an elementary quantum mechanical calculation, the transmission probability through the barrier decreases exponentially with the thickness of the barrier and the square root of the potential relative to the electron energy. Since the tunneling current exponentially varies with the tip-sample distance, a slight change in the distance (less than a fraction of the atomic length) can be detected.

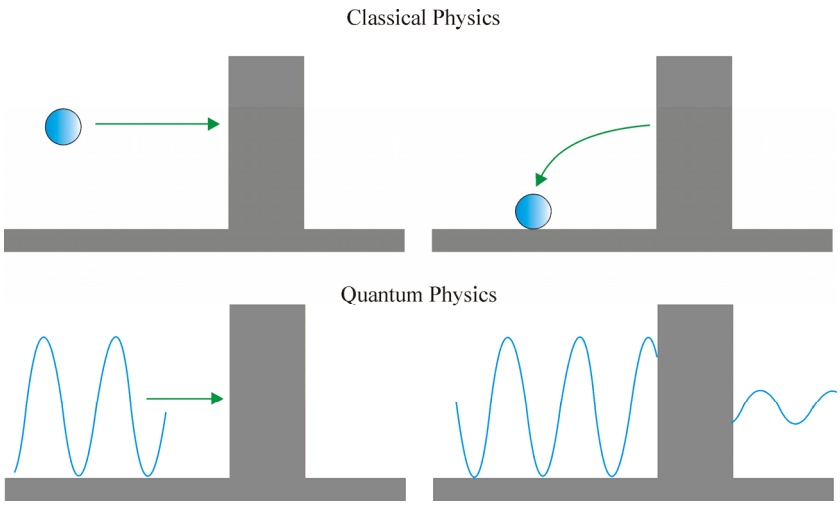

Figure 4.1 Schematic drawing representing the tunneling effect from both points of views, classical and quantum physics.

4.1.2 Working principles of STM

Operation modes

There are two different operational modes that one can use for the measurement of the tunnel current:

1. *Constant height mode*

In this operational mode, the tip scans the sample maintaining the vertical position of the tip constant, while the current is simultaneously recorded. During each measurement the tip covers a grid xy obtaining I_z values that constitute the surface image. This operational mode provides higher scanning speed compared to constant current mode and thus is particularly used for the study of dynamic processes in real time. The main advantage of this mode of operation is that it can be used at high scanning frequencies. The disadvantage is that it is only appropriate for atomically flat surfaces as otherwise the tip crash onto the surface would be unavoidable.

2. *Constant current mode*

This operational mode is also known as topographic mode and is the most frequently used mode to obtain STM images. In this mode, the tip moves across the surface of the sample while voltage and current are kept constant. The tunneling current is set to a value I_0 and then the tip scans the sample measuring in each point the corresponding tunneling current (I). If the current measured I is different from I_0, the electronic control will send a voltage V_z to the piezoelectrics to bring the tip closer to the surface or on the contrary to go away from it. During each measurement the tip covers a grid xy obtaining V_z values that constitute the topographic image.

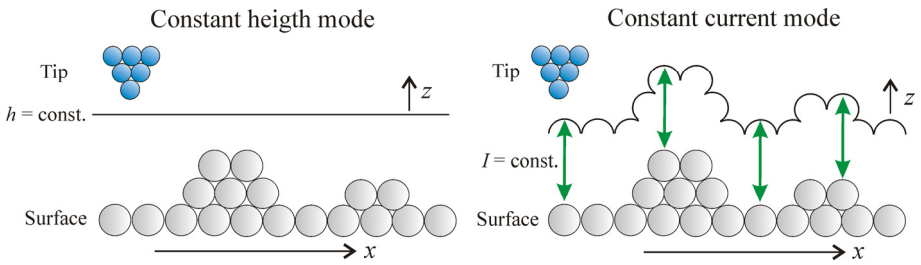

Figure 4.2 Left: constant-height mode where the measured signal is the tunneling current and Right: constant-current mode where the tunneling current is maintained constant and the signal measured is the V_z applied to the tip to keep the current constant.

Manipulation modes

Manipulation of single atoms/molecules with the STM is possible by the control and tunning of the interaction between the atoms at the end of the STM tip and the single atom/molecule on the surface that is being manipulated. There are two different manipulation modes known as lateral manipulation and vertical manipulation.

1. Lateral manipulation

A STM manipulation procedure to relocate single atoms or molecules across a surface is known as lateral manipulation.[4] The first example of lateral manipulation was demonstrated by Eigler and Schweizer in 1990 by writing the "IBM" company logo with Xe atoms on a Ni(110) surface.[5] A typical lateral manipulation procedure involves three steps: 1) vertically approach of the tip towards the target atom in order to increase the tip-atom interaction, 2) scanning the tip parallel to the surface where the atom moves under influence of the tip, and 3) retracting the tip back to the normal image-height thereby the atom is left at the final location on the surface.

The nature of atom movements and the type of tip-atom interactions during a lateral manipulation process can be determined from the STM feedback or tunneling current.[6] Three basic lateral manipulation modes are distinguished: "pushing", "pulling" and

"sliding". In the "pushing" mode, a repulsive tip-atom interaction drives the atom to move in front of the tip. In the "pulling" mode, the atom follows the tip due to attractive tip-atom interactions. In the "sliding" mode the atom is virtually bound or trapped under the tip and it moves smoothly through the surface together with the tip.

2. *Vertical manipulation*

In the vertical manipulation single atoms or molecules are transferred from tip to surface and vice versa.[7] This process is closely related to desorption and subsequent adsorption of atoms/molecules on surfaces. An "atomic switch" obtained by repeated transfer of a Xe atom between STM tip and a Ni(110) surface was the first example of vertical manipulation.[8] In this technique, the STM tip is used to pick up atoms/molecules by adjusting the variables height and field (set by current and bias).

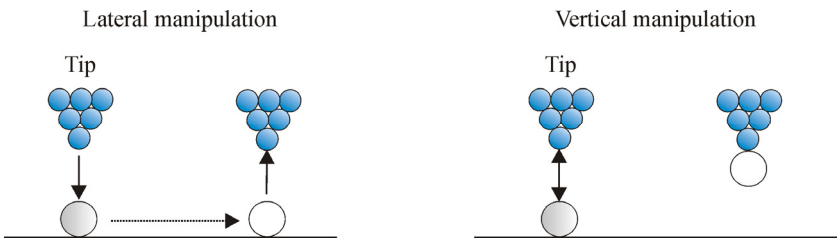

Figure 4.3 Left: Schematic drawing showing the tip action during the lateral manipulation and Right: schematic drawing of the tip action during the vertical manipulation.

4.1.3 On-surface interactions in ultra-high vacuum

Non-covalent interactions

Selective non-covalent interactions in solution have been used to direct the assembly of molecules into functional structures such as capsules,[9] rotaxanes[10] and molecular machines.[11] It has been demonstrated that weak hydrogen bonds can drive the assembly process to reversible form helicates, grids, cages, metallodendrimers, polymers and other architectures. The major difficulty in this area is to control the assembly process whilst increasing the structural complexity of the assembly. More recently, scientists have extended the concept of supramolecular organization to two dimensional assemblies on surfaces. A wide variety of highly regular and ordered supramolecular architectures, based on non-covalent interactions, have been reported on single crystal metal surfaces over the past decade.[12] Complex molecular structures held together by weak and reversible interactions such as van der Waals,[13] dipolar coupling,[14] hydrogen bonds,[15,16] and metal complexation[17] have been prepared on-surface under ultra-high vacuum (UHV) conditions.

Covalent interactions

The construction of covalently bound molecular architectures in a well-defined arrangement on surfaces is a key challenge in the field of nanotechnology. To date, only simple structures have been obtained because of the limitation of one-step connection processes. Chemical reaction has been introduced locally with the STM tip, and few cases of monocomponent polymerization have been reported. The interconnection of molecules in a controlled way directly on a surface through irreversible and robust covalent bonding offers several advantages over solution synthesis:

a) On-surface UHV experiments allow a broader range of reaction temperatures to be used. Temperatures from 4 to 600 K can be handled without risk of solvent decomposition or air oxidation of the resulting products.
b) It allows the preparation of extended 1D or 2D arrays of rigid oligomers or polymers that are not possible to obtain in solution for solubility reasons.

c) The 2D confined geometry could favor some supramolecular aggregates or reactivity that are not usually observed in solution chemistry.
d) The output from an on-surface reaction can be directly followed and characterized by UHV scanning tunneling microscopy (STM). This technique allows local spectroscopic measurements, molecular manipulations, tip-induced reactions and imaging at submolecular level.

The control over reactivity and diffusion during the covalent bond formation on a chemical reaction constitutes a promising field toward the preparation of molecular nanostructures in surfaces. In the following section we are going to summarize some relevant examples of covalent bonds formation, starting from molecular building blocks on a surface in a UHV. These important results opened up new avenues in the preparation of molecular devices and machines by functionalizing molecular surfaces.

1. Discrete Chemical Reactions

Considering the type of chemical reactions, only a few of them have been exploited to produce successful surface-assisted lateral covalent designs and inspected with ultimate spatial resolution.[18] Some examples of discrete chemical reactions based on covalent bond formation are the cyclocondensation of boronic acids,[19] Schiff base reaction of aldehydes and amines to form imine,[20] acylation reactions (yielding polyamides,[21] polyimides,[22] or polyesters,[23] respectively), carbon-carbon couplings exemplified by the Ullmann[24], the Glaser[25] and the Sonogashira reactions,[26] and cycloadditions.[27]

A nice representative example of a reaction in which discrete covalent bonds are formed on surface under ultra-high vacuum conditions is the tetramerization reaction of 1,2,4,5-tetracyanobenzene (TCNB) with iron reported by Abel *et al*.[28] The metal-directed surface reaction proceeds after deposition of TCNB molecules and iron atoms on Au(111) surface in a 4:1 stoichiometric ratio giving rise to individual cyano-functionalized phthalocyanines, $FePc(CN)_8$. The as-formed molecules self-assembled forming supramolecular networks as usually observed for different phthalocyanines, in which the metal-phthalocyanine cores are connected by hydrogen bonds.[29]

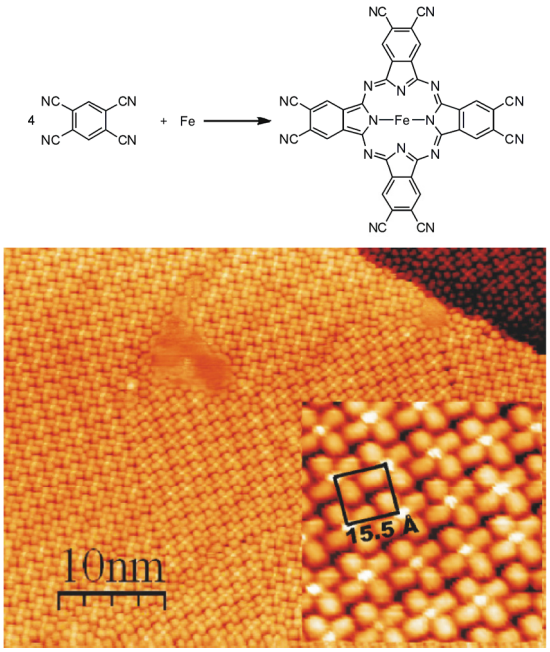

Figure 4.4 STM image of the *in situ* synthesized $FePc(CN)_8$ formed on a Au(111) surface by successive deposition of 1,2,4,5-tetracyanobenzene (TCNB) and Fe atoms in a 4:1 ratio. Inset: reaction scheme. Image adapted from reference[28]

2. *Polymerization Reactions*

The first achievements of covalent polymerization on a surface are either restricted to one-dimensional growth,[30,31] or poorly ordered 2D extension due to the irreversibility covalent bond formation process.[32,33] The possibility of extending polymer conjugation into the second dimension is thus a key point in the polymerization process.[34,35] Polymers with backbones containing extended networks of conjugated π-bonds can exhibit semiconduction behavior and thus can be used as active materials in optoelectronic devices. However, conjugated polymers are mainly 1D chains and the electron hop between chains and across disordered chain fragments slows down the charge carriers. For this reason, many efforts are been made to create 2D conjugation polymers since they may exhibit better conductivity due to the enhance charge carrier capability. The properties of 2D-conjugated polymers have been studied theoretically for more than two decades. However,

experimental efforts aimed at creating and characterizing such systems are more recent. The challenges include designing properly functionalized monomers than can react in two independent directions and identifying a suitable template to guide the formation of a continuous 2D network. Because planar and rigid 2D-conjugated polymers are in most cases insoluble, classical solution polymerization and characterization techniques are not likely to be suitable. In order to overcome this issue, atomically flat crystalline surfaces are used to template and confine polymerization reactions in two dimensions. Moreover, this technique will also allow the *in situ* characterization of the polymer formed with local probe methods such as scanning tunneling microscopy (STM).

As mentioned above, the covalent polymerization on surface is mostly restricted to the one-dimensional polymer formation. An example of covalently linked conjugated carbon nanostructures forming 1D polymeric chains have been reported by Sun *et al.*[36] in which they used the on surface Bergman cyclization reaction. The reaction precursor 1,6-di-2-naphthylhex-3-ene-1,5-diyne (DNHD) was deposited on a Cu(110) surface held at 170 K. STM images after substrate deposition clearly showed heart-shaped molecules with two elliptical lobes and one round protrusion distributed in an isolated way on the substrate and attributed to individual DNHD molecules (Figure 4.5 a). The two elliptical lobes were assigned to the two naphtyl groups and the round protrusion to the vinyl group present in the DNHD precursor. The Bergman cyclization of the DNHD molecules was initiated after sample annealing at 400 K as can be seen in the STM images obtained (Figure 4.5 b). The heart-shaped motifs disappeared and dispersed one-dimensional polymeric chains were formed by cyclization of the precursors with subsequent free radical polymerization. The robustness of the polymers formed was demonstrated by lateral STM manipulation evidencing the covalent character of the molecular chains observed.

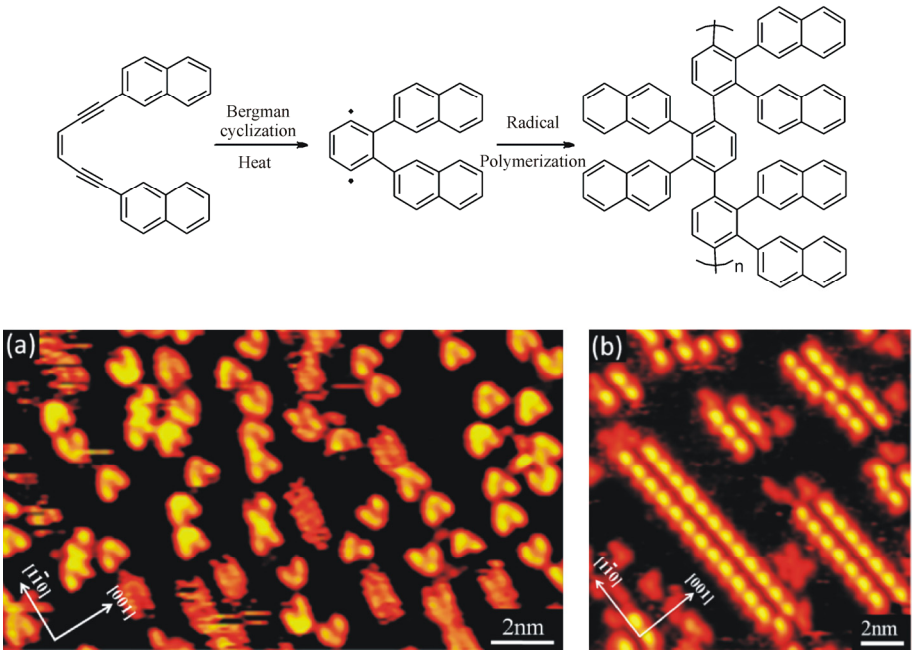

Figure 4.5. Top: Chemical drawing of the Bergman cyclization reaction and radical polymerization of 1,6-di-2-naphthylhex-3-ene-1,5-diyne (DNHD). Bottom: a) STM image after deposition of DNHD molecules on Cu(110) held at 170K. Scanning conditions: V_t = 2.5 V, I_t = 0.65 nA. b) STM image showing the formation of one-dimensional molecular chain structures after sample annealing at 400 K. Scanning conditions: V_t = -2.5 V, I_t = 0.65 nA. Image adapted from reference[36]

Surface-mediated synthesis of low-dimensional polymers from simple molecular precursors under ultra-clean conditions is a novel and rapidly emerging field with great relevance for molecular electronics, optoelectronic devices, magnetism, molecular recognition and catalysis.[37,38] Surprisingly, despite their importance in bulk chemistry and their growing relevance in 3D polymer science, pericyclic reactions have remained mostly elusive to produce surface-confined polymeric nanostructures[39]. This promising bottom-up strategy relies on a careful selection of building blocks equipped with functional groups and surfaces, whereby one-dimensional (1D) and two-dimensional (2D) nanostructures have been illustrated and a new plethora of materials is envisioned.[40,41]

4.1.4 Porphyrinoid macrocycles on surfaces

Porphyrins, phthalocyanines and their derivatives are the subject of enormous attention inspired by scientific curiosity, biological relevance and potential technological impact.[42] So far, many STM experiments have been conducted with different porphyrinoid macrocycles to understand the adsorption structure and electronic properties of adlayers. In fact, cooper phthalocyanine (CuPc) was one of the first molecules ever imaged by STM.[43] Phthalocyanines generally adsorb on solid interfaces with the molecular plane parallel to the surface and often form long-range ordered structures at monolayer coverage. The monolayer structures of phthalocyanines are often similar since they are dominated by the balance between a maximization of the coverage and the repulsion between the densely packed molecules. In the submonolayer range, the propensity to form ordered, densely-packed structures depends on the balance between attractive and repulsive intermolecular interactions. The submonolayer structures of phthalocyanines are very different, ranging from completely disordered phases to densely packed islands.

On-surface synthesis of covalent porphyrinoid networks rely mostly on the surface-assisted dissociation of carbon-hydrogen or carbon-halogen bonds, followed by carbon-carbon bond formation between adjacent molecules. An example of porphyrinoid suface-assisted polymer formation is the covalent coupling of tetraphenylporphyrins (TTPs) recently reported by Grill *et al*.[44] Different TPP-based molecules containing one, two or four bromo substituents in the *para* position of the *meso*-aryl rings were deposited onto clean Au(111) surfaces kept at room temperature. All three TTPs were found intact on the surface after the deposition process, with all bromine atoms present in the molecules and forming ordered islands (Figure 4.6 d-f). The behavior of the molecules changed when the evaporator temperature was raised to 590 K. At this high temperature the molecules became activated, with the loss of the bromine atoms giving rise radical species that are prone to the polymerization. Upon thermal diffusion, the *in situ* formed radicals reacted with each other forming macromolecular nanostructures held together through intermolecular chemical bonds. In the case of the monobrominated porphyrin (BrTPP) the exclusive formation of dimers and no longer macromolecular structures were observed, because each building block provided only one reactive site. In the same vein, the dibrominated porphyrine (*trans*-

Br_2TPP) lead to the formation of unidimensional long linear chains whereas the porphyrine containing four bromine substituents gave rise to the construction of two-dimensional polymeric networks (Figure 4.6 g-i). The strength of the newly formed intermolecular covalent bonds was tested by lateral manipulation causing the entire molecular nanostructures (dimers, chains and 2D networks) to follow the pathway of the tip without fragmentation upon pulling on one end with the STM tip. In contrast, the same experiment performed with unsubstituted TPP led to fragile islands of molecules only maintained through van der Waals interactions.

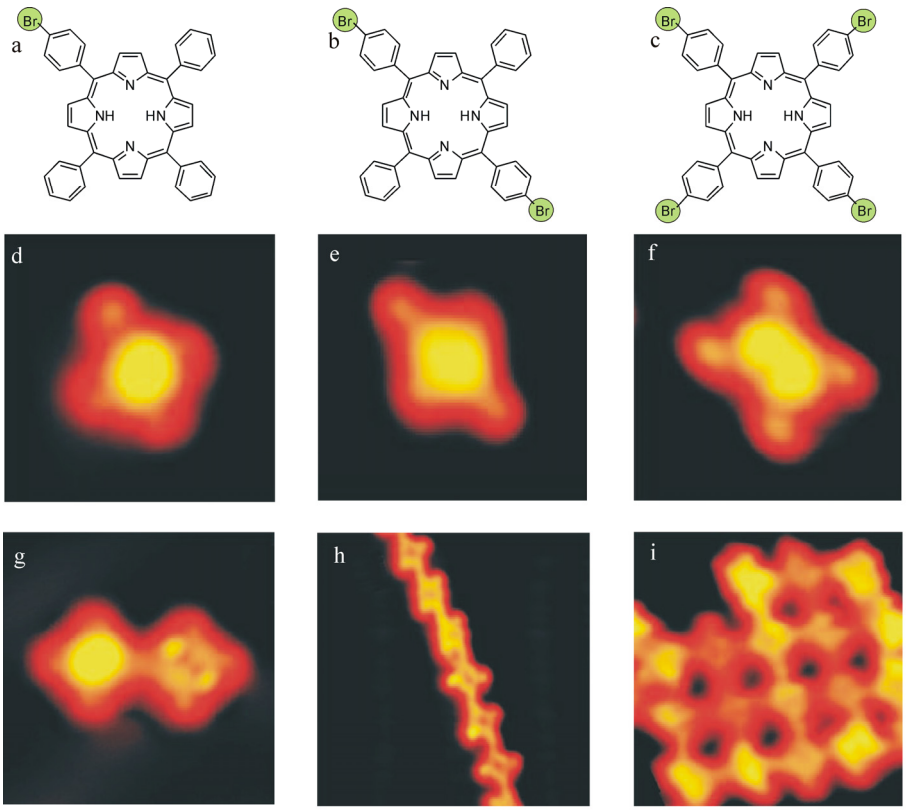

Figure 4.6 a-c) Chemical structures of the mono-, di- and tetrabrominated TPP. d-f) STM images of the intact molecules after deposition on Au(111) where the brominated legs appear larger. g-i) Detailed STM images of the nanostructures formed after sample annealing. Image adapted from reference[44]

4.1.5 Lanthanide bis(phthalocyanine) complexes on surfaces

Compared to single-decker Pc molecules, much less is known for the bonding configuration of double-decker complexes on surfaces. Their future technological application as quantum computing and high-density storage devices, are presently hampered by the difficulty of adsorbing SMMs onto surfaces, and quite importantly, by the lack of understanding on whether their magnetic properties are modified upon absorption. STM has been used to study SMMs on single crystal surfaces because of its capabilities of atomic resolution, tip manipulation and tunneling conductance measurement. In 2006, Ruiz-Molina *et al*.[45] first reported a STM study on the organization of $Tb(Pc)_2$ molecules on highly oriented pyrolytic graphite. Afterwards, double-decker lanthanoid-phthalocyanate molecules on Cu[46] and Au[47,48] surfaces were examined with STM under ultra-high vacuum and low temperature conditions.

In 2009 Yamashita *et al*. reported the direct observation of lanthanide bis(phthalocyanine) complexes on Au(111) using scanning tunneling microscopy.[47] STM images of $Tb(Pc)_2$ deposited on Au(111) surface showed two types of molecules after thermal evaporation. Figure 4.7a shows both types of molecules, one with a cross-like shape (upper part of the image) and another featuring eight-lobe structure (lower part of the figure). The alignment of the cross-like one to the surface resulted to be identical with that previously observed for H_2Pc molecules. The second one was attributed to the $Tb(Pc)_2$ double-decker. A height of 0.14 and 0.4 nm was measured for the cross-like and eight-lobe molecules respectively, which matched to the physical height of the single- and double-decker molecules. It was rationalized that the cross-like molecules corresponded to either MPc or H_2Pc, which were a part of the $Tb(Pc)_2$ molecules cracked in the deposition process.

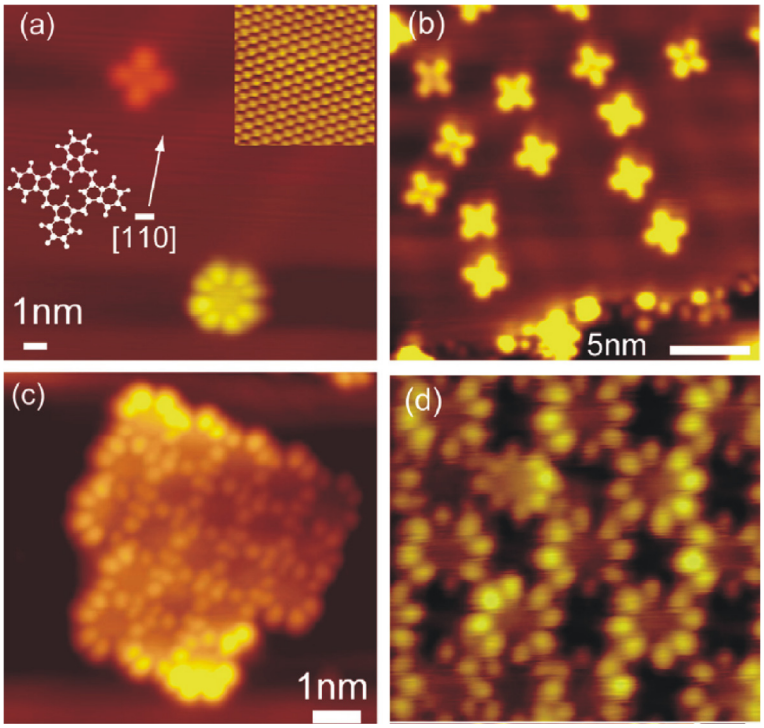

Figure 4.7 STM images of $Tb(Pc)_2$. a) molecules of single-decker (upper) and double-decker (lower). Schematic model of Pc plane is superimposed. b) single-decker molecules on the terrace part of Au(11) surface. c) $Tb(Pc)_2$ film composed of 21 molecules d) A magnified image of c).

4.2 Objectives

The future technological application of the single-molecule magnets (SMMs) as quantum computing and high-density storage devices, are presently hampered by the difficulty of adsorbing SMMs onto surfaces. The understanding on whether their magnetic properties are modified upon absorption is also a weak point: surfaces are non-innocent, as it will be shown in this chapter.

The aim of this chapter is to present a comprehensive STM study of the adsorption, self-assembly, chemical and electronic properties of two single-molecule magnet derivatives $Dy(OETAP)_2$ and $Tb(OETAP)_2$ on different metallic surfaces. Additionally, we studied the surface chemistry of the free base octaethyltetraazaporphyrin (OETAP). All these studies where done in collaboration with the groups of Prof. J. Barth (TUM, München) and Dr. D. Écija (IMDEA Nanociencia, Madrid).

4.3 Results and Discussion

4.3.1 Deposition and reactivity of the OETAP on surface

The deposition of octaethyltetraazaporphyrin (OETAP) was successfully achieved by organic molecular-beam epitaxy from a quartz crucible held at 450 K onto a clean Au(111) at room temperature. Figure 4.8 shows a high-resolution STM image of an OETAP array on Au(111) self-assembled after room temperature deposition. Each molecule is visualized as a dim center, attributed to the macrocycle, surrounded by eight brighter protrusions. They are assigned to the ethyl moieties present in the periphery of the azaporphyrine ring, in agreement with surface-confined assemblies of identically substituted porphyrinoid compounds.[49] The dense-packed architecture displays two distinctly oriented molecular species, related by a ~ 16º rotation, features a rhombic lattice (a = 28.2±1 Å, b = 14.1±1 Å, θ = 60º), and is stabilized by lateral non-covalent interactions between the ethyl substituents.

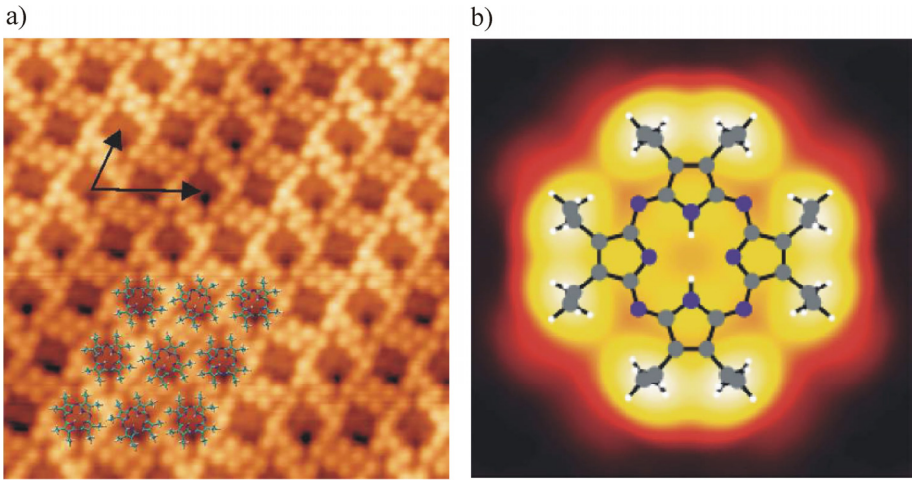

Figure 4.8 a) High-resolution STM image revealing submolecular features. Black arrows depict the lattice vectors of the rhombic unit cell. Superimposed colored atomistic models address the two distinctly oriented molecular species. Tunneling parameters: V_b = 0.5 V, I = 0.1 nA. Scale bar, 1 nm. b) STM simulated image of an individual OETAP on Au(111) at 0.5 V, with a superimposed ball-and-stick model of the molecular species. Hydrogen, carbon and nitrogen are depicted in white, grey and violet, respectively

After submonolayer deposition at room temperature, gentle annealing of the substrate to 75 ºC, 100 ºC, and 150 ºC resulted in no appreciable changes. High resolution images of the assemblies after holding the substrate at 275 ºC revealed the formation of molecular chains that were mainly confined in the face-centered cubic (fcc) regions of the Au(111) (Figure 4.9).

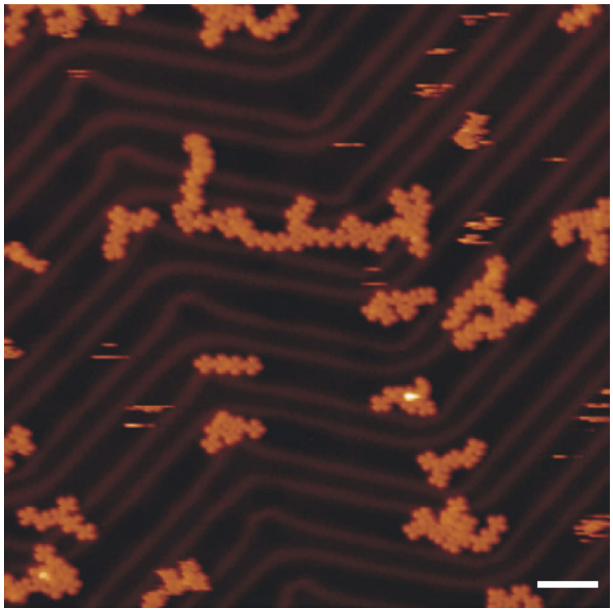

Figure 4.9 Long-range STM image displaying the formation of quasi-unidimensional polymers mainly confined to the fcc regions after deposition of OETAP on Au(111) held at room temperature and subsequent gently annealing at 275ºC. V_b = -1.5 V

A careful inspection of these chains allowed us to discern submolecular features and, thus, clarify the molecular organization. The tetrapyrrolic macrocycles cores are now visualized as dim crosses, whereas the ethyl substituents have reacted in two distinct ways:

1) Covalently linking adjacent species through the intermediacy of multiple covalent reactions

2) Undergoing an intramolecular electrocyclic ring closure (ERC) reaction with the final formation of polymeric chains, in which the repeating unit (monomer) derives from OETAP.

A statistical analysis showed that the average polymeric size was ~ 7, that the most frequent polymer comprised 6 macrocycles, and that very long polymers (>20 monomers) could be synthesized. Importantly, the majority of the monomeric entities were joined together via two covalent motifs, denote L and V (Figure 4.10). Both structural motifs are the product of multiple covalent reactions between peripheral ethyl groups from adjacent OETAP precursors, where two molecules face each other. When the two ethyl groups that initiate the intermolecular reaction lie in opposite sides of the OETAP precursors the product is an L-type motif, whereas the V-type motif is the product when the ethyl groups lie in the same side of opposite molecules. In both cases, the resulting polymer can be interpreted as phthalocyanine tapes with locally straight (L) or slightly curved (V) appearance. Notably, the thermally induced polymerization of OETAP precursors into phthalocyanine tapes seems to present a preference for the L-type coupling motif versus the V-type motif (ca 2:1). In addition, polymers are mostly quasi-unidimensional, with over 85% of monomers connected to only one or two neighbors. The remaining 15% of monomers are connected to three of the four neighbors mainly through cross motifs base on L or V coupling schemes.

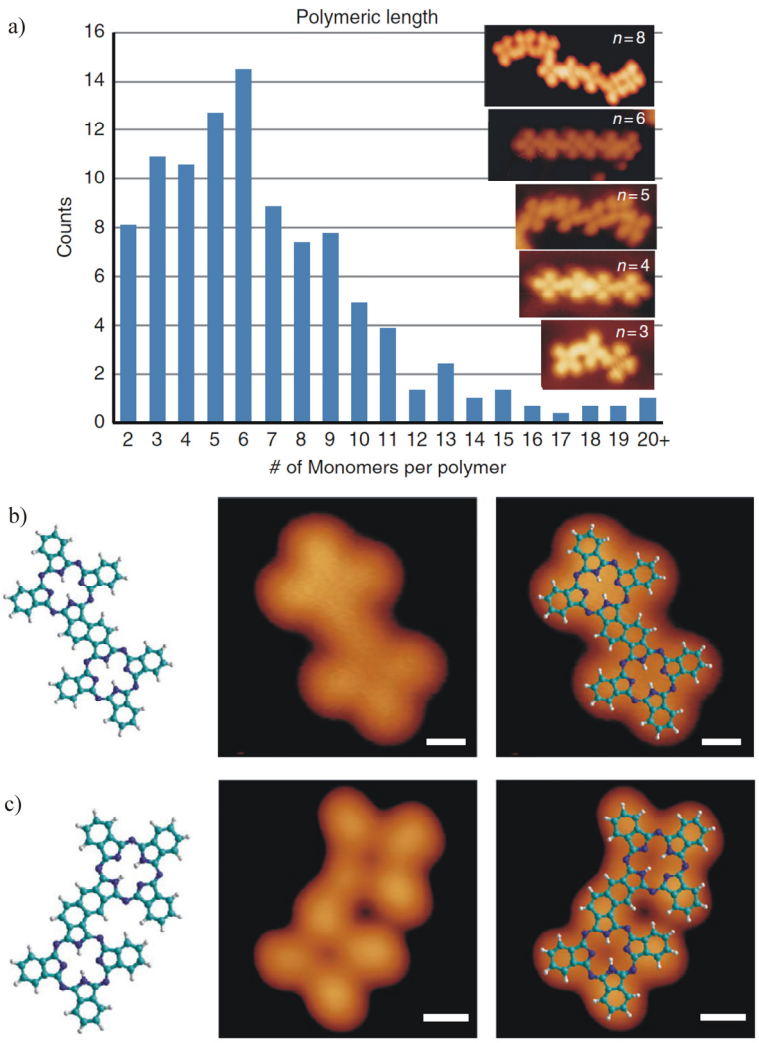

Figure 4.10 a) High-resolution STM images of polymers of distinct size (3, 4, 5, 6 and 8) and histogram of the polymeric length b) L-type covalent motif, V_b = -1.5 V, scale bar = 0.5 nm c) V-type covalent motif, V_b = -0.7 V, scale bar = 0.5nm.

Regarding the proposed covalent motifs, we are certain that the observed molecular chains are polymers and not supramolecular assemblies due to the following reasons:

1) The center-to-center distance between macrocycles is too short for a non-covalent interaction.

2) The DFT study of the reaction pathway (see below for details) is fully consistent with the experimental observations

3) Using perturbative scanning conditions, the polymers can be displaced as entire units for long distances (over 10 nm) preserving their size and shape, thus revealing a strong covalent interaction between monomers.

To test the feasibility of thermal control of the covalent reaction pathways, OETAP precursors were deposited on pristine Au(111) held at 300 ºC. As depicted in Figure 4.11, a new scenario was manifested. Instead of polymeric chains, we observe the formation of individual entities, which self-assemble into close-packed arrays based on a square unit cell. High-resolution STM imaging allowed us to discern submolecular features of the assemblies, whereby each molecule species presents four bright protrusions and a central void forming a cross-like shape. Both the molecular appearance and the self-assembled architecture are identical to those found after deposition of 2H-Pc (free base phthalocyanine) on Au(111).[50] Thus, based on our results and a comparison with the literature, we suggest that the deposition of the OETAP precursors on Au(111) held at 300 ºC gives rise to the formation of 2H-Pc species, thanks to the dehydrogenation and ring closure of their ethyl peripheries, a phenomenon similarly encountered on porphyrin derivatives.[49]

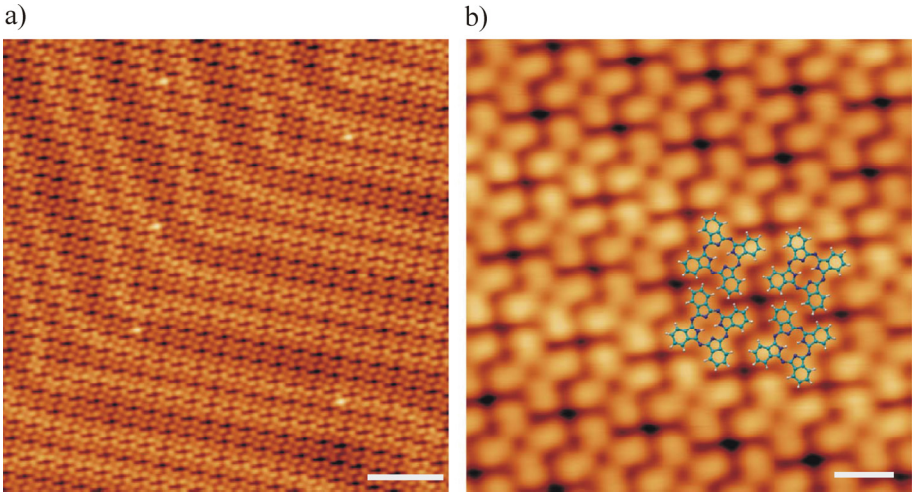

Figure 4.11 Surface-assisted synthesis and self-assembly of phthalocyanines. The deposition of OETAP species on Au(111) held at 300 ºC affords the on-surface chemical transformation of precursors into phthalocyanine species. a) Long-range STM image, revealing the close-packed supramolecular assembly and highlighting the presence of the herringbone reconstruction of Au(111), V_b = -1 V, scale bar = 5 nm. b) High-resolution STM image and superimposed modelling of the molecular constituents, which matches the reported assembly of 2H-Pc on Au(111), V_b = -1 V, scale bar = 1 nm

To address the reaction mechanisms that could plausibly explain the formation of the covalent phthalocyanine polymers and the creation of phthalocyanine monomers, a detailed analysis of the STM images collected during the annealing process was carried out. Figure 4.12 illustrates reaction intermediates observed after depositing OETAP species holding the substrate at room temperature, subsequently followed by gently annealing to 225ºC.

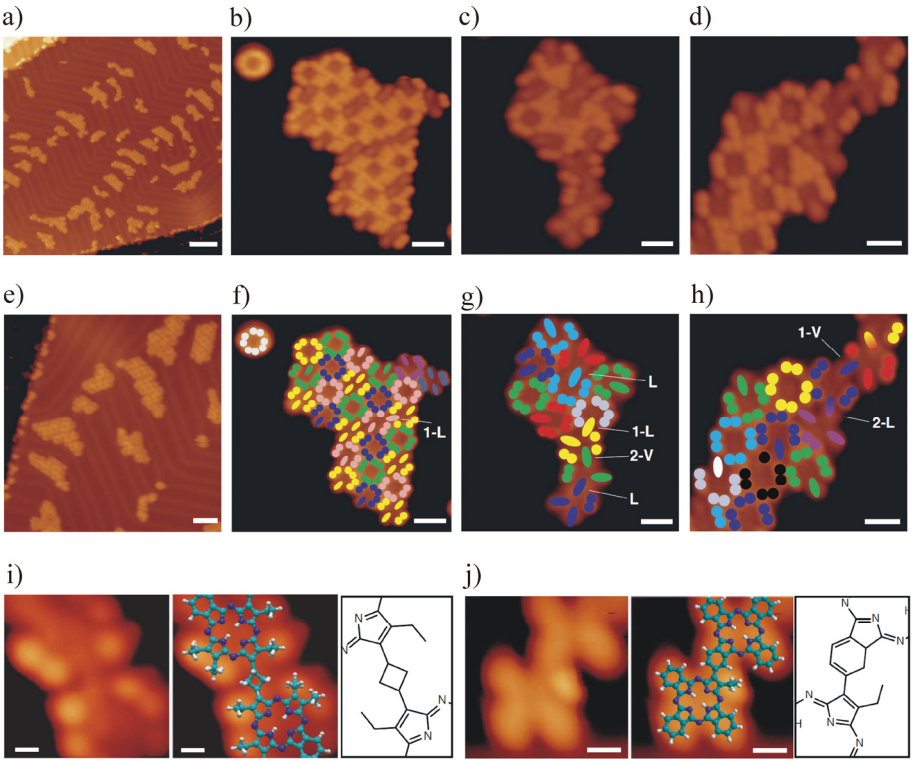

Figure 4.12 Surface-assisted formation of phthalocyanine derivatives after deposition of OETAP precursor on Au(111). a) and e) large-scale STM images showing the formation of patches of initially reacted molecules coexisting with unreacted species. b-d) High-resolution STM images and f-h) corresponding schematic coloring of the initial steps of reactions giving motifs **1-L**, **1-V**, **2-L**, **2-V** and **L**. i and j) Zoom-in of motif **1-L** and **2-L**, and superimposed modelling, together with chemical drawing insets. Colored filled dots represent ethyl moieties, bi-colored ellipses show covalent connections between adjacent species, and mono-colored ellipses represent full electrocyclic ring closures. Tunneling parameters: a) V_b = -0.8 V; b) V_b = -0.7 V; c) V_b = -0.7 v; d) V_b = -0.8 V; e) V_b = -1.2 V; i) V_b = 0.5 V and j) V_b = -1.5 V. Scale bars: a) 10 nm; b) 1.5 nm; c) 1.0 nm; d) 1.0 nm; e) 5 nm; f) 1.5 nm; g) 1.0 nm; h) 1.0 nm; i) 0.3 nm and j) 0.5 nm.

Long-range STM images show the formation of small islands mainly distributed over the fcc regions of the Au(111) surface, thus revealing the dissolution of the former OETAPs islands and subsequent self-assembly into smaller patches. High-resolution topographs allow us to discern submolecular features and elucidate the molecular packing. For clarity, Figure 4.12 f-h displays a rationalization of the distinct molecular species by superimposing a colored model. Here, dots and rods of the same color represent intact ethyl moieties and

ERC-reacted ethyl termini of the same molecule, respectively. In addition, bi-colored rods indicate links between tetrapyrrole molecular units. A minority of unreacted OETAP species, characterized by the eight-dotted appearance described above, are still observed either isolated on the surface or forming part of the supramolecular islands. However, most of the molecular precursors have experienced covalent reactions, giving rise to the reaction intermediates of the polymeric chains. The majority of OETAPs have undergone one or two ring closure reactions (intramolecular electrocyclizations) that transformed their diethyl-pyrrole units into isoindole components, which are imaged as rods. At this stage of the reaction, some of the OETAPs are also covalently linked to one another, affording distinct covalent bonding motifs, assignable to intermediates of the two main final structures (L and V). **1-L** and **2-L** represent reaction intermediates of the L-type coupling motif, whereas **1-V** and **2-V** are the corresponding analogous reaction intermediates of the V-type binding motif. We observe that the intermolecular bond in intermediate **1-L** comprises the reaction between two ethyl moieties in opposite sides of the OETAP precursors, keeping the other two ethyl peripheries of the pyrroles interact, which are visualized as bright lobes with the same height as individual unaltered OETAPs. In **2-L**, the reaction appears to have evolved, involving another ethyl group, thus keeping only one of the four initial ethyl groups unreacted. Finally, in **L**, the four ethyl groups have reacted to produce the seed of a polymeric chain.

Taking into account the initial precursors, the identified intermediates and the final products, we tentatively propose multi-step reaction mechanism for both pathways, the polymerization of OETAPs into phthalocyanine quasi-unidimensinoal tapes and the transformation of OETAP species into substituted monomeric phthalocyanines.

At the first stage of the polymeric reaction, two OETAPs face each other, positioning four ethyl moieties opposite each other, which will undergo a series of complex reactions activated by the ramp annealing of the substrate. We propose that the ethyl substituents undergo an initial dehydrogenation reaction to produce an ethenyl residue per molecule, either with *cis* or *trans* conformation (Figure 4.13). Two opposite ethenyl groups adequately oriented are susceptible to react via [2+2] cycloaddition affording intermediate **1-L** (or **–V**), which is repeatedly observed by STM imaging. Further work is necessary to

corroborate this mechanism. The L-to-V ratio in the final coupling motifs (ca 2:1) corresponds to a preferential ethyl-to-ethenyl dehydrogenation favoring the conformation where the ethenyl group lies in trans to the bond opposite to the pyrrolic nitrogen. Intermediate **1-L/V** can be considered as a dimer of two OETAP macrocycles joined together through a four-membered ring, fitting the appropriate angles and bond distances. This type of reaction, thermally forbidden by the Woodward-Hoffmann rules, is unprecedented on metallic surfaces and has only been explored on semiconductor surfaces to covalently functionalize the substrate support, whereby dangling bonds play a major role. Encouragingly, DFT simulation support the tentative [2+2] cycloaddition (vide infra).

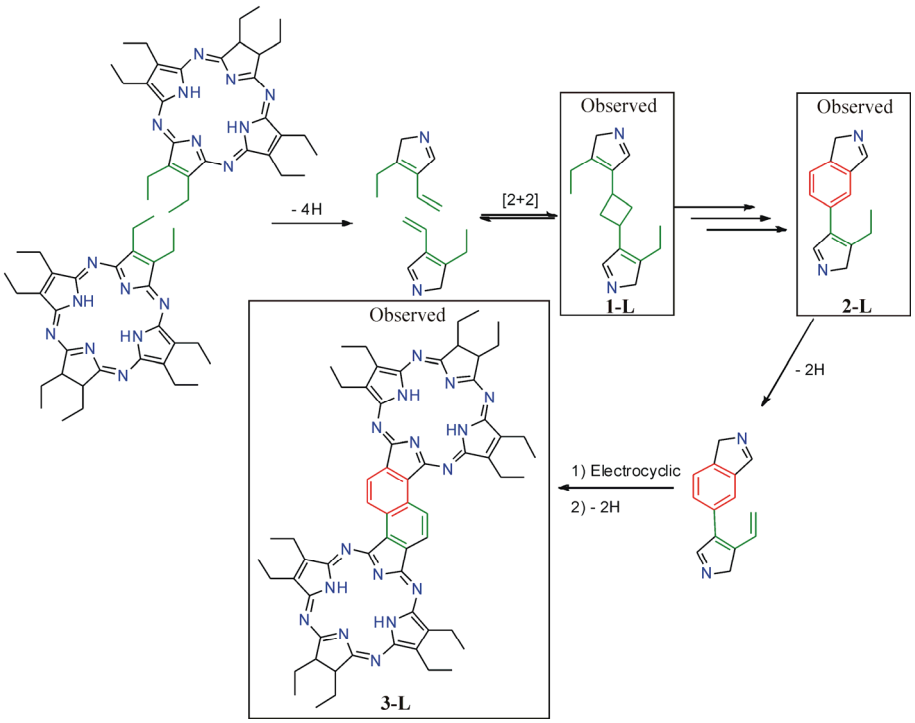

Figure 4.13 Proposed reaction mechanism describing the surface-assisted formation of phthalocyanine polymers on Au(111) with the STM-imaged intermediates **1-L** and **2-L** in the phthalocyanine dimer **3-L** formation via L-type linking.

To explain intermediate **2-L/V**, also observed by STM imaging, a series of chemical reactions, including the loss of two methylene groups (as ethene), is tentatively suggested. An additional dehydrogenation reaction of the remaining ethyl substituent and subsequent 6-π electrocyclization reaction followed by an aromatization process results in the formation of STM-characterized dimer **3**, observed in both L and V conformation, with a naphthalene spacer bridging the two tetrapyrrolic macrocylces.

During the polymerization process, we observe that the ethyl groups not involved in the construction of the covalent bridging spacer undergo a series of dehydrogenation and electrocyclic ring closures, giving rise to isoindole units, and thus providing the final phthalocyanine aspect to the polymers (Figure 4.14). In short, the dehydrogenation of the β-ethyl groups followed by the intramolecular electrocyclization of the resulting ethenyl residues transformed the 3,4-diethylpyrrole units into isoindole analogues. We provide theoretical results (see below for details) supporting our suggestion that an analogous mechanism takes place in the transformation of OETAPs into 2H-Pcs, during the deposition process of the tetraazaporphyrins on Au(111) held at 300 ºC, as previously observed for β-ethyl-substituted porhyrins.[49]

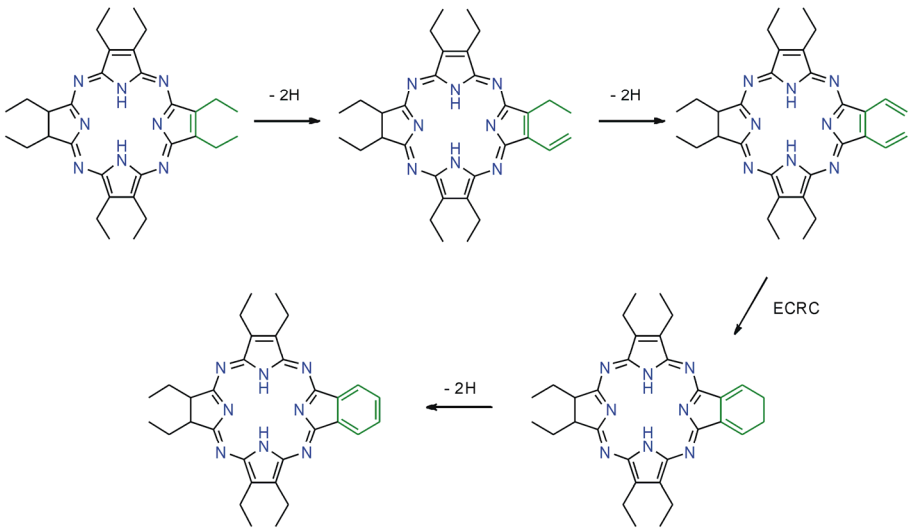

Figure 4.14 Proposed reaction mechanism describing the surface-assisted formation of phthalocyanine monomers on Au(111)

To gain additional insight into the mechanisms, DFT calculations were performed in collaboration with Dr. Jonas Björk for a model system on the Au(111) surface. The monomer electrocyclization and the initial dimerization process were studied and compared. The complete dimerization process involves a complex multi-step sequence of events and a more in-depth analysis of all reaction steps will be accounted for elsewhere. Both the monomer electrocyclization and the dimerization reaction of monomers require four preliminary dehydrogenation reactions that converted two ethyl substituents into ethenyl residues, with a largest energy barrier of 1.60 eV.

From this starting point, the monomer electrocyclization is followed by the actual ring-closing reaction, with an effective potential energy barrier of 1.82 eV as seen in figure 4.15 (the ring closure is associated with several barriers). Two dehydrogenation steps with relatively small energy barriers are required for the final aromatization process providing the isoindole units. These results suggest the possibility to tune the reaction temperature such that the ethyl-to-ethenyl transformation is triggered, without activating the ring closuring reaction owing to its significantly higher energy barrier.

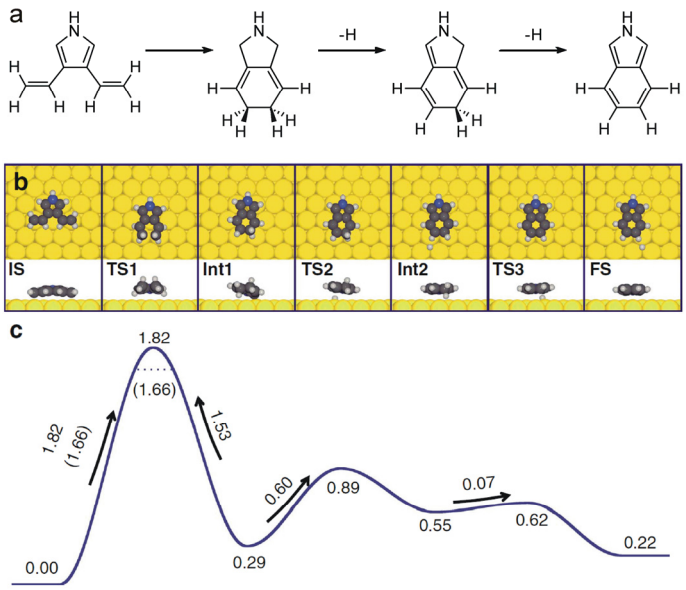

Figure 4.15 Reaction pathway considerations for a model pyrrole molecule on Au(111). a) Chemical structures of the model species involved in the monomer cyclization. b) top and side views ball models for reactants (**IS**), transition states (**TS**), reaction intermediates (**Int**) and the monomer reaction final state (**FS**) c) energy profile for the monomer cyclization. Free energy barriers are shown in parentheses and were calculated including vibrational enthalpy and entropy at 275ºC. Energies are given in units of eV.

The dimerization reaction was also investigated, starting from two monomers that have experienced a complete dehydrogenation of the ethyl residues. The reaction is initiated by a [2+2] cycloaddition with an effective potential barrier of 1.04 eV (Figure 4.16, **IS** to **Int2**). Notably, the [2+2] cycloaddition proceeds in a two-step mechanism, via an intermediate state (**Int1**) in which a carbon atom is chemically bonded to the surface. Importantly, the cycloaddition is just slightly exothermic with a reaction energy of -0.25 eV, providing a Botzmann factor of ~ 200 between **Int2** and **IS** at 275 ºC, thereby substantiating the reversibility of the coupling reaction. This supports the suggested pathway in which **IS** and **Int2** are in thermal equilibrium before the reaction proceeds in a Diels-Alder step. Future studies will unravel the information of the final steps of the dimerization.

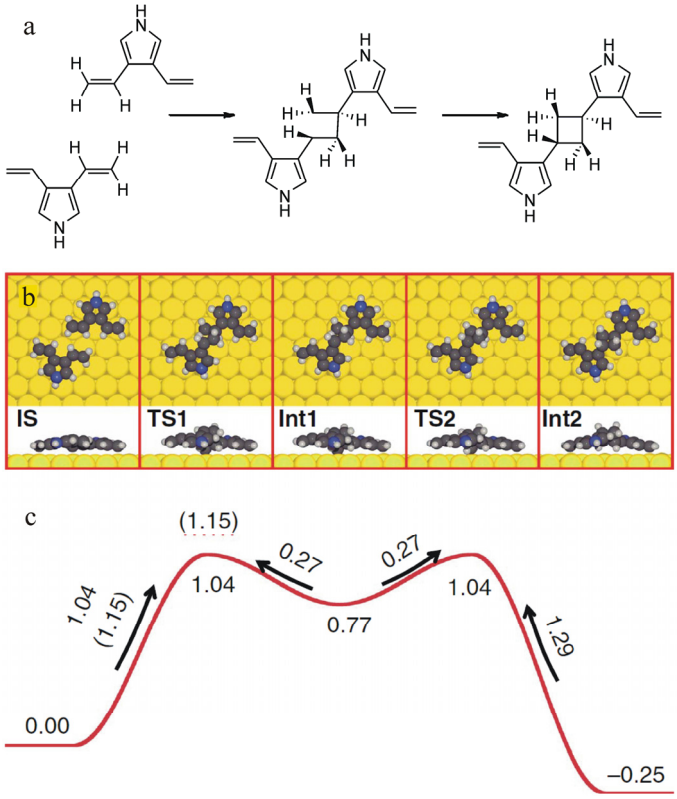

Figure 4.16 Reaction pathway considerations for a model pyrrole molecule on Au(111). a) Chemical structures of the model species involved the initial steps of the dimerization process. b) top and side views ball models for reactants (**IS**), transition states (**TS**) and reaction intermediates (**Int**) c) energy profile for the initial steps of the dimerization process. Free energy barriers are shown in parentheses and were calculated including vibrational enthalpy and entropy at 275ºC. Energies are given in units of eV.

In addition to potential energy barriers, the effect of zero-point and thermal contributions on the decisive steps of the monomer cyclization and dimerization by including vibrational enthalpy and entropy were also considered. Free energy barriers were evaluated at a temperature of 275 ºC for the initial monomer and dimerization steps. The monomer ring-closing reaction is slightly lowered by 0.16 eV whereas the free energy barrier for the dimerization is 0.11 eV larger than the corresponding potential energy barrier.

Although zero-point and thermal vibrational contributions have a small quantitative effect on the energy barriers, both the potential and the free energy landscape unambiguously demonstrate that the decisive step for the dimerization has a significantly lower barrier than the monomer cyclization, with potential energy and free energy barrier differences of 0.72 and 0.51 eV, respectively. As a result, the monomer ring-closure will occur only if the dimerization is kinetically hindered such as for extremely low coverage or in the absence of nearby non-reacted molecules. Hereby, the balance between diffusion and reaction barriers plays a crucial role, as the molecules need to meet to undergo the polymerization. These results explain why the monomer ring closure is observed for the deposition at the already heated substrate, in which situation the molecules experience the electrocyclic ring closure before meeting other species, while the intermolecular connections are formed when depositing the molecules at a room temperature substrate followed by thermal annealing allowing the precursors sufficient time to diffuse.

4.3.2 Deposition of double-deckers complexes on surfaces

The single molecule magnets $Dy(OETAP)_2$ and $Tb(OETAP)_2$, described in Chapter 3, are neutral double-decker compounds consisting in two octaethyltetraazaporphyrins coordinated by a lanthanide atom (Dy or Tb) in the center featuring a square anti-prism geometry. These novel soluble molecular species have exhibited single molecular magnetism in solution with high blocking temperatures over 50 K and 10 K, respectively, which corresponds to an activation energy for magnetization reversal of ≈ 376 K (Tb^{3+}) and ≈ 32 K (Dy^{3+}). As a result, they are promising candidates for devices exploiting single molecule magnets functionalities. $Dy(OETAP)_2$ and $Tb(OETAP)_2$ are functionalized with terminal ethyl moieties in order to enhance solubility and, more importantly, to facilitate the decoupling of the double-decker molecular backbone upon adsorption on surfaces following a flat-on geometry. In this section we will study the adsorption, self-assembly and electronic properties of $Dy(OETAP)_2$ on Cu(111) and on Au(111), and of $Tb(OETAP)_2$ on Ag(111).

The deposition of a very low coverage of $Dy(OETAP)_2$ on Cu(111) and on Au(111), and of $Tb(OETAP)_2$ on Ag(111), shows the presence of individual species on the steps and occasionally on the terraces. At negative bias, the single molecular magnets exhibit a central depression surrounded by 8 lobular protrusions (top panel of Figure 4.17 c). By assuming a flat-on adsorption, previously reported for all double-decker compounds on metallic surfaces, each lobular protrusion can be assigned unambiguously to an ethyl terminal group. At positive bias, each two ethyls belonging to the same pyrrole moiety are imaged as an elongated protrusion (bottom panel of Figure 4.17 c).

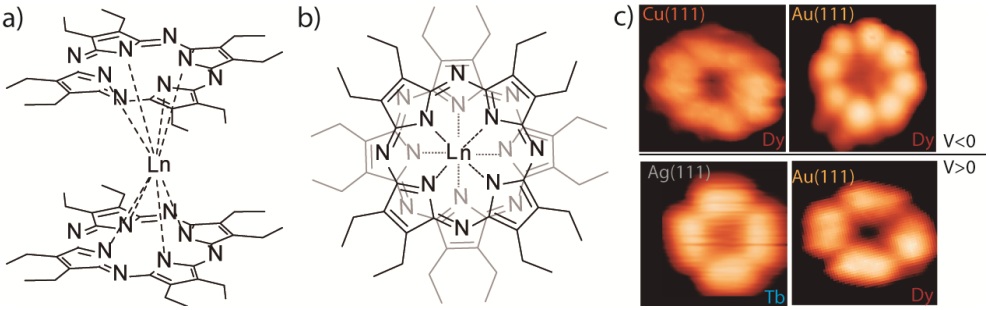

Figure 4.17 a) Chemical structure of the $Ln(OETAP)_2$ illustrated in perspective. b) Top view of the $Ln(OETAP)_2$ molecular species, and c) STM images at positive and negative bias of individual $Dy(OETAP)_2$ on Cu(111) and on Au(111), and $Tb(OETAP)_2$ species on Ag(111).

The deposition of higher coverages of molecular species lead to the formation of long-range ordered supramolecular architectures, which look like very similar for the distinct double-decker molecular species and surfaces (Figure 2). The diffusion and creation of ordered islands hints to physisorption of the molecular species, of great importance to preserve their electronic and magnetic properties.

Figure 4.18 shows a long-range STM image, a high-resolution STM image, and a model of the close-packed assembly of $Dy(OETAP)_2$ on Au(111) and of $Tb(OETAP)_2$ on Ag(111). Molecular species are clearly distinguishable and identified as depressions (macrocycles) surrounded by eight or four protrusions (ethyl moieties at negative (Figure 4.18 a,b) and positive bias (Figure 4.18 c,d), respectively). The assembly is stabilized by van der Waals intermolecular interactions between adjacent ethyl substituents, giving rise to a hexagonal network characterized by a lattice vector with an average length of 14.4 ± 0.5 Å for $Dy(OETAP)_2$ on Au(111) (equivalent results are observed on Cu(111)) and of 14.2 ± 0.5 Å for $Tb(OETAP)_2$ on Ag(111).

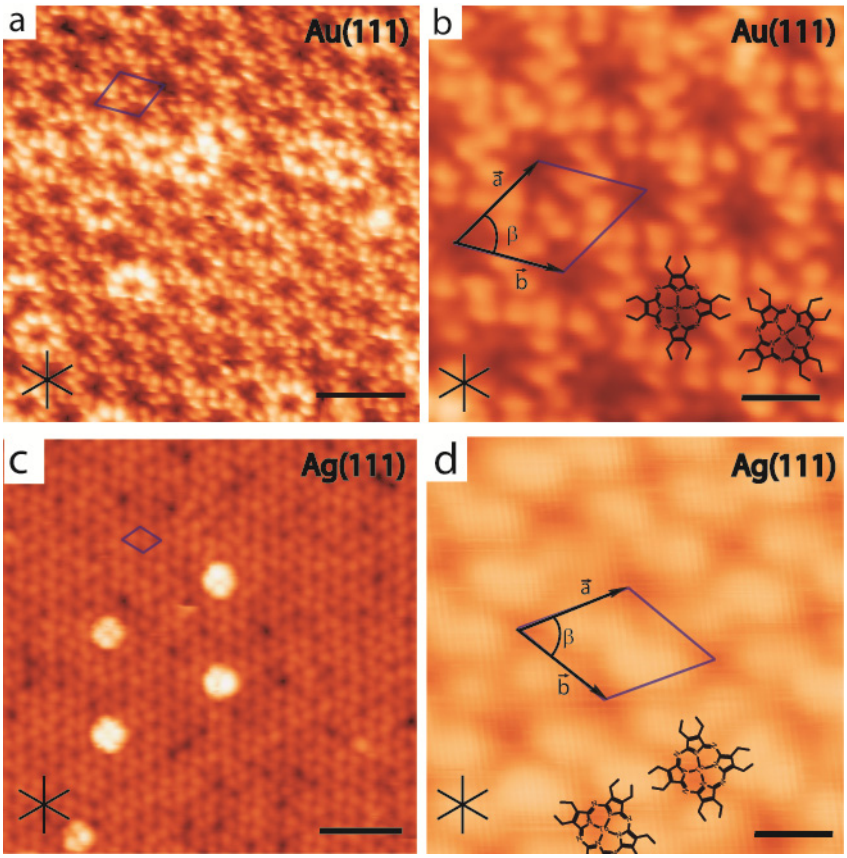

Figure 4.18 Self-assembly of $Ln(OETAP)_2$ species on coinage metals. a) Long-range STM image showing the self-assembly of $Dy(OETAP)_2$ on Au(111) featuring a hexagonal network. Black star corresponds to the high-symmetry directions of the Au(111) surface. Scale bar = 3 nm. Tunneling parameters: I_t =60 pA and V_{bias} = -2.3 V. b) Zoomed-in STM image highlighting the hexagonal described by the unit cell vectors, $\vec{a}$ and $\vec{b}$, and the angle β. Additionally, the superimposed model of $Dy(OETAP)_2$ exhibits the correlation between the eight protrusions observed in the image and the eight ethyl legs of each top monomer. Scale bar = 1 nm. Tunneling parameters: I_t = 60 pA and V_{bias} = -2.3 V. c) Long-range STM image of the self-assembly of $Tb(OETAP)_2$ on Ag(111) showing hexagonal close-packed assembly similar to those of $Dy(OETAP)_2$. Scale bar = 6nm. Tunneling parameters: I_t= 100 pA and V_{bias}= 1.5 V. d) High resolution STM image showing the unit cell vectors, which are analogous to those found for the adsorption and self-assembly of $Dy(OETAP)_2$ on Cu(111) and on Au(111). Scale bar = 1nm. Tunneling parameters: I_t= 100 pA and V_{bias}= 1.5 V.

A careful inspection on the brightness of the double-decker species reveals two different entities. Occasionally, we also observed very bright species, easily removable by normal

scanning and, thus, attributed to second layer double-decker entities (bright species in Figure 2c). In order to prove the integrity of the deposited species, we focused on the $Dy(OETAP)_2$ species and performed two distinct experiments.

First, deposition in vacuum conditions on a cold anode and subsequent NMR showed that intact [$Dy(OETAP)_2$)] were sublimated from the crucible (Figure 4.19).

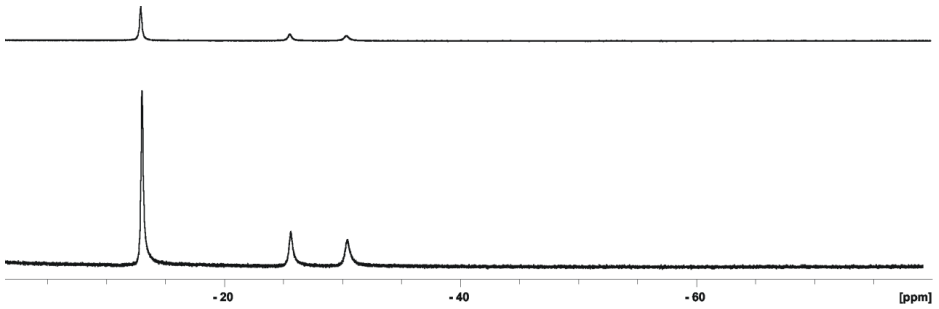

Figure 4.19 Selected region of the ^1H NMR spectra in $CDCl_3$ of $Dy(OETAP)_2$ as prepared (below) and $Dy(OETAP)_2$ sublimed at 630 K under a reduced pressure of 10 mbar (above).

Second, to discard on-surface molecular cracking due to the interaction with the substrate, we sublimated free-base OETAP molecules on Au(111). These single-decker species self-assemble into a quasi-hexagonal close-packed (Figure 4.20). Importantly, a comparison of the apparent height of double-decker *vs* single-decker species at V_{bias} = -1.5 V reveals a higher value for the double-decker entities (4.4 Å *vs* 1.4 Å), which is qualitatively consistent with our argumentation. Moreover, the islands formed by OETAP exhibit the characteristic herringbone motif of Au(111), related to the physisorption of the species. A third argument in favor of intact adsorption and self-assembly of the single molecule magnets is the lack of statistically relevant broken species on the surfaces after the deposition of $Dy(OETAP)_2$ or $Tb(OETAP)_2$ on the coinage metals. This is observed even on the more reactive Cu(111) substrate, which is not frequent for double-decker derivates,[51,52,53] and highlights the potential of $Dy(OETAP)_2$ (and analogously of $Tb(OETAP)_2$) for applications demanding thermal sublimation.

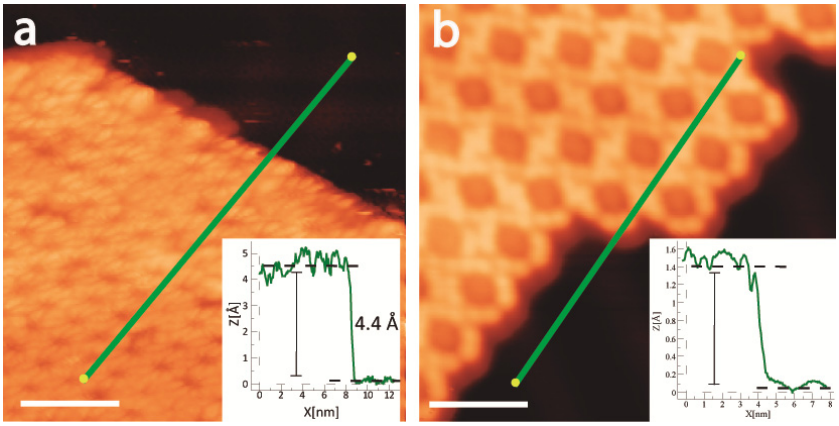

Figure 4.20 Supramolecular assembly of double-decker versus single-decker species on Au(111). a) STM image and associated height profile (green line) of a supramolecular lattice of $Dy(OETAP)_2$ on Au(111). The inset shows an average height of the islands with respect to the metal support of 4.4 ± 0.4 Å. b) STM image and associated height profile (green line) of the close-packed assembly of free base OETAP on Au(111). The inset shows an average height of the supramolecular island with respect to the metal support of 1.4 ± 0.2 Å, clearly lower than the case in a).

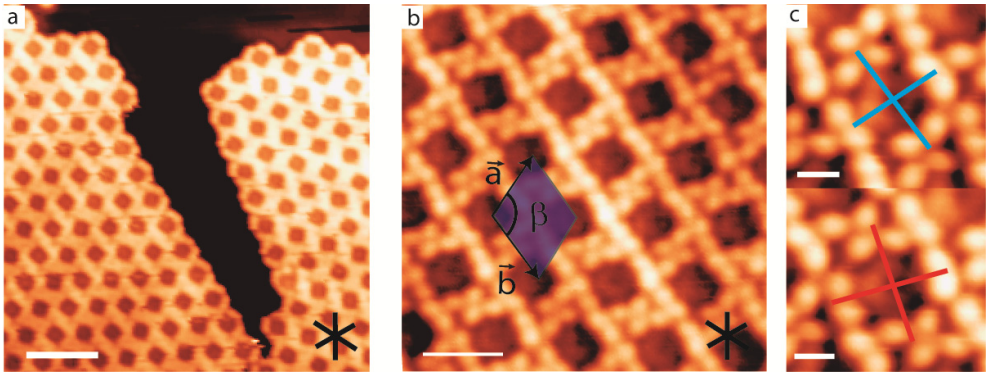

Figure 4.21 a) Long-range STM image showing two different orientations for the self-assembled phase of $Tb(OETAP)_2$ on Au(111) (I_t =50 pA, V_{bias} = -1.0 V, Scale Bar= 3nm). b) High-resolution STM image highlighting the hexagonal unit cell described by the basis vectors $\vec{a}$ and $\vec{b}$ and the angle β. The average length of the unit cell vectors is 15.1 ± 0.5 Å, and the internal angle β has a value of 121 ± 1° (I_t =25 pA, V_{bias} = 1.0 V, Scale Bar= 1.2 nm). c) Zoomed-in image showing the appearance of a single unit, completely different than $Dy(OETAP)_2$. Red and blue crosses show the two different absorption orientations of the monomers within the islands (I_t =25 pA, V_{bias} = 1.0 V, Scale Bar= 0.4 nm).

Once the geometrical properties of the supramolecular lattices were described, we performed XPS measurements to investigate the chemical and electronic properties of $Dy(OETAP)_2$ upon adsorption on Au(111) and Cu(111), respectively. Figure 4.22 shows the spectra for the C1s, N1s and Dy $3d_{\frac{5}{2}}$ core levels at monolayer and multilayer regime.

First, we focused on the monolayer regime and compare the influence of the distinct surfaces. As illustrated in the top panel of Figure 4.22, the C1s spectra showed a 0.1 eV energy shift between the samples prepared on different substrates (top left panel), no change in the case of N1s peak (top middle panel), and minute variation of 0.1 eV for the Dy $3d_{\frac{5}{2}}$ spectra (top right panel).

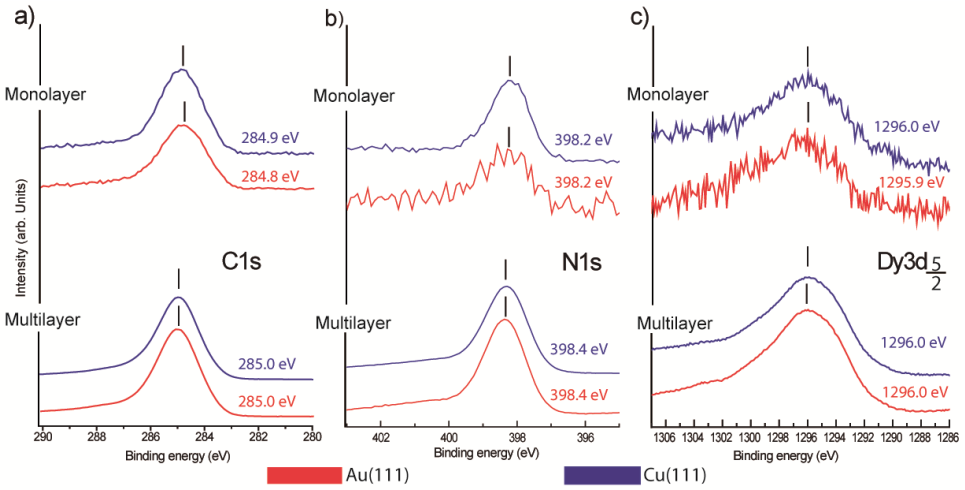

Figure 4.22 XPS spectra of the deposition of $Dy(OETAP)_2$ for monolayer and multilayer regimes on Au(111) and on Cu(111), respectively, indicating minute and negligible influence of the distinct surfaces. Red spectra depict samples grown on Au(111) and blue ones on Cu(111), respectively. a) C1s core level spectra for the monolayer and the multilayer regime. b) Spectra for N1s level highlighting an energy shit of 0.2 eV to higher energies in the multilayer sample. c) Dy $3d_{\frac{5}{2}}$ spectra showing minute differences between the multilayer and the monolayer.

In order to discard that the surfaces are similarly interacting with the absorbed single molecule magnets, we performed a multilayer deposition on Au(111) and on Cu(111), respectively, and compared the resulting XPS spectra with the monolayer deposition. Thanks to this strategy, we have access to the top layers of the sample, which are not interacting with the surface and, thus, charge transfer from the metallic support to these top

layers is strongly inhibited. For both surfaces, the C1s and the N1s core levels are shifted 0.1 and a 0.2 eV as compared to the monolayer case (bottom panel in Figure 4.22a and b, respectively). In the monolayer regime, the flat-on adsorption of the double-decker species implies that the lower tetra-azaporphyrin decker is in direct contact with the surface, which is responsible for this minute shift in binding energy. Notably, the dysprosium spectra are barely unchanged, indicating that the electronic and chemical state of the metal center is protected. On the contrary, previous XPS reports on the behavior of FePc on Ag(111), CoPc on Au(111) and CoOEP on Au(111) revealed a massive influence of the substrate for the monolayer regime, which shifts towards higher binding energies the Fe $2p_{3/2}$ peak by 1.4eV, the Co $2p_{3/2}$ peak by 2 eV for CoPc[54] and by 1.6 eV for CoOEP[54] as compared to the multilayer cases.

Finally, to expand the scope of our findings and the potential of our chemical approach, we studied the XPS fingerprints of a related double-decker species $Tb(OETAP)_2$ on Ag(111) for multilayer and monolayer regime. Figure 4.23 corroborates that the effect of the substrate on the electronic properties is negligible, in agreement with our findings for $Dy(OETAP)_2$ on Au(111) and Cu(111).

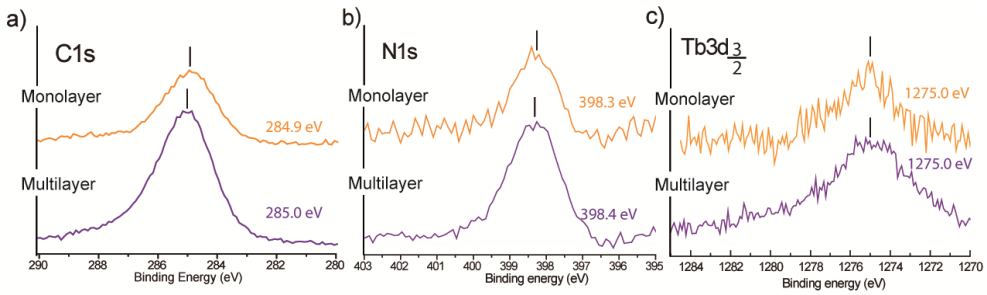

Figure 4.23 a) XPS spectra of C1s core level for $Tb(OETAP)_2$ deposited on Ag(111) in the monolayer (orange) and multilayer (violet) regime, exhibiting a minor shift of 0.1 eV in agreement with the other species. b) Similar results for the N1s core level. c) Tb $3d_{\frac{3}{2}}$ monolayer and multilayer spectra showing the decoupling of Tb with the surface.

Based on our results, we conclude that neither the ligands nor the metal chemical and electronic properties are importantly modified upon adsorption on surfaces, and thus let us

suggest that the single-ion anisotropy is preserved. Consequently, the studied double-decker species are ideal for future studies on magnetic properties on distinct surfaces, targeting for applications in magnetic storage and spin transport.

4.4 Conclusions

In summary, we have successfully introduced thermally tunable pericyclic reactions on surfaces, engineering quasi-unidimensional phthalocyanine tapes or self-assembled phthalocyanines on a well-defined Au(111). Systematic molecular-level STM observation, complemented by DFT simulations, allowed the identification of the decisive parameters for the assembly procedure and the characterization of the resulting nanoarchitectures in exquisite detail.

Our results introduce novel pathways to thermally control peryclicic reactions on surfaces allowing the induction of the growth of unprecedented polymeric heteroatomic nanoarchitectures or the production of monomeric reactions. This study discloses new avenues to grow uni- and two-dimensional polymeric nanoarchitectures embedding heteroatomic monomers. Such systems bear prospects for molecular electronics, optoelectronics and photovoltaics.

On the other hand, we present a comprehensive STM, XPS and DFT study of the adsorption, self-assembly, chemical and electronic properties of $Dy(OETAP)_2$ and $Tb(OETAP)_2$ on coinage metals. We prove the deposition of intact molecular species on Au(111), Cu(111), and Ag(111) following a physisorbed flat-on fashion and show their assembly on hexagonal close-packed networks. Systematic XPS studies reveal the negligible influence of the surface on the chemical and electronic properties of the decker ligands and the lanthanide metal, thus anticipating the protection of their single-ion anisotropy.

Our study opens new avenues to protect the single molecule magnetism of lanthanide double- decker species by a convenient synthesis of peripheral decoupling ligands, which is key for future use of these molecular species on information storage and spin transport.

4.5 Experimental section

The experiments were performed in a custom designed ultra-high vacuum system that hosts a low-temperature Omicron scanning tunneling microscope, where the base pressure was below 5×10^{-10} mbar. All STM images were taken in constant-current mode with electrochemically etched tungsten tips, applying a bias (V_b) to the sample and at a temperature of ~ 80 K. The Au(111) substrate was prepared by standard cycles of Ar^+ sputtering (800 eV) and subsequent annealing to 723 K for 10 minutes. Octaethyltetraazaporphyrin (OETAP) molecules were deposited by organic molecular beam epitaxy (OMBE) from a quartz crucible held at 450 K onto a clean Au(111) at room temperature, if not stated otherwise. If necessary, in a subsequent step, the samples were annealed with a thermal gradient of 1 ºC·s^{-1} and kept at the desired temperature for 30 min. Next, they were cooled down to room temperature with a thermal gradient of – 1 ºC·s^{-1} and finally transferred to the STM stage held at 77 K.

Periodic density functional theory (DFT) calculations were performed with the VASP code,[55] using the projector-augmented wave method.[56] Exchange-correlation effects were described by the version of the van der Waals density functional[57] (vdWDF) introduced by Hamada[58] denoted as rev-vdWDF2. Transition states were calculated using the climbing image nudged elastic band[59] and the Dimer methods.[60] STM simulations were carried out with the Tersoff-Hamann[61] approximation using the implementation by Lorente and Persson.[62]

For the deposition of the double-decker complexes, all samples were investigated in ultra-high vacuum (UHV) conditions at a base pressure of 10^{-10} mbar. Au(111), Ag(111) and Cu(111) substrates were prepared by repeating cycles of annealing to 630 K, 650 K and 730 K respectively and Ar^+ ion sputtering. $Dy(OETAP)_2$ and $Tb(OETAP)_2$ molecules were evaporated by means of organic molecular beam epitaxy out of a quartz crucible heated up to 550 K. All STM images were recorded with electrochemically etched W-tips in constant-current mode, applying voltage biases to the samples. The X-ray spectra were acquired by radiating the sample with 1486.6 eV photons coming from the Aluminum Kα transition and

collecting the emitted electrons with a commercial hemispherical detector. Curves have been fitted by Lorentzian functions directly on the acquired data; except for the nitrogen spectra on Ag(111), the dysprosium spectra on Au(111) and Cu(111) and the terbium spectra on Ag(111), which have been substrate-subtracted.

4.6 References

[1] Binnig, G.; Rohrer, H.; Gerber, C.; Weibel, E. "Tunneling through a Controllable Vacuum Gap". *Appl. Phys. Lett.* **1982**, *40*, 178.

[2] Binning, G.; Rohrer, H.; Gerber, C.; Weibel, E. "Surface Studies by Scanning Tunneling Microscopy". *Phys. Rev. Lett.* **1982**, *49*, 57.

[3] Stroscio, J. A.; Celotta, R. J. "Controlling the Dynamics of a Single Atom in Lateral Atom Manipulation". *Science* **2004**, *306*, 242.

[4] Bartels, L.; Meyer, G.; Rieder, K. H. "Basic steps of lateral manipulation of single atoms and diatomic clusters with a scanning tunneling microscope tip". *Phys. Rev. Lett.* **1997**, *79*, 697.

[5] Eigler, D. M.; Schweizer, E. K. "Positioning Single Atoms with a Scanning Tunneling Microscope". *Nature* **1990**, *344*, 524.

[6] Bouju, X.; Joachim, C.; Girard, C. "Single-atom motion during a lateral STM manipulation". *Phys. Rev. B* **1999**, *59*, R7845.

[7] Bartels, L.; Meyer, G.; Rieder, K. H. "Controlled vertical manipulation of single CO molecules with the scanning tunneling microscope: A route to chemical contrast". *Appl. Phys. Lett.* **1997**, *71*, 213.

[8] Eigler, D. M.; Lutz, C. P.; Rudge, W. E. "An Atomic Switch Realized with the Scanning Tunneling Microscope". *Nature* **1991**, *352*, 600.

[9] Adriaenssens, L.; Ballester, P. "Hydrogen bonded supramolecular capsules with functionalized interiors: the controlled orientation of included guests". *Chem. Soc. Rev.* **2013**, *42*, 3261.

[10] Scarel, F.; Ehli, C.; Guldi, D. M.; Mateo-Alonso, A. "A non-covalent strategy to prepare electron donor-acceptor rotaxanes". *Chem. Commun,* **2013**, *49*, 9452.

[11] GomezLopez, M.; Preece, J. A.; Stoddart, J. F. "The art and science of self-assembling molecular machines". *Nanotechnology* **1996**, *7*, 183.

[12] Theobald, J. A.; Oxtoby, N. S.; Phillips, M. A.; Champness, N. R.; Beton, P. H. "Controlling molecular deposition and layer structure with supramolecular surface assemblies". *Nature* **2003**, *424*, 1029.

[13] Blum, M. C.; Cavar, E.; Pivetta, M.; Patthey, F.; Schneider, W. D. "Conservation of chirality in a hierarchical supramolecular self-assembled structure with pentagonal symmetry". *Angew. Chem., Int. Ed.* **2005**, *44*, 5334.

[14] Yokoyama, T.; Yokoyama, S.; Kamikado, T.; Okuno, Y.; Mashiko, S. "Selective assembly on a surface of supramolecular aggregates with controlled size and shape". *Nature* **2001**, *413*, 619.

[15] Barth, J. V.; Weckesser, J.; Cai, C. Z.; Gunter, P.; Burgi, L.; Jeandupeux, O.; Kern, K. "Building supramolecular nanostructures at surfaces by hydrogen bonding". *Angew. Chem., Int. Ed.* **2000**, *39*, 1230.

[16] Griessl, S.; Lackinger, M.; Edelwirth, M.; Hietschold, M.; Heckl, W. M. "Self-assembled two-dimensional molecular host-guest architectures from trimesic acid". *Single Mol.* **2002**, *3*, 25.

[17] Dmitriev, A.; Spillmann, H.; Lin, N.; Barth, J. V.; Kern, K. "Modular assembly of two-dimensional metal-organic coordination networks at a metal surface". *Angew. Chem., Int. Ed.* **2003**, *42*, 2670.

[18] Lackinger, M.; Heckl, W. M. "A STM perspective on covalent intermolecular coupling reactions on surfaces". *J. Phys. D: Appl. Phys.* **2011**, *44*.

[19] Zwaneveld, N. A. A.; Pawlak, R.; Abel, M.; Catalin, D.; Gigmes, D.; Bertin, D.; Porte, L. "Organized formation of 2D extended covalent organic frameworks at surfaces". *J. Am. Chem. Soc.* **2008**, *130*, 6678.

[20] Weigelt, S.; Busse, C.; Bombis, C.; Knudsen, M. M.; Gothelf, K. V.; Strunskus, T.; Woll, C.; Dahlbom, M.; Hammer, B.; Laegsgaard, E.; Besenbacher, F.; Linderoth, T. R. "Covalent interlinking of an aldehyde and an amine on a Au(111) surface in ultrahigh vacuum". *Angew. Chem., Int. Ed.* **2007**, *46*, 9227.

[21] Schmitz, C. H.; Ikonomov, J.; Sokolowski, M. "Two-Dimensional Ordering of Poly(p-phenylene-terephthalamide) on the Ag(111) Surface Investigated by Scanning Tunneling Microscopy". *J. Phys. Chem. C* **2009**, *113*, 11984.

[22] Treier, M.; Richardson, N. V.; Fasel, R. "Fabrication of Surface-Supported Low-Dimensional Polyimide Networks". *J. Am. Chem. Soc.* **2008**, *130*, 14054.

[23] Marele, A. C.; Mas-Balleste, R.; Terracciano, L.; Rodriguez-Fernandez, J.; Berlanga, I.; Alexandre, S. S.; Otero, R.; Gallego, J. M.; Zamora, F.; Gomez-Rodriguez, J. M. "Formation of a surface covalent organic framework based on polyester condensation". *Chem. Commun,* **2012**, *48*, 6779.

[24] Lafferentz, L.; Eberhardt, V.; Dri, C.; Africh, C.; Comelli, G.; Esch, F.; Hecht, S.; Grill, L. "Controlling on-surface polymerization by hierarchical and substrate-directed growth". *Nat. Chem.* **2012**, *4*, 215.

[25] Zhang, Y. Q.; Kepcija, N.; Kleinschrodt, M.; Diller, K.; Fischer, S.; Papageorgiou, A. C.; Allegretti, F.; Bjork, J.; Klyatskaya, S.; Klappenberger, F.; Ruben, M.; Barth, J. V. "Homo-coupling of terminal alkynes on a noble metal surface". *Nat. Commun.* **2012**, *3*.

[26] Sanchez-Sanchez, C.; Orozco, N.; Holgado, J. P.; Beaumont, S. K.; Kyriakou, G.; Watson, D. J.; Gonzalez-Elipe, A. R.; Feria, L.; Sanz, J. F.; Lambert, R. M. "Sonogashira Cross-Coupling and Homocoupling on a Silver Surface: Chlorobenzene and Phenylacetylene on Ag(100)". *J. Am. Chem. Soc.* **2015**, *137*, 940.

[27] Bebensee, F.; Bombis, C.; Vadapoo, S. R.; Cramer, J. R.; Besenbacher, F.; Gothelf, K. V.; Linderoth, T. R. "On-Surface Azide-Alkyne Cycloaddition on Cu(111): Does It "Click" in Ultrahigh Vacuum?". *J. Am. Chem. Soc.* **2013**, *135*, 2136.

[28] Abel, M.; Clair, S.; Ourdjini, O.; Mossoyan, M.; Porte, L. "Single Layer of Polymeric Fe-Phthalocyanine: An Organometallic Sheet on Metal and Thin Insulating Film". *J. Am. Chem. Soc.* **2011**, *133*, 1203.

[29] Gopakumar, T. G.; Tang, H.; Thiel, W. R.; Hietschold, M. "Porous network structure of octacyano-metal-free phthalocyanine on the basal plane of highly oriented pyrolytic graphite". *J. Phys. Chem. C* **2008**, *112*, 7698.

[30] Lafferentz, L.; Ample, F.; Yu, H.; Hecht, S.; Joachim, C.; Grill, L. "Conductance of a Single Conjugated Polymer as a Continuous Function of Its Length". *Science* **2009**, *323*, 1193.

[31] Cai, J. M.; Ruffieux, P.; Jaafar, R.; Bieri, M.; Braun, T.; Blankenburg, S.; Muoth, M.; Seitsonen, A. P.; Saleh, M.; Feng, X. L.; Mullen, K.; Fasel, R. "Atomically precise bottom-up fabrication of graphene nanoribbons". *Nature* **2010**, *466*, 470.

[32] Gourdon, A. "On-surface covalent coupling in ultrahigh vacuum". *Angew. Chem., Int. Ed.* **2008**, *47*, 6950.

[33] Bieri, M.; Treier, M.; Cai, J. M.; Ait-Mansour, K.; Ruffieux, P.; Groning, O.; Groning, P.; Kastler, M.; Rieger, R.; Feng, X. L.; Mullen, K.; Fasel, R. "Porous graphenes: two-dimensional polymer synthesis with atomic precision". *Chem. Commun,* **2009**, 6919.

[34] Perepichka, D. F.; Rosei, F. "Chemistry Extending Polymer Conjugation into the Second Dimension". *Science* **2009**, *323*, 216.

[35] Sakamoto, J.; van Heijst, J.; Lukin, O.; Schluter, A. D. "Two-Dimensional Polymers: Just a Dream of Synthetic Chemists?". *Angew. Chem., Int. Ed.* **2009**, *48*, 1030.

[36] Sun, Q.; Zhang, C.; Li, Z. W.; Kong, H. H.; Tan, Q. G.; Hu, A. G.; Xu, W. "On-Surface Formation of One-Dimensional Polyphenylene through Bergman Cyclization". *J. Am. Chem. Soc.* **2013**, *135*, 8448.

[37] Franc, G.; Gourdon, A. "Covalent networks through on-surface chemistry in ultra-high vacuum: state-of-the-art and recent developments". *Phys. Chem. Chem. Phys.* **2011**, *13*, 14283.

[38] Liu, X. H.; Guan, C. Z.; Wang, D.; Wan, L. J. "Graphene-Like Single-Layered Covalent Organic Frameworks: Synthesis Strategies and Application Prospects". *Adv. Mater.* **2014**, *26*, 6912.

[39] Arado, O. D.; Monig, H.; Wagner, H.; Franke, J. H.; Langewisch, G.; Held, P. A.; Studer, A.; Fuchs, H. "On-Surface Azide-Alkyne Cycloaddition on Au(111)". *Acs Nano* **2013**, *7*, 8509.

[40] Grill, L.; Dyer, M.; Lafferentz, L.; Persson, M.; Peters, M. V.; Hecht, S. "Nano-architectures by covalent assembly of molecular building blocks". *Nat. Nanotechnol.* **2007**, *2*, 687.

[41] Bieri, M.; Nguyen, M. T.; Groning, O.; Cai, J. M.; Treier, M.; Ait-Mansour, K.; Ruffieux, P.; Pignedoli, C. A.; Passerone, D.; Kastler, M.; Mullen, K.; Fasel, R. "Two-

Dimensional Polymer Formation on Surfaces: Insight into the Roles of Precursor Mobility and Reactivity". *J. Am. Chem. Soc.* **2010**, *132*, 16669.

[42] Auwarter, W.; Ecija, D.; Klappenberger, F.; Barth, J. V. "Porphyrins at interfaces". *Nat. Chem.* **2015**, *7*, 105.

[43] Gimzewski, J. K.; Stoll, E.; Schlittler, R. R. "Scanning Tunneling Microscopy of Individual Molecules of Copper Phthalocyanine Adsorbed on Polycrystalline Silver Surfaces". *Surf. Sci.* **1987**, *181*, 267.

[44] Grill, L.; Dyer, M.; Lafferentz, L.; Persson, M.; Peters, M. V.; Hecht, S. "Nano-architectures by covalent assembly of molecular building blocks". *Nat. Nanotechnol.* **2007**, *2*, 687.

[45] Gomez-Segura, J.; Diez-Perez, I.; Ishikawa, N.; Nakano, M.; Veciana, J.; Ruiz-Molina, D. "2-D Self-assembly of the bis(phthalocyaninato)terbium(iii) single-molecule magnet studied by scanning tunnelling microscopy". *Chem. Commun,* **2006**, 2866.

[46] Stepanow, S.; Honolka, J.; Gambardella, P.; Vitali, L.; Abdurakhmanova, N.; Tseng, T.-C.; Rauschenbach, S.; Tait, S. L.; Sessi, V.; Klyatskaya, S.; Ruben, M.; Kern, K. "Spin and Orbital Magnetic Moment Anisotropies of Monodispersed Bis(Phthalocyaninato)Terbium on a Copper Surface". *J. Am. Chem. Soc.* **2010**, *132*, 11900.

[47] Katoh, K.; Yoshida, Y.; Yamashita, M.; Miyasaka, H.; Breedlove, B. K.; Kajiwara, T.; Takaishi, S.; Ishikawa, N.; Isshiki, H.; Zhang, Y. F.; Komeda, T.; Yamagishi, M.; Takeya, J. "Direct Observation of Lanthanide(III)-Phthalocyanine Molecules on Au(111) by Using Scanning Tunneling Microscopy and Scanning Tunneling Spectroscopy and Thin-Film Field-Effect Transistor Properties of Tb(III)- and Dy(III)-Phthalocyanine Molecules". *J. Am. Chem. Soc.* **2009**, *131*, 9967.

[48] Komeda, T.; Isshiki, H.; Liu, J.; Zhang, Y.-F.; Lorente, N.; Katoh, K.; Breedlove, B. K.; Yamashita, M. "Observation and electric current control of a local spin in a single-molecule magnet". *Nat Commun* **2011**, *2*, 217.

[49] Heinrich, B. W.; Ahmadi, G.; Muller, V. L.; Braun, L.; Pascual, J. I.; Franke, K. J. "Change of the Magnetic Coupling of a Metal-Organic Complex with the Substrate by a Stepwise Ligand Reaction". *Nano Lett.* **2013**, *13*, 4840.

[50] Komeda, T.; Isshiki, H.; Liu, J. "Metal-free phthalocyanine (H2Pc) molecule adsorbed on the Au(111) surface: formation of a wide domain along a single lattice direction". *Science and Technology of Advanced Materials* **2010**, *11*.

[51] Vitali, L.; Fabris, S.; Conte, A.; Brink, S.; Ruben, M.; Baroni, S.; Kern, K. "Electronic Structure of Surface-supported Bis(phthalocyaninato) terbium(III) Single Molecular Magnets". *Nano Lett.* **2008**, *8*, 3364.

[52] Écija, D.; Auwärter, W.; Vijayaraghavan, S.; Seufert, K.; Bischoff, F.; Tashiro, K.; Barth, J. V. "Assembly and Manipulation of Rotatable Cerium Porphyrinato Sandwich Complexes on a Surface". *Angewandte Chemie International Edition* **2011**, *50*, 3872.

[53] Toader, M.; Knupfer, M.; Zahn, D. R. T.; Hietschold, M. "Initial Growth of Lutetium(III) Bis-phthalocyanine on Ag(111) Surface". *J. Am. Chem. Soc.* **2011**, *133*, 5538.

[54] Bai, Y. "Photoelectron spectroscopic investigations of porphyrins and phthalocyanines on Ag(111) and Au(111): adsorption and reactivity". Friedrich-Alexander-Universität Erlangen-Nürnberg, 2010.

[55] Kresse, G.; Furthmuller, J. "Efficient iterative schemes for ab initio total-energy calculations using a plane-wave basis set". *Phys. Rev. B* **1996**, *54*, 11169.

[56] Blochl, P. E. "Projector Augmented-Wave Method". *Phys. Rev. B* **1994**, *50*, 17953.

[57] Dion, M.; Rydberg, H.; Schroder, E.; Langreth, D. C.; Lundqvist, B. I. "Van der Waals density functional for general geometries". *Phys. Rev. Lett.* **2004**, *92*.

[58] Hamada, I. "van der Waals density functional made accurate". *Phys. Rev. B* **2014**, *89*.

[59] Henkelman, G.; Uberuaga, B. P.; Jonsson, H. "A climbing image nudged elastic band method for finding saddle points and minimum energy paths". *J. Chem. Phys.* **2000**, *113*, 9901.

[60] Kaestner, J.; Sherwood, P. "Superlinearly converging dimer method for transition state search". *J. Chem. Phys.* **2008**, *128*.

[61] Tersoff, J.; Hamann, D. R. "Theory and Application for the Scanning Tunneling Microscope". *Phys. Rev. Lett.* **1983**, *50*, 1998.

[62] Lorente, N.; Persson, M. "Theoretical aspects of tunneling-current-induced bond excitation and breaking at surfaces". *Faraday Discuss.* **2000**, *117*, 277.

UNIVERSITAT ROVIRA I VIRGILI
SYNTHESIS OF TETRA-AZAPORPHYRINS, PHTHALOCYANINES AND LANTHANIDE DOUBLE-DECKER SANDWICH COMPLEXES
Nelson Giménez Agulló

UNIVERSITAT ROVIRA I VIRGILI
SYNTHESIS OF TETRA-AZAPORPHYRINS, PHTHALOCYANINES AND LANTHANIDE DOUBLE-DECKER SANDWICH COMPLEXES
Nelson Giménez Agulló

List of abbreviations

ac	-	Alternating Current
Ac		Acetate
ºC	-	Celsius
CD	-	Circular Dichroism
COSY	-	Correlation spectroscopy
CV	-	Cyclic Voltammetry
DBU	-	1,8-Diazabicycloundec-7-ene
dc		Direct Current
DCM	-	Dichloromethane
DD		Double Decker
DFT	-	Density functional theory
DLS		Dynamic Light Scattering
DMF		Dimetylformamide
DMSO	-	Dimethylsulfoxide
DOSY	-	Diffusion Ordered Spectroscopy
DPV		Differential Pulse Voltammetry
emu		Electromagnetic units
EPR		Electron Paramagnetic Resonance
equiv.	-	Equivalent
ESI	-	Electrospray ionization
ESR		Electron Spin Resonance

FAB		Fast Atom Bombardment
fcc		Face-centered Cubic
FT-IR	-	Fourier-transform infrared spectroscopy
HPLC	-	High performance liquid chromatography
HRMS	-	High resolution mass spectrometry
IR	-	Infrared
K	-	Kelvin
kcal	-	kilocalorie
Ln		Lanthanide
MALDI	-	Matrix-assisted laser desorption ionization
Hz	-	Hertz
MCE		Magnetocaloric Effect
MM3	-	Molecular mechanics force field
MPc		Metallophthalocyanine
MS	-	Mass spectrometry
NMR	-	Nuclear magnetic resonance
Oe		Oersted
OETAP		Octaethyltetraazaporphyrin
OMBE		Organic Molecular Beam Epitaxy
Pc	-	Phthalocyanine
PDT		Photodynamic Therapy
PXRD	-	Powder X-Ray Diffraction
QTM		Quantum Tunneling of Magnetization

SMM		Single-Molecule Magnet
SQUID		Superconducting Quantum Interference Device
STM		Scanning Tunneling Microscopy
T		Tesla
TAP		Tetraazaporphyrine
TBA		Tetrabutylammonium
TEM		Transmission Electron Microscopy
THF	-	Tetrahydrofurane
TLC	-	Thin layer chromatography
TON		Turnover Number
TS	-	Transition state
UHV		Ultra High Vacuum
UV	-	Ultraviolet
V		Volt
W		Watt
XPS		X-Ray Photoelectron Spectroscopy

UNIVERSITAT ROVIRA I VIRGILI
SYNTHESIS OF TETRA-AZAPORPHYRINS, PHTHALOCYANINES AND LANTHANIDE DOUBLE-DECKER SANDWICH COMPLEXES
Nelson Giménez Agulló

UNIVERSITAT ROVIRA I VIRGILI
SYNTHESIS OF TETRA-AZAPORPHYRINS, PHTHALOCYANINES AND LANTHANIDE DOUBLE-DECKER SANDWICH COMPLEXES
Nelson Giménez Agulló

UNIVERSITAT ROVIRA I VIRGILI
SYNTHESIS OF TETRA-AZAPORPHYRINS, PHTHALOCYANINES AND LANTHANIDE DOUBLE-DECKER SANDWICH COMPLEXES
Nelson Giménez Agulló